Climate signals in coastal morphodynamics observed from optical satellite imagery

Marcan Graffin

RÉPUBLIQUE FRANÇAISE
Liberté Égalité Fraternité

Université de Toulouse

Doctorat de l'Université de Toulouse

Observation de l'influence de la variabilité climatique sur la morphodynamique côtière à partir de l'imagerie satellitaire optique

Thèse présentée et soutenue, le 28 novembre 2025 par

Marcan GRAFFIN

École doctorale
SDU2E - Sciences de l'Univers, de l'Environnement et de l'Espace

Spécialité
Océan, Atmosphère, Climat

Unité de recherche
LEGOS - Laboratoire d'Etudes en Géophysique et Océanographie Spatiale

Thèse dirigée par
Rafaël ALMAR et Erwin BERGSMA

Composition du jury
Mme Florence BIROL, Présidente, Université de Toulouse
Mme France FLOC'H, Rapporteure, Université de Bretagne Occidentale
M. Edward ANTHONY, Rapporteur, Aix-Marseille Université
M. Bruno CASTELLE, Examinateur, CNRS Aquitaine
M. Rafaël ALMAR, Directeur de thèse, IRD Occitanie-Toulouse
M. Erwin BERGSMA, Co-directeur de thèse, CNES

RÉSUMÉ (FR)

L'évolution des côtes sableuses, soumises à une large variétés de pressions naturelles et anthropiques, demeure encore mal comprise à l'échelle globale. Parallèlement, l'essor de l'observation de la Terre par satellite offre un accès sans précédent à des données spatio-temporelles étendues, ouvrant de nouvelles perspectives pour l'analyse de la morphodynamique côtière.

Dans ce contexte, cette thèse vise à mieux comprendre la dynamique des côtes sableuses à l'échelle mondiale à travers l'étude de l'évolution du trait de côte, ligne d'interface terre/mer, sur plusieurs décennies, en lien avec les modes de variabilité climatique. À cette fin, une chaîne de traitement automatisée a été développée en Python, pour extraire, traiter et analyser les images des missions Sentinel-2 et Landsat (5, 7, 8, 9). Combinant plusieurs indices spectraux et méthodes de seuillage, elle permet l'application systématique d'approches personnalisables.

1) Une validation sur huit sites ateliers met en évidence une forte dépendance de la précision des mesures aux conditions environnementales locales. Les sites macro-tidaux, en particulier, présentent une sensibilité accrue aux méthodes utilisées, générant des séries temporelles de positions du trait de côte plus bruitées. Cette hétérogénéité a permis d'établir des lois empiriques liant l'erreur de détection à la pente de plage et l'amplitude de marée, offrant un cadre pour évaluer la fiabilité des observations dans des zones dépourvues de données de terrain. 2) L'outil a ensuite été appliqué à la façade pacifique nord-américaine pour produire un jeu de données couvrant 25 ans (1997–2022). L'analyse met en évidence des variations saisonnières marquées selon la latitude, avec des excursions du trait de côte dépassant 25 m dans les états de Washington et Oregon, contre moins de 10 m au sud de la Californie. Ces fluctuations sont fortement corrélées à la puissance des vagues dans le nord de la région, tandis qu'en Basse-Californie, elles sont davantage liées aux variations du niveau de la mer. À l'échelle interannuelle, les réponses morphodynamiques varient selon les régions : au sud, les variations sont modérées et concentrées lors des épisodes ENSO (El Niño Southern Oscillation), alors qu'au nord, les réponses sont plus complexes et moins systématiques. Cette étude souligne l'influence spatiale différenciée d'ENSO, qui module la trajectoire et l'intensité des tempêtes hivernales, affectant les dynamiques d'érosion. 3) Une étude complémentaire approfondit ensuite la compréhension du trait de côte en se basant sur des données de terrain sur quatre sites pour étudier l'évolution des profils de plage intertidaux à l'aide de méthodes statistiques. Cette étude permet d'identifier une dynamique structurées autour de deux mécanismes principaux : la translation du profil intertidal et l'évolution de sa pente. Cette étude intérroge la nature ambivalente du trait de côte, qui peut être appréhendé soit comme un indicateur purement morphologique — défini comme l'intersection entre une élévation donnée et le profil de plage —, soit comme un indicateur hydro-morphologique, dont la position intègre les variations spatio-temporelles du niveau d'eau liées aux forçages climatiques. Ces deux conceptions impliquent des dynamiques distinctes, compliquant davantage l'interprétation de l'évolution du trait de côte, qui elle même n'est qu'un indicateur de l'évolution globale de la plage.

Enfin, cette thèse ouvre des perspectives concrètes pour la surveillance côtière à grande échelle, en proposant une méthodologie reproductible qui s'imbrique dans d'autres axes d'observations et de modélisations de la hydro-morphodynamique côtière, permettant de mieux comprendre et anticiper les évolutions littorales et d'appuyer la prise de décision dans un contexte de changement global.

Mots clés : Géomorphologie côtière, Trait de côte, Variabilité climatique, Satellite, Télédétection

ABSTRACT (EN)

The evolution of sandy coasts, subject to a wide variety of natural and anthropogenic pressures, remains poorly understood at the global scale. At the same time, the rapid expansion of Earth observation from satellites provides unprecedented access to extensive spatio-temporal datasets, opening new perspectives for the analysis of coastal morphodynamics.

In this context, this thesis aims to improve our understanding of sandy coast dynamics worldwide through the study of shoreline evolution — the land–sea interface — over several decades, in connection with large-scale climate variability modes. To this end, an automated processing chain was developed in Python to extract, process, and analyze images from the Sentinel-2 and Landsat (5, 7, 8, 9) missions. Combining multiple spectral indices and thresholding methods, it allows for the systematic application of customizable approaches.

1) Validation across eight pilot sites highlights a strong dependence of measurement accuracy on local environmental conditions. Macrotidal sites, in particular, exhibit increased sensitivity to the methods applied, producing noisier shoreline position time series. This heterogeneity enabled the derivation of empirical relationships linking detection errors to beach slope and tidal range, providing a framework for assessing the reliability of observations in areas lacking in situ data. 2) The tool was then applied to the North American Pacific coast to generate a dataset spanning 25 years (1997–2022). The analysis reveals pronounced seasonal variations according to latitude, with shoreline excursions exceeding 25 m in Washington and Oregon, compared to less than 10 m in southern California. These fluctuations are strongly correlated with wave power in the north of the region, while in Baja California they are more closely linked to sea-level variability. At the interannual scale, morphodynamic responses vary across regions: in the south, changes are moderate and concentrated during ENSO (El Niño–Southern Oscillation) events, whereas in the north responses are more complex and less systematic. This study underscores the differentiated spatial influence of ENSO, which modulates the trajectory and intensity of winter storms, thereby affecting erosion dynamics. 3)A complementary study further explores the shoreline concept by analyzing field data from four sites to investigate the evolution of intertidal beach profiles using statistical methods. This analysis identifies a dynamic structured around two main mechanisms: translation of the intertidal profile and changes in its slope. It also questions the ambivalent nature of the shoreline, which can be understood either as a purely morphological indicator — defined as the intersection between a given elevation and the beach profile — or as a hydro-morphological indicator, whose position reflects spatio-temporal variations in water level driven by climatic forcing. These two conceptualizations imply distinct dynamics, further complicating the interpretation of shoreline change, which is itself not directly representative of the overall beach evolution.

Finally, this thesis opens concrete perspectives for large-scale coastal monitoring by proposing a reproducible methodology that integrates with other observational and modeling approaches in coastal hydro-morphodynamics. This framework contributes to the understanding and anticipation of coastal change and supporting decision-making in the context of global change.

Keywords: Coastal geomorphology, Shoreline, Climate variability, Satellite, Remote Sensing

Remerciements

Je tiens à remercier toutes les personnes qui m'ont permis de faire de la recherche, ce que je considère être le plus beau métier du monde à ce jour, et celles et ceux m'ont soutenu, aimé et tiré vers le haut.

À mes directeurs de thèse, Rafael et Erwin, qui m'ont accordé leur confiance, qui m'ont laissé chercher là où la curiosité me menait, qui m'ont conseillé et écouté quand je doutais, merci beaucoup. Rafael, tu m'avais déjà accordé ta confiance deux ans plus tôt lorsque d'un stage de césure sur un premier sujet exploratoire (avec Vincent et Sébastien), puis pour pour une seconde étude (avec Julien!), lorsque mon projet de séjour au Canada a été annulé, merci pour tes idées et ton gout de la recherche qui m'ont inspirés. Erwin, tu as souvent veillé à ce qu'on prenne le temps de parler longuement, de la thèse et du reste, pour que chaque réunion soit agréable et utile. Tu as à coeur de faire les choses pleinement, et je te remercie pour cette rigueur et ce gout du détail. J'espère que nous garderons cette dynamique de recherche à trois, fingers crossed !

Aux autres chercheurs et chercheuses qui m'ont mis sur les rails de la recherche, merci. À Raphaël Maurin, avec qui j'ai vécu ma première expérience du travail de recherche, qui ne s'est jamais positionné comme un supérieur, et qui m'a partagé son gout de la rigueur et de la curiosité scientifique. To Peter, who trusted me enough to welcome me in his team (twice), who put me in charge of a cool study with a lot of autonomy, brought me to field campaigns, and for his guidance and kind words that have always encouraged me.

Aux collègues, qui font de la vie au labo un super cadre pour faire une thèse! Yohan, le coup de foudre amical, merci pour ton écoute et tes réflexions spontannées, je suis heureux que nous restions amis (et collègues!) malgré la distance. Il sortira un jour ce *Quenet and Graffin*! Juliette, nos discussions improvisées me manquent, tes avis me semblent toujours justes, j'espère que tu continueras à me les partager encore longtemps! Salomé, la vie de co-bureau nous va si bien, merci pour ta bonne humeur permanente, pour tes anecdotes, pour tes recommandations de films, pour les parties d'échecs, pour ton sens de la fête, et surtout pour nos discussions de recherche! Longue vie à notre amitié (et à notre collaboration scientifique uhu). Adrien et Paul, on s'est suivi au labo depuis quelques années déjà mais c'est surtout lors de cette dernière année de thèse que je vous aie réellement découvert. Content de rester au labo pour continuer à vous connaître, à causer et faire la fête, big bisous. Et à ceux que je n'ai pas encore cités, Adrien (the spurious mixing one), Lucie, Wagner, les vieux et nouveaux doctorants, et jeunes non-permanents qui participent tant à la bonne ambiance au labo! Les permanents, Julien, Fabrice, Lionel, et les autres, merci pour l'intégration et les chouettes discussions au soleil sur les terasses de Toulouse! Aux administratifs du LEGOS, qui font beaucoup pour que ce labo tienne debout, merci. À l'équipe CNES, Vincent, Stéphanie, Olivier, et les autres, qui m'ont accueilli et ont toujours été bienveillants, merci beaucoup. And thanks to the OSU (ex) colleagues, Meredith, Mohsen, Carson, and the others, for the great times I had in Corvallis.

À mes ami.e.s, qui me soutiennent/supportent depuis plus ou moins longtemps. Paul, mon plus vieil ami, qui n'oublie jamais de m'envoyer un message pour me dire bonne chance, pour me souhaiter un joyeux anniversaire, pour me demander quand est-ce que je retourne à Brest pour qu'on se voit. À Yann et Paul, avec qui j'ai tant ri, et avec qui boire un verre en terrasse est un

sport national, ouvrant la voie à des discussions passionnées qui me manquent toujours. To the friends I met in Corvallis, Ridwana who brought me so much in such a short time, and Dakota the nicest person I could have become friend with–I miss you. Aux toulousaings, rencontrés en école pour la plupart, et qui sont si chers à mon coeur. Jules qui a été mon premier ami dans cette ville inconnue, avec qui j'ai vécu pendant plus de 2 ans (confinement inclu), et sans doute la personne la plus gentille que je connaisse. Anatole, que j'ai d'abord détesté avant d'adorer, à qui je parle de tout mais aussi avec qui je n'ai pas forcément besoin de parler pour apprécier le temps qui passe. Guillaume, avec qui la vie est si simple, avec qui je décompresse quand j'ai bossé jusqu'à 20h, qui n'a même plus besoin de demander le lieu de rendez-vous quand on sort boire un coup (au cas où, Bear's House), qui est toujours partant pour faire quoi que ce soit ensemble (et qui a fait quelques figures de cette thèse ehe). Adrien, qui me partage tant de choses (une minute de silence pour toutes les musiques que tu m'as conseillé et que je n'ai jamais écouté), naturel enthousiaste avec qui le temps n'est jamais gris. Marianne, les moments avec toi passent à une vitesse, j'aime tes gouts et tes avis sur les gens, nos débats animés me manquent, hâte au prochain café/terrasse! Clément et Simon, je ne suis pas fan de Paris, mais je continuerai à venir pour vous y retrouver, et je vous garde une place au chaud, chez moi, quand vous voulez. Nicolas, Matthieu, éternels compagnons de vacances et de jeux qui rendent joyeuse la routine toulousaine. Lucie, qui me manque depuis qu'elle est partie loin. Et Lucie, la joie incarnée, avec qui je partage ma date d'anniversaire et mon amour pour Guillaume (lol). Nathan, le mystérieux de la bande que je suis heureux de découvrir un peu plus au fil des ans. Florentin, l'entertainer, que je gagnerait à voir plus souvent. À Thomas et Jeanne, pour les supers moments passés ensembles, et nos prochains séjours à quatre! À mes amies 1/1, avec qui on se voit seul et ça nous va très bien. Justine, qui m'a aidé à garder le moral pendant ma première année et qui est devenue une grande amie. Ergane, amie qui me connait si bien, qui m'écoute quand je parle trop, qui me contredit quand je dis de n'importe quoi (sans me faire sentir nul), pour qui tout est à discuter, merci de m'avoir fait grandir sur tous les plans.

À ma maman qui m'a tant aimé, qui s'est toujours soucié de mon bonheur, et qui m'a donné toute les clés pour devenir une bonne personne; à mon papa, pour l'amour, la joie, et la curiosité qu'il m'a transmis; à mon frère qui s'illustre par sa générosité et son intelligence, et que j'aimerais voir plus, et à Charlotte, que je suis heureux de compter dans la famille. À la famille plus éloignée, que je vois peu mais à qui je pense souvent.

À Iona, que j'aime tant.

Contents

v

Contents ix

List of Figures xiii

List of Tables xvii

Introduction générale (FR) 1

General introduction (EN) 7

I State of the art 13
- I.1 Climate variability and coastal impacts . . . 13
  - I.1.1 A definition of climate : a frame to assess for coastal morphodynamics at seasonal to interdecadal scales . . . 13
  - I.1.2 Seasonal climate variability . . . 17
  - I.1.3 Interannual climate variability . . . 19
  - I.1.4 Decadal and longer-term climate variability . . . 21
- I.2 Sandy beaches hydro-morphodynamics . . . 24
  - I.2.1 The beach system . . . 24
  - I.2.2 Beach morphodynamics . . . 28
  - I.2.3 In-situ survey of the beach system . . . 33
    - I.2.3.1 Beach elevation profiles . . . 34
    - I.2.3.2 Shoreline position . . . 36
    - I.2.3.3 Higher-order indicators of shoreline variability . . . 38
- I.3 Satellite-based monitoring of the beach . . . 39
  - I.3.1 A tool suited for climate-related coastal hydro-morphodynamics monitoring . . . 40
  - I.3.2 Deriving waterline positions from optical satellite-imagery . . . 41
  - I.3.3 Challenges of satellite-derived waterline and shoreline methods . . . 45
  - I.3.4 Large scale satellite-based coastal monitoring . . . 47

II Building and validating methods for large-scale shoreline acquisition 51
- II.1 Introduction . . . 51
- II.2 Methods . . . 53
  - II.2.1 Study Sites . . . 53
  - II.2.2 A modular algorithm for waterline extraction from optical satellite imagery . . . 54
    - II.2.2.1 Collection of images and pre-processing . . . 55
    - II.2.2.2 Water-differentiating indices . . . 56
    - II.2.2.3 Segmentation . . . 58
    - II.2.2.4 Post-processing . . . 60
    - II.2.2.5 Validation process . . . 62
- II.3 Results . . . 64

II.3.1 Qualification of waterline time series accuracy . . . 64
II.3.2 Deriving shorelines from waterlines . . . 67
II.3.3 Uncertainties and error proxies . . . 71
II.3.4 Seasonal, interannual, and longer-term variability of the shoreline position . . . 76
II.4 Discussion . . . 79
II.5 Chapter Conclusion . . . 82

III Study case : Seasonal and ENSO-driven waterline variability along the North American West Coast 85
III.1 Introduction . . . 85
III.2 Methods . . . 87
III.2.1 Satellite-derived waterline data . . . 87
III.2.2 Deriving trends, seasonal cycles and anomalies . . . 91
III.2.3 Data and statistical tests for climate variability analysis . . . 92
III.3 Results . . . 94
III.3.1 Long-term trends of shoreline change . . . 96
III.3.2 Seasonal patterns of shoreline change . . . 96
III.3.3 Interannual variability and ENSO-driven hydro-morphodynamics . . . 101
III.4 Discussion . . . 110
III.5 Chapter Conclusion . . . 112

IV The shoreline behaviour among the complex beach system 115
IV.1 Introduction . . . 115
IV.2 Methods . . . 117
IV.2.1 Beach profiles and derived proxies . . . 117
IV.2.2 Temporal decomposition of coastal indicators . . . 121
IV.2.3 Modeling of Beach Profile Changes . . . 122
IV.2.4 Statistical Analysis . . . 123
IV.2.5 Additional Data . . . 124
IV.3 Results . . . 124
IV.3.1 Waterline and shoreline variability . . . 124
IV.3.2 Representativeness of shoreline proxies in describing intertidal beach morphodynamics . . . 127
IV.3.3 The 3D intertidal profile variability . . . 130
IV.4 Discussion . . . 135
IV.5 Chapter Conclusion . . . 138

V Discussion and Perspectives 141
V.1 Contrasted shoreline definitions as indicators of coastal change . . . 142
V.1.1 Conceptual distinctions between waterline and datum-based shoreline definitions 142
V.1.2 Potential limits of using shoreline indicators as a proxy for beach morphodynamics 145
V.1.3 A broader conception of the beach and its dynamics . . . 148
V.2 Towards more robust methods for satellite-derived nearshore monitoring . . . 150
V.2.1 Future of satellite-derived shoreline monitoring . . . 150
V.2.2 Integration of alternative satellite-derived beach features for a richer representation of the coastal system . . . 156
V.2.3 The potential of remotely-sensed topography-bathymetry continuum . . . 158

V.3 What role for satellite-based monitoring in predicting coastal risks ? 161

Conclusion générale (FR) **165**

General conclusion (EN) **169**

A Analyses of the SDW/SDS validation : Supplementary Figures **171**
A.1 Distribution of SDW errors 171
A.2 Validation : Beach slopes, trends, seasonal cycles and interannual varaibility 176
A.3 Influence of the ROI size and satellite mission used 188

B Influence of ENSO on coastal hydro-morphodynamics : Supplementary Figures **191**
B.1 Statistical links between ENSO and coastal hydrodynamics along the NAWC 191
B.2 Northeastern Pacific response to ENSO 193

C Coupled dynamics of the waterline and the sandbar **195**
C.1 Short context of the research 195
C.2 Methods 195
C.2.1 Satellite-derived waterline data 195
C.2.2 Satellite-derived sandbar data 196
C.2.3 Equilibrium model 196
C.2.4 Additional data 198
C.3 Preliminary results 198
C.3.1 Shoreline and sandbar positions patterns 198
C.3.2 Accounting for the sandbar positions to model shoreline positions based on equilibrium models 205

Acronyms **209**

Bibliography **211**

List of Figures

I.1 Climate, climate variability and climate change at human time scales . . . 15
I.2 Winter/summer influence on significant wave height . . . 18
I.3 Influence of ENSO on significant wave height . . . 22
I.4 Schematic representation of the beach system, with conceptual boundaries of the shoreface and the relative timescales of morphological change. Arrows indicate the relative magnitudes of sediment transport rates. The area where waterline and tidal datum-based shorelines are usually derived is highlighted in red. Figure adapted by *Anthony and Aagaard (2020)*; beach background image from Google Earth. . . . 25
I.5 Global repartition of tide ranges . . . 27
I.6 The Brunn Rule . . . 31
I.7 Beach elevation profiles and derived shoreline time series . . . 35
I.8 Comparison between processes, modeling and observations spatio-temporal scales . . . 42
I.9 Typical workflow of optical SDW methods . . . 45

II.1 Presentation of the study sites . . . 55
II.2 Example of SDW method flow chart . . . 56
II.3 Water-differentiating indices . . . 57
II.4 Illustration of the different thresholding methods . . . 59
II.5 Showcase of image filtering based on cloud coverage at Duck, NC, USA . . . 61
II.6 The IQR outlier removal method . . . 62
II.7 SDW accuracy at the Duck, Narrabeen, Torrey Pines and Truc Vert . . . 65
II.8 SDW accuracy at the Perranporth, Porsmilin, Slapton Sands and Vougot . . . 66
II.9 Validation of satellite-derived beach slopes using LM-based methods . . . 68
II.10 SDS accuracy at the Duck, Narrabeen, Torrey Pines and Truc Vert . . . 69
II.11 SDS accuracy at the Perranporth, Porsmilin, Slapton Sands and Vougot . . . 71
II.12 SDS error benchmarks relative to observed shoreline change . . . 72
II.13 Evolution of minimum detectable shoreline change as a function of the observation uncertainty and number of observations . . . 73
II.14 Q-Q plots and distributions of SDW errors . . . 74
II.15 Empirical relationships between SDW/SDS detection errors, tidal range and beach slope . . . 75
II.16 Validation of long-term shoreline change trends (LM-based methods) . . . 77
II.17 Validation of seasonal cycles of shoreline change (LM-based methods) . . . 78
II.18 Validation of interannual variability of shoreline change (LM-based methods) . . . 79

III.1 The North American West Coast . . . 88
III.2 Validation of FES and SSALTO-DUACS outputs at 4 locations along the NAWC . . . 90
III.3 Validation of SDW at Torrey Pines, USA, and Ensenada, Mexico . . . 91
III.4 Satellite-derived waterlines along the North American West Coast (1984–2024) . . . 94
III.5 Estimated cRMSE of the SDW data . . . 95
III.6 SDW seasonal cycle amplitudes along the NAWC . . . 97
III.7 Coastal driver climatologies . . . 99
III.8 Correlations between waterline change and coastal drivers at the seasonal scale . . . 100

III.9 Intercorrelations among coastal drivers at the seasonal scale . . . 101
III.10 Interannual waterline change along the NAWC . . . 102
III.11 ENSO indices evolution between 1997-2022 . . . 103
III.12 Correlation between regionally-averaged waterline anomalies and climate modes . . . 104
III.13 Signal-to-Noise Ratios (SNR) of waterline anomaly changes during El Niño/La Niña relatively to ENSO neutral phases (1997-2022) . . . 106
III.14 Relation between winter-averaged Multivariate ENSO Index (MEI) and wave energy at four sites along the NAWC . . . 107
III.15 Hydrodynamic and morphological responses to ENSO phases and El Niño flavors during winter (1997-2022) along the NAWC . . . 108

IV.1 Mechanisms driving waterline change . . . 116
IV.2 Study sites . . . 118
IV.3 Timestacks of intertidal beach profiles and their temporal variability . . . 120
IV.4 Temporal patterns of intertidal beach changes. . . . 122
IV.5 Shoreline and waterline time series. . . . 125
IV.6 Decomposition of the waterline position signal in hydrodynamic and morphodynamic parts. . . . 127
IV.7 Correlations between shoreline positions from different elevations. . . . 128
IV.8 Representativeness of the MSL-shoreline to describe the intertidal profile variability. . . . 129
IV.9 Decomposition of the intertidal beach profile variability. . . . 132
IV.10 Translation/rotation model of beach profile variability applied at Porsmilin. . . . 133
IV.11 Quantification of waterline displacement components . . . 135

V.1 Beach elevation profiles at Grayland, WA, USA . . . 147
V.2 Forecasting coastal vulnerability from remotely-sensed data across timescales . . . 162

A.1 Histograms showing distributions of the SDW errors derived from Otsu-based algorithms. . . . 172
A.2 Histograms showing distributions of the SDW errors derived from LM-based algorithms. . . . 173
A.3 Histograms showing distributions of the SDW errors derived from MSV-based algorithms. . . . 174
A.4 Histograms showing distributions of the SDW errors derived from WP-based algorithms. . . . 175
A.5 Validation of intertidal beach slopes (Otsu thresholding) . . . 176
A.6 Validation of intertidal beach slopes (MSV thresholding) . . . 177
A.7 Validation of intertidal beach slopes (WP thresholding) . . . 178
A.8 Validation of the long-term trends of shoreline change (Otsu thresholding) . . . 179
A.9 Validation of the long-term trends of shoreline change (MSV thresholding) . . . 180
A.10 Validation of the long-term trends of shoreline change (WP thresholding) . . . 181
A.11 Validation of the seasonal variability of shoreline change (Otsu) thresholding) . . . 182
A.12 Validation of the seasonal variability of shoreline change (MSV) thresholding) . . . 183
A.13 Validation of the seasonal variability of shoreline change (WP) thresholding) . . . 184
A.14 Validation of the interannual variability of shoreline change (Otsu thresholding) . . . 185
A.15 Validation of the interannual variability of shoreline change (MSV thresholding) . . . 186
A.16 Validation of the interannual variability of shoreline change (WP thresholding) . . . 187
A.17 Taylor's diagram of SDW methods (small ROIs) . . . 188
A.18 Sentinel-2 vs Landsat : SDW errors (LM thresholding) . . . 189

B.1 SNR analysis of ENSO-driven waterline anomaly change, per season and region . . . 192

B.2 SLA and morphological responses to ENSO phases and El Niño flavors during winter (1997-2022) along the NAWC with a high threshold . . . 193
B.3 Wave and morphological responses to ENSO phases and El Niño flavors during winter (1997-2022) along the NAWC with a low threshold . . . 194
B.4 SLA and morphological responses to ENSO phases and El Niño flavors during winter (1997-2022) along the NAWC with a low threshold . . . 194

C.1 Ensenada : Wave/sandbar correlations . . . 199
C.2 Ensenada : Wave/shoreline correlations . . . 200
C.3 Ensenada : Shoreline/Sandbar correlations . . . 201
C.4 Torrey Pines : Wave/sandbar correlations . . . 202
C.5 Torrey Pines : Wave/shoreline correlations . . . 203
C.6 Torrey Pines : Shoreline/Sandbar correlations . . . 204
C.7 ShoreFor applied at Ensenada . . . 205
C.8 ShoreFor applied at Torrey Pines . . . 206
C.9 Modified ShoreFor applied at Ensenada . . . 207
C.10 Modified ShoreFor applied at Torrey Pines . . . 208

List of Tables

I.1 Summary of the main optical satellite missions used for coastal monitoring 41
I.2 Water-differentiating indices and their formula 43

II.1 Summary of the methods yielding the best accuracies at each site 67

III.1 Long-term waterline change trends along the NAWC (2000-2022) 96
III.2 Regional waterline position anomaly responses to ENSO phases 109

IV.1 Model performances in capturing intertidal beach morphodynamics 134

Introduction générale (FR)

Les côtes, qui séparent les terres de la mer, sont des interfaces complexes soumises à une myriade de processus hydrodynamiques, atmosphériques, géologiques et anthropiques (Syvitski et al. (2022)). Des plus petites turbulences aux dynamiques à l'échelle globale qui contrôlent le niveau de la mer et la position de la croûte terrestre, les côtes sont façonnées par ces processus à toutes les échelles spatio-temporelles (Vitousek et al. (2023a)). Les côtes sont diverses : elles peuvent se présenter sous la forme de falaises rocheuses, de mangroves, de zones couvertes de glace, de structures artificielles ou de plages de sable et de galets. Cette diversité de formes et de processus est à l'origine de la complexité des côtes et de leur morphodynamique, c'est-à-dire de l'évolution de leur morphologie. Comprendre comment les côtes se déforment au fil du temps est motivé à la fois par l'intérêt pour cette complexité et, plus important encore, par le fait que les côtes concentrent une part importante des activités humaines, si bien que leur évolution a des conséquences sociétales majeures (Cazenave and Cozannet (2014)).

Parmi tous les types de côtes, les plages occupent une place particulière, puisqu'elles couvrent environ un tiers des littoraux non glacés (Luijendijk et al., 2018) et jouent un rôle socio-économique important. Une plage se définit comme une zone côtière où des sédiments meubles — limons, sable, galets, etc. — s'accumulent pour former un relief interagissant avec les vagues, les courants et le vent. La morphologie moyenne d'une plage dépend largement des caractéristiques du sédiment et des conditions de forçage moyennes qui s'y appliquent (Wright and Short (1984); Masselink and Short (1993)), tandis que la morphodynamique des plages est principalement contrôlée par le bilan sédimentaire — c'est-à-dire la différence entre les apports et les pertes de sédiment (Anthony et al. (2006); Ruggiero et al. (2016)) — ainsi que par la redistribution interne de ces sédiments due aux processus locaux (Anthony and Aagaard (2020)).

Les processus de transport sédimentaire sont pour la plupart continus, et les plages s'adaptent en permanence aux fluctuations de ces mécanismes. Ces processus continus sont influencés par deux types principaux de variabilité : météorologique et climatique. Un événement météorologique est un phénomène de courte durée, tel qu'une tempête, qui redistribue rapidement le sédiment de la plage et entraîne souvent l'érosion du profil suivie d'un rétablissement progressif (Castelle and Masselink (2023)). En revanche, les fluctuations climatiques se manifestent sur des périodes plus longues, incluant des variations de précipitations, de régime de vagues ou encore du niveau

de la mer. Elles sont contrôlées par des mécanismes connus, tels que l'alternance des saisons, le changement climatique anthropique ou encore les modes climatiques à grande échelle comme El Niño–Oscillation australe (ENSO). Ces fluctuations climatiques entraînent des modifications graduelles mais persistantes de la morphologie des plages (Ruggiero et al. (2005)). Ainsi, la morphodynamique des plages résulte de la superposition de processus à long terme et d'événements ponctuels. Les événements météorologiques sont hautement imprévisibles et peuvent provoquer des changements rapides et drastiques du relief des plages (Masselink et al. (2016); Harley et al. (2022)), tandis que les variations climatiques façonnent la morphologie des plages de manière plus prévisible (Ranasinghe et al. (2004); Barnard et al. (2015)).

Au-delà de la dualité météorologie–climat, une autre distinction apparaît : celle entre la morphologie de la plage et le niveau de la mer. En effet, si la morphologie de la plage varie, la définition même de la plage — comme interface entre la terre et la mer — évolue également au fil du temps, tant météorologiquement que climatiquement, sous l'influence des variations du niveau de la mer (Serafin et al. (2017); Woodworth et al. (2019)). En parallele de ces deux échelles — variations météorologiques à court terme et fluctuations climatiques à long terme — se situe un troisième type de forçage régulier : la marée astronomique. À l'échelle quotidienne, la marée constitue un processus cyclique prévisible qui module, souvent de manière dominante, le niveau de la mer sans être lié ni à la météo ponctuelle, ni au climat à long terme (Masselink and Short (1993)).

Cette perspective conduit à deux approches complémentaires pour étudier l'évolution des plages. La première, l'approche géomorphologique, se concentre sur les changements du relief de la plage, tandis que la seconde, l'approche océanographique, s'intéresse à l'évolution du niveau côtier de la mer. Naturellement, ces approches sont interdépendantes : comprendre la morphodynamique des plages nécessite de prendre en compte le niveau de la mer, et évaluer l'évolution du front de mer et ses implications pour les inondations ne peut se faire indépendamment de la géomorphologie côtière. Néanmoins, historiquement, ces deux approches ont donné naissance à deux communautés de recherche distinctes, chacune utilisant sa propre terminologie et ses propres techniques de mesure.

Les géomorphologues côtiers s'intéressent principalement au volume de sédiment et à la morphologie des plages, tandis que les océanographes côtiers étudient l'évolution du niveau de la mer le long du littoral. La jonction de ces deux champs de recherche se cristallise autour d'un objet

géophysique à la fois central et ambigu : le trait de côte. Cet objet, apparemment simple, recouvre en réalité de multiples définitions selon les disciplines et les contextes d'étude, intégrant tantôt des aspects géomorphologiques, tantôt des aspects océanographiques, et souvent les deux à la fois (Boak and Turner (2005)). L'une des définitions les plus intuitives considère le trait de côte comme la ligne d'eau — l'interface instantanée entre terre et mer au moment de l'observation, marquant la limite entre les zones immergées et émergées. Bien que simple, cette définition illustre déjà la complexité du trait de côte : il dépend à la fois de la morphologie côtière et du niveau de la mer au moment de la mesure, constituant ainsi un indicateur hybride à l'interface des deux approches.

La ligne d'eau constitue une manière intuitive de définir le trait de côte, car elle est visuellement évidente et a longtemps servi de repère pratique pour décrire l'interface terre–mer. Historiquement, le suivi du trait de côte reposait sur des observations visuelles, puis a été amélioré grâce aux photographies aériennes et aux vidéos côtières. Aujourd'hui, avec le développement de la télédétection satellitaire, les progrès des méthodes numériques (par ex., Vos et al. (2019b)) et l'accès facilité aux données (Gorelick et al. (2017)), le trait de côte peut être mesuré à grande échelle, de manière fréquente et sur de longues périodes. Cela permet de dépasser les perspectives locales et d'observer comment le climat et l'activité humaine ont façonné les plages au cours des dernières décennies. Cependant, cette extension d'échelle comporte des limites : la résolution spatiale et temporelle des données satellitaires reste limitée, les volumes de données exigent un traitement et une validation importants, et les méthodes d'extraction automatisées sont encore imparfaites. Malgré les progrès, les observations globales du trait de côte ont donné lieu à relativement peu d'études de synthèse. Des approches pionnières ont néanmoins fourni des chiffres clés — parfois débattus — sur « l'état des plages du monde » (Luijendijk et al. (2018)), montrant par exemple que les plages représentent environ 31% des littoraux non glacés et que près de la moitié connaissent des déplacements de trait de côte supérieurs à 0,5 m/an. Dans l'ensemble, la cartographie mondiale des dynamiques du trait de côte reste encore largement incomplète (Vitousek et al. (2023a)), notamment en ce qui concerne la saisonnalité, la variabilité interannuelle et leur réponse à la montée du niveau de la mer.

Dans cette thèse, nous cherchons à approfondir notre compréhension de l'influence de la variabilité climatique sur l'évolution du trait de côte. Cette tâche, qui vise à être adoptée à l'échelle globale, se heurte à plusieurs limitations méthodologiques et théoriques que nous abor-

dons à travers les études présentées ici. Les travaux proposés visent à développer des outils méthodologiques et conceptuels permettant de mieux appréhender les interactions entre variabilité climatique et évolution du trait de côte à des échelles globales et décennales à partir d'observations satellitaires optiques. Ils traitent des questions scientifiques suivantes : **Quelles sont les forçages et les amplitudes des cycles saisonniers d'évolution du trait de côte? Quelles signatures de la variabilité climatique interannuelle apparaissent dans l'évolution du trait de côte à l'échelle globale? Peut-on relier quantitativement l'évolution observée des plages aux grands modes climatiques [e.g., ENSO]? Quelles sont les limites de l'utilisation de l'évolution du trait de côte comme indicateur de la morphodynamique côtière?** Ces questions scientifiques s'accompagnent de questionnements méthodologiques : **Comment mesurer de manière robuste le trait de côte à partir d'images satellitaires? Comment tenir compte systématiquement des biais liés aux conditions d'observation (marée, houle)? Comment dissocier les signaux climatiques des autres sources de variabilité de la position du trait de côte?**

Ce manuscrit aborde ces problématiques à travers cinq chapitres. Le chapitre 1 est consacré à la construction d'un état de l'art, qui constitue la base bibliographique permettant de situer ce travail dans un contexte scientifique dense, à la fois sur les questions de morphodynamique côtière, d'évolution du niveau de la mer, de variabilité climatique et de méthodes de télédétection. Le chapitre 2 approfondit l'étude des moyens d'observation à travers une série d'applications et de validations des méthodes de suivi du trait de côte par imagerie satellite optique sur huit sites parmi les plus surveillés au monde. Les résultats de ce chapitre motivent le choix de la méthodologie appliquée dans le chapitre suivant. Le chapitre 3 présente une application à grande échelle de notre capacité de suivi du trait de côte à partir de l'imagerie satellite: il s'agit d'une étude de la côte ouest de l'Amérique du Nord, qui nous renseigne sur la variabilité du trait de côte à l'échelle continentale, à l'échelle saisonnière mais aussi interannuelle, notamment sous l'influence d'ENSO. Le chapitre 4 s'intéresse à la relation entre l'évolution du trait de côte et celle du profil de plage dans son ensemble. Nous y questionnons dans quelle mesure le trait de côte reflète fidèlement la dynamique globale de la plage, et comment certains éléments morphologiques, telles que les barres sableuses, influencent et parfois contrôlent directement la position du trait de côte. Enfin, le chapitre 5 propose une synthèse des résultats, discute les apports méthodologiques et

scientifiques de ce travail, et ouvre sur les perspectives futures pour une meilleure compréhension des interactions entre variabilité climatique et dynamiques côtières à l'échelle globale.

General introduction (EN)

Coasts, which separate land from sea, are complex interfaces subject to a myriad of hydrodynamic, atmospheric, geological, and anthropogenic processes (Syvitski et al. (2022)). From the smallest turbulence to global-scale dynamics that control sea level and the position of the Earth's crust, coasts are shaped by these processes across all spatial and temporal scales (Vitousek et al. (2023a)). Coasts are diverse: they can take the form of rocky cliffs, mangroves, ice-covered areas, engineered structures, or sandy and gravel beaches. This diversity of forms and processes is reflected in the complexity of coastal morphodynamics, that is, the evolution of coastal morphology. Understanding how coasts deform over time is motivated both by an interest in this complexity and, more importantly, by the fact that coasts concentrate a significant portion of human activity, so that their evolution has major societal consequences (Cazenave and Cozannet (2014)).

Among all types of coasts, beaches occupy a special place, as they cover roughly one-third of ice-free shorelines (Luijendijk et al. (2018)) and play an important socio-economic role. A beach is defined as a coastal area where unconsolidated sediment — silts, sand, pebbles, etc. — accumulates to form a relief interacting with waves, currents, and wind. The average morphology of a beach largely depends on the sediment characteristics and the mean forcing conditions applied to it (Wright and Short (1984); Masselink and Short (1993)), whereas beach morphodynamics are primarily controlled by the sediment budget — the difference between sediment gains and losses (Anthony et al. (2006); Ruggiero et al. (2016)) — and the internal redistribution of these sediments due to local processes (Anthony and Aagaard (2020)).

The sediment transport processes are mostly continuous, and beaches constantly adapt to fluctuations in these mechanisms. These continuous processes are influenced by two main types of variability: meteorological and climatic. A meteorological event is a short-term phenomenon, such as a storm, which rapidly redistributes beach sediment and often results in profile erosion followed by gradual recovery (Castelle and Masselink (2023)). In contrast, climatic fluctuations are longer-term manifestations, including variations in precipitation, wave regime, or sea level. They are driven by known mechanisms such as seasonal cycles, anthropogenic climate change (Ranasinghe (2016)), or large-scale climate modes like El Niño–Southern Oscillation (ENSO) (Barnard et al. (2017)). These climatic fluctuations lead to gradual but persistent changes in beach morphology (Ruggiero et al. (2005)). Thus, beach morphodynamics result from a super-

position of long-term processes and short-term events. Meteorological events are predictable only a few days or weeks in advance and can cause rapid and drastic changes in beach topography (Masselink et al. (2016); Harley et al. (2022)), whereas climatic variations shape beach morphology in a more predictable manner (Ranasinghe et al. (2004); Barnard et al. (2015)).

Beyond the meteorology–climate duality, there is another distinction: that between beach morphology and sea level. Indeed, while beach morphology varies, the very definition of the beach — as the interface between land and sea — also evolves over time, both meteorologically and climatically, under the influence of sea level variations (Serafin et al. (2017); Woodworth et al. (2019)). Between these two scales — short-term meteorological variations and long-term climatic fluctuations — lies a third type of regular forcing: the astronomical tide. On a daily timescale, the astronomical tide constitutes a predictable cyclic process, which modulates, often dominantly, sea level without being related to either short-term weather or long-term climate (Masselink and Short (1993)).

This additional perspective gives rise to two complementary approaches to studying beach evolution. The first, the geomorphological approach, focuses on changes in beach topography, while the second, the oceanographic approach, examines coastal sea-level. Naturally, these approaches are interdependent: understanding beach morphodynamics requires considering sea level, and assessing shoreline evolution and its implications for flooding cannot be separated from coastal geomorphology. Nonetheless, these two approaches have historically fostered two largely separate research communities, each with its own measurement techniques and terminology.

Coastal geomorphologists primarily focus on beach sediment volume and morphology, whereas coastal oceanographers study sea level evolution along the coast. The intersection of these research fields converges on a single, yet ambiguous, geophysical object: the shoreline. This seemingly simple object has multiple definitions depending on discipline and context, encompassing geomorphological aspects, oceanographic aspects, or both (Boak and Turner (2005)). One of the most intuitive definitions considers the shoreline as the waterline — the instantaneous interface between land and sea at the time of observation, marking the boundary between submerged and emerged areas. Although simple, this definition already illustrates the complexity of the shoreline: it depends on both coastal morphology and sea level at the time of measurement, making it a hybrid indicator at the interface of the two approaches.

The waterline is an intuitive way to define the shoreline because it is visually obvious, making

it a longstanding practical marker for describing the land–sea interface. Historically, shoreline monitoring relied on visual observations, later enhanced by aerial photography and coastal video surveys. Today, with the rise of satellite remote sensing, advances in numerical methods (e.g., Vos et al. (2019b)), and improved access to data (e.g., Gorelick et al. (2017)), the shoreline can be measured at large scales, with high frequency, and over long periods. This allows us to go beyond local geomorphological perspectives and observe how climate and human activity have shaped beaches over recent decades. Nevertheless, this scaling up comes with constraints: satellite data spatial and temporal resolution remains limited, data volumes require extensive processing and validation, and automated extraction methods are still imperfect. Despite significant advances, global shoreline observations have yielded relatively few synthesis studies. Pioneering approaches have nevertheless provided key — though sometimes debated — figures on "The state of the world's beaches" (Luijendijk et al. (2018)), revealing, for instance, that beaches account for roughly 31% of ice-free coastlines and that nearly half experience shoreline shifts exceeding 0.5 m/year. Overall, global mapping of shoreline dynamics remains largely incomplete (Vitousek et al. (2023a)), especially regarding seasonality, interannual variability, and their response to rising sea levels.

In this thesis, we aim to enhance our understanding of the influence of climate variability on shoreline evolution. This task, aimed to be pursued at a global scale, is challenged by several methodological and theoretical limitations that we address through the studies presented here. The work presented proposes methodological and conceptual tools to better understand interactions between climate variability and shoreline evolution at global and decadal scales using optical satellite observations. It addresses the following scientific questions: **What are the amplitudes and drivers of seasonal cycles in shoreline evolution? What signatures of climate variability appear in shoreline changes at the large spatial scales? Can observed beach hydromorphodynamics be quantitatively linked to large-scale climate modes (e.g., ENSO)? What are the limitations of using the shoreline as an indicator of coastal morphodynamic change?** These scientific questions are accompanied by methodological questions: **Can the shoreline be robustly measured from satellite imagery? Can observation biases (tide, wave conditions) be systematically accounted for? Can climate signals be separated from other sources of shoreline variability?**

This manuscript addresses these issues in five chapters. Chapter 1 presents a state-of-the-

art review, providing the bibliographic foundation to situate this work within a dense scientific context, covering coastal morphodynamics, sea level evolution, climate variability, and remote sensing methods. Chapter 2 focuses on observation methods through a series of applications and validations of shoreline detection on eight of the most monitored sites worldwide. The results of this chapter inform the methodology applied in the following chapter. Chapter 3 presents a large-scale application of shoreline monitoring: the west coast of North America, providing insights into shoreline variability at continental, seasonal, and interannual scales, particularly under the influence of ENSO. Chapter 4 examines the relationship between shoreline evolution and the intertidal beach profile, questioning to what extent shoreline proxies accurately reflects overall beach morphodynamics. Finally, Chapter 5 synthesizes the results, discusses the methodological and scientific contributions of this work, and outlines future perspectives for better understanding interactions between climate variability and coastal dynamics at the global scale.

Chapter I

State of the art

This chapter presents a large source-based contextualization of the thesis, within the three major fields supporting this research : climate variability, sandy beaches hydro-morphodynamics, and remote sensing. It is intended to provide the essential concepts on which this thesis is built.

Contents

I.1 Climate variability and coastal impacts . . . 13
- I.1.1 A definition of climate : a frame to assess for coastal morphodynamics at seasonal to interdecadal scales . . . 13
- I.1.2 Seasonal climate variability . . . 17
- I.1.3 Interannual climate variability . . . 19
- I.1.4 Decadal and longer-term climate variability . . . 21

I.2 Sandy beaches hydro-morphodynamics . . . 24
- I.2.1 The beach system . . . 24
- I.2.2 Beach morphodynamics . . . 28
- I.2.3 In-situ survey of the beach system . . . 33
  - I.2.3.1 Beach elevation profiles . . . 34
  - I.2.3.2 Shoreline position . . . 36
  - I.2.3.3 Higher-order indicators of shoreline variability . . . 38

I.3 Satellite-based monitoring of the beach . . . 39
- I.3.1 A tool suited for climate-related coastal hydro-morphodynamics monitoring . . . 40
- I.3.2 Deriving waterline positions from optical satellite-imagery . . . 41
- I.3.3 Challenges of satellite-derived waterline and shoreline methods . . . 45
- I.3.4 Large scale satellite-based coastal monitoring . . . 47

I.1 Climate variability and coastal impacts

I.1.1 A definition of climate : a frame to assess for coastal morphodynamics at seasonal to interdecadal scales

The characterization of a climate relies on the definition of scales of interest, which are the scales considered to qualify a system through its properties. It must be acknowledged, however, that

this task is complicated: general definitions are elusive and their relevance is usually confined to a specific scale. Systems like global ocean and atmosphere can be characterized by a range of properties (temperature, pressure, velocity, etc.) that evolve in space and time. At a scale long-enough so the fluctuations of the properties of the system converge to a stable mean (not necessarily constant, but not influenced by high-frequency variations relative to the studied scale), we can define a climate. Each property can be attributed a mean value, that represents the mean state of the system over the considered scales. It can also be attributed a standard deviation from the mean value, quantifying the 'normal' deviations of this dynamic property from the mean state, that can be called weather. In other words, climate emerges from the aggregation of weather over space (within the studied system) and time, where the distribution of events defines the statistical properties—mean, variance, and tails—that describe the system at the chosen scale. Extremes are defined relatively to this frame, they take the form of large magnitude, sudden, and short-lived deviations from the mean state (e.g., an isolated heat wave, or unusually high waves due to a single storm).

Deviations from the mean state that persist over extended periods, or that oscillate consistently with a known return period, constitute climate variability. In this framework, the characterization of climate, variability, and extremes is inherently statistical and scale-dependent. From this arises a working definition: **Climate is the statistical description of the state of a system over a given spatio-temporal scale, and climate variability is the statistical description of deviations from the mean state over the same scales**.

In the following, we focus on climate variability at human-relevant timescales, up to several decades, across the earth observing satellite era (1980s–2020s). At these scales, seasonal cycles are embedded within the normal distribution of climate, yet they are sufficiently persistent that long records reveal recurrent shifts in the median state depending on the time of year (e.g., Young (1999); Woodworth et al. (2019)). Interannual variability similarly produces anomalies that, when viewed over multidecadal periods, appear as systematic fluctuations of the mean state tied to the recurrence of large-scale coupled atmosphere–ocean modes (e.g., Barnard et al. (2015); Woodworth et al. (2019)).

Climate variability must not be confounded with climate change, which can be described as a persistent trend in the ocean-atmosphere variability operating at decadal to centennial scales, primarily driven by anthropogenic greenhouse gas emissions. Climate change overlaps and interacts with natural climate variability but does not replace it (e.g., Cai et al. (2021)).

It is important to acknowledge that the magnitude of natural climate variability depends on the timescale considered. Over geological timescales of millions of years, natural processes such as orbital forcing (e.g., Timmermann et al. (2007)) or long-term carbon cycle feedbacks (Friedlingstein (2015)) have produced climate shifts far more dramatic than those observed under present anthropogenic change. However, when restricting the analysis to seasonal, interannual, or interdecadal timescales—the scales relevant to human planning and adaptation—natural variability remains bounded within ranges that are distinct from the persistent, externally forced trends associated with anthropogenic climate change. In this sense, it is both meaningful and necessary to distinguish between short- to medium-term climate variability and the unprecedented long-term trajectory of human-driven climate change. All the above considerations are illustrated schematically on Figure I.1.

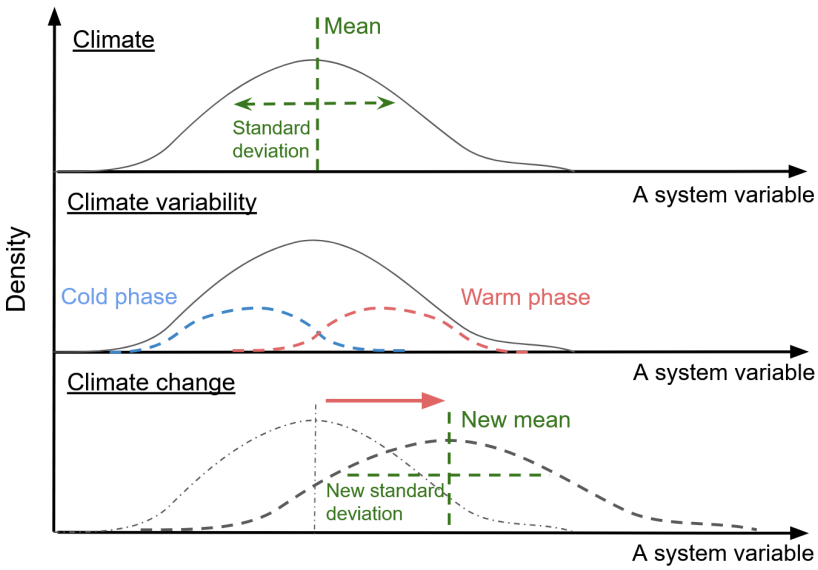

FIGURE I.1 Schematic representation of climate, climate variability and climate change as distributions of values that can take a variable of the system. Here climate variability refers to the contemporary climate variability that is not driven by anthropogenic green-house gazes emissions (i.e., climate change) nor geological-scale climate variability, and cold/warm phases are used as examples to illustrate climate variability (e.g., winter/summer influence on mid-latitude temperatures).

The concept of climate variability can be directly applied to coastal environments, where atmospheric and oceanic drivers drive the variability of hydro-morphodynamic processes. The primary

climate-forced drivers include:

- Wave characteristics: Variability in wave height, period, and direction, which controls sediment transport, resulting in topography/bathymetry evolution. Waves respond to both local wind fields and remote storm activity (e.g., Boucharel et al. (2021b)), with seasonal cycles often producing predictable patterns of wave generation (e.g., Boucharel et al. (2021a)), and interannual or decadal oscillations modulating longer-term variability (e.g., Allan and Komar (2006)). Wave characteristics are conventionally derived from the wave energy spectrum, which distributes wave energy across frequencies and directions and provides a basis for calculating key parameters of the sea state. Wave characteristics are commonly measured by wave buoys and include significant wave height (noted H_s, the average height, trough to crest, of the highest one-third of waves in a given wave record), the peak wave period (noted T_p, period corresponding to the peak of the wave energy spectrum) and the mean wave direction (the energy-weighted average direction from which waves propagate).

- Sea-level: Variability in coastal sea level influences the capacity of waves to induce sediment transport. Sea level responds to a range of mechanisms, including steric effects, atmospheric pressure variations (inverse barometer effect), wave setup and runup, tides, and river discharge (e.g., Meade and Emery (1971); Thompson and Hamon (1980); Pugh and Woodworth (2014)). Seasonal cycles, such as thermal expansion and large-scale wind-driven circulation, often produce predictable patterns of sea-level change (Woodworth et al. (2019)), while interannual and decadal climate oscillations, including ENSO and the Pacific Decadal Oscillation (PDO), further modulate its variability (e.g., Allan and Komar (2006)). Sea-level characteristics are commonly measured by tide gauges, pressure sensors, or satellite altimetry, providing time series that can be analyzed to extract key parameters such as mean sea level, sea-level anomalies, tidal range, and extreme water levels (Holgate et al. (2013); Lionel et al. (2023)). These measurements are essential for understanding both short-term hydrodynamic forcing and long-term trends that shape coastal morphodynamics

- Riverine sediment supply: Variability in riverine sediment input influences coastal morphodynamics by altering the coastal sediment budget. Changes in precipitation and hydrological regimes introduce additional variability in both coastal sea level (e.g., Durand

et al. (2019)) and sediment delivery (Syvitski et al. (2003)). Large precipitation events, such as those occurring during monsoonal cycles (Clift and Jonell (2021)), as well as sequences of wildfires followed by intense flooding (Barnard and Warrick (2010); Warrick et al. (2022)), generate pulses of sediment that can be transported to and deposited along adjacent beaches. Riverine sediment supply is commonly quantified using gauged discharge and sediment concentration measurements (Syvitski et al. (2003)), which can be integrated to estimate sediment fluxes to the coast using models based on precipitation, temperature and watershed topography (Syvitski and Milliman (2007)).

By framing coastal morphodynamics statistically, in the same way as atmospheric and oceanic climate, we can describe both the mean state of a coast and its variability over multiple scales. This approach enables the identification of recurring patterns, extreme events, and long-term trends, providing a scientific basis for risk assessment at human-relevant timescales—from seasonal maintenance to multi-decadal planning. A central question that arises from this perspective is: **through which mechanisms is global climate variability downscaled into local coastal hydro-morphodynamics, and how does this interaction vary across regions and temporal scales?**

In summary, the climate framework—understood as the statistical description of a system across a given range of scales—offers a unifying enables the link of seasonal and interannual atmospheric and oceanic variability to coastal processes. Seasonal variability, interannual to interdecadal climate modes, and long-term climate change all produce fluctuations that shape the nearshore hydrodynamics and, in turn, impact the coast, influencing hazards such as erosion and flooding. Understanding these linkages is therefore essential for anticipating coastal responses and implementing timely adaptation measures (Ranasinghe et al. (2023)).

I.1.2 Seasonal climate variability

Seasonal variability is the most fundamental mode of climate variability relevant to human timescales. It arises from the Earth's annual revolution around the Sun, which induces systematic changes in solar radiation at different latitudes and, consequently, predictable cycles in atmospheric and oceanic circulation (Gill and Niller (1973)). These cycles regulate temperature, pressure, winds,

precipitation, and ocean currents, which together shape the seasonal patterns of sea level and wave climate observed at the coast (Tsimplis and Woodworth (1994)).

One important seasonal driver is the modulation of large-scale wind systems. At mid-latitudes, the position and intensity of the jet streams shift between summer and winter, altering the storm tracks of extratropical cyclones. In the Northern Hemisphere, winter jet streams strengthen and migrate equatorward, leading to more frequent and intense storm activity in the North Pacific and North Atlantic Chang et al. (2002), and therefore larger wave heights along exposed coasts. Conversely, during summer, the jet streams weaken and shift poleward, resulting in calmer wave climates at many temperate shorelines Chang et al. (2002). In tropical regions, monsoon circulations are the dominant expression of seasonality. Driven by seasonal shifts in land–sea thermal contrast, monsoons strongly modulate wind stress, precipitation, and river discharge into coastal areas (Ha et al. (2012)). Tropical cyclone activity is also seasonal: for example, the Eastern Pacific Hurricane (EPH) season, affecting the tropical areas on the Eastern Pacific, typically extends from late spring to autumn, with peak activity in August–September, generating extreme waves and storm surges along coasts of Mexico and Central America (Gunther and Cross (1984)).

These mechanisms drive large seasonal fluctuations in wave climate, as illustrated for the significant wave height on Figure I.2.

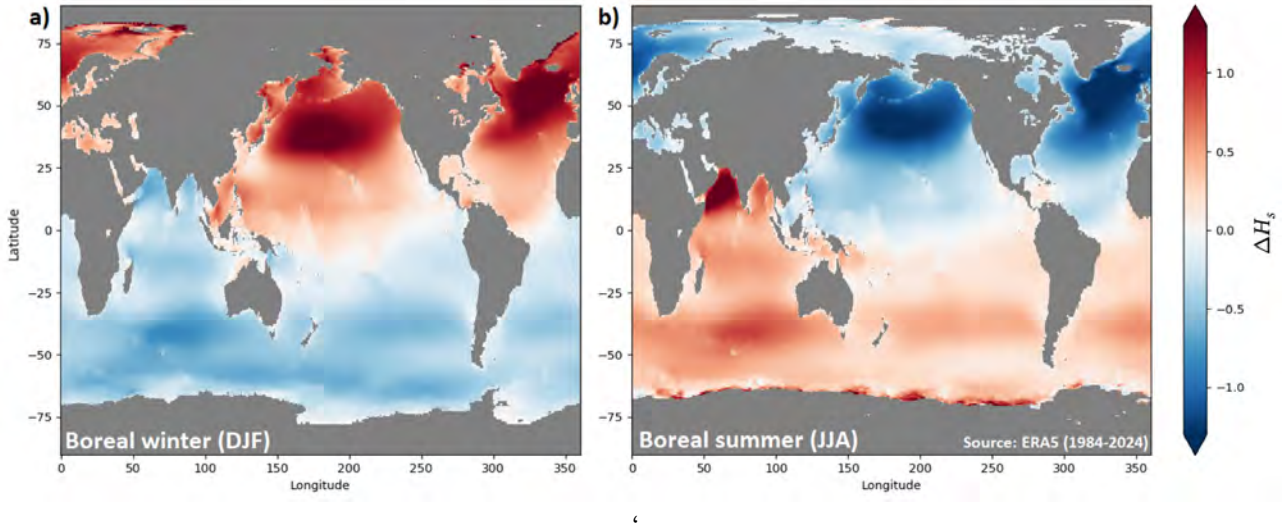

FIGURE I.2 Composites of detrended significant wave height ΔH_s (in meters) during boreal **a)** winter and **b)** summer. Composites are calculated from ERA5 monthly significant wave height product between 1984-2024. The boreal winter (summer) season is defined as December-January-February (June-July, August).

Seasonal changes in winds also drive upwelling and downwelling processes along eastern boundary currents (Middleton and Cirano (1999)), such as the California Current (Huyer (1983)). During summer, persistent alongshore equatorward winds induce offshore Ekman transport of surface waters, which is compensated by the upwelling of cooler, nutrient-rich water from depth (Rykaczewski and Checkley (2008)). This upwelling lowers coastal sea level through the offshore transport of surface waters and modifies stratification by bringing colder, denser water to the surface (Jung and Cho (2020)). In winter, weaker or reversed winds suppress upwelling and can induce downwelling, which elevates coastal sea level by driving surface waters shoreward (Huyer (1983))

Coastal sea levels also oscillate seasonally due to steric changes and hydrological forcing. Seasonal warming in summer causes thermal expansion of the upper ocean, raising sea level, while winter cooling contracts the water column and reduces sea level (Chambers (2006)). Additional contributions arise from atmospheric pressure variations and river runoff, with amplitudes that can reach several decimeters (Woodworth et al. (2019)). Seasonal amplitudes of the sea level are typically larger along continental shelves than in the open ocean because shallow-water processes amplify the atmospheric and oceanic forcing (Woodworth et al. (2019)).

I.1.3 Interannual climate variability

On interannual timescales, climate variability is largely governed by coupled atmosphere–ocean oscillations, commonly referred to as climate modes. These modes are expressed as coherent patterns of sea surface temperature (SST), sea level pressure (SLP), and wind anomalies that arise from feedbacks between the ocean and the atmosphere (McPhaden et al. (2006)). They have far-reaching effects on storm tracks, precipitation regimes, ocean circulation (Wang et al. (2017)), and ultimately on coastal sea level and wave climate (Allan and Komar (2006); Barnard et al. (2015)).

The most influential of these is ENSO, which dominates variability in the tropical Pacific with a typical recurrence interval of about five years, though its events are irregular in timing and intensity (Timmermann et al. (2018)). ENSO oscillates between warm phases (El Niño) and cold

phases (La Niña). During El Niño, weakened easterly trade winds allow warm water to expand eastward across the equatorial Pacific, deepening the thermocline in the eastern basin and suppressing coastal upwelling (Rasmusson and Carpenter (1982)). This oceanic reorganization is accompanied by shifts in atmospheric convection and sea level pressure, lowering pressure over the central Pacific and altering global circulation patterns (McPhaden et al. (2006)). La Niña represents the opposite phase, with strengthened easterlies, enhanced upwelling in the eastern Pacific, and shoaling of the thermocline (Rasmusson and Carpenter (1982)). ENSO events strongly influence sea level along Pacific coasts through the generation of equatorial Kelvin waves, which travel eastward across the basin and, upon reaching the American continent, continue poleward as coastal trapped waves (Enfield and Allen (1980)). These processes result in coherent, basin-wide anomalies in mean and extreme sea levels, which in turn affect coastal hazards. ENSO also modulates the occurrence of storms and the distribution of wave energy, redistributing coastal impacts over thousands of kilometers (Barnard et al. (2015)). Beyond the traditional dichotomy of El Niño and La Niña, recent studies emphasize the diversity of ENSO events, with distinctions often drawn between Eastern Pacific (EP) El Niños, characterized by strong warming in the far eastern equatorial Pacific, and Central Pacific (CP) El Niños , where anomalies are confined to the central basin (Takahashi et al. (2011)). These variants differ in their teleconnections and thus in their regional coastal impacts, underscoring the complexity of ENSO as a driver of interannual variability.

Other climate modes, sometimes interacting with ENSO, also shape interannual variability at regional to basin scales. The Indian Ocean Dipole (IOD, Saji and Yamagata (2003a)) is defined by opposing SST anomalies between the western and eastern equatorial Indian Ocean, altering monsoon circulation and driving sea level anomalies across the basin. The North Atlantic Oscillation (NAO, Hurrell (1995)) arises from changes in the pressure gradient between the Azores High and the Icelandic Low, modulating the strength and position of the westerly jet stream and storm tracks over the North Atlantic, thereby influencing sea level and wave climate along both European and North American coasts. The PDO (Mantua and Hare (2002)), while operating on longer timescales, also reflects basin-scale SST anomalies that influence the background state upon which ENSO operates, and thus can amplify or dampen its impacts.

These modes are typically quantified using statistical indices based on observed anomalies. ENSO is monitored through indices such as the Southern Oscillation Index (SOI, Ropelewski and Jones (1987)), calculated from the SLP difference between Tahiti and Darwin, and the Oceanic Niño Index (ONI, Trenberth and Hurrell (1994)), defined as SST anomalies in the central and eastern equatorial Pacific. The Multivariate ENSO Index (MEI, Wolter and Timlin (1998)) couples these equatorial pressure and temperature anomalies to form an integrated metric quantifying ENSO phases and intensity. The IOD index is based on the SST anomaly difference between the western and southeastern equatorial Indian Ocean. The Nothern Atlantic Oscillation (NOA) index is defined from the normalized pressure gradient between the Azores and Iceland. Other modes are identified through empirical orthogonal function analysis of SST anomalies, such as the PDO is the North Pacific Ocean, or EP and CP ENSO indices in the equatorial Pacific. These indices provide standardized measures of the strength and phase of climate modes, enabling comparison across events and facilitating the attribution of observed sea level and wave climate variability to these large-scale processes.

This large, basin-scale variability in SST and SLP drives massive changes of wind circulation, affecting both wave and sea-level, including at the coast. As an example, figure I.3 illustrates the ENSO-driven changes in significant wave height worldwide. Mean variations in significant wave height linked to ENSO are generally smaller than those driven by the seasonal cycle. Yet, these effects are not independent but superimpose, leading to combined influences on wave climate (Boucharel et al. (2021a)).

In summary, interannual variability is primarily expressed through atmosphere–ocean climate modes, which couple SST, pressure, and wind anomalies across vast regions. Through atmospheric teleconnections, these modes imprint coherent signals on coastal sea level, storminess, and wave climate worldwide, with strong implications for coastal hazards and long-term shoreline evolution (e.g., Barnard et al. (2015)).

I.1.4 Decadal and longer-term climate variability

Longer-term climate variability encompasses decadal oscillations and persistent trends, including the PDO, long-term shifts in ENSO amplitude, and progressive anthropogenic climate change.

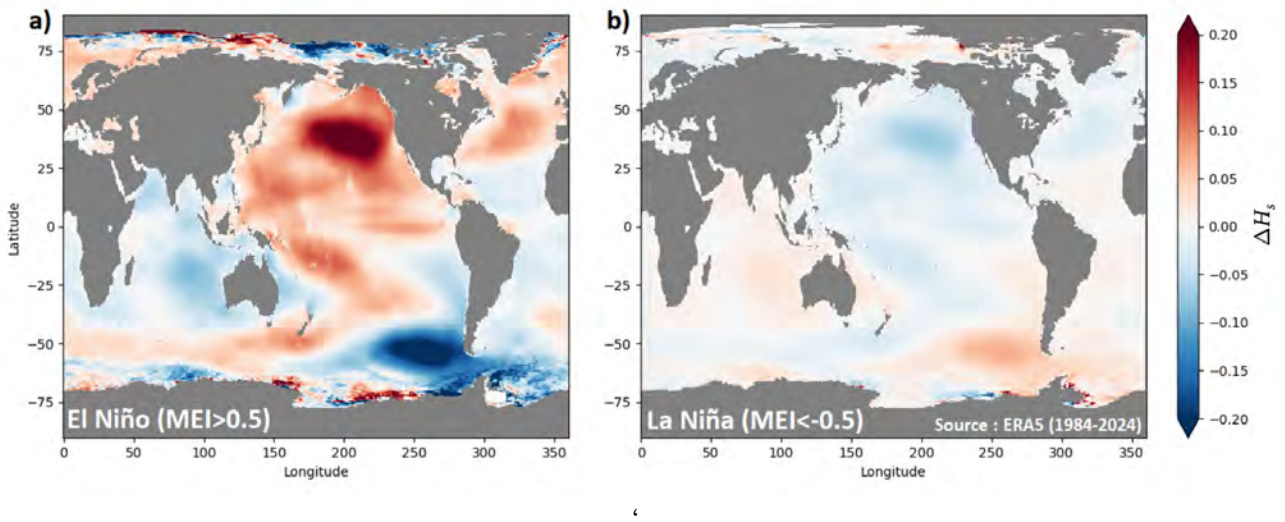

FIGURE I.3 Composites of detrended significant wave height ΔH_s (in meters) during **a)** El Niño and **b)** La Niña. Composites are calculated from ERA5 monthly significant wave height product between 1984-2024. El Niño (La Niña) are defined as months for which $MEI > 0.5$ ($MEI < -0.5$).

These modes influence baseline wave energy, storm frequency, and mean sea level, and they determine the longer-term risk of coastal erosion (e.g., Mantua and Hare (2002); Saji and Yamagata (2003b)). For example, decadal increases in North Pacific storm intensities have been linked to warming in the western tropical Pacific, suggesting a coupling between climate change and interannual variability (e.g., Graham and Diaz (2001)). Understanding these interactions is essential for predicting the combined effects of natural oscillations and anthropogenic forcing on coastal morphology and hazard exposure.

Among long-term climate drivers, global mean sea-level rise in response to climate change is expected to be the most consequential for coastlines (e.g., Ranasinghe and Stive (2009); Ranasinghe (2016); Vousdoukas et al. (2018)). Since the late 19th century, global mean sea level has risen by about 20 cm, which is equivalent to a typical amplitude of sea-level variability at the seasonal scale (Barroso et al. (2024)), with the rate of rise accelerating over recent decades in response to anthropogenic warming (IPCC (2022)). This rise is primarily driven by a combination of thermal expansion of seawater (steric effects) due to ocean warming (Church and White (2011)) and mass contributions through land ice melting from mountain glaciers or ice sheets in Greenland and Antarctica (Zemp et al. (2019))

Sea-level rise not only raises the mean sea-level but also amplifies the impacts of extreme

coastal events (Cazenave and Cozannet (2014); Vousdoukas et al. (2018); Taherkhani et al. (2020)). A modest increase in mean sea level translates into a large increase in the frequency of exceedance of historical flood thresholds. Events that were once considered “100-year floods” in terms of return period may occur annually or even multiple times per year by the end of the century in many regions (Vousdoukas et al. (2018); Tebaldi et al. (2021)). Moreover, sea-level rise interacts with waves, storm surges, and tides to produce compound flooding events, which are increasingly recognized as critical hazards for coastal infrastructure and communities (Wahl et al. (2015); Bevacqua et al. (2019)).

Climate change is also projected to alter storm characteristics, with implications for wave climate and coastal morphodynamics. While there is regional variability, several studies suggest an increase in the intensity of tropical cyclones, the poleward migration of storm tracks, and a general tendency toward more energetic waves in some mid-latitude regions (e.g., Melet et al. (2020)). Along the U.S. West Coast, evidence indicates a decadal increase in storm wave heights since the mid-20th century, particularly in the Pacific Northwest (e.g., Allan and Komar (2002b,a)). In combination with elevated sea levels, such intensification of wave climate enhances runup, overtopping, and erosion hazards (Leung et al. (2024).

The combined effect of long-term sea-level rise and changes in extremes is a progressive shift in the frequency, magnitude, and spatial footprint of coastal hazards. Erosion of beaches, drowning of wetlands, salinization of estuaries, and chronic flooding of low-lying areas are already being observed worldwide (IPCC (2022); Ranasinghe (2016)). Looking forward, anthropogenic climate change will likely surpass natural modes of variability as the dominant driver of coastal evolution at decadal to centennial scales, necessitating robust adaptation strategies.

I.2 Sandy beaches hydro-morphodynamics

I.2.1 The beach system

A clear definition of the beach is necessary to set the stage for the analyses conducted in this thesis. The beach is an area of loose sediments boarding the edges of a sea, a lake, or even a river. From a geomorphology perspective, it can be almost exhaustively describe by its sediment composition and its shape. Both vary in space and time (Prodger et al. (2016); Arias et al. (2025)). Actually, the boundaries of a beach can be defined as the limit beyond which these two properties no longer change, or change very little, relatively to a considered time scale. The larger the time scale considered, the broader the beach system seaward.

On the long timescales, going over decades to millennia, the seaward boundary of the beach can be called the wave base (Anthony et al. (2006)). It separates the lower shoreface from the inner shelf. The inner shelf is a virtually static environment that is too deep for sediment to be mobilized by waves, energetic or not, and is therefore almost never active at such temporal scales. The lower shoreface is a large slow varying area significantly evolving and exchanging sediment with the upper parts of the beach over scales longer than annual (Aagaard (2014); Ruggiero et al. (2016)). As depth decreases, interactions between coming waves and the shoreface become stronger, increasing sediment transport and resulting in more dynamic morphologies of the bed. The Depth of Closure (DoC) is a conceptual depth (Hallermeier (1980)) that marks the approximate transition between the actively mobilized upper shoreface and the more stable lower shoreface. Reported values typically fall within 3–15 m, depending on local wave climate.

The upper shoreface integrates the temporal scales of evolution of the lower shoreface, but can also significantly change at the seasonal scale. The upper shoreface if often called the surf zone, which is rather associated to the waves behavior as they reach the shore, dissipate most of their energy interacting with the bed, and eventually break at some point over the upper shoreface, or on the shoreline. Some sites exhibit one or several sandbars, sand formation resulting from repeated wave/bed interactions, and playing a role of "wave breaker" (Wright and Short (1984); Lippmann and Holman (1990)). The surf zone is therefore describe as the area where waves undergo deformation and breaking. The outer surf zone, located seaward of bars, is character-

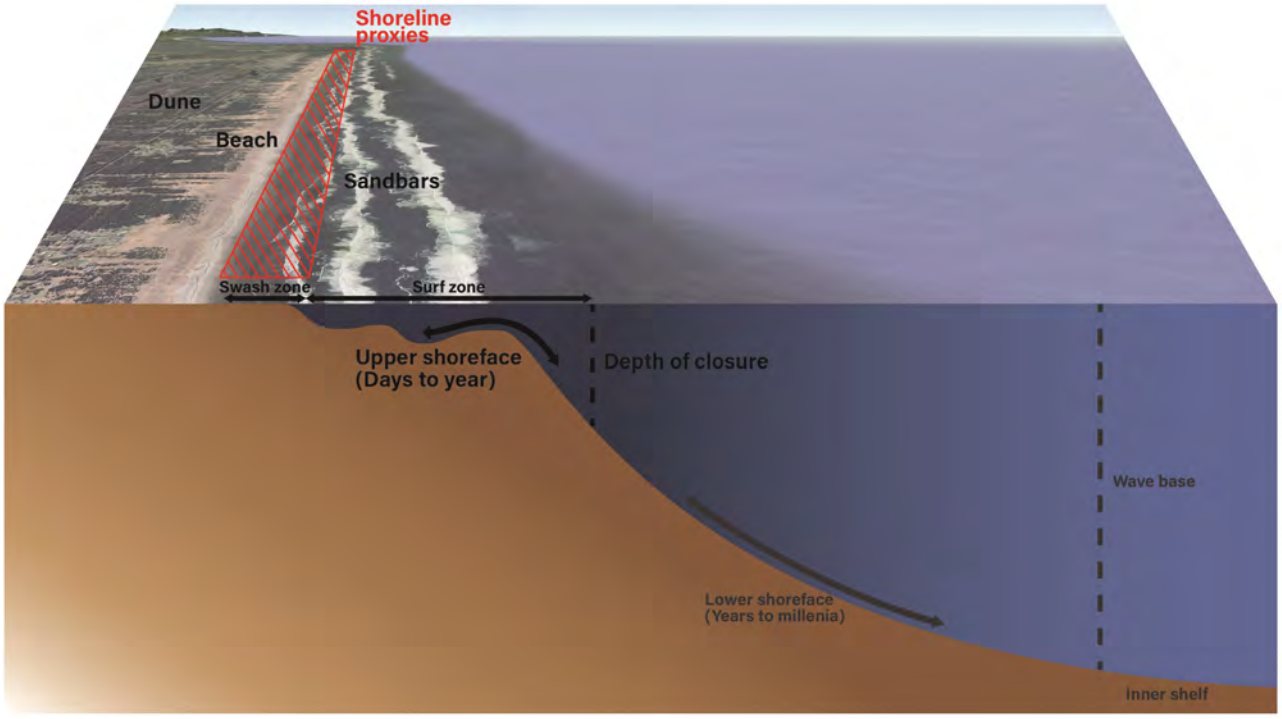

FIGURE I.4 Schematic representation of the beach system, with conceptual boundaries of the shoreface and the relative timescales of morphological change. Arrows indicate the relative magnitudes of sediment transport rates. The area where waterline and tidal datum-based shorelines are usually derived is highlighted in red. Figure adapted by *Anthony and Aagaard (2020)*; beach background image from Google Earth.

ized by rapid wave transformation and initial breaking. The inner surf zone, extending from the inner break point—typically over or just shoreward of bars—to the shoreline, is the shallower water zone (in the order of a few meters of depth) of broken wave propagation to the shoreline, it may include zones of wave reformation and secondary breaking, particularly over barred profiles.

The shoreline, place where the sea surface meets the beach, is hit by each breaking wave, experiences morphological changes at the wave-to-wave scale. The portion of the beach where waves run up and back is called the swash zone. This zone is alternately submerged during uprush and exposed during backwash. It is a highly dynamic area where sediment is continuously transported, and deposited. The swash zone is the place of the immediate response of the shoreline to incoming wave energy.

Upper on the beach is the part of the beach that is rarely under water. There, the sediment is usually dry and exposed to mobilization by the wind. The sediment transport goes with the wind

direction. When blowing offshore (in direction of the sea), the sediment can land in the surf zone and be mobilized by the waves. Inversely, onshore blowing winds tend to transport the sediment landward, which will eventually be trapped into coastal vegetation and progressively form what is called in dune (Moore et al. (2025)).

A visual representation of these different portions of the beach, with the associated magnitudes and scales of morphological changes, as well as the successive steps of wave propagation shoreward, is displayed on Figure I.4.

To these considerations, mostly focusing on waves, must be added the role of coastal sea level. Coastal sea-level varies across space and time, driven by multiple mechanisms acting and interacting at different scales. Coastal sea-level is linked to deep-ocean sea-level, through mechanisms operating at long time scales such as climate-driven global sea-level variations, but is also influenced by purely coastal mechanisms, such as the river runoff (Meade and Emery (1971); Piecuch et al. (2018)) or the wave setup (Thompson and Hamon (1980); Stockdon et al. (2006)). Over a wide spectrum of timescales, going from the hour to decades, and for a vast majority of sites, coastal sea-level variability is dominated by tides (Pugh and Woodworth (2014)). Tides are the periodic rise and fall of sea level mainly controlled by the gravitational attraction of the Moon and the Sun, combined with the rotation of the Earth. They occur with regular cycles, most commonly twice a day (semidiurnal) or once a day (diurnal), and can vary in amplitude from a few centimeters to several meters depending on the location. The large-scale, depth-uniform response to this astronomical forcing is known as the barotropic tide, which is relatively well understood and can be predicted with high accuracy by models (Lionel et al. (2023)). In contrast, when these tidal motions interact with ocean stratification and seafloor topography, they can generate baroclinic tides (internal tides), whose dynamics are more complex. The average difference of the tide-driven sea level fluctuations between a low and a high state if referred to as tide range. The global repartition of tide ranges is displayed on Figure I.5.

At the coast, the tide range is used to classify beaches (Davies (1964)) within three categories (tide range being a continuum, the classification can be finer). Microtidal beaches are those where the tidal range is less than 2 meters, mesotidal beaches correspond to tidal ranges between 2 and

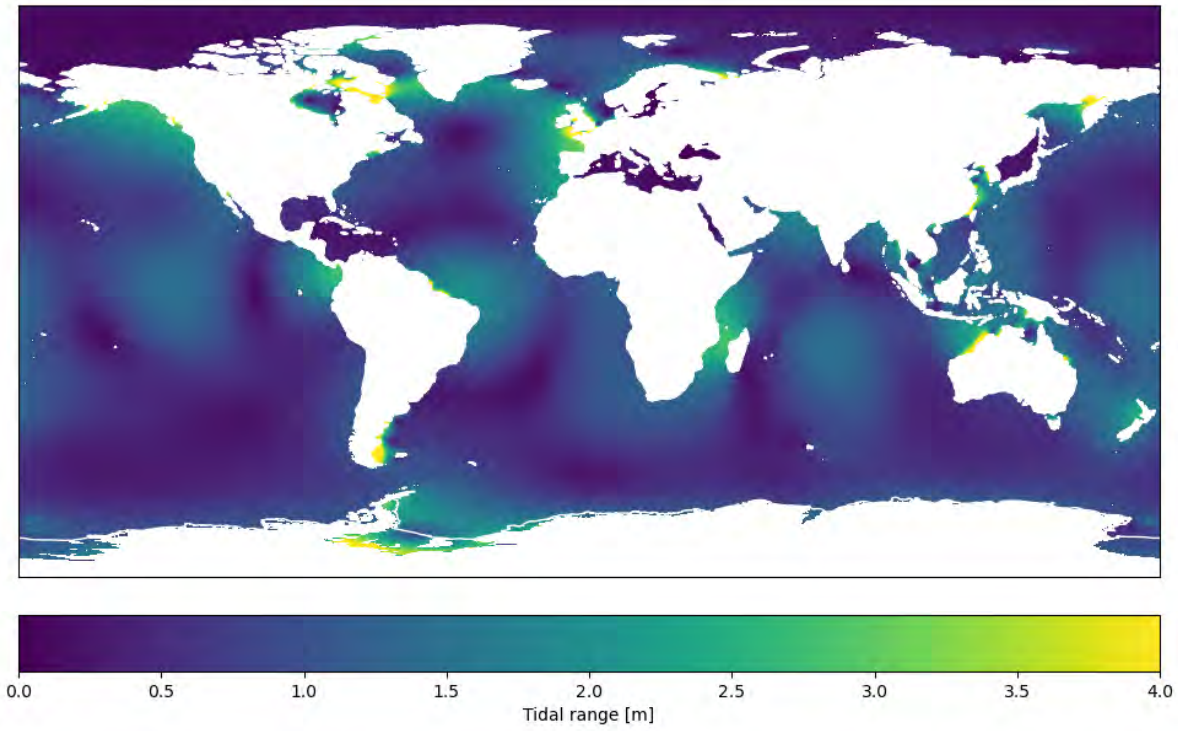

FIGURE I.5 Global map of tidal range, computed as three times the standard deviation of hourly barotropic tide variations over a 3-year period (FES2022, from 34 tidal constituents).

4 meters, and macrotidal beaches are characterized by tidal ranges exceeding 4 meters. The action of waves on coastal sediment transport depends on their intrinsic characteristics (height, period, angle of incidence) but is always mediated by water depth. Tides, as the dominant driver of coastal sea-level variability, modulate this depth over a wide range of timescales, thereby conditioning the extent and intensity of wave–bed interactions. At the microtidal end of the spectrum, wave processes exert a strong and localized control on beach morphology, as their action is confined to a narrow vertical range. With increasing tidal range, as in mesotidal settings, the vertical excursion of the wave action zone broadens, leading to more complex and spatially variable patterns of sediment transport. At the macrotidal end, tides govern the distribution of wave energy across an extensive cross-shore profile, reducing concentration at any given elevation but amplifying the spatial extent of morphodynamic adjustments.

By outlining a general description of what constitutes a beach, we establish the foundation necessary to explore the general concepts of coastal morphodynamics as presented in the literature.

I.2.2 Beach morphodynamics

The understanding of processes shaping the coast is reflected in the way coastal scientists and engineers model beach dynamics. Models have been developped to understand and predict beach morphodynamics, and its possible societal implications, at time scales that are relevant for engineering and decision-making, meaning from the storm scale to decades (Miller and Dean (2004)). Reviews of the different types of model (Roelvink and Brøker (1993)) identified categories of quantitative models : empirical models (e.g., Larson et al. (1989); Kamphuis (1991)), process-based models (e.g., Bertin et al. (2009)) and equilibrium models (e.g., Yates et al. (2009); Davidson et al. (2013)).

Process-based models are the models the closest to the general physics equation of mechanics (e.g., Navier-Stokes equations), in terms of morphodynamics, they can consist in explicitely modeling wave propagation and breaking, in describing the shoreface as a deformable surface controlled by transport due to the wave-induced bottom stress (e.g., Wilson (2023)), in a description of a portion of a beach as a grain pile, where the motion of each single grain in calculated according to the surrounding flow and grain-to-grain contact (e.g., Pähtz et al. (2015)). Despite their strong physical foundation, process-based models face important challenges. Their complexity often makes them computationally expensive, particularly when resolving fine-scale processes such as fluid-to-grain and grain-to-grain interactions (Elghannay and Tafti (2018)) under realistic conditions in a coastal environment. They require extensive input data—wave, current, sediment properties—at resolutions that are rarely available, which make them rely on modeled/idealized data [e.g., spheric sand grains with varying diameters (Maurin et al. (2018))], constraining their use in realistic environmental settings. Similarly, the accumulation of parameterizations and boundary conditions needed to make them tractable introduces uncertainties and limits their predictive skill (Fortunato et al. (2009)). As a result, while process-based models offer detailed insight into specific mechanisms, their practical application to large spatial domains or long-term morphodynamic evolution remains constrained.

Empirical models are result-oriented approaches built from the observation of a single case or a set of cases. In the context of beach morphodynamics, they consist of relating the observed morphological behavior to variables expected to act as drivers—such as waves, tides, or sediment grain

size—by establishing relationships that best fit the observations. Empirical models, while simply applicable, face several limitations (e.g., refer to Toomey et al. (2024) on the use of runup estimations derived from the formulation of Stockdon et al. (2006)). Because they are derived from specific case studies, their applicability is often restricted, with relationships that may not transfer well to other sites or conditions. They depend heavily on the quality and representativeness of the calibration data, and by reducing complex, nonlinear processes to simple correlations, they risk oversimplification. As a result, their predictive capacity is weak when extrapolated beyond observed ranges—such as under climate change scenarios—and they offer limited mechanistic insight into the processes driving coastal hydro-morphodynamics. Nowadays, the designation of empirical models has been largely replaced by that of data-driven models, reflecting the growing use of statistical and machine learning techniques. These approaches build on the same principle of deriving relationships from observations but rely on larger datasets and more sophisticated algorithms (e.g., Najar et al. (2022); Dalinghaus et al. (2023); Ibaceta and Harley (2024)) to capture complex, nonlinear dependencies. Unlike traditional empirical models, which were often limited to simple regressions, data-driven models can integrate diverse sources of information and uncover patterns that are not immediately apparent, potentially yielding improved predictive capacity. However, data-driven models, despite their increasing sophistication, do not provide a complete answer to our need for understanding of coastal morphodynamics. Their strength lies in prediction, but they often function as black boxes, offering limited insight into the underlying physical mechanisms. Moreover, their performance depends heavily on the availability and quality of large, representative datasets, which remain scarce in many coastal regions (Almar et al. (2024b)).

Equilibrium models are models based on the equilibrium concept. In a few words, equilibrium in coastal morphodynamics is the concept that a beach system reaches a balanced state with the nearshore conditions when these conditions remain constant. In other words, a beach defined by a given (and constant) grain size distribution, wave climate, and sea level will tend toward a characteristic shape, rather refereed to as 'state', that reflects these conditions (Wright and Short (1984); Masselink and Short (1993); Castelle and Masselink (2023)). Under this perspective, coastal morphodynamics can be seen as the expression of an instantaneous lack of equilibrium, or disequilibrium, with beaches continually reshaping themselves in response to a set of forcings

that are themselves constantly changing (Bruun (1954); Miller and Dean (2004); Davidson et al. (2013)). Equilibrium models occupy a hybrid position between data-driven and process-based approaches. They are inspired by physical processes, from which reduced-complexity formulations are derived, yet they rely on calibration to adjust key parameters and fit observed behaviors. Their simplicity, derived from well-grounded physical processes, makes them easily applicable and adaptable to a wide range of beaches at seasonal to interdecadal scales, which represents an interesting trade-off between applicability and physical realism, explaining why they are so popular and have been used in many locations (e.g., Splinter et al. (2014); Ludka et al. (2015); Lemos et al. (2018); Labarthe et al. (2023)).

The Brunn Rule (Bruun Per (1962)) is known as the first model of coastal morphodynamics using this concept, stating that the shoreline does not respond passively to sea-level rise -where "passive response" is understood as the straightforward displacement of the waterline on a fixed beach profile driven by sea-level fluctuations- but in a more complex way with the beach profile adapting to the rising water level by eroding near the shoreline, resulting in an even more pronounced shoreline retreat (displacement landward). The overall recession of the shoreline was described as

$$R = \frac{S \times L}{h + B} \tag{I.1}$$

with R the recession of the shoreline, S the vertical extent of sea-level rise, h the DoC, L the horizontal distance between the shoreline (before recession) and the DoC, and B the dune height, all expressed meters. Figure I.6 illustrates how shoreline retreat is modeled following the Brunn rule.

The Brunn rule has been largely criticized for its simplicity and overuse (e.g., Pilkey and Cooper (2002)). Other models have followed, focusing more on wave action to characterize seasonal and interannual morphological changes. Among them, models developed by Yates et al. (2009) and Davidson et al. (2013) have been widely adopted by the coastal modeling community (Vitousek et al. (2017)). Under their original simplest version, these models link shoreline change to changes in incoming waves as follow:

$$dX/dt = f(\Delta F) \tag{I.2}$$

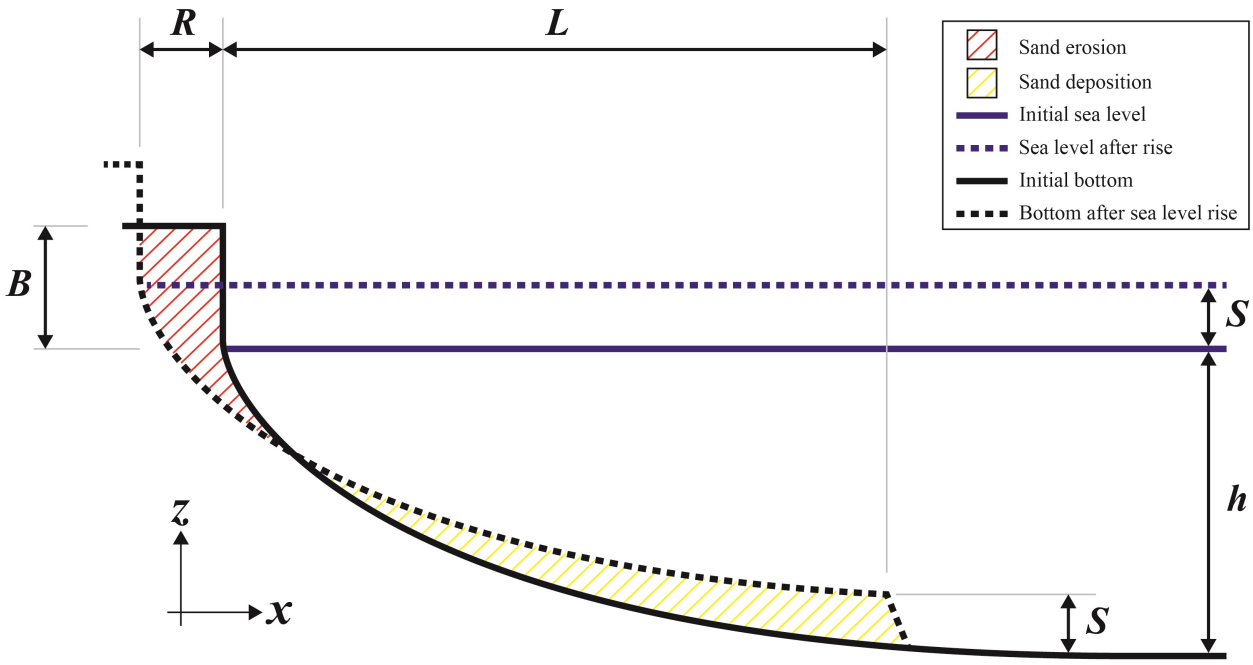

FIGURE I.6 Schematic representation of the evolution of the beach profile, including the shoreline, following the Brunn rule (*Brunn, 1962*).

with F the wave forcing, that can take the form of wave power, wave energy, wave height, or other metrics derived from the wave characteristics. ΔF is the difference between the instantaneous forcing $F(t)$ and the equilibrium forcing F_{eq} for which the system is balanced.

In the conception of Yates et al. (2009), the forcing variable is wave energy, and the equilibrium value of wave energy is calculated as each time step as a linear function of the instantaneous shoreline position.

In the conception of Davidson et al. (2013), the forcing variable is the Dean parameter Ω expressed as

$$\Omega = H_s/(T_p\omega) \tag{I.3}$$

where H_s and T_p are the significant wave height and wave peak period, respectively, and ω is the sediment fall velocity usually characterized at the scale of the beach by the median diameter of the grain distribution noted d_{50}. This parameter places the theoretical settling velocity of the

sediment into context with respect to the characteristics of the waves that mobilize it. The equilibrium Dean parameter Ω_{eq} is calculated as a weighted average of the antecedent Dean parameter values, with a calibration parameter ϕ called beach memory parameter.

Most equilibrium approaches are primarily focused on wave-driven dynamics, including purely cross-shore mechanisms as described above, and mixed cross-shore/longshore conceptions (e.g., Vitousek et al. (2017); Jaramillo et al. (2021)). In practice, sea-level variations are often introduced only as an external term, for instance by adding a background trend to account for the long-term trend of shoreline change, hybridly comprising sea-level rise and/or interannual wave climate variability morphodynamics (Kuriyama et al. (2012)). Recent developments have explicitly emphasized the inclusion of sea-level rise into equilibrium-type models, treating it as an additive driver of shoreline change alongside wave forcing (e.g., Vitousek et al. (2017); D'Anna et al. (2022); Vitousek et al. (2023b)). However, current equilibrium approaches typically lack a proper conceptualization of the feedbacks between sea-level change and wave-induced processes, overlooking how these drivers interact across intermediate scales, from storms to seasonal cycles and interannual fluctuations. This gap leaves unresolved a fundamental question: **how do sea-level variations and wave forcing combine and interact across scales to shape coastal morphodynamics, and ultimately drive shoreline change?** Addressing this question requires not only modeling these interactions, but also leveraging systematic observations to disentangle the relative influence of sea level and waves across timescales.

Models remain invaluable tools, as their predictive capacity is essential for anticipating beach morphodynamics and informing management strategies. Yet they must evolve in parallel with sustained observations, which both characterize the present state of beaches and provide the data necessary to calibrate and validate model behavior. In this way, modeling and observation form a complementary framework, each reinforcing the other in the pursuit of a more reliable understanding of coastal change.

I.2.3 In-situ survey of the beach system

Surveying is essential for understanding the dynamic evolution of the coast, which act both as natural buffers against waves and storms and as socio-ecological hotspots (Barnard et al. (2021); Moore et al. (2025)). Beach monitoring is the counterpart to beach modeling: it provides the empirical foundation upon which both scientific understanding and predictive approaches are built. Because beaches are highly dynamic environments, subject to rapid and multiscale changes, observations must capture both their evolution and the forcings that drive it. This requires identifying which physical metrics best describe beach morphology and morphodynamics, and deploying appropriate observational techniques adapted to different spatial and temporal scales.

Hydrodynamic forcings such as wave height, period, and direction are typically measured using offshore instruments deployed in the nearshore or continental shelf. Wave buoys, moored at fixed locations, and pressure sensors, installed at a known depth, remain the most widely used tools: they record sea surface motion and, through spectral analysis, provide estimates of significant wave height and dominant period (Long and Oltman-Shay (1991)). Wave buoys additionally allow estimation of mean wave direction. Acoustic Doppler Current Profilers (ADCPs) extend these capabilities by measuring both pressure and velocity profiles, enabling a more complete characterization of wave and current interactions with the shoreface. Tides and other fluctuations of the sea-level, on the other hand, can be monitored through tide gauges — essentially buoys or fixed stations equipped with pressure transducers — which record sea-level variations at high temporal resolution [with many institutions providing public access to the instantaneous measured and modeled sea-level (e.g., SHOM, NOAA, UKHO)] and over long temporal scales (Holgate et al. (2013)).

Beach morphology and its changes can straightforwardly be captured by measurements of the beach topography and/or bathymetry. A regularly surveyed beach profile (PF595) at Torrey Pines, CA, USA (Ludka et al. (2019)) is displayed on Figure I.7 illustrating the different morphological metrics that can be monitored and derived.

I.2.3.1 Beach elevation profiles

At a given time, the most comprehensive description of beach morphology is the complete topography–bathymetry continuum, in which every point of the beach, defined by its longitude and latitude (or a another set of plan coordinates), is associated with an elevation referenced to a fixed vertical datum $z(x, y)$.

In practice, beach monitoring has often focused on cross-shore profiles $z(x)$, discretizing the beach at regular intervals Δy. These profiles typically describe the elevation from the highest point of the subaerial beach down to the shoreline [e.g., survey at Truc-Vert, France (Castelle et al. (2020)) and at Guisseny, France (Suanez et al. (2023))], and in some cases extend offshore to include bathymetry reaching depths of several meters [e.g., surveys along the Columbia River mouth (Ruggiero et al. (2005)), at Duck, NC, USA (Pianca et al. (2015)), or at Torrey Pines, CA, USA (Ludka et al. (2019)) as illustrated on Figure I.7.a]. Beach elevation profiles are collected primarily through in-situ surveys including land surveying with with tapes, leveling rods (Shalowitz (1962, 1964)), simple yet effective technics such as the Emery method emerged [developed by Emery (1961) and used in the 80s to monitor Narrabeen beach in Australia (Turner et al. (2016))], as well as modern techniques using Global Navigation Satellite System (GNSS) information for the exposed part of the beach (e.g., Ruggiero et al. (2005); Castelle et al. (2020); Suanez et al. (2023)), coupled with echo-sounders for the bathymetry part (e.g., Ruggiero et al. (2005)). These methods, and especially the more recent ones, are associated with high-accuracy data with subdecimetric errors (Castelle et al. (2020); McCarroll et al. (2023)), to which can be added uncertainties on the instantaneous sea-level when conducting bathymetry surveys (Ruggiero et al. (2005)). However, these methods are labor-intensive and time-consuming, making it challenging to cover long stretches of coast or to maintain high-frequency temporal observations over extended periods (Vitousek et al. (2023a)). To date, the number of sites over which have been performed regular beach profile surveys (one a year or more), over a long period of time (more than a decade), and made publicly available (on publicly accessible repositories) is limited to a few dozens, mostly located in Western Europe (e.g., Castelle et al. (2020); Bertin et al. (2022); McCarroll et al. (2023)), North America (e.g., Ruggiero et al. (2005); Ludka et al. (2019)), East Asia (e.g., Banno et al. (2020)), and Australia (e.g., Turner et al. (2016)). Sites with the same characteristics and for which the bathymetry section is surveyed are even fewer.

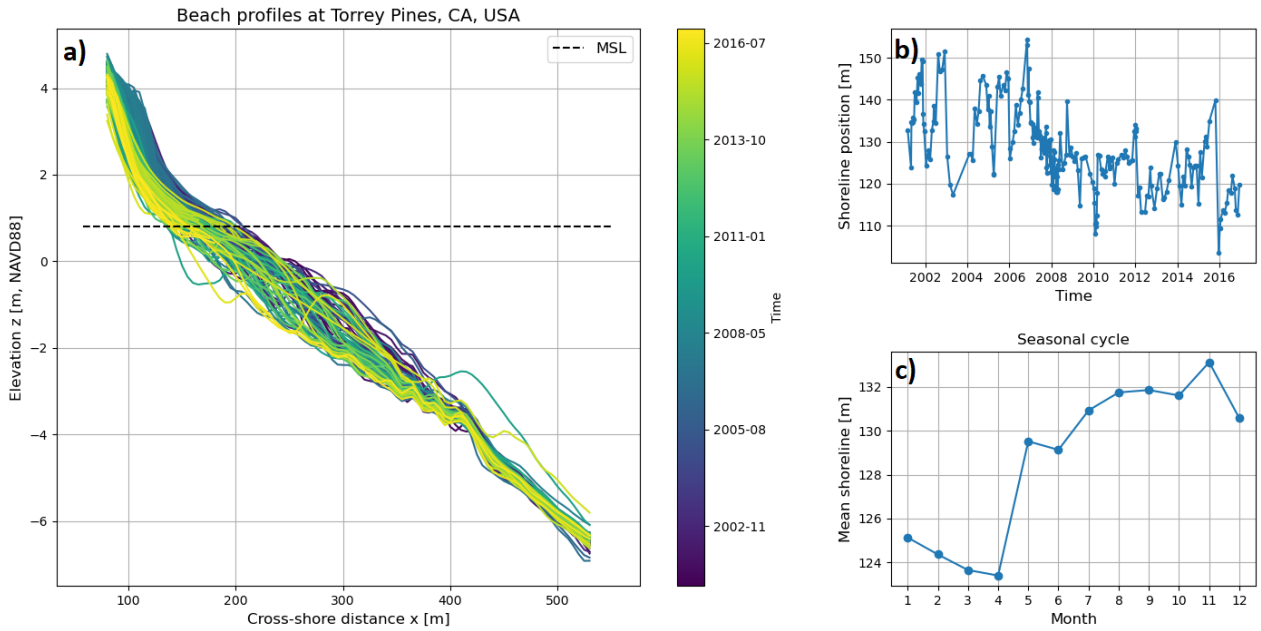

FIGURE I.7 (a) Beach elevation profiles, (b) datum-based shoreline time series, and (c) seasonal cycle of shoreline position at Torrey Pines, CA, USA (profile ID : PF595). The cross-shore shoreline position time series is calculated as the intersection between the elevation $z = 0.8$ m , NAVD88 (represented as a black dashed line on panel a) and the beach elevation profiles.

The comparison of two consecutive measurements of the same beach profile provides valuable information on profile morphodynamics, as it reveals which parts of the profile have eroded or accreted. A common way to quantify these changes is through sand volume estimates, derived from beach elevation profiles by calculating the gain or loss of cross-sectional area. When profiles are spaced closely enough, these sectional changes can be extrapolated to volumetric changes across the entire beach, thereby indicating the net sediment gain or loss between observations. This method is commonly applied to quantify sediment losses following storm events (Barnard and Warrick (2010); Masselink et al. (2016)) or, over longer timescales, to assess chronic erosion or accretion trends (Ruggiero et al. (2016)). More broadly, the net volume of sediment change represents an integrated metric that most faithfully reflects beach evolution. This measure is of particular interest for coastal management and decision-making, as it can be directly translated into the volume of sand required to maintain or restore a beach through nourishment interventions (Amrouni et al. (2024)).

In many cases, a parallel is drawn between changes in beach volume—most often subaerial vol-

ume—and variations in another widely used metric: shoreline position (e.g., Barnard and Warrick (2010); Barnard et al. (2017)). The shoreline is often described as the intersection between the sea surface and the land, yet this seemingly simple definition can be interpreted and adapted in multiple ways depending on the application, resulting in dozens of distinct shoreline definitions (Boak and Turner (2005)). Its relative simplicity, ease of interpretation, and broad availability have made it one of the most widely used indicators of coastal change by researchers, engineers, and coastal planners over the past decades (McAllister et al. (2022)).

I.2.3.2 Shoreline position

Beyond a generic definition of the physical interface between land and water (Boak and Turner (2005)), the shoreline is an inherently ambiguous object. This ambiguity arises from the highly dynamic nature of the nearshore zone, where hydrodynamic conditions change at a large variety of frequencies, and from the heterogeneity of coastal settings. For instance, on a beach with a large tidal range, the land–sea interface can shift dramatically over the course of a day. If two measurements are taken at different tidal stages, the apparent shoreline change will primarily reflect tidal variation rather than any genuine morphological evolution. As a result, researchers and practitioners have adopted different shoreline definitions depending on the characteristics of the sites they monitor and the observational methods available to them. A common way to categorize shoreline indicators is the datum-based and proxy-based categorization.

Datum-based shoreline measurements rely on fixed vertical references, such as geodetic benchmarks or tidal datums, to ensure consistency and comparability across observations (Ruggiero et al. (2003)). They are typically derived from beach elevation profiles, with the shoreline defined at a constant reference elevation. These reference elevations are generally tied to the local tidal regime and may correspond, for example, to Mean High Water (MHW), representing the average sea level during high tide; Mean Low Water (MLW), the average level during low tide; or Mean Sea Level (MSL), the long-term average of sea level. Such means must be calculated over extended periods of sea-level observations—19 years, as recommended by Shalowitz (1962)—to fully account for all tidal constituents. The main advantage of deriving shoreline positions from beach elevation profiles is that any observed change directly reflects actual topographic evolutions, and therefore implies a corresponding change in sediment volume. However, because these

positions are extracted from detailed elevation profiles, datum-based shorelines are just as labor-intensive to obtain as topographic data themselves. As a result, their application remains limited to the relatively few locations where systematic beach topography monitoring is carried out.

Proxy-based indicators, by contrast, rely on visually identifiable features and are generally easier to obtain, particularly with the advent of global satellite imagery (McAllister et al. (2022); Vitousek et al. (2023a)). Common examples include the instantaneous shoreline position (the land–sea interface at the moment of image acquisition), the high-water line (often identified by a debris line or the wet/dry sand boundary), and the vegetation edge (Boak and Turner (2005)). Because they can be derived from top-view imagery, these indicators are convenient for long-term monitoring and for assessing shoreline change over large spatial scales. However, a key limitation of most proxy-based data—except for the vegetation edge—is their sensitivity to sea-level variability. Changes in proxy-based shoreline positions reflect not only morphological change but also the influence of hydrodynamic processes such as tides, wave setup, and storm surge (Ruggiero et al. (2003); Moore et al. (2006)), altering the sea-level and therefore biasing straightforward conclusions on morphological changes of the beach from the shoreline position estimate. In this thesis, we refer to land/sea interface proxy-based shorelines as waterlines. Waterline positions can be corrected from dynamic sea-level signals to get closer to what can be defined as shoreline positions (i.e., reflecting the morphological evolution of the beach).

Despite its apparent simplicity, the shoreline proxy embodies a dual character. On one side, it offers an integrated and easily extractable representation of coastal change, condensing the combined influence of hydrodynamic forcing, sediment transport, and sea-level fluctuations into a single, scalable metric. This makes it an invaluable tool for long-term monitoring, large-scale comparisons, and operational applications. On the other side, precisely because it integrates the complexity of a three-dimensional, cross-shore–integrated system into a two-dimensional line, much of the underlying morphodynamic signal is obscured. Processes such as profile steepening, dune erosion, or offshore bar dynamics may not be faithfully captured in shoreline variability, and different shoreline definitions can even lead to diverging interpretations of change. Thus, while powerful, the direct transferability of shoreline position into total volume change is limited (see, for instance, Stive et al. (2002), which demonstrates how the low water line, high water

line, and dune foot can exhibit markedly different variability). This apparent trade-off between simplicity and accessibility raises a central question: **can satellite-derived shoreline proxies reliably inform on beach morphodynamics across scales?**

I.2.3.3 Higher-order indicators of shoreline variability

Beyond time series of shoreline position changes, beach morphodynamics can be characterized using more integrated metrics that reflect their longer-term behavior. Two commonly used integrated metrics are the long-term trend and the seasonal cycle of shoreline change.

Long-term trends summarize shoreline movement over extended periods, allowing net change to be expressed as an annual rate in meters per year. This metric is widely used to determine whether a beach is experiencing net erosion or accretion (e.g., Luijendijk et al. (2018)), providing a first-order indicator of overall coastal stability. Trends are usually derived from time series of shoreline change using linear regressions (e.g., Luijendijk et al. (2018)) or more refined technics such as spectral analyses (e.g., Warrick et al. (2025a)). Trends are particularly valuable for coastal planners, as they capture the anticipated morphodynamics of a beach and highlight that some processes are driving persistent changes—for example, an imbalance in the sediment budget (Warrick et al. (2019)) and/or persistent evolutions in hydrodynamic forcing (Allan and Komar (2006)).

Time series of shoreline position can also be detrended—that is, corrected for the long-term trend—to emphasize shorter-term fluctuations, particularly seasonal variability. Seasonal variability is often summarized as a climatology, commonly referred to as the seasonal cycle, which represents the mean shoreline position for each month of the year. These data are useful for understanding the timing and magnitude of recurrent seasonal processes, such as storm and wave climate cycles, and for informing coastal management decisions that need to account for predictable intra-annual changes in beach morphology.

Residuals can be obtained by removing both the long-term trend and the seasonal cycle from a shoreline position time series. These residuals highlight short-term, episodic changes, such as those induced by individual storms, extreme waves, or anomalous hydrodynamic events. They

can also reveal interannual fluctuations in shoreline position that may be attributed to climate modes (e.g., Graffin et al. (2023)). Analyzing these residuals allows for quantification of the magnitude and frequency of short-term events, improves our understanding of the beach's response to high-energy perturbations, and provides insight into post-storm recovery. Additionally, they enhance our understanding of how beach morphology adapts to persistent interannual variations in wave climate and sea level, offering complementary information to both long-term trends and seasonal metrics.

Together, these metrics provide an integrated and informative description of the shoreline position variability, capturing the short-term response to high-energy events, the predictable seasonal evolution of the shoreline, broader modulations at interannual to interdecadal scales driven by climate modes, and longer-term changes under persistently evolving conditions. This information seems useful, not only for advancing our scientific understanding of coastal processes, but also for supporting socio-economic decision-making in a climate change context, such as the design of coastal protection measures (Le Xuan et al. (2022)), planning of beach nourishment projects (Amrouni et al. (2024)), management of recreational areas, and mitigation of risks to coastal communities and infrastructure (e.g., Dada et al. (2024); Turner et al. (2024)). However, despite their importance, such knowledge remains poorly documented or entirely unknown across the vast majority of the world's coastlines (Vitousek et al. (2023a)), highlighting the pressing need to extend monitoring efforts.

I.3 Satellite-based monitoring of the beach

Our understanding of beach morphodynamics remains limited for most of the world's coastlines (Vitousek et al. (2023a)), largely because traditional monitoring methods are costly and labor-intensive, restricting both temporal and spatial coverage. This presents a fundamental challenge: the dominant processes shaping beaches—wave-driven morphodynamics and coastal sea-level variations—operate across broad spatial and temporal scales, which cannot be fully captured by localized, short-term measurements. Without observations at matching scales, our ability to understand and model the links between forcing and morphological response is inherently con-

strained.

I.3.1 A tool suited for climate-related coastal hydro-morphodynamics monitoring

Satellite imagery, whose availability has increased (Turner et al. (2021)) and whose accessibility has been enhanced by cloud-computing platforms (Gorelick et al. (2017)), offers a powerful means to address this scale mismatch in coastal monitoring. Over the past four decades, systematic Earth observation missions have created an unparalleled archive of global imagery. Optical sensors capture reflected sunlight across multiple spectral bands, providing high-quality multispectral data ideal for detecting water–land boundaries. Radar sensors, such as Sentinel-1's synthetic aperture radar (SAR), actively sense the surface using microwave signals. While optical imagery enables shoreline extraction under clear-sky conditions, radar imagery can theoretically delineate shorelines in cloudy or low-light environments, allowing continuous monitoring. However, the inherent noise in SAR imagery has so far limited its systematic application for shoreline delineation (e.g., Paz-Delgado et al. (2022); Angelini et al. (2024); Savastano et al. (2024)).

The Landsat program—beginning with early missions and continuing through Landsat 5 (1984), Landsat 7 (1999), Landsat 8 (2013), and Landsat 9 (2021)—provides the longest continuous record of multispectral imagery with global coverage with a medium resolution (30 m pixels, 16-days revisit per mission). Sentinel-2, launched in 2015 under the Copernicus program, offers higher temporal resolution (5-day revisit with two satellites) and improved spatial resolution (10–20 m pixels), enabling consistent, repeated, long-term coverage of most coastlines worldwide (Bergsma and Almar (2020)). Beyond these long-standing platforms, newer high-resolution sensors have further expanded monitoring opportunities. For example, PlanetScope provides 3 m-resolution imagery, allowing for precise shoreline mapping (Doherty et al. (2022)), and VENuS deliver daily 5 m-resolution imagery specifically tailored to coastal monitoring (Bergsma et al. (2021)). Together, these complementary data streams extend the spatiotemporal scales at which shoreline dynamics can be observed, bridging the gap between global continuity and local detail. Table I.1 summarizes the characteristics of the main Earth-observing optical satellite missions

TABLE I.1 Summary of the main optical satellite missions used for coastal monitoring. R, G, B, NIR, and SWIR 1 & 2 (listed from the shortest to the largest wavelength) refer to red, green, blue, near-infrared, and shortwave infrared (bands 1 and 2), respectively. * The listed bands are those commonly used for water-differentiating index calculations (see below); additional bands are available for most satellite missions.

Name	Period of activity	Revisit Period	Resolution	Available bands*
Landsat 5	1984-2013	16 days	30 m	R, G, B, NIR, SWIR1&2
Landsat 7	1999-2025	16 days	30 m	R, G, B, NIR, SWIR1&2
Landsat 8	2013-present	16 days	30 m	R, G, B, NIR, SWIR1&2
Sentinel-2	2015-present	5 days	10-20 m	R, G, B, NIR, SWIR1&2
PlanetScope	2016-present	sub-daily	3.7 m	R, G, B, NIR
VENuS	2017-present	1 days	5 m	R, G, B, NIR
Landsat 9	2021-present	16 days	30 m	R, G, B, NIR, SWIR1&2

used for geoscience applications.

Although still coarser in spatial resolution than in situ measurements, this constellation of satellite missions now allows systematic tracking of beach responses to a wide range of forcing mechanisms, from individual storms to seasonal cycles, interannual climate variability, and long-term changes (Vitousek et al. (2023a)).

Figure I.8 roughly situates the contribution of Earth-observing satellite imagery within the broader landscape of coastal science, illustrating the overlap between processes, modeling approaches, and observational techniques spatiotemporal scales of application. Satellite-derived data can theoretically be used to observe the beach hydro-morphodynamic response to a large diversity of mechanisms. By filling these gaps, satellites could provide the long-term, large-scale datasets essential for empirical, data-driven, and equilibrium modeling approaches.

I.3.2 Deriving waterline positions from optical satellite-imagery

Optical satellite imagery can be used to derived the instantaneous land/sea interface position, commonly referred to as waterline, through methods called Satellite-Derived Waterline (SDW) methods. SDW extraction from multispectral imagery typically relies on two fundamental processing steps: (i) band combination, where the multispectral information is aggregated into a single index or band-enhanced image that accentuates the contrast between water and non-water pixels, and (ii) segmentation, where the shoreline is delineated by identifying the land–sea interface from the resulting image (e.g., Bishop-Taylor et al. (2019a); Vos et al. (2019b)).

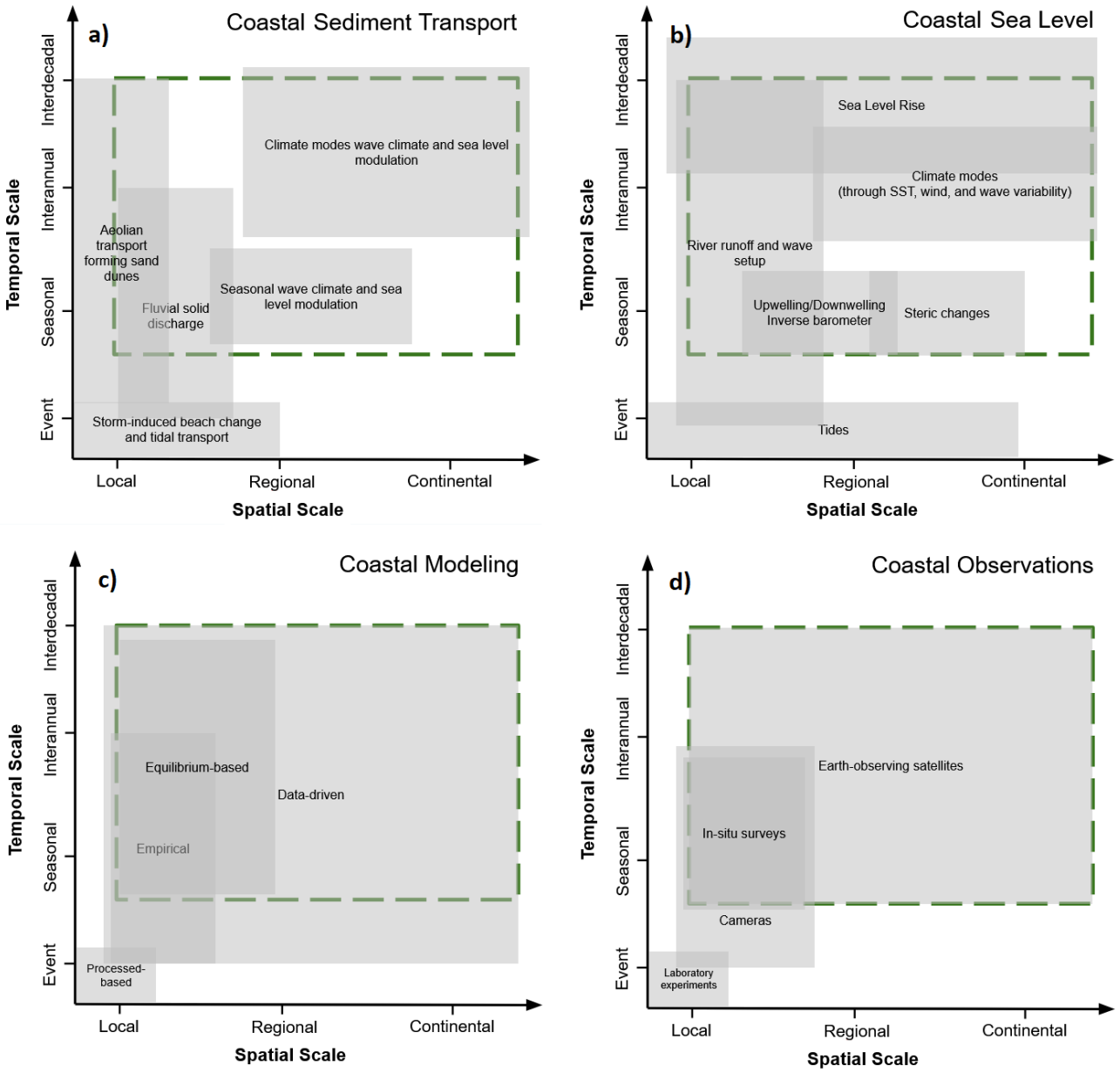

FIGURE I.8 Schematic representation of (a–b) the processes driving coastal hydro-morphodynamics, (c) the main modeling approaches, and (d) the monitoring techniques, all positioned according to their respective spatio-temporal scales of application. The sea level panel is adapted from *Woodworth et al., 2019*, the sediment transport and coastal observation panels are adapted from *Vitousek et al., 2023*. The green dashed frame delimits the application scales of satellite-based monitoring (*Vitousek et al., 2023*).

Since the launch of the first Earth-observing satellites, several spectral indices have been developed to enhance contrast between water and non-water features. The Normalized Difference Water Index (NDWI; McFEETERS (1996)) was among the earliest, combining green and near-infrared (NIR) reflectance to delineate water bodies. Pixels with positive NDWI values were clas-

TABLE I.2 Water-differentiating indices and their formula. G, B, NIR, SWIR1 and SWIR2 refer to the green, blue, near-infrared and shortwave-infrared (1 and 2) provided by the optical sensors of Landsat (5, 7, 8 and 9) and Sentinel-2 missions.

NDWI	$(G-NIR)/(G+NIR)$
MNDWI	$(G-SWIR1)/(G+SWIR1)$
AWEIsh	$2.5\times G+B-(1.5\times SWIR1+0.25\times SWIR2+1.5\times NIR)$
AWEIns	$4\times G-(4\times SWIR1+2.75\times SWIR2+0.25\times NIR)$
SCoWI	$2\times G+B-(0.75\times SWIR1+0.5\times SWIR2+2\times NIR)$

sified as land, while negative values indicated water. Although straightforward, this approach struggled in areas with dense vegetation or urban surfaces, which often exhibited spectral responses close to water (Xu (2006)).

To improve separability, Xu (2006) introduced the Modified NDWI (MNDWI), replacing the NIR band with the shortwave infrared (SWIR) band (Landsat and Sentinel-2 missions have two different SWIR bands, the SWIR1 band, the shortest wavelength of the two, is generally used when calculating the MNDWI). This modification enhanced performance in built-up and vegetated areas. Yet, both NDWI and MNDWI showed reduced accuracy in conditions with strong shadows, turbid waters, or dark surfaces. Addressing these challenges, Feyisa et al. (2014) proposed the Automated Water Extraction Index (AWEI), with two variants tailored for shadowed (AWEIsh) and non-shadowed (AWEIns) environments. Their results demonstrated higher accuracy and more stable thresholds across diverse landscapes.

More recently, challenges specific to coastal environments have been highlighted. For instance, wave breaking and foam introduce noise into traditional indices, reducing their ability to delineate true waterlines. To overcome this, Bergsma et al. (2024) developed the Subtractive Coastal Water Index (SCoWI), a purpose-built index optimized for sandy beach environments, including those with turbid waters. This development underscores both the maturity of spectral index methods and the continuing need for specialized indices adapted to coastal conditions. Table I.2 summarizes and shortly describe the aforementioned indices.

Once a water-differentiating index is computed, thresholding is required to distinguish water from land. The earliest approaches used fixed thresholds, such as the NDWI $= 0$ proposed by McFEETERS (1996), but these proved inadequate across diverse environments (Xu (2006); Ji

et al. (2009)). Since then, adaptive thresholding methods have emerged.

Because water indices typically yield bimodal pixel distributions (land vs. water), this property has been exploited by a variety of algorithms. The Weighted Peaks (WP) method (Harley et al. (2019)) estimates the optimal threshold as a weighted mean of the two distribution peaks, with best results optained at the Austrlian beach of Narrabeen when the threshold is shifted toward the "dry" peak—about 30% of the peak-to-peak distance (Doherty et al. (2022)). While effective, this method requires an a priori assumption about the relative positions of the peaks, potentially limiting its direct transferability to other sites.

The Minimum Shoreline Variability (MSV) method (Almar et al. (2012)) defines the optimal threshold as the one that minimizes shoreline position variability across consecutive thresholds. Initially developed for video-based shoreline extraction at high-energy macrotidal beaches (e.g., Truc Vert), the method has not yet been systematically applied to satellite imagery, but conceptually offers a promising approach for challenging environments.

Another widely used non-parametric approach is Otsu's method (Otsu (1979)), which identifies the threshold maximizing inter-class variance in a bimodal distribution. This method has been extensively applied in shoreline mapping from satellite imagery (e.g., Bishop-Taylor et al. (2019a); Vos et al. (2019b)). However, its reliance on strict bimodality limits accuracy environments when the pixel distribution is skewed. That can be the case when monitoring sites with large intertidal beach (Castelle et al. (2021); Graffin et al. (2023); Konstantinou et al. (2023)), or in turbid environements (Bergsma et al. (2024)). To refine this approach, Bergsma et al. (2024) proposed the Local Minimum (LM) method, which adjusts Otsu's threshold by locating a nearby local minimum in the distribution, improving robustness in non-ideal conditions.

Toolkits such as CoastSat (Vos et al. (2019b)), SHOREX (Sánchez-García et al. (2020)), or CASSIE (Almeida et al. (2021)) have automated these processes of band combination and segmentation based on automatic thresholding methods coupled with sub-pixelic delineation of the waterline using Marching Square algorithms (Cipolletti et al. (2012)), allowing users to generate time series of SDW positions from publicly available satellite imagery, which can be projected

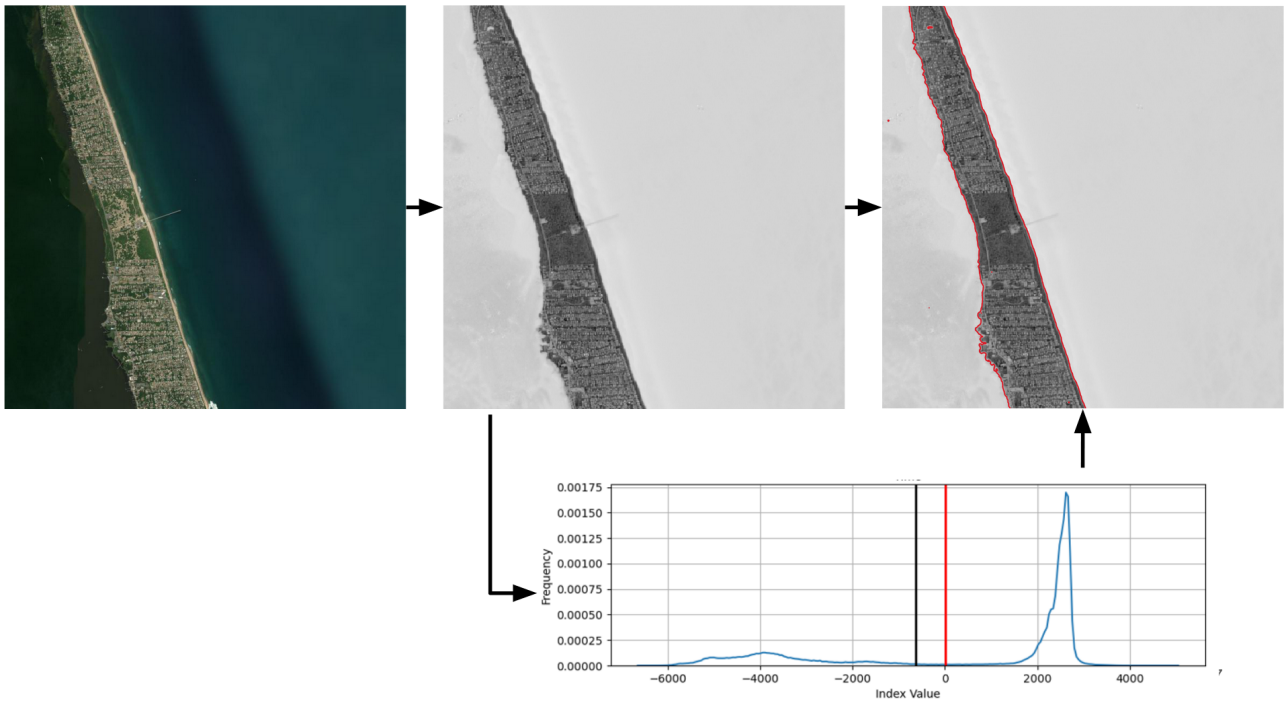

FIGURE I.9 Schematic application of the SDW method on a Sentinel-2 image. The grayscale panel shows the water-differentiating index map, with the corresponding pixel-value distribution displayed in the histogram. Two thresholds are indicated: the Otsu threshold (black line) and the LM method threshold (in red). The extracted waterline, obtained using the LM threshold, is delineated in red. The right panel zooms in on the resulting contour, highlighting its sub-pixel precision as derived with the Marching Squares algorithm (*Cipoletti et al., 2012*).

along transects perpendicular to the shoreline to get at each transect a time series of cross-shore waterline position. Figure I.9 illustrate the shoreline delineation process from an initial multi-spectral Sentinel-2 image of Duck, NC, USA.

I.3.3 Challenges of satellite-derived waterline and shoreline methods

As the instantaneous waterline is strongly influenced by short-term hydrodynamic processes—including tides, wave setup, runup, and storm surge—it cannot be directly interpreted as a stable shoreline proxy. To enable consistent monitoring and comparability with in situ observations, Satellite-derived waterlines are therefore often corrected using external datasets, resulting in Satellite-Derived Shorelines (SDS). These standardized shoreline proxies are typically referenced to tidal datums such as MSL or MHW, which are also the most common reference levels for datum-based in situ shoreline measurements (e.g., Vos et al. (2019b); Castelle et al. (2021)). Theoretically, horizontal displacement of the waterline relative to the reference shoreline can be expressed as

$$\Delta X_{hydro} = \frac{\eta - z_{ref}}{tan\beta}, \tag{I.4}$$

where η is the water level (from tide gauge observations or computed from models) at the time of image acquisition, z_{ref} is the elevation of the chosen reference datum (e.g., MSL or MHW), and $tan\beta$ is the mean beach slope between η and z_{ref}.

However, in practice, the information required for accurate corrections is rarely available, and several simplifying assumptions are typically adopted. First, water level variability is most often reduced to the tidal component, which can be measured from nearby tide gauges or modeled using global or regional tidal models [e.g., FES2022 (Lionel et al. (2023))]. Some studies attempt to refine this approach by accounting for additional variability due to wave runup, applying parameterizations of swash and setup (e.g., Stockdon et al. (2006); Senechal et al. (2011)) to estimate and correct its contribution (e.g., Castelle et al. (2021); Graffin et al. (2023)). Second, the local beach slope between the instantaneous water level and the chosen reference elevation is generally unknown, except where independent beach profile data exist. For the vast majority of sites lacking such data, the mean slope can be estimated using the methodology proposed by Vos et al. (2020), which derives an optimal slope from time series of waterline positions by minimizing tidal aliasing. While useful, this method produces a single representative slope for the entire profile and period covered by the dataset—an assumption that oversimplifies the natural variability of beach morphology. Its limitations are particularly pronounced at sites with wide intertidal zones, where the profile deviates strongly from a constant slope, and at sites with highly dynamic beach slopes.

Beyond the dynamic nature of sea level, which limits the interpretability of SDW data, several additional challenges remain. First, the spatial resolution of optical imagery is a fundamental constraint: even with sub-pixel techniques, Landsat and Sentinel-2 data typically yield shoreline accuracies of ∼10 m (Vos et al. (2019a); Sánchez-García et al. (2020)) and can reach dozens of meters (Bishop-Taylor et al. (2019a); Vos et al. (2019b); Graffin et al. (2023)) at challenging sites, often exceeding the magnitude of short-term shoreline changes measured in situ (Vos et al. (2023b)). Second, the automation of detection algorithms can introduce misclassifications for a variety of reasons, including cloud cover, ambiguity of the waterline position over wet or reflec-

tive beaches, and the presence of shallow waters. Particularly, at sites exhibiting a large intertidal beach, the waterline can be confounded with the wet/dry sand line, or fall in the middle of the wet intertidal beach (Castelle et al. (2021); Konstantinou et al. (2023); Graffin et al. (2023)). Such errors highlight the necessity of improving segmentation methods when observing complex environements, but also require either rigorous visual inspection of extracted shorelines (Castelle et al. (2021, 2022); Konstantinou et al. (2023)) or the development of robust automated filtering methods to identify and exclude erroneous data (Graffin et al. (2023)). Finally, the inherent diversity of coastal settings means that no single approach has yet proven universally reliable, with method performance remaining site-specific (McAllister et al. (2022)).

I.3.4 Large scale satellite-based coastal monitoring

Despite their limitations, SDW methods have opened new frontiers in coastal monitoring, transforming the field from "data-poor" to "data-rich" (Vitousek et al. (2023a)). The unprecedented wealth of shoreline information now available has enabled large-scale studies that go beyond local case analyses to provide key insights into global and regional coastal dynamics. The pioneering efforts in this direction are those of Luijendijk et al. (2018) and Mentaschi et al. (2018), both of which produced global assessments of shoreline evolution from the 1980s to the late 2010s, albeit with different methodologies.

Luijendijk et al. (2018) focused on cross-shore shoreline position trends estimated at transects spaced 500 m apart along the world's coasts. Using a machine-learning-based classification approach, they reported that about one-third (31%) of the global ice-free coastline is sandy, and that roughly one-quarter of these sandy beaches were eroding (24%) while another quarter were accreting (21%) at rates exceeding 0.5 m/yr. Their method relied on yearly composites of NDWI-derived coastal images, from which shoreline contours were extracted using Otsu's thresholding method. Long-term shoreline trends were then derived by fitting linear regressions to the annual shoreline time series.

In contrast, Mentaschi et al. (2018) based their study on the Global Surface Water Explorer (Pekel et al. (2016)), a pixel-level classification of surface water presence derived from Landsat 5,

7, and 8 imagery spanning 1984–2015. Relying on a combination of "expert systems, visual analytics, and evidential reasoning," they estimated shoreline changes and associated land loss/gain, concluding that globally about 15,000 km^2 of land had been lost to the sea over three decades.

These pioneer works have since been followed by a new generation of large-scale monitoring frameworks, applied to specific coastal environments such as sandy beaches (e.g., Vos et al. (2023a)), deltas (e.g., Nienhuis et al. (2020)), or to all coastal types (e.g., Almar et al. (2023)), estimating contributions of climate variability (ENSO in particular) and human interventions on large scale shoreline change. However, such large-scale applications are often associated to concerns from the coastal community. Limitations in resolution, uncertainties in land–sea boundary detection, challenges in transect generation, and the management of outliers all complicate robust shoreline trend estimation. As a result, the reception of these studies has been mixed, sparking debates about both the scientific validity and the practical utility of global-scale coastal monitoring—illustrated, for instance, by the Almar/Warrick (Almar et al. (2023); Warrick et al. (2024); Almar et al. (2024b)) and the Nienhuis/Zăinescu exchanges (Nienhuis et al. (2020); Zăinescu et al. (2023); Nienhuis et al. (2023)).

In parallel, benchmarking initiatives have sought to systematically evaluate automated shoreline extraction methods against ground-truth datasets (e.g., Bishop-Taylor et al. (2019a); Vos et al. (2023b)). These efforts have underscored the difficulties in producing reliable shoreline time series from a single automated workflow, further highlighting the need for methodological refinement and site-specific adaptations.

Together, these developments raise a fundamental question: **How can satellite-derived waterlines and shorelines support the monitoring of coastal change, and with what uncertainties?**

Chapter II

Building and validating methods for large-scale shoreline acquisition

Most of the content presented in this chapter is derived from the article *Towards a global assessment of sandy shorelines: Systematic extraction and validation of optical satellite-derived coastal indicators at various sites* written by *Graffin et al., 2025* and published *Remote Sensing of Environment (Elsevier)*.

Contents

II.1 Introduction **51**

II.2 Methods **53**
II.2.1 Study Sites 53
II.2.2 A modular algorithm for waterline extraction from optical satellite imagery 54
II.2.2.1 Collection of images and pre-processing 55
II.2.2.2 Water-differentiating indices 56
II.2.2.3 Segmentation 58
II.2.2.4 Post-processing 60
II.2.2.5 Validation process 62

II.3 Results **64**
II.3.1 Qualification of waterline time series accuracy 64
II.3.2 Deriving shorelines from waterlines 67
II.3.3 Uncertainties and error proxies 71
II.3.4 Seasonal, interannual, and longer-term variability of the shoreline position 76

II.4 Discussion **79**

II.5 Chapter Conclusion **82**

II.1 Introduction

Remote sensing has become central to coastal monitoring, complementing traditional in situ and airborne methods that, while accurate, are costly and limited in coverage and frequency

(e.g., LiDAR, UAVs, video systems; Holman (2007); A. H. Sallenger et al. (2003); Jessin et al. (2023)). Advances in Earth-observing satellites (Turner et al. (2021)), cloud computing (Gorelick et al. (2017)), and algorithm development (e.g., CoastSat, CASSIE, SHOREX; Vos et al. (2019b); Almeida et al. (2021); Sánchez-García et al. (2020)) have enabled shoreline monitoring at local to global scales (Luijendijk et al. (2018); Bishop-Taylor et al. (2021); Castelle et al. (2022)). Most approaches rely on extracting satellite-derived waterlines (SDW) or shorelines (SDS) from multispectral imagery (mainly Sentinel-2 and Landsat), using combinations of water-differentiating indices and thresholding techniques. Reported accuracies typically range from 5–15 m, depending on site conditions, algorithms, and post-processing efforts (Vitousek et al. (2023a); Castelle et al. (2021); Vos et al. (2019a)). However, performance can degrade at high-energy, macrotidal sites, where tidal and wave effects complicate waterline detection (Castelle et al. (2021); Graffin et al. (2023)).

While many studies have refined SDW extraction through post-processing (e.g., tide and wave corrections), only a few have critically examined the detection methods themselves, particularly the choice of indices and thresholding techniques. For instance, Doherty et al. (2022) tested different water indices and thresholding methods for PlanetScope imagery, identifying NIR–blue differencing combined with the WP method (Harley et al. (2019)) as the most accurate for SDS at Narrabeen, Australia. Vos et al. (2023b) compared five SDW algorithms across four sites but did not disentangle the relative contributions of segmentation versus index selection. Similarly, Bishop-Taylor et al. (2019a) assessed indices, thresholding, and resolution across coastal types, finding that AWEIsh with Otsu's method was robust, but their analysis relied on remote and synthetic data rather than in situ validation. None of these studies have addressed the issue of image selection—such as filtering out low-quality acquisitions with high cloud cover or erroneous waterlines—, or outlier removal, which is critical for large-scale SDW applications (Graffin et al. (2023)). While these efforts demonstrate significant progress, further work is still needed to systematically evaluate and optimize detection methods across diverse coastal settings.

Building on these advances, this study develops a customizable Python toolkit (linked to Google Earth Engine cloud platform) to test multiple combinations of indices and thresholding methods across diverse coastal settings. Using eight well-monitored sites, we validate SDW and SDS time

series and assess how environmental conditions—such as tidal range, wave energy, and beach slope—influence algorithm performance. This study also introduces two methods to mitigate the influence of erroneous detections in the final SDW/SDS time series. Our aim is to evaluate the scalability of unsupervised satellite-derived shoreline monitoring for large scale application purposes, and to provide recommendations for selecting processing approaches suited to different coastal environments.

II.2 Methods

II.2.1 Study Sites

This study encompasses eight diverse coastal sites, each selected for their long-term beach elevation profile datasets (<10 years, overlapping with Landsat 5–9 and Sentinel-2) measured at monthly or finer resolution. Together, they span a wide range of wave climates, tidal regimes, and sediment types, providing a robust framework to evaluate the performance of satellite-derived shoreline extraction algorithms under contrasting environmental conditions (Figure II.1).

- **Duck (North Carolina, USA)** – A microtidal beach and one of the most extensively monitored coastal sites worldwide, serving as a reference for remote sensing validation. It is characterized by a low to moderate wave climate ($H_s \approx 0.9$ m; $T_p \approx 9$ s), medium sand ($d_{50} \approx 0.3$ mm), and a relatively steep intertidal slope (0.1 m/m) (Pianca et al. (2015)).

- **Narrabeen (New South Wales, Australia)** – Another microtidal beach, monitored since the early 1980s. It experiences moderate wave energy ($H_s \approx 1.4$ m; $T_p \approx 8.8$ s), has medium sand ($d_{50} \approx 0.3$ mm), and a steep intertidal slope (~ 0.1 m/m) (Turner et al. (2016)).

- **Perranporth (England, UK)** – A macrotidal, cliff-backed beach with high wave energy ($H_s \approx 1.6$ m; $T_p \approx 10$–11 s). The beach is gently sloping (0.02 m/m), covered with medium sand ($d_{50} \approx 0.33$ mm), and partially engineered with seawalls and periodic sand redistribution (McCarroll et al. (2023)).

- **Porsmilin (Brittany, France)** – A sheltered macrotidal pocket beach in the Iroise Sea, subject to moderate wave energy ($H_s \approx 0.7$ m; $T_p \approx 10$ s). Sediment is predominantly medium sand ($d_{50} \approx 0.32$ mm), with cross-shore variability including coarser grains ($d_{50} \sim 0.7$ mm)

near intertidal bar crests (Floc'h et al. (2016)). The intertidal slope is gentle ($\sim$ 0.05 m/m), and monitoring has been consistent since the early 2010s (Bertin et al. (2022)).

- **Slapton Sands (South Devon, UK)** – A gravel beach along a low-energy coastline. Wave conditions are mild ($H_s \approx 0.75$ m; $T_p \approx 8$ s). The beach is composed of coarse gravel and pebbles (2–10 mm) and exhibits a steep intertidal slope ($\sim$ 0.15 m/m) (McCarroll et al. (2023)).

- **Torrey Pines (California, USA)** – A mesotidal, cliff-backed sandy beach with energetic conditions ($H_s \approx 1.1$ m; $T_p \approx 13.2$ s). It consists of fine sand ($d_{50} \approx 0.2$ mm) and has a moderate intertidal slope ($\sim$ 0.05 m/m) (Ludka et al. (2019)).

- **Truc Vert (SW France)** – A mesotidal, dune-backed Atlantic beach with moderate energy ($H_s \approx 1.1$ m; $T_p \approx 9$ s). It is composed of medium sand ($d_{50} \approx 0.35$ mm) and has a gentle intertidal slope ($\sim$ 0.04 m/m) (Castelle et al. (2020)).

- **Le Vougot (Brittany, France)** – A macrotidal, dune-backed beach with a complex topography–bathymetry continuum influenced by rocky reefs and islets. It is exposed to moderate energy ($H_s \approx 1.2$ m; $T_p \approx$ 9–10 s), has medium sand ($d_{50} \approx$ 0.25–0.32 mm), and a gentle intertidal slope ($\sim$ 0.03 m/m) (Suanez et al. (2023)).

II.2.2 A modular algorithm for waterline extraction from optical satellite imagery

The customizable waterline extraction algorithm developed in this study—publicly available at https://github.com/CNES/shoreliner—provides a flexible, modular framework for deriving accurate shorelines from satellite imagery in an unsupervised manner (i.e., no manual image selection or a priori data) across diverse coastal environments. Designed to accommodate the varied needs of coastal researchers, the framework allows customization of each of the four main steps: preprocessing of optical images, band combination, segmentation, and optional post-processing of delineated and projected shorelines. This flexibility enables users to tailor analyses to the environmental conditions of each site or to test multiple methods and compare outputs against ground truth to identify the most suitable algorithm. All steps, from acquiring images from publicly available MSI collections to estimating local beach slope from waterline time series, are implemented

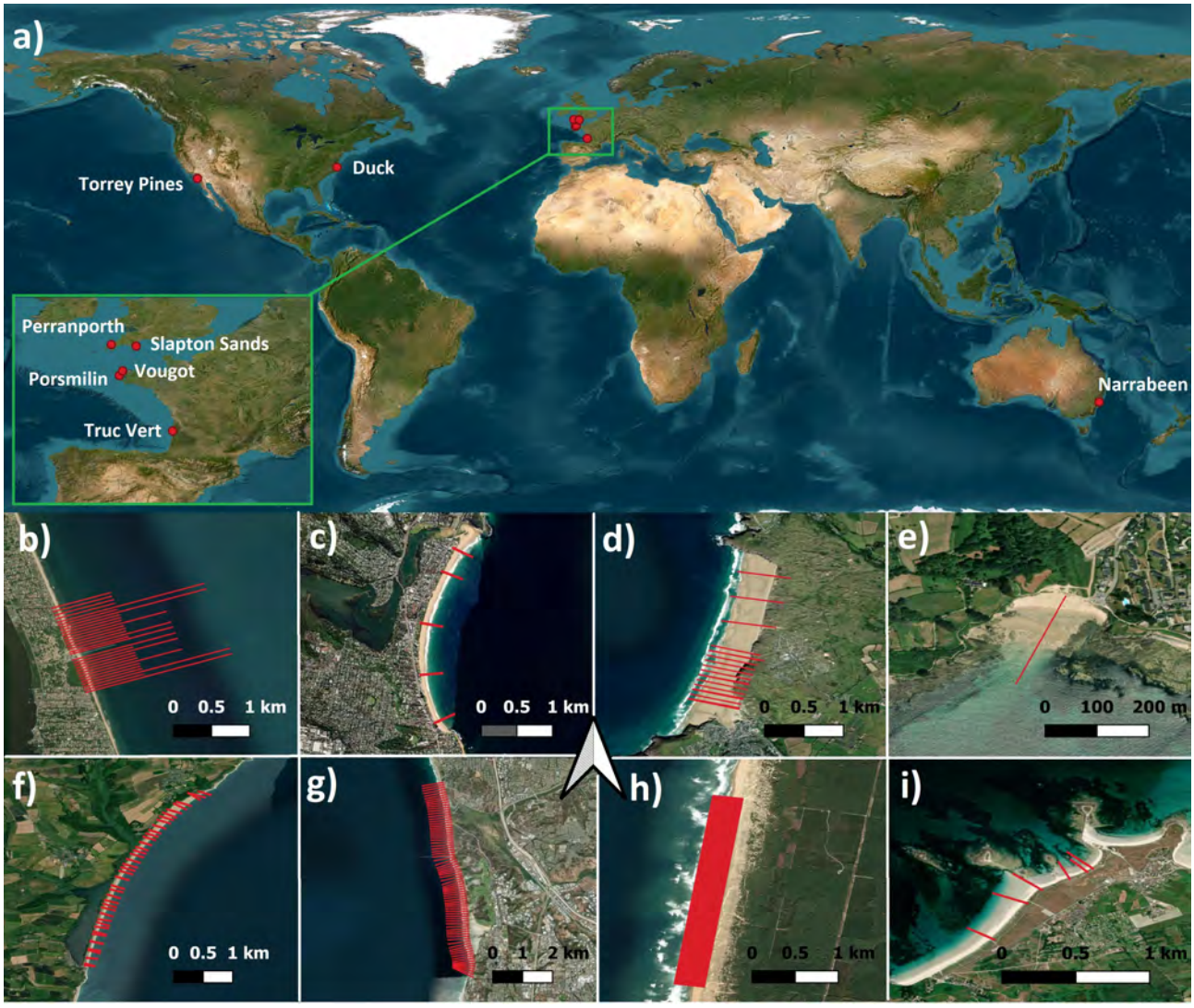

FIGURE II.1 **a)** Location of the eight validation sites and **b–i)** corresponding aerial views: **b)** Duck (NC, USA); **c)** Narrabeen (Australia); **d)** Perranporth (England); **e)** Porsmilin (France); **f)** Slapton Sands (England); **g)** Torrey Pines (CA, USA); **h)** Truc Vert (France); **i)** Le Vougot (France). Red lines indicate the transects along which beach elevation surveys were conducted. Background maps are provided by the ESRI World Imagery layer.

within a single toolkit. When initiating a new coastal monitoring project, the toolkit generates a conceptual graph detailing all processes involved in extracting the chosen coastal indicator, as illustrated in Figure II.2.

II.2.2.1 Collection of images and pre-processing

In this study, we use top-of-atmosphere reflectance images from Landsat 5, 7, 8, and 9, as well as Sentinel-2 (Tier L1-C), accessed via the Google Earth Engine API (Gorelick et al. (2017)). For each site, we collect images spanning the period of in-situ monitoring and with cloud cover below

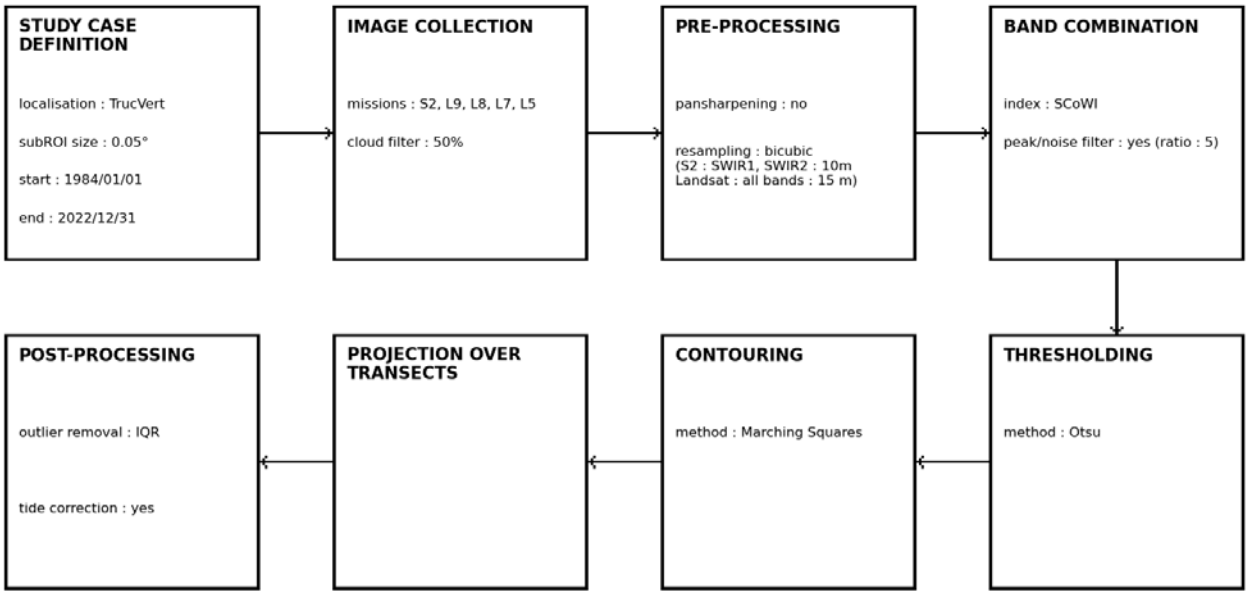

FIGURE II.2 Example of algorithm parameterization for an application at Truc Vert, France, using the SCoWI index and Otsu's thresholding method. This diagram is automatically generated by the extraction toolkit when initiating a new waterline acquisition.

50%. The images are cropped into 5 km squares centered on the monitored site. At Torrey Pines, which extends slightly beyond 5 km, the area is divided into two sub-sites to ensure complete coverage with 5 km squares. A bicubic resampling function is applied to enhance spatial resolution, increasing Landsat imagery from 30 to 15 m (all bands) and Sentinel-2 SWIR1 and SWIR2 bands from 20 to 10 m.

II.2.2.2 Water-differentiating indices

The resulting collection of images is converted into monochromatic images using water-differentiating indices. The five indices considered in this study are NDWI McFEETERS (1996), MNDWI Xu (2006), SCoWI Bergsma et al. (2024), $AWEI_{sh}$, and $AWEI_{ns}$ Feyisa et al. (2014). These indices are defined as:

$$NDWI = \frac{G - NIR}{G + NIR} \tag{II.1}$$

$$MNDWI = \frac{G - SWIR1}{G + SWIR1} \tag{II.2}$$

$$AWEI_{\text{sh}} = 2.5 \times G + B - (1.5 \times SWIR1 + 0.25 \times SWIR2 + 1.5 \times NIR) \tag{II.3}$$

$$AWEI_{\text{ns}} = 4 \times G - (4 \times SWIR1 + 2.75 \times SWIR2 + 0.25 \times NIR) \tag{II.4}$$

$$SCoWI = 2 \times G + B - (0.75 \times SWIR1 + 0.5 \times SWIR2 + 2 \times NIR) \tag{II.5}$$

where B, G, NIR, SWIR1, and SWIR2 denote the blue, green, near-infrared, and short-wave infrared (1 and 2) bands, respectively. While other indices exist for monitoring land–water interfaces, we focus on these five for simplicity and to highlight the challenges of using a single method for large-scale coastal monitoring. Figure II.3 shows the greyscale images produced by these formulations, illustrated here for Truc Vert beach.

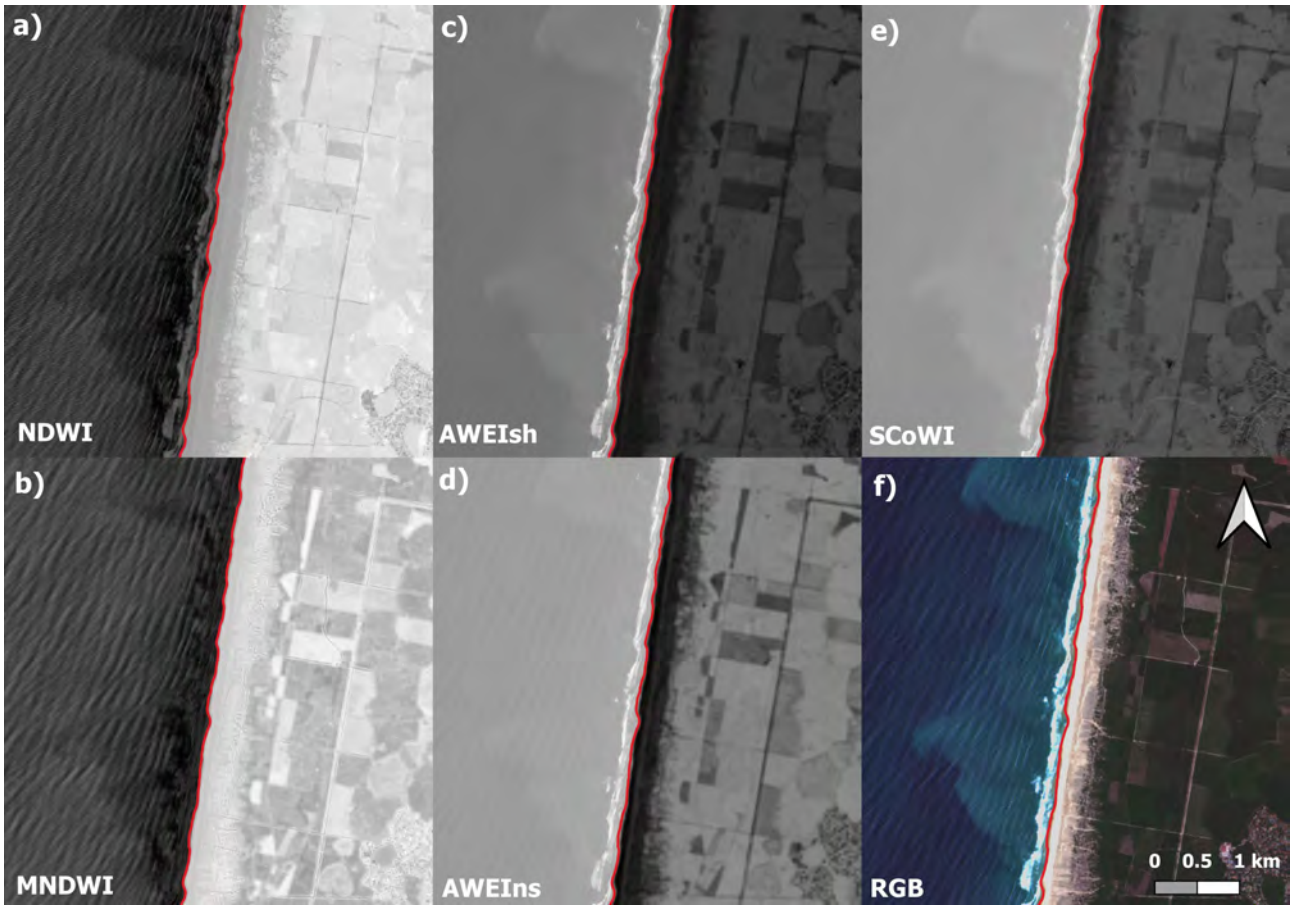

FIGURE II.3 Greyscale outputs of different water-differentiating indices at Truc Vert, France. The red line represents a waterline manually delineated from visual inspection of the RGB image shown in panel (f).

II.2.2.3 Segmentation

In this study, we applied various thresholding methods to identify the optimal pixel value separating land and sea pixels. Coupled with a contouring algorithm, thresholding allows generating a waterline as a unique iso-contour corresponding to a given pixel value in a chosen water-differentiating index. We evaluated four thresholding methods:

- **Otsu's thresholding method** (Otsu (1979)) determines the threshold t_{otsu} that maximizes the inter-class variance $V(x)$ in a bimodal pixel distribution:

$$t_{\text{otsu}} = \arg\max_x V(x), \quad x_0 \leq x \leq x_N, \tag{II.6}$$

  where x_0 and x_N are the minimum and maximum pixel intensities.

- **Local Minimum (LM) method** (Bergsma et al. (2024)) refines the Otsu threshold by identifying local maxima on either side of t_{otsu} to define an interval $[x_1, x_2]$, with $x_1 \leq t_{\text{otsu}} \leq x_2$ and $x_1, x_2 \in [x_0, x_N]$. The LM threshold t_{min} is then the local minimum of the histogram $h(x)$ within this interval:

$$t_{\text{min}} = \arg\min_{x \in [x_1, x_2]} h(x), \tag{II.7}$$

  providing a more robust separation than standard Otsu for skewed or non-ideal bimodal distributions.

- **Minimum Shoreline Variability (MSV) method** (Almar et al. (2012)) identifies the most stable waterline by evaluating a set of M linearly spaced thresholds ($M = 100$) between x_1 and x_2. For each threshold t_m, a waterline L_m is extracted using the Marching Squares algorithm Lorensen and Cline (1987); Cipolletti et al. (2012), and its stability is quantified as:

$$\frac{\Delta L_m}{L_m} = \frac{L_{m+1} - L_m}{L_m}. \tag{II.8}$$

  The optimal threshold is the one minimizing waterline variability:

$$t_{\text{MSV}} = \arg\min_m \left(\frac{\Delta L_m}{L_m} \right), \quad m \in [1, M-1]. \tag{II.9}$$

- **Weighted Peaks (WP) method** (Harley et al. (2019); Doherty et al. (2022)) selects the

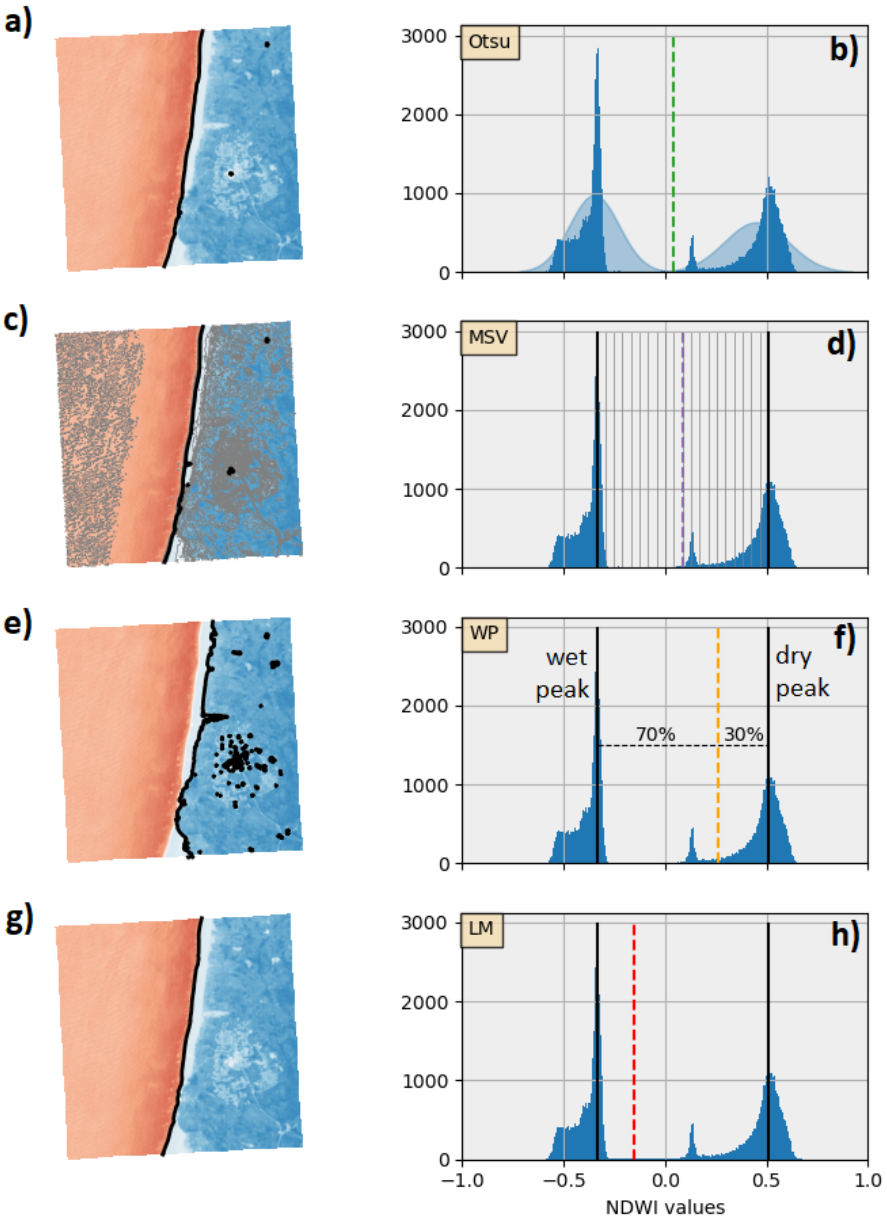

FIGURE II.4 Test cases of waterline extraction at Perranporth from a Sentinel-2 NDWI image using (a) Otsu, (c) MSV, (e) WP, and (g) LM thresholding methods. Middle panels show histograms of NDWI pixel values with the identified thresholds. Blue shaded Gaussian distributions on panel b illustrate the pixel distribution. Panel i shows the Sentinel-2 true color image. Thin grey lines on panel d indicate intermediate waterline extractions for MSV, also shown on panel c. Solid black lines on panels d, f, and h represent the dry and wet peaks used for MSV, WP, and LM methods.

threshold between the 'wet' and 'dry' peaks of the pixel intensity distribution:

$$t_{\mathrm{WP}} = x_{wet} - 0.7 \times (x_{dry} - x_{wet}), \tag{II.10}$$

where x_{wet} and x_{dry} correspond to the pixel intensities of wet and dry peaks, respectively, corresponding to x_1 and x_2 in LM method formalism.

Figure II.4 illustrates these four methods applied to the same NDWI image and histogram at

Perranporth during high tide. Panel b shows Gaussian fits for Otsu's thresholding. Panel d illustrates MSV waterlines generated from multiple thresholds, with the most stable selected. Panel f shows the WP threshold as a weighted average between wet and dry peaks, and panel h displays the LM threshold at the local histogram minimum between the peaks.

The determined threshold is then used to delineate the land–sea interface using the Marching Squares contouring method Lorensen and Cline (1987); Cipolletti et al. (2012). In this study, segmentations based on Otsu, LM, MSV, and WP thresholding methods are referred to as Otsu-based, LM-based, MSV-based, and WP-based segmentation, respectively. The resulting lines are considered waterlines, representing the land–sea interface at the acquisition time of the images, influenced by tides, waves, and other sources of sea-level variability. By projecting these lines onto transects perpendicular to the coast, we obtain time series of the cross-shore waterline position at each transect. A detected waterline must intersect the transect directly to be measured; otherwise, the value is assigned as NaN.

Processing efficiency of the shoreline detection pipeline was evaluated for the different thresholding methods. On a standard workstation (Intel i7-11700, 2.7 GHz, 8 GB RAM), processing a single image over a typical region of interest (ROI, ∼30 km^2) takes approximately 0.3 s for Otsu, LM, or WP methods, and 3 s for the more computationally demanding MSV method. Projecting waterlines onto transects requires 5 ms per image per transect, meaning that processing 1000 images across 20 transects takes roughly 400 s. Monochromatic image sizes range from approximately 500 kB (Landsat, 15 m) to 1.2 MB (Sentinel-2, 10 m) for a standard ROI.

II.2.2.4 Post-processing

We introduce two new post-processing steps to ensure that waterline data extracted in an unsupervised way are reliable :

1. Image quality filtering. Images can exhibit noisy or highly non-bimodal pixel distributions, often due to cloud cover. While Sentinel-2 and Landsat 5–9 provide cloud coverage metadata for each full-scene image, these values may not accurately reflect local conditions in cropped coastal areas. Even light cloud cover can obscure the coastline and impair detection. To address this, we

implemented a filter based on the histogram of pixel values (after band combination).

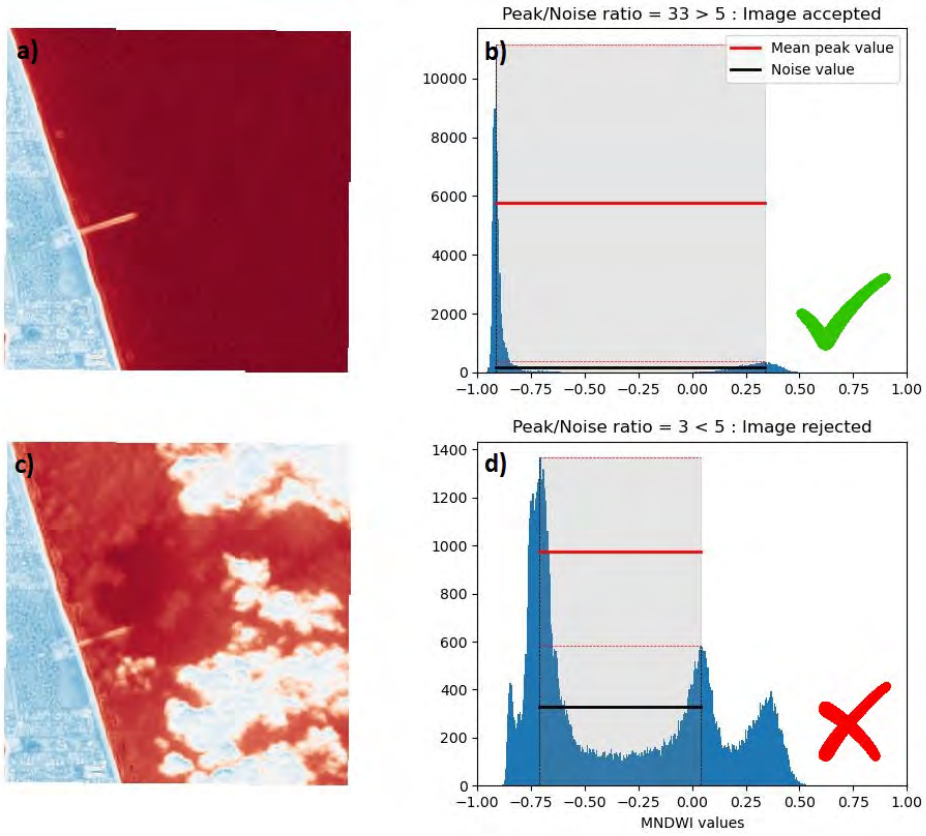

FIGURE II.5 MNDWI image of Duck without **a)** and with **c)** cloud coverage, and associated MNDWI values histograms **b) and d)**. Mean peaks value (solid red line) represents the mean of occurences of the land-pixel mode peak and sea-pixel mode peak. Noise value (solid black line) represents the mean of occurences of all MNDWI values between the two peaks. If the ratio between the mean peak and noise values is below 5, the image is discarded.

Specifically, we check that the average of the peak occurrences on either side of the segmentation threshold exceeds the average number of occurrences of values between the peaks multiplied by a coefficient n (here set to 5). Figure II.5 illustrates the effect of this filter. This step ensures that images with cloud-induced artifacts are excluded from waterline extraction.

2. Outlier removal in SDW time series. Despite the image filtering step, erroneous waterline detections can still occur. To remove obvious outliers from the SDW time series, we applied the inter-quartile range (IQR) method. Points lying outside the interval $[Q_1 - 1.5 \times IQR, Q_3 + 1.5 \times IQR]$, where Q_1 and Q_3 are the first and third quartiles, and $IQR = Q_3 - Q_1$, are discarded. Figure II.6 illustrates the IQR-based outlier removal procedure. Black dashed lines indicate the IQR thresholds, and outliers are highlighted in red.

When generating SDS time series, we apply tide correction using modeled tide level. We use FES2022 (Lionel et al. (2023)), which provide tide levels with vertical accuracy of approximately

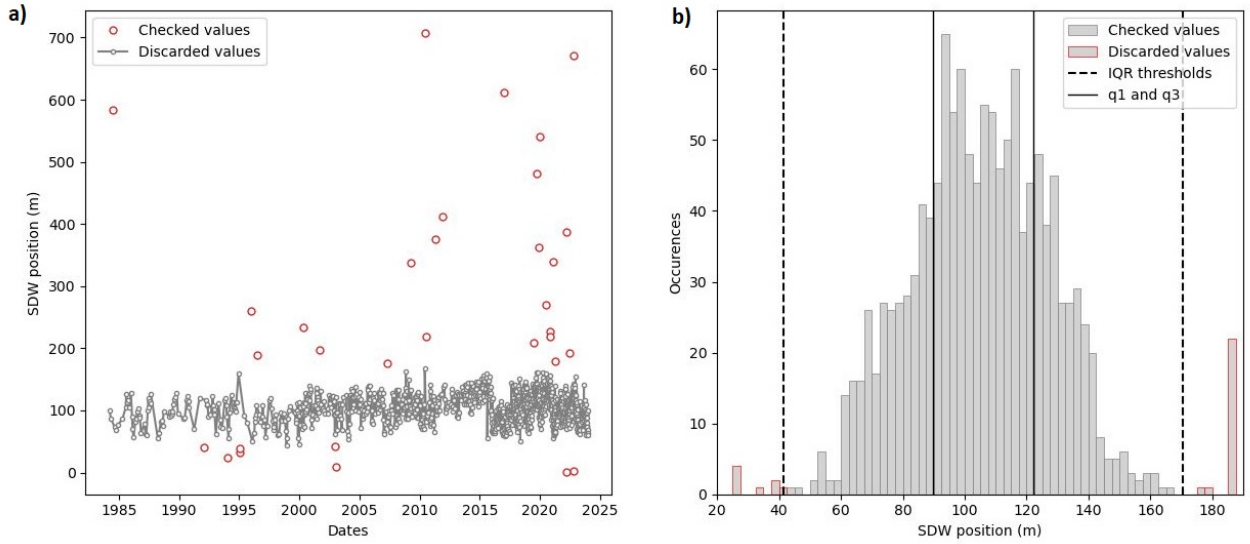

FIGURE II.6 Time series (**a**) and distribution (**b**) of SDW cross-shore positions. Solid black lines indicate the first and third quartiles, and dashed lines represent the IQR limits. Values beyond the IQR range, shown in red, are considered outliers and removed from the time series.

10 cm (Graffin et al. (2025)). The average beach slope $\tan\beta$ is first estimated following (Vos et al. (2020)), by minimizing tidal aliasing in the waterline time series. Tide-corrected waterline positions are then computed as:

$$\Delta X_{\text{tide}} = \frac{z_{\text{ref}} - \eta_{\text{tide}}}{\tan\beta}, \tag{II.11}$$

where z_{ref} is the reference elevation to which the shoreline is projected, and η_{tide} is the modeled tide elevation at the time of image acquisition. In this study, tide-corrected SDW positions are referred to as SDS (at mean sea level), though other sources of water level variability exist. We discuss this point below, after description of the results.

II.2.2.5 Validation process

At each site and for each transect, SDW extraction algorithms were evaluated by comparing time series of waterline positions derived from satellite imagery with in-situ measurements from beach elevation profiles. For each available beach profile, the satellite acquisition closest in time was identified, with a maximum allowable difference of 14 days. Using the FES2022 tide model Lionel et al. (2023), the tidal elevation at the exact satellite overpass time was computed. On the corresponding beach profile, the cross-shore position matching this modeled tidal level was extracted, representing the expected in-situ waterline at the time of acquisition. Repeating this process for all profiles generated time series of in-situ waterline positions, directly comparable

with satellite-derived positions along each transect and site. FES2022 provides high-resolution global tidal predictions (phase and amplitude of 34 tidal constituents) by combining advanced hydrodynamic simulations with state-of-the-art bathymetry and calibration against water level observations, with an estimated vertical accuracy of ∼10 cm Lionel et al. (2023); Graffin et al. (2025).

Satellite-derived waterlines and shorelines were systematically compared to in-situ data. The robustness of the validation was quantified using summary statistics based on the error distribution:

- Error : $\epsilon_i = y_i - x_i,\ i \in [\![1; N]\!]$
- Centered root-mean-square error ($cRMSE$) : $\sigma_\epsilon = \sqrt{\frac{1}{N-1}\Sigma_{i=1}^{N}(\epsilon_i - \overline{\epsilon})^2}$
- Bias : $bias = \frac{1}{N}\Sigma_{i=1}^{N}\epsilon_i$

where y_i are the in-situ observations, x_i are the satellite-derived estimates, N is the number of matching pairs, and $\overline{X}$ denotes the mean of the set X.

SDW and SDS time series validations are also presented using Taylor diagrams Taylor (2001), which simultaneously visualize correlation, amplitude (standard deviation), and cRMSE between estimators and observations. Metrics are defined as:

- Standard deviation : $\sigma_x = \sqrt{\frac{1}{N-1}\Sigma_{i=1}^{n}(x_i - \overline{x})^2}$; $\sigma_y = \sqrt{\frac{1}{N-1}\Sigma_{i=1}^{N}(y_i - \overline{y})^2}$
- Pearson's correlation : $R_{x,y} = \frac{\Sigma_{i=1}^{N}(x_i - \overline{x})(y_i - \overline{y})}{\sqrt{\Sigma_{i=1}^{N}(x_i - \overline{x})^2} \cdot \sqrt{\Sigma_{i=1}^{N}(y_i - \overline{y})^2}}$

The large number of estimator-observation pairs in this study (8 sites × 5 indices × 4 thresholding methods × N_t transects × N_p points per transect) makes comprehensive illustration challenging. Taylor diagrams provide a compact and holistic representation. Validation results are reported per site as the mean performance across transects, including only transects with more than 120 matching in-situ/satellite observations.

We also validate integrated metrics derived from waterline and shoreline time series: mean intertidal beach slopes, long-term trends, seasonal cycles, and interannual variability of shore-

line position. SDS time series are resampled at monthly intervals to obtain a uniform temporal resolution. From these monthly series:

- **Long-term trend:** computed as the slope of the linear regression over the monthly-sampled SDS time series.
- **Seasonal cycle:** obtained as the climatology, i.e., the average value for each month of the year, of the detrended monthly series.
- **Interannual variability:** calculated as the standard deviation of the year-sampled detrended series.

Transects for which beach slope estimation failed (e.g., algorithm returned the maximum evaluated slope of 0.2 m/m) were excluded from the validation of slopes, trends, seasonal cycles, and interannual variability.

II.3 Results

II.3.1 Qualification of waterline time series accuracy

The primary objective of this study is to assess errors in SDW time series along 335 transects spanning eight diverse coastal sites, using five water-differentiating indices and four segmentation methods. This yields a total of 6700 SDW position time series validated against ground truth data, posing challenges for comprehensive presentation. For clarity, we predominantly rely on Taylor diagrams to illustrate algorithm performances per site. Figures II.7 and II.8 show performances of the 20 index-thresholding combinations across the eight sites. Figure II.7 focuses on the four micro- to meso-tidal sites (Duck, Narrabeen, Torrey Pines, and Truc Vert), while Figure II.8 displays results for the four macro-tidal sites (Perranporth, Porsmilin, Slapton Sands, and Vougot).

At the four low tidal range sites (Figure II.7), most methods perform consistently well, with correlations above 0.7 and centered RMSE below 15 m. Narrabeen (panel b) shows the highest accuracy, with most methods achieving correlations above 0.8 and cRMSE below 9 m. Truc Vert (panel d) exhibits lower accuracy, with cRMSE exceeding 25 m and more heterogeneous method performance. Across these sites, methods based on SCoWI and AWEIsh consistently rank

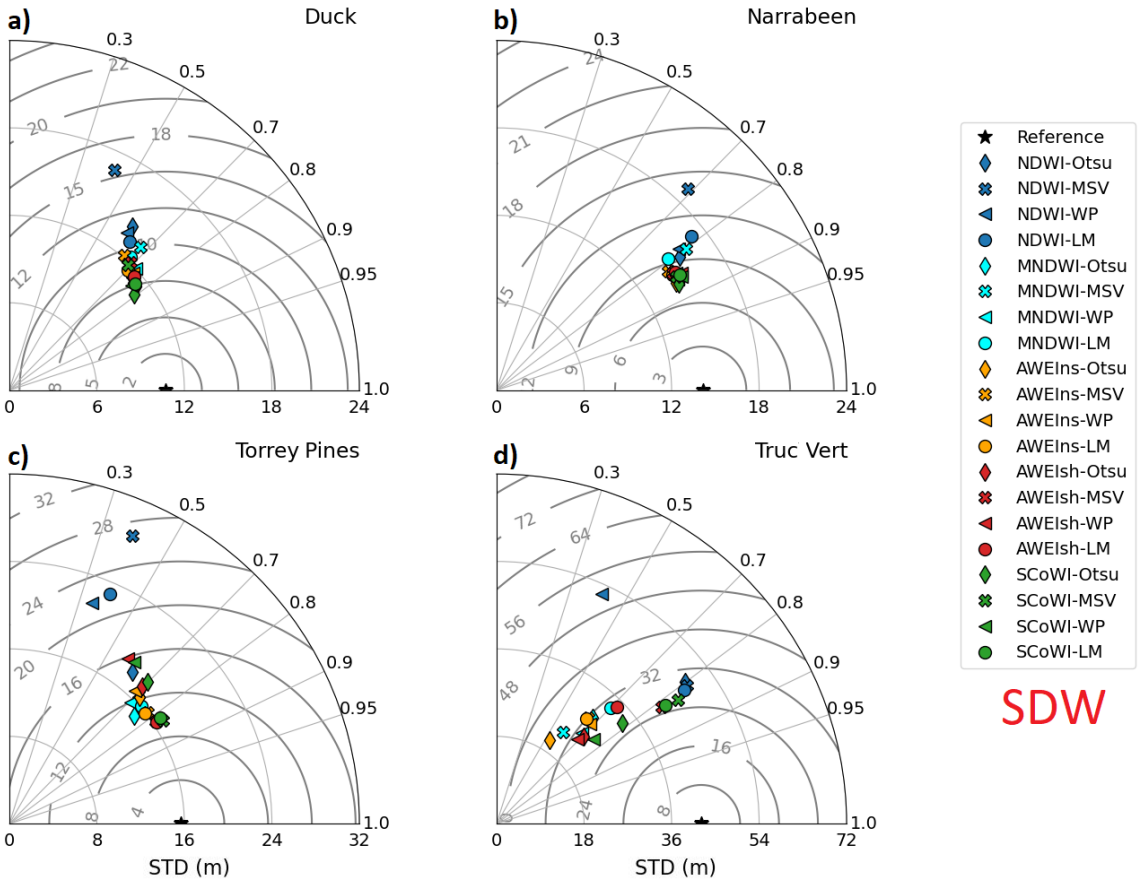

FIGURE II.7 Taylor diagrams of SDW measurements at (a) Duck, (b) Narrabeen, (c) Torrey Pines, and (d) Truc Vert. Each point represents the mean performance of an index/thresholding combination: radial distance indicates the SD of the SDW time series, angle corresponds to Pearson correlation with in-situ measurements (black star on x-axis), and centered RMSE is shown as circular arcs.

among the top five performers, particularly SCoWI-LM, SCoWI-Otsu, and AWEIsh-MSV. NDWI-based approaches generally underperform, especially NDWI-MSV, while MNDWI- and AWEIns-based methods typically occupy the main performance group. No single thresholding method dominates across these sites.

At the macro-tidal sites (Figure II.8), performances are more scattered. Top-tier methods achieve correlations of 0.9, while the lowest-performing methods fall below 0.3. Centered RMSE varies widely, from below 10 m at Slapton Sands to 40 m for the best methods at Perranporth. No single index consistently outperforms others, though NDWI- and SCoWI-based methods frequently appear among top performers. Notably, NDWI-LM, NDWI-Otsu, and SCoWI-LM rank among the best at three out of four sites. LM-based thresholding generally outperforms other approaches, while WP-based methods yield poorer results overall.

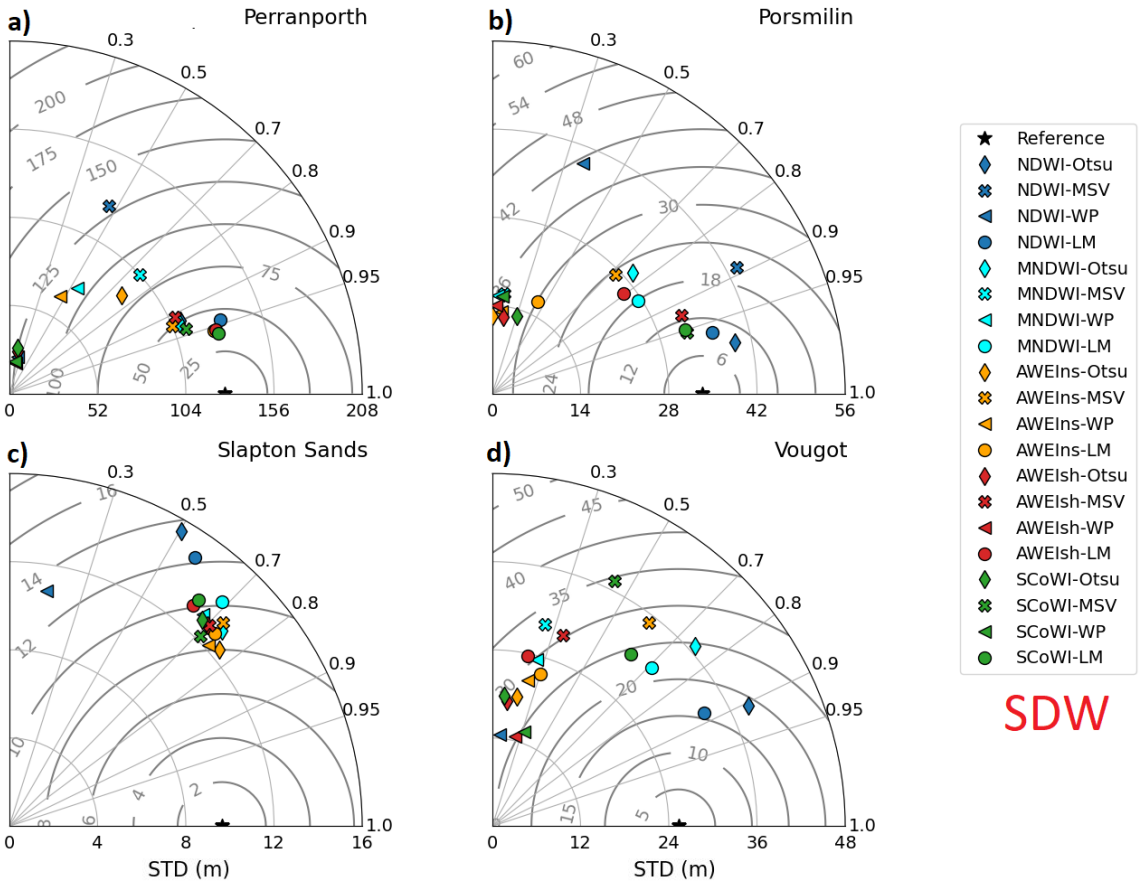

FIGURE II.8 Taylor diagrams of SDW measurements at (a) Perranporth, (b) Porsmilin, (c) Slapton Sands, and (d) Vougot. Representation is identical to Figure II.7.

Table II.1 summarizes the results by listing the 5 top-performing methods at each site, sorted per cRMSE. LM thresholding appears in 17 of 40 (8 sites x top 5 performers) top slots, indicating broad effectiveness across indices and sites. Otsu is represented in 11 slots, while SCoWI-based methods appear 15 times. SCoWI-LM ranks among the top five for six sites, making it the most consistently high-performing combination.

Appendix A contains additional figures that were not included in the main body of the chapter to avoid overloading it, but which provide a more detailed description of site-to-site results. In particular, distribution of errors at each site and for each methods are displayed (Figures X-Y).

TABLE II.1 Top five index-thresholding combinations for each site based on centered RMSE.

Site	1st	2nd	3rd	4th	5th
Duck	SCoWI-Otsu (6.90 m)	AWEIsh-Otsu (7.42 m)	SCoWI-WP (7.56 m)	SCoWI-LM (7.57 m)	AWEIns-Otsu (7.72 m)
Narrabeen	SCoWI-Otsu (7.50 m)	AWEIns-Otsu (7.61 m)	AWEIns-WP (7.78 m)	AWEIsh-Otsu (7.90 m)	SCoWI-WP (7.92 m)
Torrey Pines	AWEIsh-LM (9.77 m)	AWEIsh-MSV (9.89 m)	SCoWI-MSV (9.92 m)	SCoWI-LM (10.07 m)	AWEIns-LM (10.78 m)
Truc Vert	AWEIsh-MSV (25.30 m)	SCoWI-LM (25.45 m)	SCoWI-MSV (26.03 m)	SCoWI-Otsu (26.43 m)	NDWI-LM (27.82 m)
Perranporth	SCoWI-LM (35.70 m)	MNDWI-LM (37.83 m)	AWEIns-LM (37.95 m)	AWEIsh-LM (38.30 m)	NDWI-LM (43.74 m)
Porsmilin	NDWI-Otsu (9.67 m)	NDWI-LM (9.87 m)	SCoWI-MSV (10.08 m)	SCoWI-LM (10.56 m)	AWEIsh-MSV (12.89 m)
Slapton Sands	AWEIns-Otsu (8.01 m)	AWEIns-WP (8.23 m)	SCoWI-MSV (8.69 m)	AWEIns-LM (8.75 m)	MNDWI-Otsu (8.87 m)
Vougot	NDWI-LM (15.78 m)	NDWI-Otsu (18.97 m)	MNDWI-LM (21.82 m)	SCoWI-LM (24.24 m)	MNDWI-Otsu (24.57 m)

II.3.2 Deriving shorelines from waterlines

At most coastal sites, astronomical tides represent the primary source of water level variability. These tidal levels can be estimated with high confidence using global tidal models. In this study, we employ FES2022 (Lionel et al. (2023)), which provides estimates of astronomical tide levels with an uncertainty on the order of 10 cm. Such outputs can be used to derive datum-based shoreline positions through the correction term shown in Equation II.11. This correction assumes a uniform intertidal beach slope, allowing the instantaneous waterline to be linearly transferred to a selected elevation datum (e.g., MSL). Beach slope information can be obtained from in-situ measurements or inferred using the approach of Vos et al. (2020), which provides a satellite-derived estimation of the average beach slope, assigning each beach profile a unique intertidal slope.

Figure II.9 compares the beach slopes estimated using the method of Vos et al. (2020) with the mean upper intertidal slopes derived by linear regression over the profiles between MSL and MHW elevations. In this study, estimated slopes are derived from LM-based algorithms for the five indices, as LM-based SDW time series are relatively accurate and stable across all indices considered. Validation results for other thresholding methods (Otsu, MSV, and WP) are provided in the Appendix A (Figures A.5-A.7).

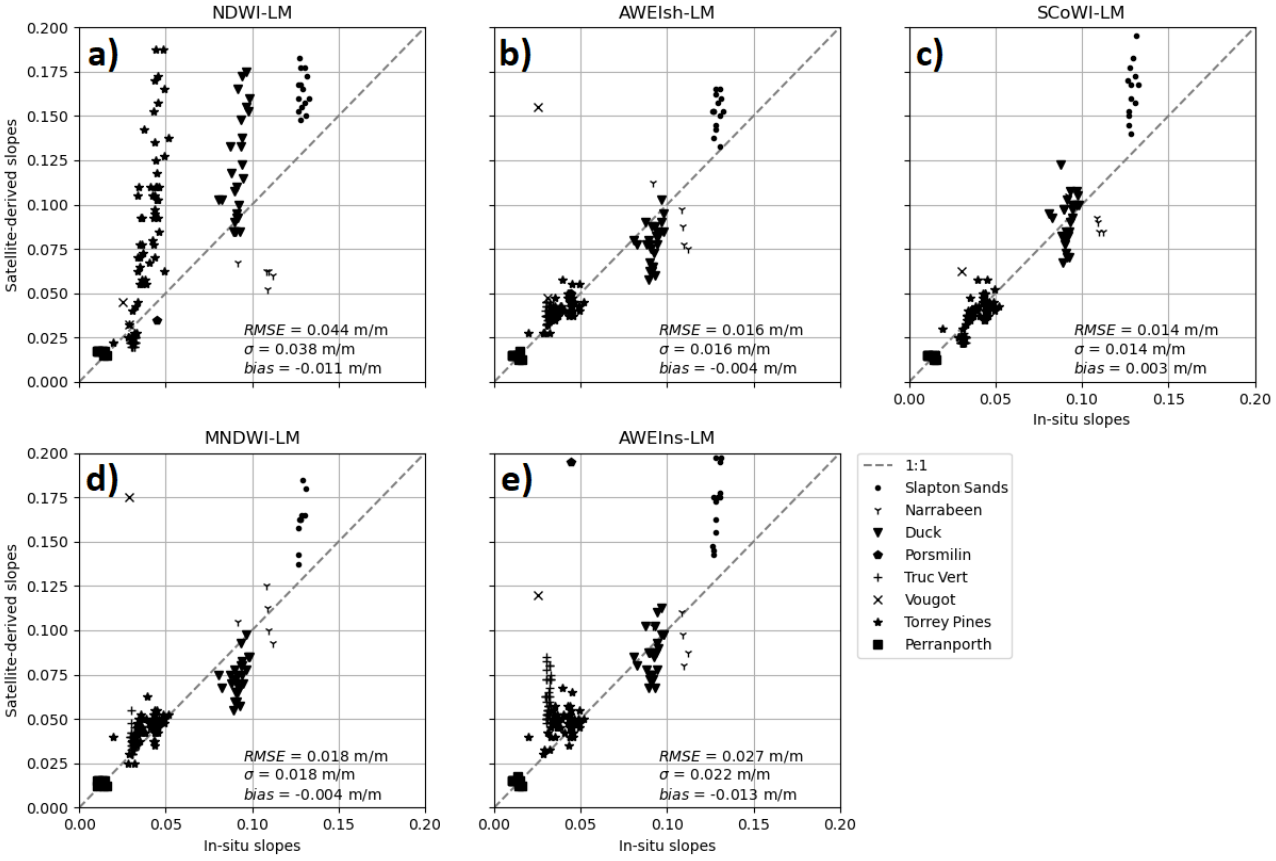

FIGURE II.9 Comparison of satellite-derived and in-situ intertidal beach slopes across the eight validation sites. Satellite-derived slopes are estimated from waterline position time series computed using LM-based algorithms applied to the following indices: **a)** NDWI, **b)** AWEIsh, **c)** SCoWI, **d)** MNDWI, and **e)** AWEIns.

Validation of intertidal beach slope estimates derived from LM-based SDW time series is shown in Figure II.9, with results displayed across five panels, one per index. Ground-truth slopes were computed from beach elevation profiles between MSL and MHW and averaged over time, then compared against the constant satellite-derived slope estimates. Overall, the results show good agreement, particularly in capturing inter-site variability. However, intra-site variability is less accurately reproduced, especially at steeper sites such as Slapton Sands, Duck, and Narrabeen, where estimation errors are higher.In contrast, flatter beaches such as Perranporth, Truc Vert, and Torrey Pines yield more accurate slope predictions. RMSE values range from 0.013 m/m for SCoWI-based estimates to 0.044 m/m for NDWI-based estimates, confirming the relatively poor performance of the NDWI-LM algorithm at Duck and Torrey Pines. Notably, NDWI-based slope estimates improve when combined with Otsu thresholding, as illustrated in Appendix A, Figure A.5. Slope estimates generally exhibit absolute bias below 0.01 m/m, indicating no systematic over- or underestimation in deriving the upper intertidal beach slope using the method of Vos

et al. (2020). Overall, slope estimation performances are consistent with SDW time series accuracy, with index-thresholding combinations yielding the most accurate time series also producing the best slope estimates (e.g., SCoWI-LM, AWEIsh-MSV).

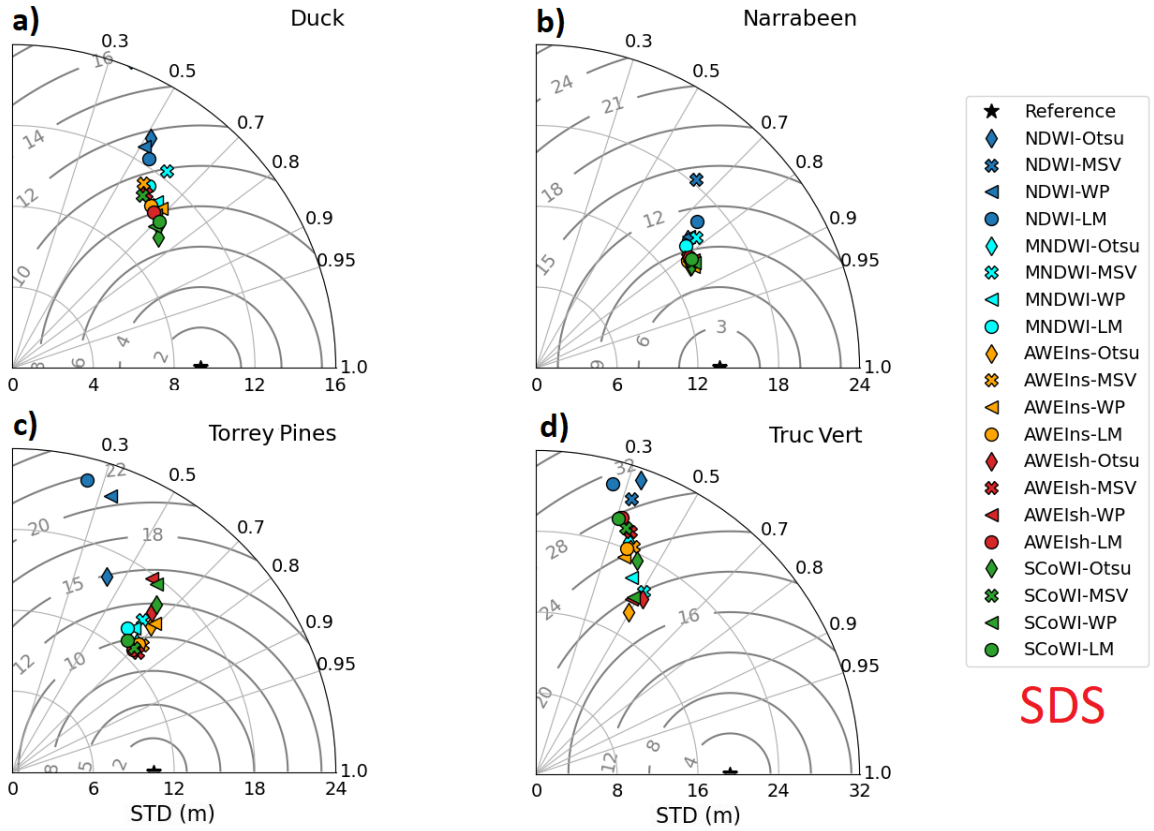

FIGURE II.10 Taylor diagrams of SDS measurements at (a) Duck, (b) Narrabeen, (c) Torrey Pines, and (d) Truc Vert, illustrating the performance of 20 method combinations (index/thresholding pairs). Each point in the polar plots represents the mean performance of a method: the radial distance indicates the standard deviation of the SDS time series, while the angle corresponds to the mean Pearson correlation with the reference (in-situ measurements, shown as a black star on the x-axis). The centered RMSE is represented by circular arcs centered on the reference point.

Using these slope estimates, tide correction terms were computed for each SDW position time series. The resulting MSL-shoreline validations are displayed as Taylor diagrams in Figures II.10 and II.11. Note that only astronomical tides are accounted for in the water level correction, while other less predictable processes, such as wave runup, also contribute to water level variability.

Among the four low tidal range sites (Figure II.10), most methods show reasonably consistent performance, although generally lower than for SDW extraction. Pearson's correlation coefficients typically remain above 0.6, with cRMSEs around 10 m for most methods, except at Truc

Vert, where even the best-performing methods yield correlations of 0.5 and cRMSEs of 20 m. Narrabeen (panel b) stands out with the highest accuracy, where several methods achieve correlations above 0.8 and cRMSEs below 9 m.

Methods based on the SCoWI, AWEIns, and AWEIsh indices continue to perform best overall, frequently appearing among the top five performers across the sites. Interestingly, combinations such as SCoWI-LM and AWEIsh-MSV, which provided the best SDW extraction for these four sites, now show relatively large errors at Torrey Pines compared to the top-performing methods there, namely AWEIsh-Otsu and AWEIns-Otsu. NDWI-based methods generally perform poorly, consistently underperforming across all sites, while MNDWI- and AWEIns-based methods typically occupy intermediate positions, clustered within the main group of methods. No single thresholding technique dominates across all sites in terms of shoreline accuracy.

Among the four macro-tidal sites (Figure II.11), algorithm performances are more dispersed than in the low tidal range group, with correlations generally below 0.6. Centered RMSE values vary markedly by site: at Slapton Sands, all methods remain below 15 m, whereas at Perranporth, even the best-performing methods exceed 25 m. No single index consistently dominates across these sites, although NDWI- and SCoWI-based methods frequently appear among the top performers. As observed for SDW extraction, LM-based thresholding generally yields better SDS results across indices and sites, except at Slapton Sands, where all methods perform similarly, with LM-based methods positioned toward the lower end of the main cluster. SDS extraction at Vougot yields poor results, as no method successfully captures the limited variability of this complex macro-tidal environment.

A notable observation from the SDS time series validation is the systematic overestimation of the standard deviations. Across all sites, there is a consistent positive bias in the standard deviation of shoreline positions derived from satellite imagery. At locations such as Slapton Sands and Vougot, the standard deviation of SDS time series can be up to twice that of the in-situ measurements, indicating potential limitations in capturing the true variability of the shoreline at these sites.

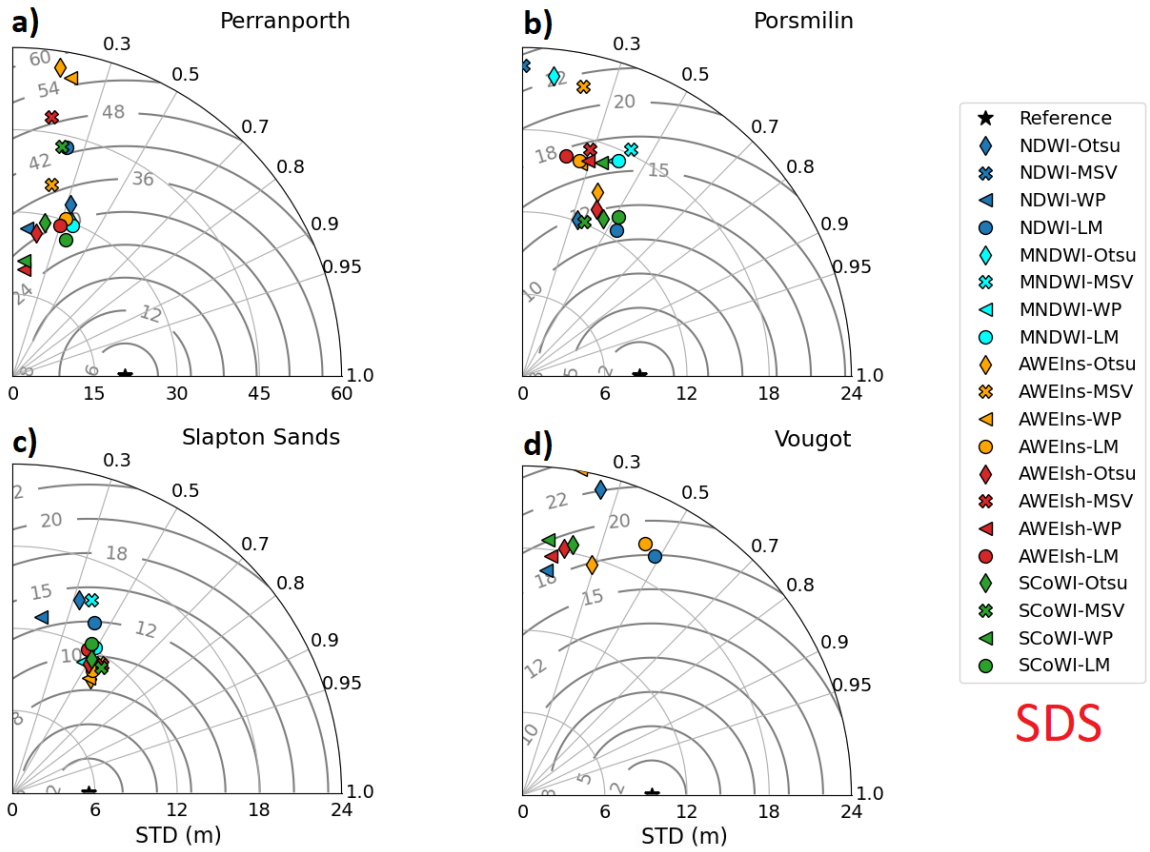

FIGURE II.11 Taylor diagrams of SDS measurements at (a) Perranporth, (b) Porsmilin, (c) Slapton Sands, and (d) Vougot, illustrating the performance of 20 method combinations (index/thresholding pairs). Each point in the polar plots represents the mean performance of a method: the radial distance indicates the standard deviation of the SDS time series, while the angle corresponds to the mean Pearson correlation with the reference (in-situ measurements, shown as a black star on the x-axis). The centered RMSE is represented by circular arcs centered on the reference point.

II.3.3 Uncertainties and error proxies

The comparison between satellite-derived shorelines and ground-truth MSL shorelines allows for the estimation of the expected error associated with remote shoreline detection from Sentinel-2 and Landsat imagery. However, the significance of a given cRMSE value depends strongly on the intrinsic morphodynamics of each site. In other words, the utility of remotely sensed shoreline time series is more sensitive to measurement accuracy at sites with low natural shoreline variability, whereas sites experiencing large natural shoreline movements can tolerate higher noise levels while still capturing meaningful patterns of change.

Figure II.12, inspired by Vos et al. (2023b), illustrates the distribution of shoreline position changes between consecutive in-situ measurements alongside the cRMSE of satellite-derived shore-

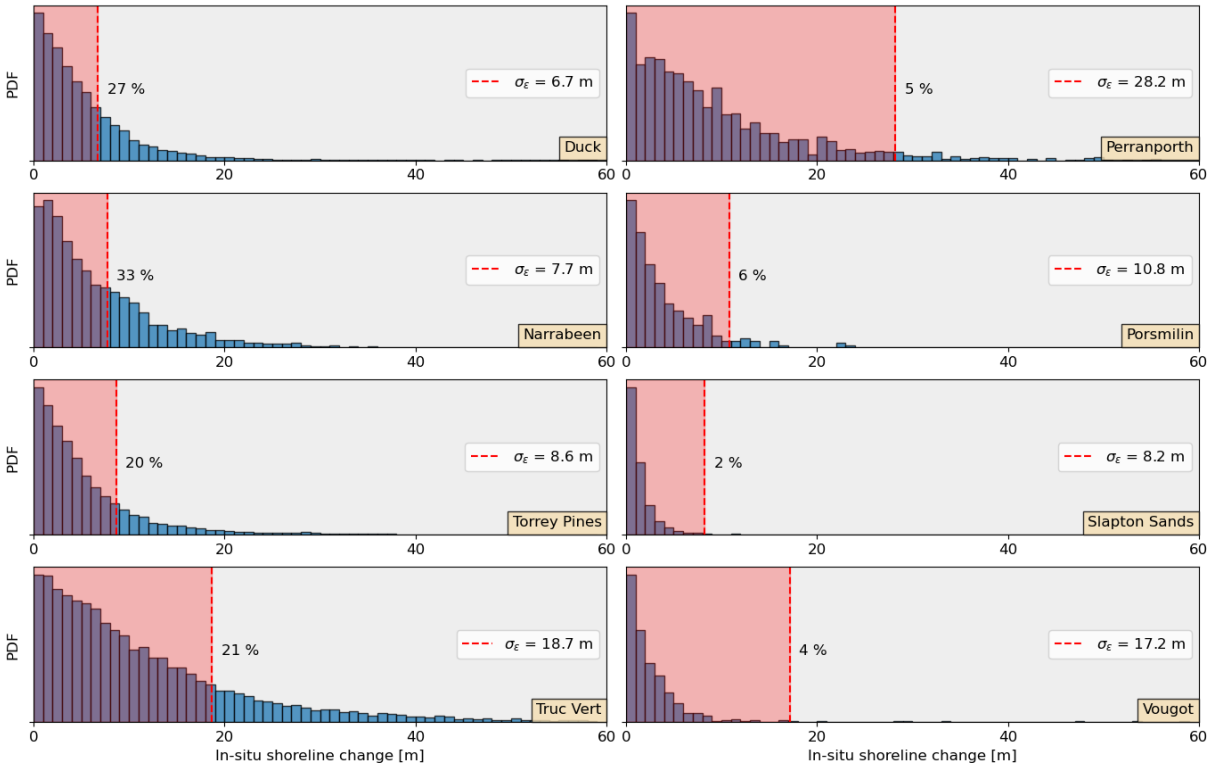

FIGURE II.12 Distributions of shoreline change between consecutive in-situ measurements at the 8 study sites. Red dashed lines indicate the mean cRMSE of the 5 best-performing SDS methods at each site. The percentage shown represents the proportion of in-situ shoreline changes that exceed the corresponding mean cRMSE.

lines (computed from the five best-performing index-threshold combinations at each site) for all eight study sites. At all sites, the majority of in-situ shoreline changes between two measurements are below 20 meters, and most of these changes fall below the corresponding cRMSE. This indicates that, particularly at macro-tidal sites, the noise in SDS-derived shoreline positions often exceeds the magnitude of actual short-term changes. Specifically, between 94% and 98% of in-situ shoreline changes at macro-tidal sites are smaller than the SDS noise level. Narrabeen is an exception, with roughly one-third of shoreline changes exceeding the SDS cRMSE, making it the most reliably monitored site remotely. Conversely, at Slapton Sands, 98% of shoreline changes are below the cRMSE, highlighting the difficulty of distinguishing true shoreline change from measurement noise at this site on a satellite measurement-to-measurement basis.

SDS-derived time series can be resampled or aggregated (e.g., using monthly means) to produce more reliable estimates at coarser temporal resolutions. Assuming errors are normally distributed, it is possible to estimate the minimum shoreline position change detectable at a 95%

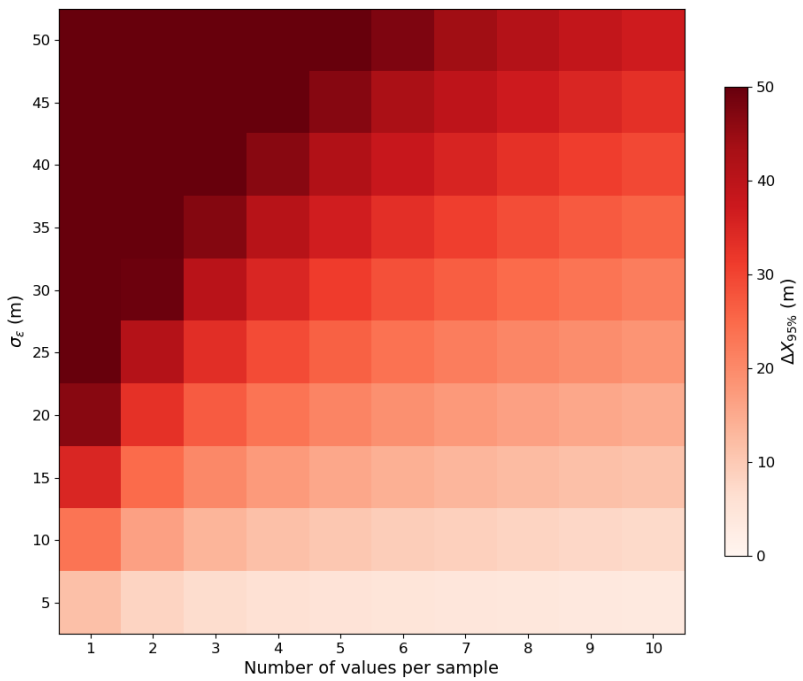

FIGURE II.13 Heatmap showing the minimum shoreline change detectable at a 95% confidence level, computed using Eq. II.12.

confidence level, based on the cRMSE of the observations and the number N of values averaged together during resampling. Figure II.13 illustrates this accuracy–resolution trade-off. The minimum detectable change at the 95% confidence level is given by:

$$\Delta X_{95\%} = 1.675\sqrt{2}\frac{\sigma_\epsilon}{\sqrt{N}} \tag{II.12}$$

where σ_ϵ is the cRMSE, and N is the number of observations per aggregated sample. As expected, increasing the number of observations per time unit reduces the threshold for reliable change detection. However, detection errors are not strictly normally distributed, as illustrated on Figure II.14, which limits the direct applicability of this formulation, particularly at more challenging sites where deviations from Gaussian behavior are pronounced. Nevertheless, this approach provides a useful framework for evaluating time series derived from measurements with known uncertainties.

Accurate estimation of SDW/SDS errors is essential to quantify $\Delta X_{95\%}$, which can only be determined through validation against ground-truth data. However, as shown in Figure II.1, validation sites are sparse and largely concentrated in developed, high-latitude regions, leaving vast portions of the world's coastlines unvalidated. Consequently, an *a priori* assessment of SDW/SDS

errors at any site must rely on identifying error-contributing factors that can be inferred without ground-truth data.

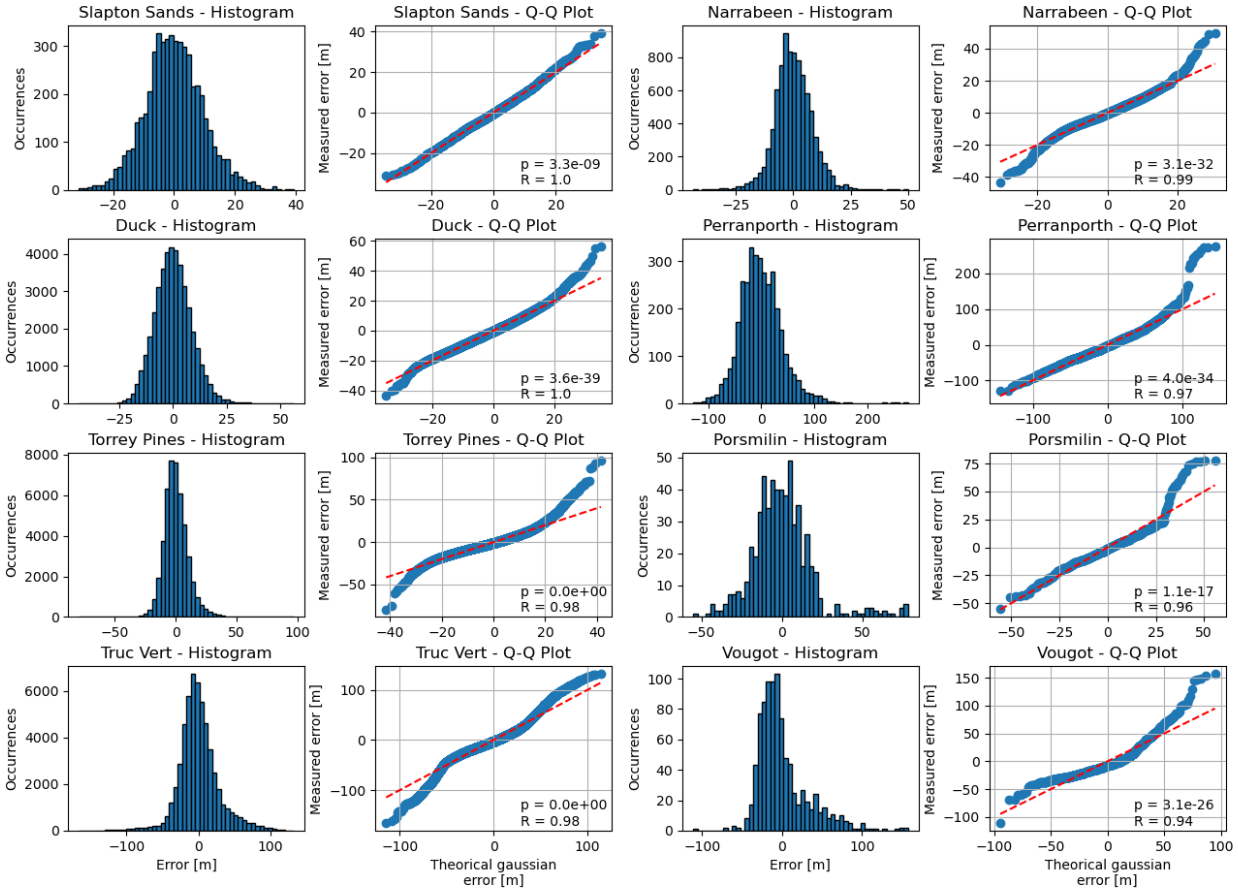

FIGURE II.14 Distributions and Q-Q plots of SDW errors obtained at the 8 sites with the top 5 performing methods (evaluated at each site). The Pearson's correlations of the errors with they're associated expected gaussian values are displayed, as well as the p-value of the Shapiro-Wilk test (here attesting for the non strictly-gaussian distributions of the errors).

Previous studies (Castelle et al. (2021); Konstantinou et al. (2023); Graffin et al. (2023)) have shown that certain site characteristics make shoreline detection more challenging. Two primary factors are large tidal cycles and low intertidal slopes, both of which reduce detection accuracy. This relationship is quantitatively confirmed in Figure II.15, which compares detection errors—represented by the mean cRMSE from the five best-performing index-segmentation combinations at each site—with two geometric indicators: the inverse of the beach slope (panel a) and tidal excursion, defined as the tidal range divided by the beach slope (panel b). In both cases, errors increase approximately linearly, with squared Pearson correlation coefficients exceeding

0.8.

Interestingly, at gently sloped sites, SDW detection errors are greater than errors in estimating MSL shoreline positions, which is counter-intuitive because SDS time series include a tide correction step. This discrepancy is further discussed in the Discussion section.

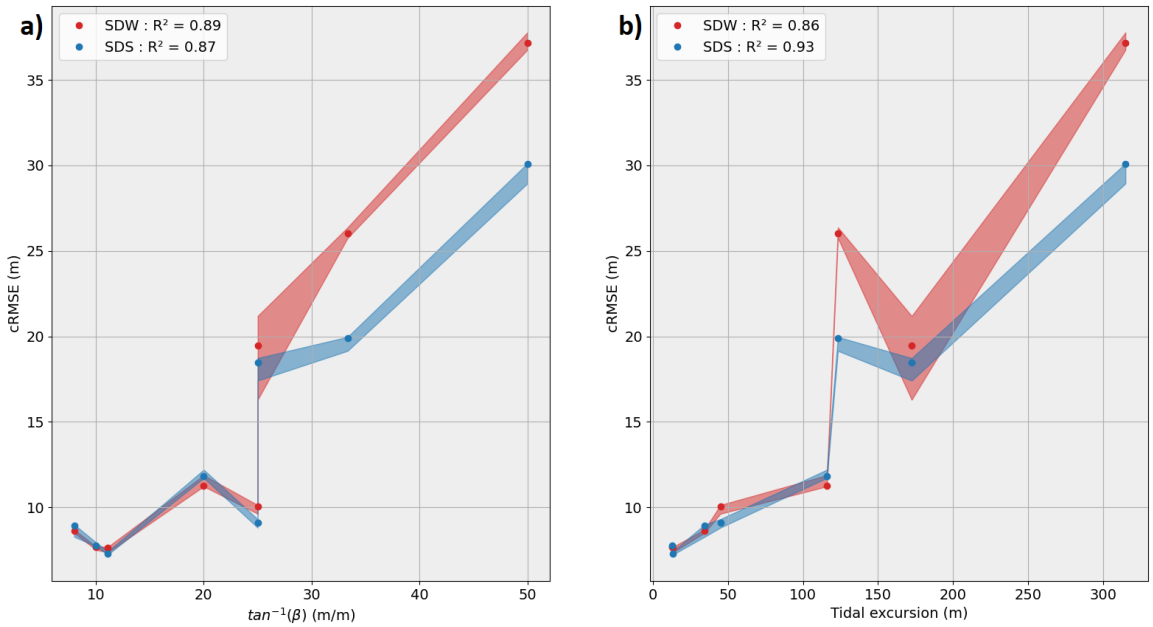

FIGURE II.15 Relationship between the cRMSE of the SDW/SDS time series and (a) the inverse of beach slope, and (b) tidal excursion. The error is represented as the mean cRMSE across the 10 best-performing methods, shown as dots (red for SDW, blue for SDS). Shaded areas indicate the interquartile range (first to third quartile) of the cRMSE distribution for the same methods, per site.

Sites with steep beach profiles, such as Duck, Narrabeen, and Slapton Sands, exhibit relatively small errors, typically around 10 m. Conversely, sites like Truc Vert and Perranporth, combining broad tidal ranges with gentle slopes, show substantially larger errors—often comparable to the tidal excursion itself. Intermediate behavior is observed at Torrey Pines and Vougot; Torrey Pines is relatively less challenging due to its long, uninterrupted sandy shoreline, whereas Vougot's mixed sandy–rocky environment increases detection complexity. Although Perranporth may act as an outlier due to its extreme tidal range, the overall pattern is observable across the other seven sites, particularly when considering tidal excursion.

A clear contrast emerges between low tide excursion sites (Duck, Narrabeen, Slapton Sands,

Torrey Pines), with tidal ranges below 50 m and errors under 10 m, and intermediate tidal excursion sites (Perranporth, Truc Vert, Vougot), with tidal ranges exceeding 100 m and errors between 20–40 m. For sites with tidal excursions below 50 m, errors appear less sensitive to tidal range, suggesting that other factors, such as MSI pixel resolution and processes like wave run-up, dominate. Based on the performance of the algorithms across the eight sites, a first-order indicator of error (mean errors associated with SDS and SDW per site) as a function of tidal excursion can be approximated by the linear relationships

$$cRMSE \sim 5 + 0.5\ tan^{-1}\beta \tag{II.13}$$

or

$$cRMSE \sim 5 + 0.09\ \Delta X_{tide}, \tag{II.14}$$

where ΔX_{tide} is the tidal excursion. Applied to a beach with a slope $tan\beta = 0.05$ m/m and tidal range $TR = 3$ m (Tide excursion $\Delta X_{tide} = 60$ m), Eq. II.13 and II.14 provide estimated cRMSE of 15 m and 10.4 m, respectively.

II.3.4 Seasonal, interannual, and longer-term variability of the shoreline position

Time series of shoreline position not only provide intrinsic positional information but also enable the extraction of key metrics that describe beach dynamics. Here, we evaluate the performance of shoreline detection algorithms in accurately estimating long-term trends, seasonal cycles, and interannual variability derived from shoreline position time series. Similar to beach slope estimation, we present validation results for long-term trends and seasonal cycles using the LM-based algorithms, while validations figures for the other three thresholding methods are provided in the Appendix A (Figures A.8-A.16).

Figure II.16 compares long-term shoreline change trends derived from satellite-based SDS time series against in-situ MSL shoreline measurements across five spectral indices. Overall, satellite-derived trends agree well with field measurements, with RMSE values ranging from 0.8 to 1.1 m/yr. Accuracy varies among sites, with locations like Perranporth and Truc Vert showing larger errors due to less reliable SDS time series (refer to Appendix A A.8-A.10). Satellite-derived trends

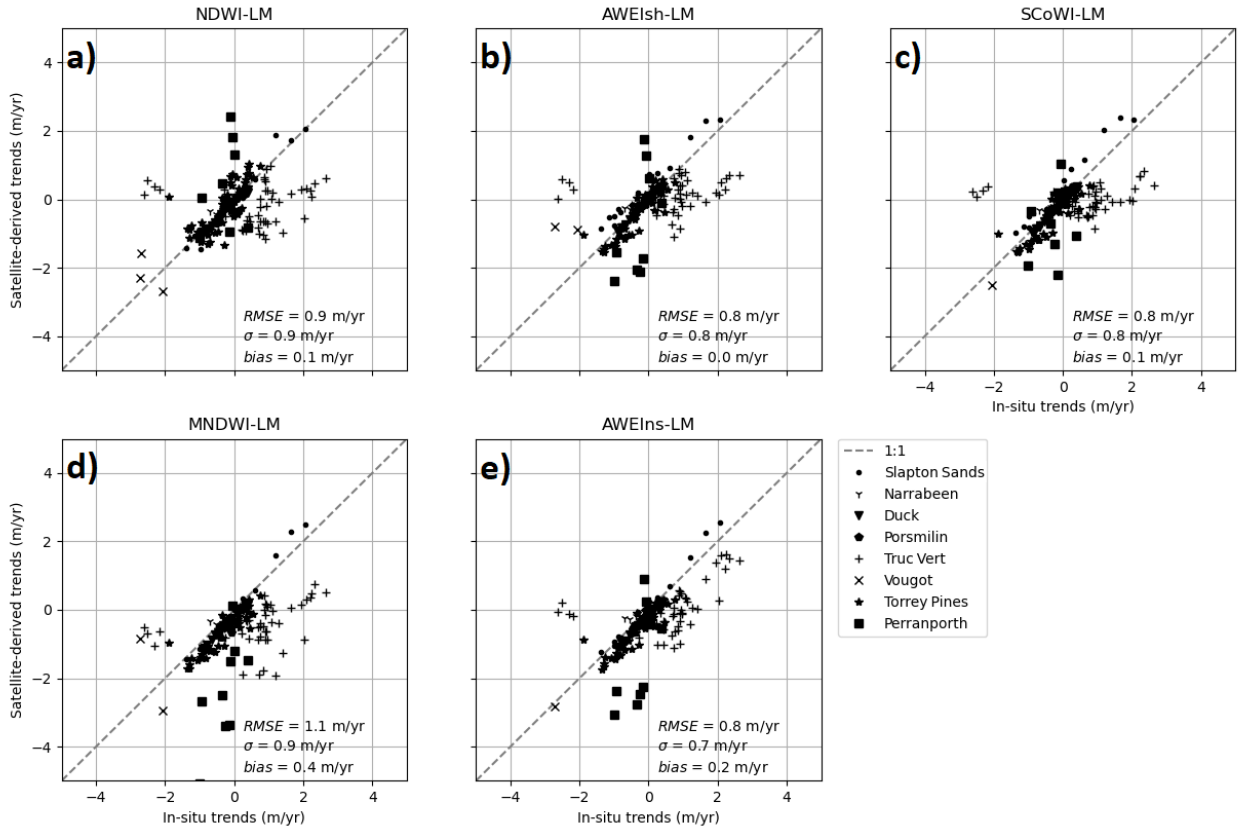

FIGURE II.16 Satellite-derived trends are obtained from waterline position time series using algorithms based on **a)** NDWI, **b)** AWEIsh, **c)** SCoWI, **d)** MNDWI, and **e)** AWEIns indices, combined with the LM thresholding method.

generally exhibit a slight negative bias, typically below 0.2 m/yr. Among the methods, NDWI-MSV and AWEIns-MSV yield the least accurate results (RMSE > 1.5 m/yr), whereas AWEIsh-Otsu achieves the best agreement (RMSE = 0.7 m/yr). Overall, methods based on AWEIsh, SCoWI, and MNDWI indices produce stable and accurate trend estimates across thresholding techniques, while Otsu and LM thresholding methods consistently deliver reliable results across indices.

Figure II.17 compares SDS-derived seasonal cycles (LM thresholding) with in-situ MSL shoreline seasonal cycles across the five spectral indices. Validation uses the standard deviation of shoreline position, reflecting seasonal cycle amplitude. Satellite-derived standard deviations generally align with field data, though several outliers exist, with differences exceeding 5 m in some cases. Root-Mean-Square Error (RMSE) values range from 2.3 to 4.0 m using LM thresholding (2.3–14.5 m across all thresholding methods). Biases range between 0.8–2.1 m (0.8–10.7 m across all methods), indicating that systematic overestimation is comparable to random variability. NDWI-WP performs poorest (RMSE > 10 m), while MNDWI-LM achieves the best agreement

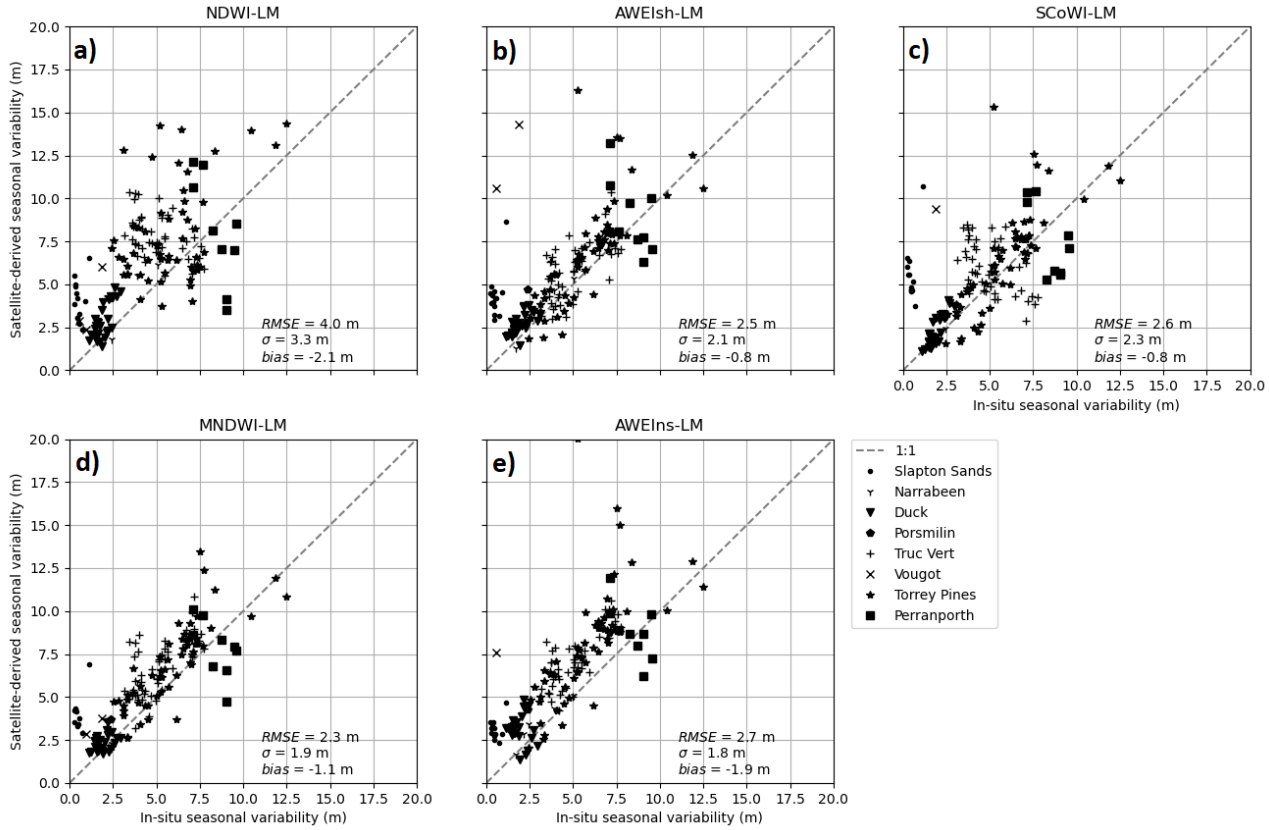

FIGURE II.17 Satellite-derived standard deviations of seasonal cycles obtained from waterline position time series using algorithms based on **a)** NDWI, **b)** AWEIsh, **c)** SCoWI, **d)** MNDWI, and **e)** AWEIns indices, combined with the LM thresholding method.

(RMSE = 2.3 m). MNDWI-based methods are generally stable across thresholding techniques, and LM thresholding provides the most consistent results across MNDWI, AWEIsh, AWEIns, and SCoWI indices.

Figure II.18 presents the validation of SDS-derived interannual fluctuations (LM thresholding) against in-situ MSL shoreline positions, across the five spectral indices. Validation uses the standard deviation of yearly-averaged shoreline positions, reflecting year-to-year shoreline variability. Satellite-derived standard deviations generally agree with field data, although outliers appear, particularly at macrotidal sites such as Perranporth and Vougot. RMSE values range from 1.9–2.7 m using LM thresholding (1.8–11.2 m including all thresholding methods). Biases are low relative to seasonal cycle validation, typically $< \pm 0.5$ m (NDWI-based methods show slightly higher bias, >1 m). NDWI-WP performs worst (RMSE > 10 m), while AWEIns-MSV provides the best agreement (RMSE = 1.8 m). Overall, AWEIns- and SCoWI-based methods are stable and

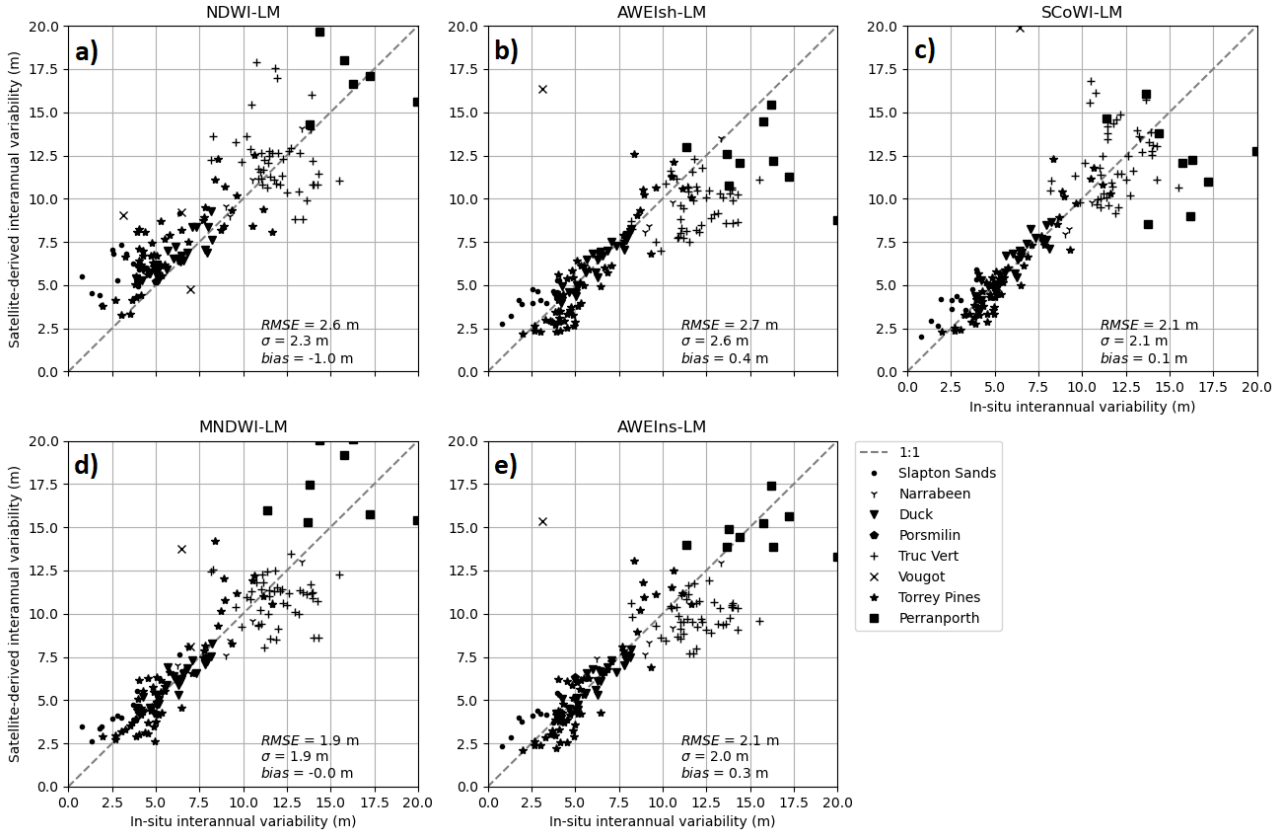

FIGURE II.18 Satellite-derived standard deviations of yearly-averaged shoreline change are obtained from waterline position time series using algorithms based on **a)** NDWI, **b)** AWEIsh, **c)** SCoWI, **d)** MNDWI, and **e)** AWEIns indices, combined with the LM thresholding method.

accurate across thresholding techniques, with LM and Otsu thresholds performing most consistently across indices.

II.4 Discussion

This study leveraged beach elevation profiles from hundreds of transects across eight diverse coastal sites to evaluate the capacity of 20 satellite-derived waterline (SDW) methods to automatically and reliably track SDW time series. The chosen validation sites differ widely in morphology, hydrodynamics, and tidal regime, enabling a robust test of algorithm performance under heterogeneous conditions. As shown here and in previous works (e.g., Bishop-Taylor et al. (2019a); Vos et al. (2023b)), SDW algorithm performances are highly site-dependent. No single method outperforms the others consistently across all sites. However, some approaches appeared

more stable, with SCoWI- and AWEIsh-based indices and LM-based segmentation techniques often ranking among the top performers. This suggests these combinations may be preferable when working at new sites without prior knowledge.

At Duck and Narrabeen, most algorithms achieved sub-pixel accuracy, with cRMSE values below the widely accepted 10–15 m threshold, and showed limited sensitivity to algorithm choice. In contrast, challenging sites like Vougot and Perranporth yielded cRMSE values above 25 m for most methods, highlighting the importance of site-specific factors in SDW accuracy. Macro-tidal environments, and more generally, beaches with large tidal excursions due to the combination of high tidal ranges and low slopes, tended to yield the largest SDW/SDS errors. These errors are multi-factorial: (i) small vertical water-level uncertainties translate into large horizontal errors on gentle slopes, (ii) non-linear intertidal profiles reduce the accuracy of tidal correction, and (iii) ambiguous optical states in the lower intertidal zone reduce waterline detection reliability. These issues are well documented across diverse sites (e.g., Castelle et al. (2021); Konstantinou et al. (2023); Graffin et al. (2023).

Segmentation method choice was particularly critical at meso- and macro-tidal sites. Histogram-thresholding methods such as Otsu's and WP often struggled when wet/dry intensity distributions were not clearly separated, leading to poor delineation. LM-based segmentation generally improved results by refining Otsu's threshold with local information, while MSV methods also provided improvements by integrating spatial coherence. LM overall outperformed MSV, although both showed potential at macro-tidal sites when paired with indices such as AWEIns, AWEIsh, or SCoWI. In this work, we deliberately avoided learning-based or optimized thresholds to focus on robust, automatic approaches that can be applied consistently without user intervention.

Strong correlations between satellite-derived and in-situ measurements indicate that waterline changes were successfully tracked by most methods. Interestingly, site dynamics appear to modulate performance: microtidal sites with small tidal excursions exhibited low variability in algorithm performance but lower signal-to-noise ratios, while macro-tidal sites showed the opposite pattern. This interplay helps explain the relatively consistent performance of beach slope estimation across sites, even when SDW positional accuracy varied substantially.

The study also demonstrated the importance of automated filtering steps. We excluded images with more than 50% cloud cover, filtered by pixel intensity distributions to remove ambiguous cases, and applied transect-specific IQR filtering to remove outliers. Such processes are essential to ensure exploitable time series, particularly for large-scale applications, although their influence on algorithm performance deserves further investigation. Additional methodological aspects, such as ROI size, showed limited influence on overall results.

Other sources of uncertainty were only partially explored. For example, we did not explicitly assess the influence of sand type, turbidity, or georeferencing errors. Differences between Landsat and Sentinel-2 were found to be minor, though Sentinel-2 imagery provided slightly higher accuracy. As expected, minimum error levels remain constrained by the spatial resolution of the sensors, and SDW position errors cannot drop below a few metres. Tidal corrections based on astronomical models also introduce uncertainty, as they do not capture wave setup, run-up, or sea-level anomalies.

A key outcome of this study is the quantification of the minimum detectable shoreline change. At many sites, fewer than 25% of consecutive SDS measurements exceeded the local error threshold, particularly at macro-tidal beaches. This reduces their utility for high-frequency shoreline variability but does not invalidate their broader value. By aggregating observations in time (monthly/seasonal composites) or space (regional averages), robust shoreline dynamics emerge. Indeed, integrated metrics such as long-term trends, interannual variability, and seasonal cycles of shoreline change were well captured by the top-performing methods, with accuracies of <1 m/yr for long-term trends, and <2.5–3 m for interannual and seasonal variability, respectively. These findings underscore the benefits of aggregating noisy data to extract meaningful signals (Vos et al. (2019a); Warrick et al. (2025b)).

Finally, empirical relationships linking detection error to environmental factors such as tidal range and beach slope enable the estimation of confidence bounds on SDS time series globally. These relationships should be interpreted cautiously, as they are derived from a limited set of eight validation sites and do not encompass all possible sources of error. Nevertheless, they represent a

first step toward quantifying uncertainties in SDW/SDS extraction across diverse coastal settings.

II.5 Chapter Conclusion

This study benchmarked 20 unsupervised satellite-derived waterline (SDW) and shoreline (SDS) extraction methods across eight morphologically and hydrodynamically diverse sites, coupled with FES2022 tide model outputs. Results confirmed that accuracy is strongly site- and condition-dependent, with robust combinations of water indices (e.g., SCoWI, AWEIsh) and segmentation methods (e.g., LM-based approaches) producing the most reliable results. Performance was highest at micro- to meso-tidal sites, where sub-pixel errors could be achieved, and lowest at macro-tidal, low-sloping beaches, where large tidal excursions amplify vertical uncertainties and complicate waterline detection. Tidal excursion emerged as a first-order predictor of error magnitude, offering a useful metric to anticipate uncertainties in automated shoreline time series.

Beyond individual detections, this study highlights the robustness of integrated metrics derived from SDW/SDS time series. Seasonal cycles, long-term shoreline trends, and interannual variability can be reliably extracted even when single observations are noisy, since aggregating multiple observations reduces error and enhances signal stability. This demonstrates that while automated waterline detection remains sensitive to environmental and methodological choices, composite indicators provide a strong foundation for large-scale shoreline monitoring.

Methodologically, this work establishes a transparent and modular framework for evaluating SDW approaches, with interchangeable processing steps that facilitate adaptation and scalability. Limitations remain, particularly the reliance on optical imagery, residual uncertainties in tide corrections, and sensitivity to ambiguous wet/dry states. Future progress lies in refining automated segmentation and filtering, incorporating complementary datasets (e.g., SAR, high-resolution sensors, dense time series), and leveraging advances in cloud-based geospatial platforms for planetary-scale monitoring.

Building on this methodological foundation, the next chapter applies a validated SDW ap-

proach, the SCoWI-LM method which demonstrated robust performances across diverse sites, along the North American West Coast (U.S. West Coast and Mexican Baja California). This case study demonstrates how shoreline time series can capture climate-driven variability across seasonal and interannual scales, providing a proof of concept for large-scale, automated shoreline monitoring.

Chapter III

Study case : Seasonal and ENSO-driven waterline variability along the North American West Coast

Most of the content presented in this chapter is derived from the article *Waterline responses to climate forcing along the North American West Coast* written by Graffin et al. (2025) and published in *Communications Earth & Environment (Springer Nature)*.

Contents

III.1 Introduction **85**

III.2 Methods **87**
III.2.1 Satellite-derived waterline data 87
III.2.2 Deriving trends, seasonal cycles and anomalies 91
III.2.3 Data and statistical tests for climate variability analysis 92

III.3 Results **94**
III.3.1 Long-term trends of shoreline change 96
III.3.2 Seasonal patterns of shoreline change 96
III.3.3 Interannual variability and ENSO-driven hydro-morphodynamics 101

III.4 Discussion **110**

III.5 Chapter Conclusion **112**

III.1 Introduction

The present study investigates the response of the North American West Coast (NAWC) to seasonal and interannual climate forcing using satellite-derived waterline (SDW) observations. While large-scale coastal monitoring from satellite imagery has expanded considerably in recent years (Vitousek et al. (2023a)), most studies remain either site-specific (e.g., Castelle et al. (2021);

Graffin et al. (2023); Kümmerer et al. (2025)) or global but coarse in spatio-temporal resolution (e.g., Luijendijk et al. (2018); Almar et al. (2023)). Few have examined regional-scale coastal dynamics at fine spatial resolution (e.g., Vos et al. (2023a)), which is critical to capture heterogeneity in morphodynamic and hydrodynamic responses to climate variability at seasonal and interannual temporal scales, which are technically observable (e.g., Vos et al. (2019a), also refer to the previous chapter). Here, we address this gap by applying a newly generated 25-year dataset of satellite-derived waterline positions to the NAWC, a 4,000-km-long, morphologically diverse coastal region spanning from northern Washington (48°N) to Baja California Sur, Mexico (23°N). This region is particularly well suited for a study on the influence of climate variability on coastal morphodynamics and shoreline change as it is directly exposed to the Pacific Ocean strongly influenced by the climate mode ENSO, and the ocean climate in the mid latitudes is largely modulated at the seasonal scale (refer the Climate Variability section in Chapter I and to Figures I.2 and I.3). Our approach leverages sub-kilometric resolution (250-m transects), enabling fine-scale analyses rarely achieved at such regional scales.

The NAWC encompasses five distinct subregions (Figure III.1), each characterized by different geomorphic settings, wave climates, and sea-level variability:

1. **Pacific Northwest (PNW)** – From northern Washington to northern California, exposed to energetic extratropical storms, with strongly seasonal wave heights (1.5 m in summer to 3–4 m in winter, exceeding 5 m during strong El Niños) and mean sea-level rising by ∼0.25 m in winter Ruggiero et al. (2005, 2010).

2. **Northern California (NCA)** – From the northern part California state to Point Sur, NCA experiences a strong seasonality of its wave climates, similar to and also impacted by extratropical storms but slightly weaker than in the PNW. Its wave climate fluctuate largely over the year, with monthly averaged wave heights ranging from 1.5 in summer to 3 m in winter. The regional also exhibits a moderate seasonal sea-level cycle of ∼10 cm Xu (1999); Bromirski (2023).

3. **Southern California (SCA)** – From Point Sur to the U.S.–Mexico border, SCA is influenced by both North Pacific and Southern Hemisphere swells, which are largely altered by the Channel Islands. Monthly-averaged wave heights range from 1–2 m, with strong spatial

variability and a seasonal sea-level cycle of ∼0.2 m Adams et al. (2008); Hegermiller et al. (2017).

4. **Baja California (BC)** – From the U.S.–Mexico border to Guerrero Negro, BC is characterized by arid coastal plains exposed to winter North Pacific swells, summer Southern Hemisphere swells, and episodic tropical cyclones. Monthly averaged wave heights typically range from 1 m in summer to 2 m in winter, and exceeding 3 m during some winter storm events Ruiz de Alegría-Arzaburu et al. (2022b,a).

5. **Baja California Sur (BCS)** – Extending to the southern tip of the peninsula, BCS is influenced by North Pacific swells, Southern Hemisphere swells, and Eastern Pacific tropical cyclones. Wave heights typically range between 1-2 m, increasing during winter and tropical cyclone events, with seasonal sea-level anomalies of ∼15 cm Franco-Ochoa et al. (2020).

By focusing on this diverse coastal system, our objectives are threefold: (i) to assess how seasonal cycles in wave climate and sea level drive shoreline dynamics along the NAWC, (ii) to evaluate the imprint of ENSO phases on coastal variability at a regional scale, and (iii) to quantify the degree of spatial heterogeneity in coastal responses to climate variability across regions.

This study complements prior continental and global work Vos et al. (2023a); Almar et al. (2023); Castelle et al. (2024) by providing a high-resolution, region-specific assessment of climate-driven shoreline variability. The results aim to advance understanding of coastal morphodynamics under seasonal and ENSO forcing, with direct implications for regional coastal management and adaptation.

III.2 Methods

III.2.1 Satellite-derived waterline data

For this study, we generated a dataset of SDW using publicly available multi-spectral imagery from Sentinel-2 and Landsat 5, 7, 8, and 9. The methodology follows (Bergsma et al. (2024)), where spectral bands are combined to form the Subtractive Coastal Water Index (SCoWI):

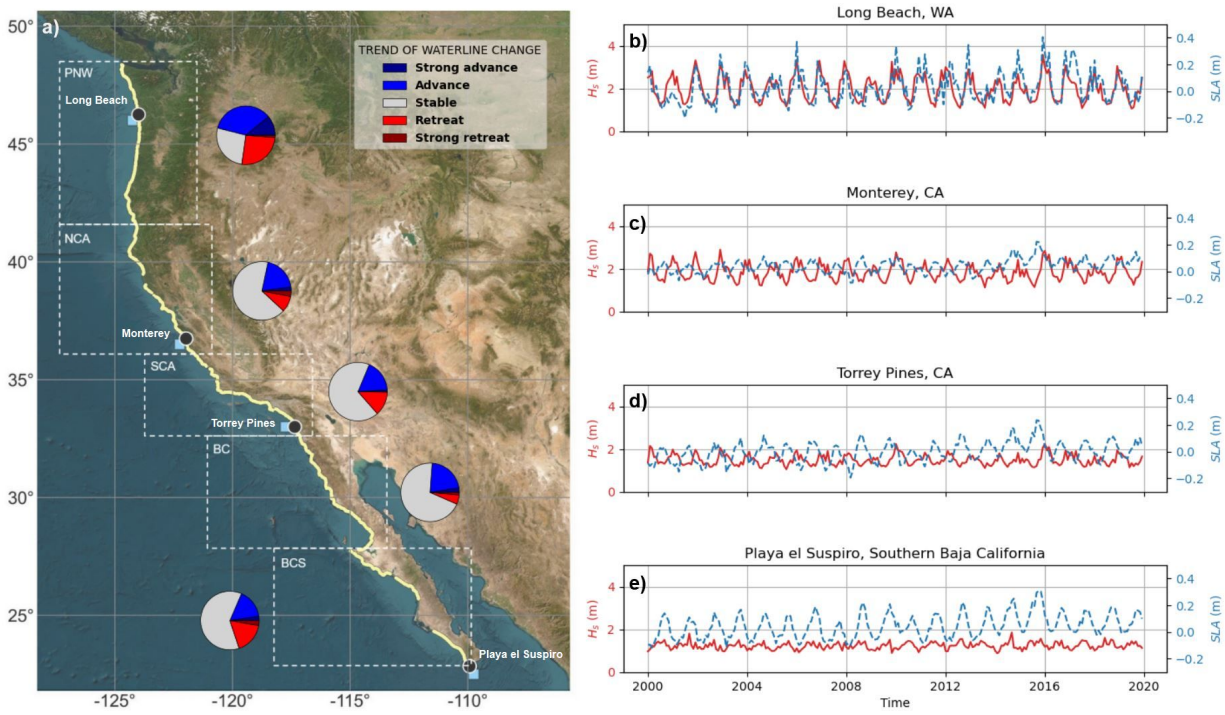

FIGURE III.1 Map of the North American West Coast, the monitored coastline is shown in light yellow. Dashed boxes delineate the different subregions of the study area. Pie charts show the regional distribution of advancing/retreating waterline trends during 2000-2022 derived from the dataset presented in this study. **(b-e)** : Time series of monthly averaged significant wave height (H_s, red) and sea level anomaly (SLA, blue) at Long Beach, WA, Monterey, CA, Torrey Pines, CA and Playa el Suspiro, Baja California Sur (from top to bottom) between 2000-2020, with wave data from ERA5 dataset (*ECMWF, 2020*) and sea-level provided by *NOAA* tide gauges (replaced by AVISO (*CNES, 2020*) data at Playa el Suspiro). Black circles (blue squares) on the panel (a) indicate locations of the 4 sites (closest ERA5 wave model nodes) described on the right panels. The lateral boundaries of the rectangles delineating the subregions are intended solely to visually illustrate the extent of each subregion and should not be interpreted as representing the offshore or nearshore limits of the coastal system. We use the ESRI World Imagery layer as the background map.

$$SCoWI = B + 2 \times (G - NIR) - 0.5 \times SWIR1 - 0.75 \times SWIR2, \quad \text{(III.1)}$$

with B, G, NIR, $SWIR1$, and $SWIR2$ denoting the blue, green, near-infrared, and short-wave infrared bands. As shown in Bergsma et al. (2024), SCoWI effectively separates land and water pixels, including surf and white-water.

Pre-processing. Prior to band combination, Landsat 7–9 images (originally 30 m) were resampled to 15 m, and Sentinel-2 SWIR1/2 bands (originally 20 m) were resampled to 10 m. The cloud-contaminated image filter, introduced in the previous chapter, was applied to discard error-prone images, based on the histogram of SCoWI values.

Waterline extraction. For each image, the local minimum method, a refinement of Otsu's thresholding method (Otsu (1979); Bergsma et al. (2024)) was applied to the SCoWI pixel value distributions, selecting the local minimum between wet and dry peaks. The land–sea interface was then delineated using a marching squares algorithm (Cipolletti et al. (2012)). Extracted waterlines were projected onto transects spaced every 250 m along the NAWC, using the GSHHS shoreline dataset (Wessel and Smith (1996)) as baseline. Non-sandy transects, identified from the Hulskamp et al. (2023) beach classification and visual inspection, were discarded (40% of the initial set of transects has been removed at this step).

Corrections. At each transect, waterline time series were corrected for tidal variability using the approach of Vos et al. (2020), which estimates the mean intertidal beach slope β from waterline time series. The astronomical tide correction term is given by:

$$\Delta X_{tide}(t) = \frac{\eta_{tide}(t)}{\tan(\beta)}, \tag{III.2}$$

where $\eta_{tide}(t)$ is the astronomical tide level (FES2022 model, Lionel et al. (2023), using 34 tide constituents).

FES2022 outputs were validated at four NAWC sites, the results of this validation ($|bias| < 10$ cm, $R^2 \geq 0.95$) are shown on Figure III.2.

Sensor biases were assessed by cross-comparing overlapping missions with Landsat 7 as reference; systematic offsets were removed, and transects with bias > 25 m were discarded (representing 4% of the initial amount of sandy transects). Outliers were identified using the interquartile range (IQR) test and removed. Corrected series were aggregated into monthly composites. Missing months were interpolated using cubic interpolation within a 25-month window; if more than half the values in the first half of the window were missing, no interpolation was applied.

Final dataset construction. From the initial number of transects (datasets were generated: (i) transects with continuous coverage from 2000–2022 (9% of sandy transects removed), used for trend and seasonal cycle analyses; (ii) transects with continuous coverage from 1997–2022 (16%), used for ENSO analysis. Transects with $\tan(\beta) > 0.3$ were discarded (representing 7% of initial amount of sandy transects). The final dataset comprised 7,182 transects for (i) and 6,072

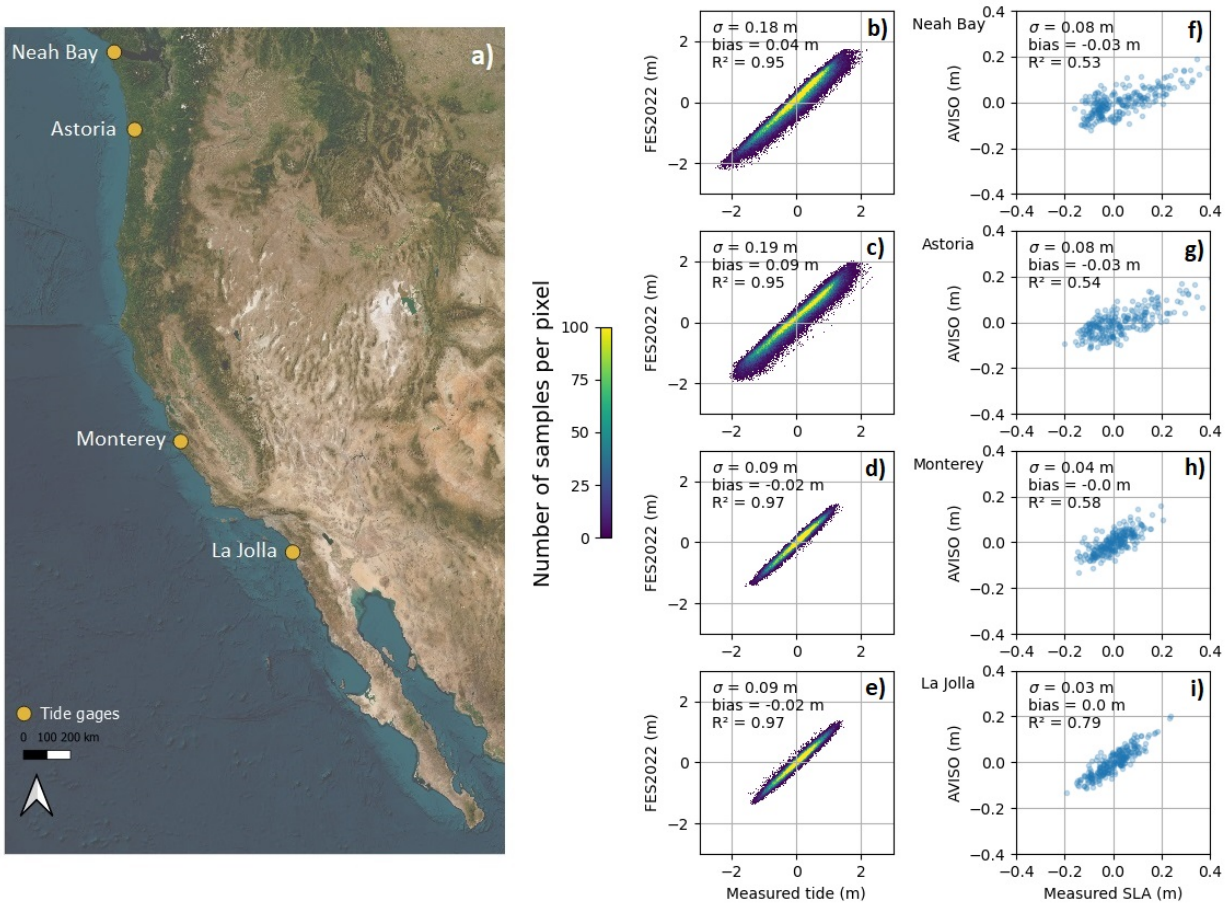

FIGURE III.2 **(b-e)** Comparison between measured (NOAA tide gauges) and modeled (FES2022, Lionel et al. (2023)) tide data. **(f-i)** Comparison between measured (PSMSL, Holgate et al. (2013)) and modeled (AVISO, *CNES*) monthly sea-level anomalies. We use the ESRI World Imagery layer as the background map.

for (ii), with median spacing of ∼275 m. Processing was distributed over 987 sub-areas (∼0.05° each). In total, 810,897 images were processed (average 822 per sub-area), with pre-processing on Google Earth Engine (Gorelick et al. (2017)) and segmentation/post-processing on CNES HPC clusters.

Validation. Monthly waterlines were validated at Torrey Pines (Ludka et al. (2019), $\sigma \sim 12$ m) and Ensenada (Ruiz de Alegría-Arzaburu et al. (2022a), $\sigma \sim 7$ m). The results of this validation, shown on Figure III.3, highlight strong agreement between SDW and in-situ data, with performance comparable to state-of-the-art methods (refer to the previous chapter, or Vos et al. (2023b)). No systematic bias was found between Sentinel-2 and Landsat, confirming method transferability.

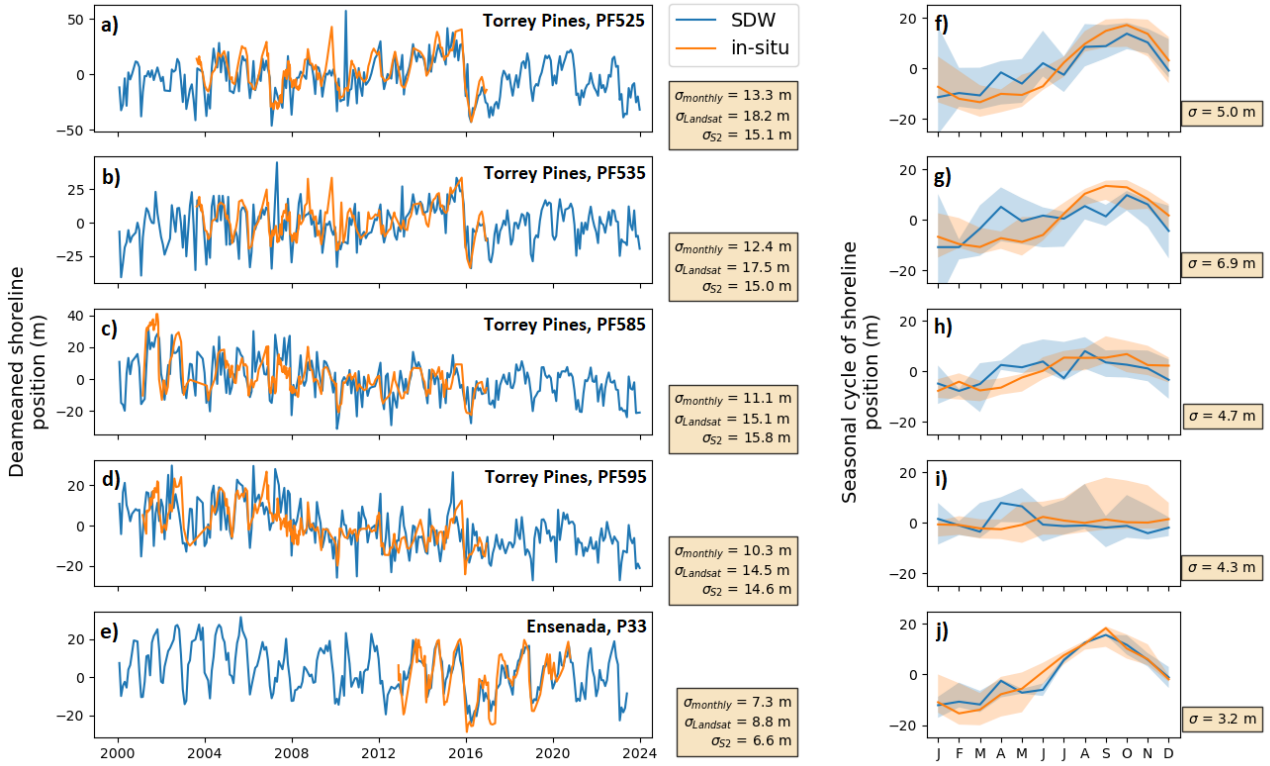

FIGURE III.3 **(a-e)** Time series of shoreline change at four monitored sites, showing both the in-situ and monthly-sampled SDW data. Standard errors for monthly SDW and invidual SDW measurements with a distinction between Landsat and Sentinel-2 measurements are displayed. **(f-j)** Seasonal cycle of shoreline change from SDW data and in-situ shoreline data. Standard deviation in monthly estimation of the seasonal cycle are shown by the shades. Standard error of the seasonal cycle is displayed. Ground truth data at Torrey Pines are derived from beach elevation profiles (PF525, PF535, PF585, PF595) as MSL datum-based shorelines (Ludka et al. (2019)), and ground truth data at Ensenada (profile P33) is in the form of a 1-m elevation contour shoreline time series (Ruiz de Alegría-Arzaburu et al. (2022a)).

III.2.2 Deriving trends, seasonal cycles and anomalies

Trend, seasonal cycle, and anomaly derivation. Trends were estimated using the Theil-Sen estimator (Theil (1992); Sen (1968)), which defines the slope of a time series as the median of the slopes of all lines passing through pairs of points in the time series considered. From the slope and the corresponding intercept, we reconstruct the time dependent trend signal as

$$X_{trend}(t) = \frac{a}{12}t + b, \tag{III.3}$$

where a is the trend (m/yr).

Seasonal cycles were estimated as monthly averages of detrended positions X_w^d,

$$\overline{X^d_{wm}} = \frac{1}{N_m}\Sigma_{t\in m}X^d_{w,t}, \tag{III.4}$$

and reconstructed as $X_{season}(t)$. The seasonal range was defined as

$$\Delta X_{season} = \max(X_{season}(t)) - \min(X_{season}(t)). \tag{III.5}$$

Anomalies were then defined as residuals:

$$X_{residuals}(t) = X_w(t) - [X_{trend}(t) + X_{season}(t)]. \tag{III.6}$$

III.2.3 Data and statistical tests for climate variability analysis

The share of variance of a signal X explained by another signal Y is expressed as

$$VarExp(X,Y) = 100 \times \left(1 - \frac{Var(X-Y)}{Var(X)}\right), \tag{III.7}$$

In this study, the explained variance is used to quantify the share of variance of X, the full waterline signal, explained by $Y = X_{trend} + X_{season}$.

Signal-to-noise ratio (SNR).. We rely on Signal-to-Noise Ratio (SNR) analysis to quantify how anomalous waterline positions during specific events deviate from baseline conditions. The method consists in comparing the distribution of waterline position anomalies during a given event i to the distribution of anomalies observed during normal (neutral) states of the system. The SNR for event i is defined as:

$$SNR_i = \frac{|\mu_i - \mu_{ref}|}{\sigma_{ref}}, \tag{III.8}$$

where μ_i is the median anomaly during event i, while μ_{ref} and σ_{ref} are the median and standard deviation of anomalies during baseline states. A higher SNR_i indicates that the distribution of anomalies associated with the event is more clearly separated from the variability observed under normal conditions.

Climate modes and atmospheric forcing. Climate modes analysis have been conducted based on Multivariate ENSO Index (MEI) (Wolter and Timlin (1998)), as well as Eastern Pacific (EP) and Central Pacific (CP) indexes (Takahashi et al. (2011)) under the form of monthly sampled time series. Winter (DJF) ENSO conditions were determined based on a seasonal resampling of the MEI, EP and CP indexes. We defined the various ENSO conditions and flavors as

$$\begin{cases} El\ Nino\ : \begin{cases} Mixed\ :\ MEI > m \times \sigma_{MEI},\ CP > m \times \sigma_{CP}\ and\ EP > m \times \sigma_{EP} \\ Central\ :\ MEI > m \times \sigma_{MEI},\ CP > m \times \sigma_{CP}\ and\ |EP| < m \times \sigma_{EP} \\ Eastern\ :\ MEI > m \times \sigma_{MEI},\ EP > m \times \sigma_{EP}\ and\ |CP| < m \times \sigma_{CP} \end{cases} \\ La\ Nina\ :\ MEI < -m \times \sigma_{MEI} \\ Neutral\ :\ |MEI| < m \times \sigma_{MEI} \end{cases} \tag{III.9}$$

with MEI the Multivariate ENSO Index, EP and CP the Eastern and Central Pacific indexes, respectively, σ_{MEI}, σ_{EP} and σ_{CP} their standard deviations, and m a threshold rate set at 1. The standard deviation of these metrics is approximately 1, with slight variations depending on the time series window studied.

Significant wave height (H_s), peak wave period (T_p), and mean wave direction (θ) data used in this chapter were obtained from the ERA5 reanalysis, sampled at a monthly resolution with a spatial resolution of 0.5°.

Eddy Kinetic Energy (EKE) was used as an indicator of atmospheric variability, calculated as:

$$EKE = 0.5(u'^2 + v'^2), \tag{III.10}$$

where u' and v' are the 14-day high-pass filtered daily zonal and meridional wind components at 200 hPa from ERA5. EKE values were averaged monthly.

Sea-level anomaly (SLA) data, defined as deviations of sea level from the mean sea surface

height, were obtained from the monthly SSALTO-DUACS products distributed by AVISO. These global products span the period 1993 to present and have a spatial resolution of 0.25°. A comparison between this product and monthly-sampled coastal sea-level measurements from tide gauges is shown in Figure III.2, indicating a good fit but an overall underestimation of the modeled sea levels ($\sigma \sim 5$ cm).

III.3 Results

Following the aforementioned methodology, we collected time series of waterline contours along the NAWC from publicly available satellite imagery and projected them onto transects roughly spaced 250 m apart, yielding cross-shore waterline position time series, that we have corrected from the astronomical tide and sampled at a monthly resolution. The extracted data are presented on Figure III.4.

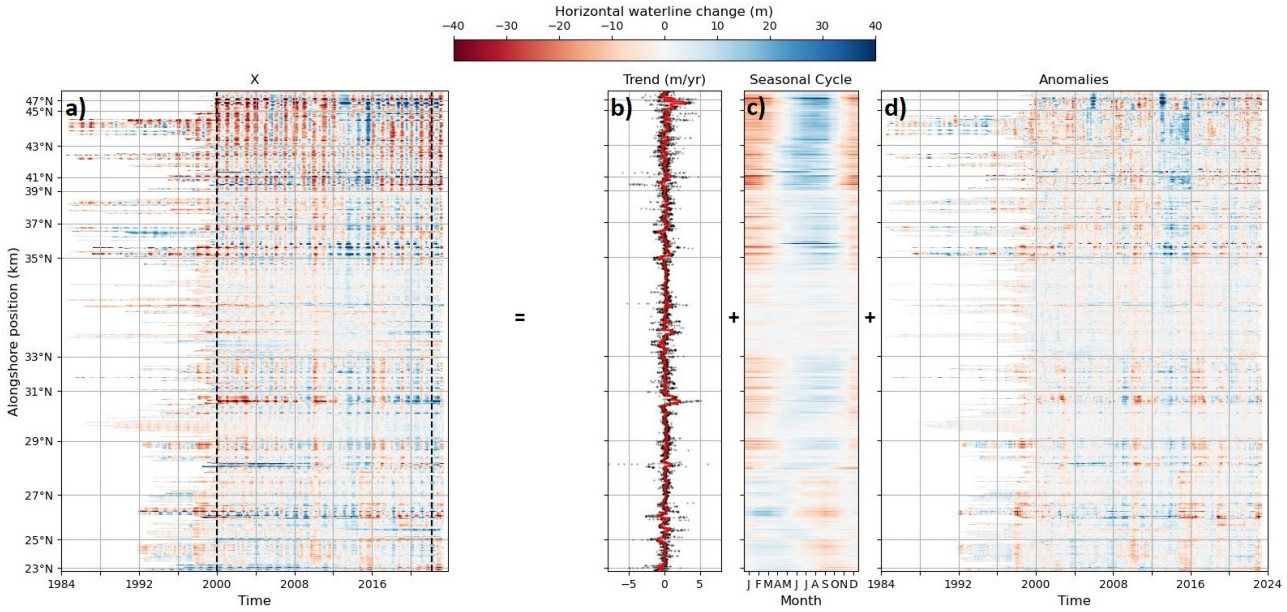

FIGURE III.4 **(a)** Spatio-temporal evolution of waterline positions, demeaned to highlight deviations from the mean. Black dashed lines indicate the 2000–2022 period used for deriving trends and seasonal cycles. **(b)** Alongshore distribution of waterline change trends from 2000–2022. Black dots represent local trends, while the red line shows a 30 km-averaged regional trend. **(c)** Alongshore distribution of the average seasonal cycle of waterline positions, derived from the 2000–2022 time series. **(d)** Spatio-temporal evolution of waterline position anomalies, after removing trends and seasonal signals.

At each transect, the waterline position time series, X_w, can be decomposed as

$$X_w(t) = X_{seasonal}(t) + X_{trend}(t) + X_{residuals}(t), \tag{III.11}$$

where $X_{seasonal}$ and X_{trend} represent the seasonal cycle and long-term trend of waterline change, respectively, and $X_{residuals}$ captures the remaining variability, that we suppose to be primarily associated with interannual fluctuations and we further analyze in this section.

Associated with these data, we also computed the expected SDW following the approach developed in the previous chapter. The spectral analysis of the SDW time series allows for the estimation of the average beach slope, which, when combined with the tidal range modeled by FES2022, provides an estimate of the order of accuracy of our SDW product along the NAWC that we show on Figure III.5.

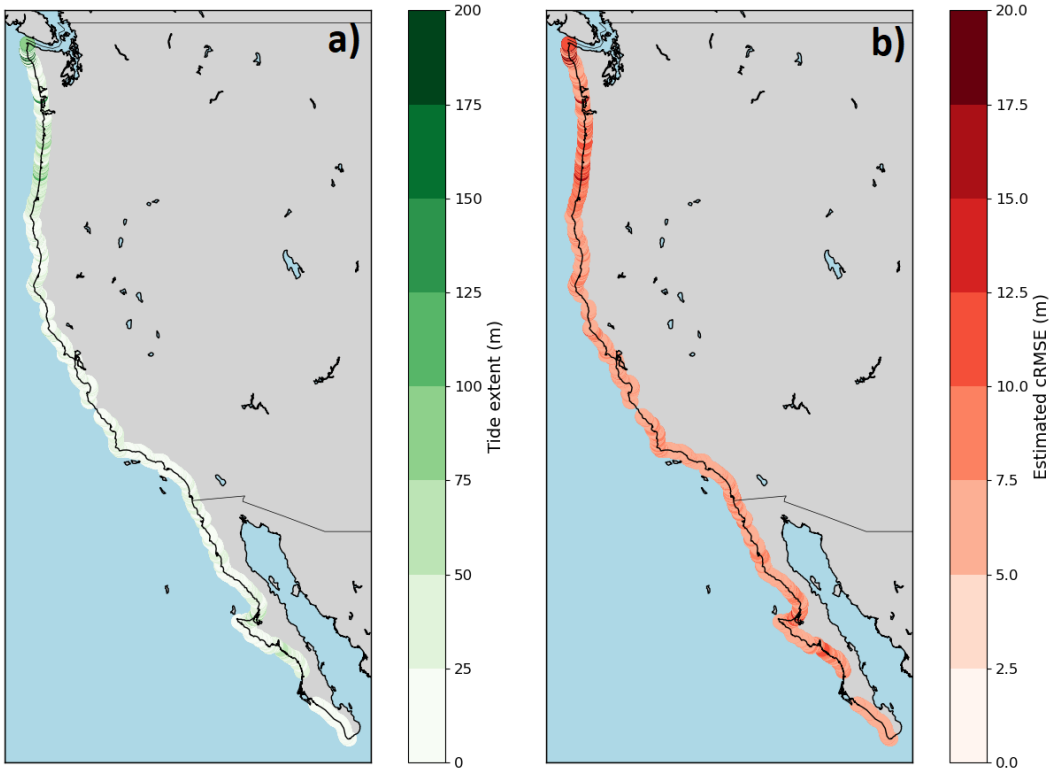

FIGURE III.5 Spatial distribution of **(a)** tide excursion, defined as the ratio of the tidal range by the mean beach slope, and **(b)** estimated cRMSE (centered RMSE), calculated from Eq. II.14.

Tide excursion is below 100 m along most of the NAWC coastline, resulting in estimated cRMSE (of individuals waterline position estimates) below 15 m at most sites. The largest tide excursions are found in Oregon and Washington states, in the USA, resulting in the largest estimations of cRMSE reaching up to 14.6m (99th percentile). The first quartile, median and third quartile of estimated cRMSE along the NAWC are respectively 6.3, 6.9, and 7.7 m, respectively. Note that we discarded transects for which the estimated beach slope, derived using the approach of Vos

et al. (2020), yielded unrealistic values (e.g., $\tan\beta = 0.3$). Such cases are more likely to occur at sites characterized by large tidal ranges and gentle slopes, where the detection of the waterline is more challenging, resulting in more mistedections preventing an accurate estimation of the slope. These potentially problematic sites have been removed from the analysis.

III.3.1 Long-term trends of shoreline change

Figure III.1 shows the regional distribution of waterline change trends along the NAWC. Among the 7,182 sandy-coast transects considered, 75% passed the Mann-Kendall test for trend significance (Mann (1945)), fairly evenly distributed across the five regions delineated in Figure III.1a. Using the trend classification of Luijendijk et al. (2018), 55% of transects exhibit stable trends (absolute change below 0.5 m/yr), while approximately 28% are advancing and 17% are retreating. The PNW shows the highest proportion of advancing beaches: among transects with significant trends, 46% are accreting, with 11% exceeding 2 m/yr. The other four regions are relatively stable, with over half of beaches showing absolute significant trends below 0.5 m/yr and only a small fraction (up to 5%) experiencing strong erosion or accretion. BCS is the only region with more eroding than accreting transects, with 20% in retreat and 3% retreating faster than 2 m/yr. A summary of these trends by region is provided on Table III.1.

TABLE III.1 Waterline change trends of the NAWC (2000-2022) are reported, with values in parentheses indicating trends that passed the Mann-Kendall significance test. Categories are defined as follows: Advance—waterline moving seaward; Retreat—waterline moving landward; Stable—absolute change rate below 0.5 m/yr; Strong—absolute change rate above 2 m/yr.

Area	**Strong retreat**	**Retreat**	**Stable**	**Advance**	**Strong advance**
PNW	0.8 (1.2) %	18.4 (26.0) %	48.7 (26.7) %	24.4 (35.0) %	7.7 (11.1) %
NCA	2.4 (3.4) %	11.5 (16.2) %	64.4 (49.7) %	20.0 (28.2) %	1.8 (2.5) %
SCA	0.3 (0.3) %	12.3 (15.6) %	69.1 (60.9) %	17.1 (21.7) %	1.2 (1.5) %
BC	1.4 (1.8) %	5.2 (6.6) %	69.6 (61.3) %	21.4 (27.2) %	2.5 (3.2) %
BCS	2.0 (2.7) %	12.8 (17.1) %	71.3 (61.6) %	12.1 (16.2) %	1.8 (2.4) %
All	1.3 (1.7) %	11.7 (15.5) %	62.5 (54.7) %	18.5 (24.5) %	2.6 (3.5) %

III.3.2 Seasonal patterns of shoreline change

Superimposed on these trends, the seasonal excursion of the waterline position at each transect allows for a comparative assessment of shoreline response relative to its forcing. Seasonal variability of the waterline along sandy beaches is computed as the monthly mean climatology over

2000–2022, with 99% of transects showing statistically significant correlations (p-value < 0.05) with the full waterline time series. The seasonal excursions of the waterline, meaning the range of the climatology of waterline change presented on Figure III.4, are shown for the whole NAWC on the map Figure III.6

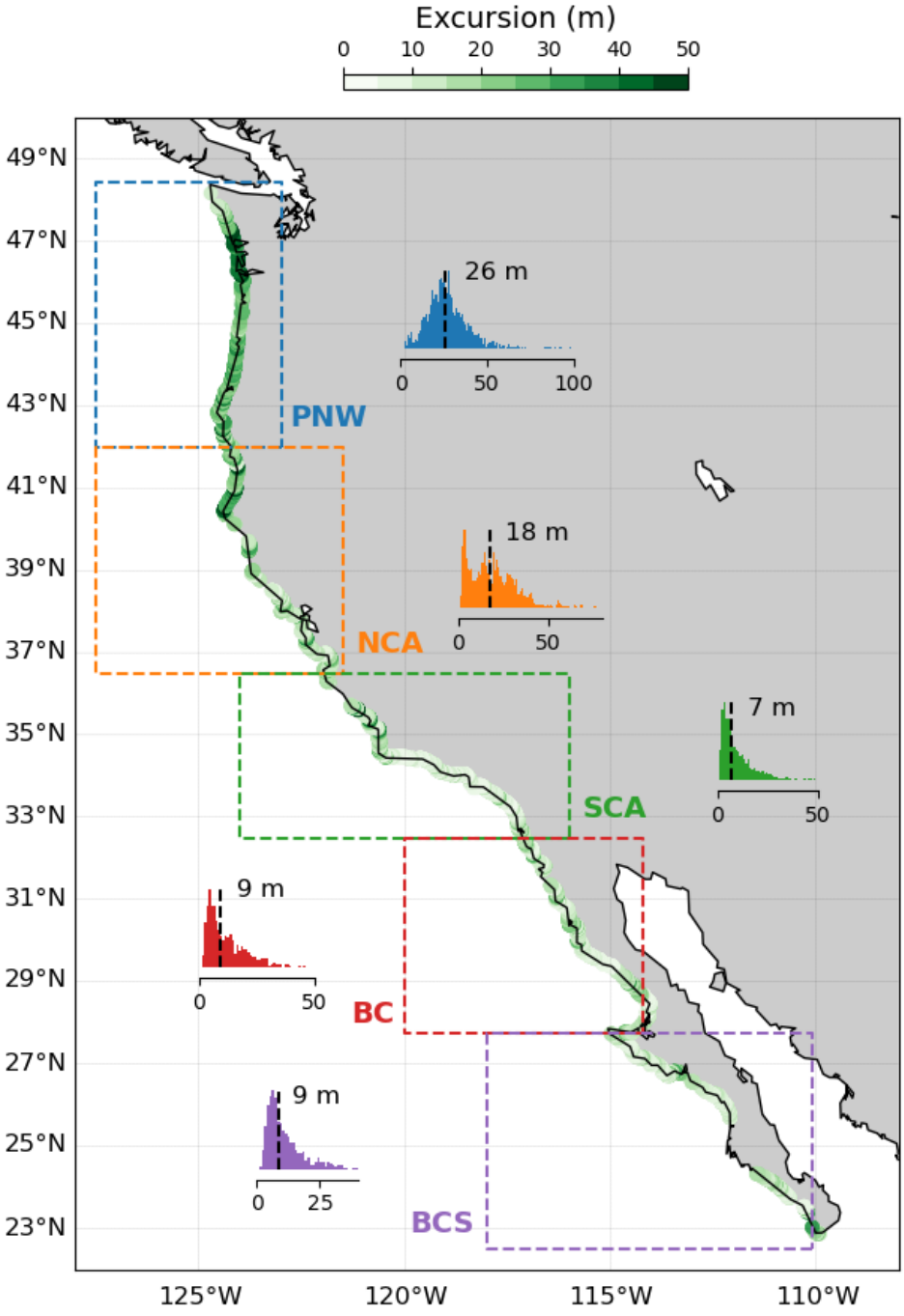

FIGURE III.6 Spatial distributions of the seasonal waterline excursion along the NAWC. Regional distributions of these excursions are shown as histograms. The median seasonal waterline excursion over each region is marked on the histogram as a dotted black line. *The background map was generated using Python's mpl_toolkits.basemap library.*

A first observation is that the magnitude of seasonal excursions decreases southward. In the

PNW, beaches show large seasonal shifts, with excursions exceeding 25 m on average (median 26 m; $q_1 = 19.4$ m, $q_3 = 33.3$ m). This decreases to a median of 17.9 m in NCA ($q_1 = 8.8$ m, $q_3 = 27.9$ m) and under 10 m in SCA (median 7.3 m, $q_1 = 4.0$ m, $q_3 = 13.6$ m), BC (median 9.3 m, $q_1 = 5.1$ m, $q_3 = 16.8$ m) and BCS (median 8.7 m, $q_1 = 5.9$ m, $q_3 = 13.9$ m). As illustrated in Figure III.6e, seasonal cycles are largely in phase from 48°N to 29°N, with beaches widest from May to November (peaking in summer) and narrowest until the following May (peaking in winter). A notable phase shift occurs between 28°N and 27°N, near southern BC and BCS, where the timing of maximum and minimum beach width shifts to late winter and late summer, respectively. In Baja California Sur, seasonal cycles are nearly out of phase with those in northern regions.

These seasonal excursions, along with their phase, can be directly compared to the seasonal cycles of coastal forcings. Figure III.7 illustrates the seasonal-scale relationships between fluctuations in wave power (demeaned), wave direction, and sea level, and the corresponding waterline position changes.

Seasonal cycles of demeaned wave power display strong and spatially coherent patterns along the PNW, NCA, northern SCA, and BC, with higher wave power in winter and lower values in summer. The amplitude of these fluctuations generally decreases with decreasing latitude. In contrast, southern SCA and BCS exhibit weaker and less spatially uniform seasonal fluctuations in wave power.

Wave direction also shows clear seasonal patterns. The PNW experiences predominantly westward waves in winter and northwestward waves in summer, whereas NCA and northern SCA receive northwestward waves year-round. Southern SCA, particularly in sheltered portions, sees waves from the west in winter and from the southwest in summer. BC exhibits a north-to-south gradient: its northern portion transitions from northwest waves in winter to southwest waves in summer, while the southern portion remains dominated by northwest waves throughout the year. In BCS, wave direction alternates seasonally between northwest in winter and southwest in summer, with southwest waves becoming increasingly dominant toward the southernmost coast.

Monthly mean sea level (MMSL) exhibits a pronounced seasonal cycle along the entire NAWC,

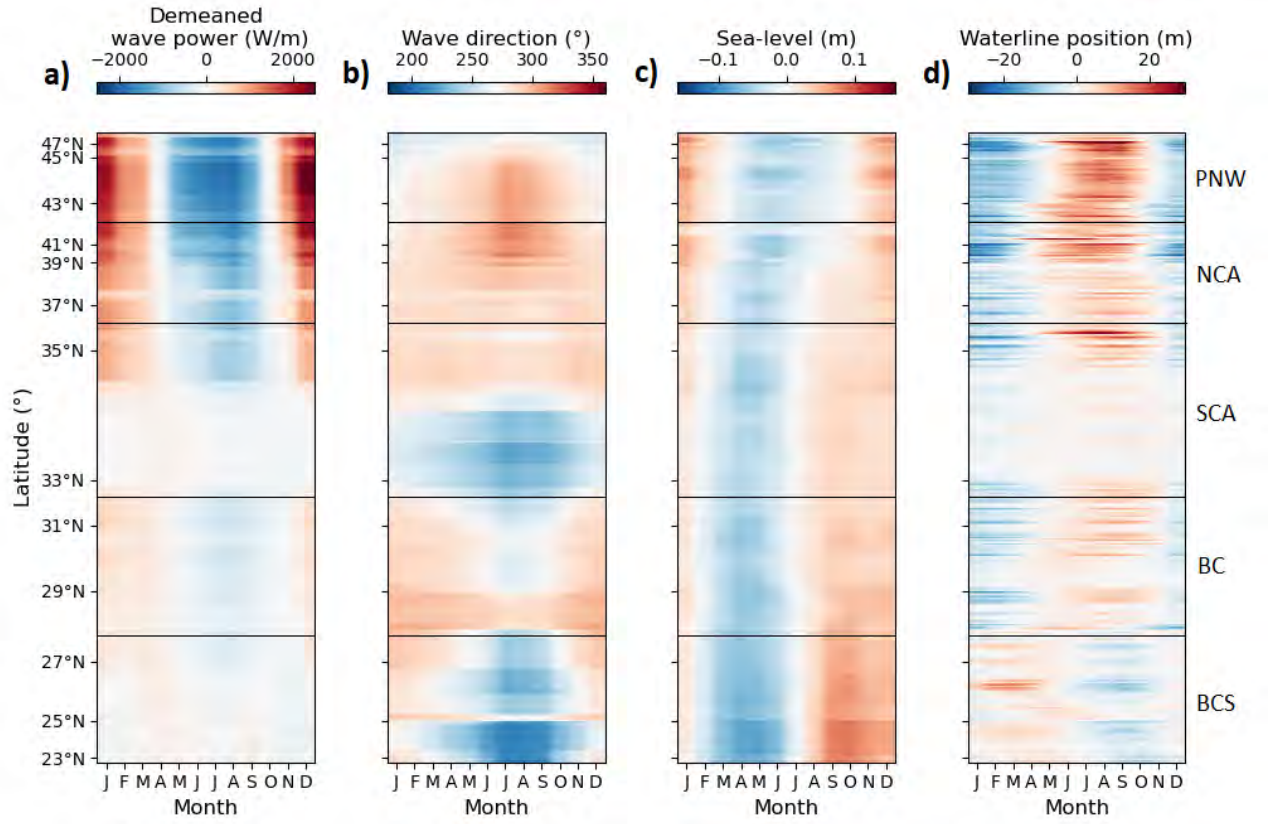

FIGURE III.7 Seasonal cycles of demeaned wave power **(a)**, wave direction **(b)**, MMSL **(c)**, and waterline position **(d)** as functions of the alongshore position along the NAWC. Wave power P_{wave} is calculated as $P_{wave} = \rho g H_s^2 T_p/(64\pi)$ where H_s and T_p are the monthly averaged significant wave height and peak wave period, respectively, and provided by ERA5 (*ECMWF, 2020*).

although the timing of peak levels varies regionally. In the PNW and northern NCA, MMSL peaks in winter and reaches its minimum in summer. Further south, from southern NCA to southern BCS, the seasonal peak shifts, with higher sea levels in spring and lower levels in fall. The amplitude of this seasonal cycle gradually increases toward the southernmost extent of the NAWC.

Waterline position generally follows the seasonal pattern of wave power, with wider beaches in summer and narrower beaches in winter along the PNW, NCA, northern SCA, and BC. In southern SCA, however, the seasonal cycle of waterline position is weaker and spatially less uniform, reflecting the reduced amplitude of seasonal wave power fluctuations. In BCS, the seasonal pattern differs: the widest beaches occur in winter and spring, and the narrowest in summer and fall. A moderate but significant correlation is observed between latitude and seasonal waterline excursion ($R = 0.40$, $p < 0.01$), indicating that higher latitudes generally experience greater seasonal variability in waterline position.

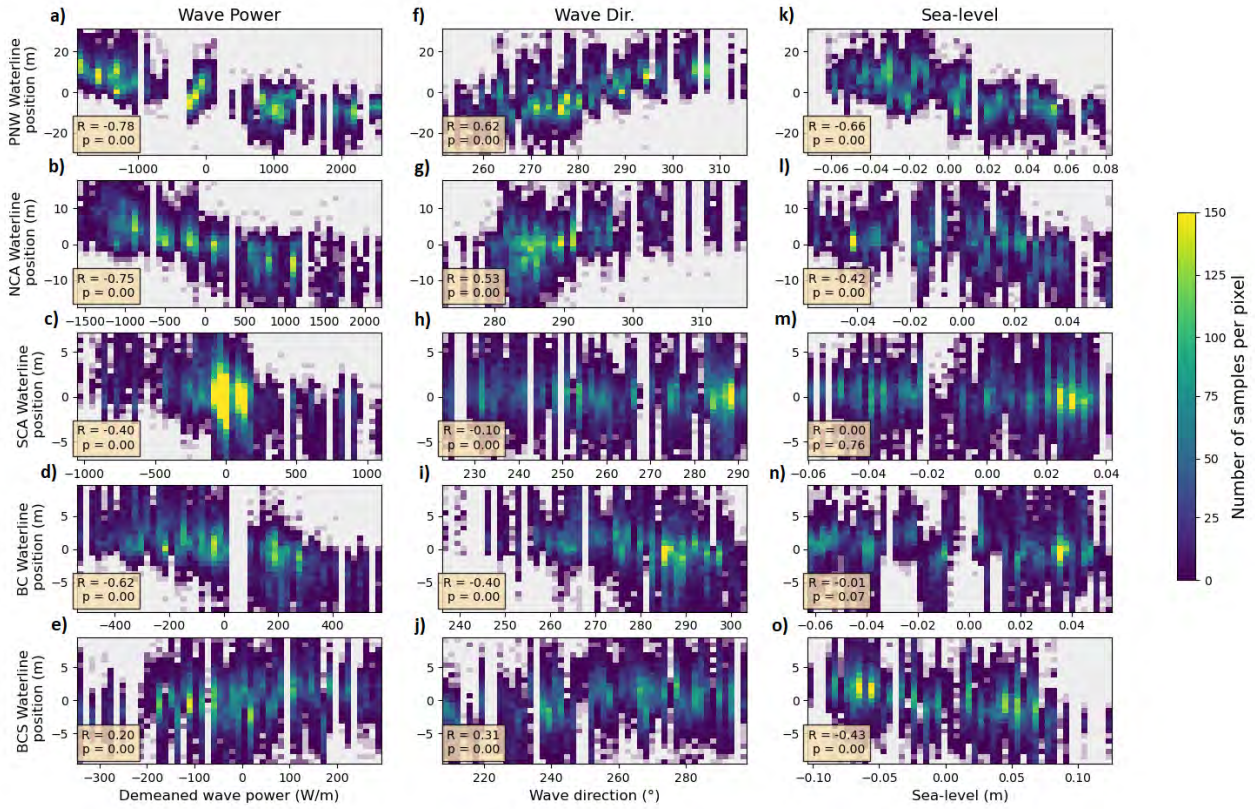

FIGURE III.8 Density plots showing the relation between seasonal cycles of waterline position and **(a-e)** deameaned wave power, **(f-j)** wave direction, **(k-o)** sea-level anomalies for each transect of the 5 subregion of the NAWC. Pearson correlations and associated significance levels are also displayed.

To quantify the relationship between seasonal waterline excursions and their potential drivers, Figure III.8 illustrates the relations between waterline position and each driver across the five subregions. In PNW, waterline position shows moderate-to-strong correlations with wave power, wave direction, and MMSL ($R = -0.78$, 0.62, and -0.66, respectively). Similar but slightly weaker correlations are observed in NCA ($R = -0.75$, 0.53, and -0.42, in the same order). In SCA, wave power shows moderate correlations with waterline position ($R = -0.40$), while wave direction and MMSL exhibit weak correlations (-0.10 and 0.00, respectively). Along BC, both wave power and wave direction show moderate and significant correlations with waterline position ($R = -0.62$ and -0.40), whereas in BCS, correlations remain weak-to-moderate, with the strongest correlation observed for MMSL ($R = -0.43$). All correlations are found to be significant at a 1% significance level ($p - value < 0.01$), except for correlations between MMSL and waterline positions in SCA and BC ($p - value > 0.05$).

A supplementary analysis of intercorrelations among the drivers, shown Figure III.9, indicates that in the PNW and NCA, wave power, wave direction, and MMSL are moderately-to-strongly inter-correlated (PNW : $0.59 < |R| < 0.92$; NCA : $0.40 < |R| < 0.68$), suggesting a coherent seasonal forcing. Conversely, in SCA, BC, and BCS, the three drivers exhibit weak interdependence, reflecting a more complex and spatially variable set of forcing mechanisms, except in BC where wave power and direction are strongly correlated ($R = 0.68$), highlighting this seasonal switch between stronger North Pacific swells in winter and weaker South Pacific swells in summer experienced by the norther part of the region.

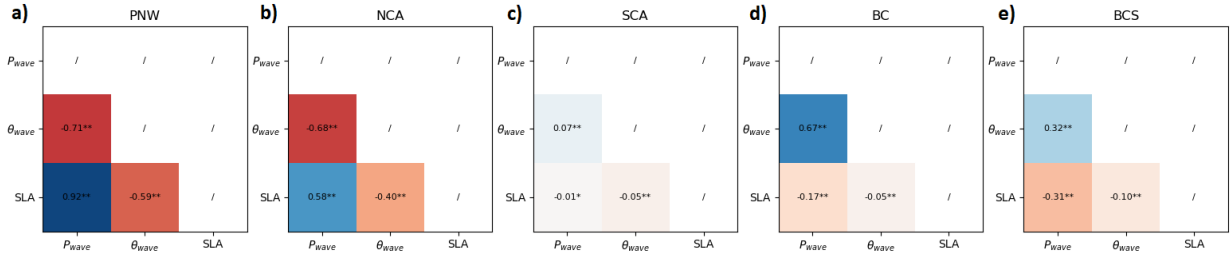

FIGURE III.9 Heatmaps showing the Pearson's correlations between seasonal cycles of wave power, wave direction and sea-level, gathered per subregions. Correlation significant at a 5% (1%) significance level are marked with "*" ("**").

III.3.3 Interannual variability and ENSO-driven hydro-morphodynamics

The sum of the trend (X_{trend}) and seasonal cycle (X_{season}) explains, on average, about 35% of the variance in cross-shore waterline position (X_w) along the NAWC (see Methods), leaving roughly two-thirds of the variability unexplained. While this unexplained variance can arise from multiple sources, the monthly sampling and rigorous post-processing applied to remove noise unrelated to coastal dynamics suggest that a substantial portion reflects interannual to decadal waterline variability, likely driven by climate modes. To explore this, we analyze waterline position anomalies—detrended and cleared of the monthly climatology—at interannual to decadal scales. Given the prominence of the 1997–1998 El Niño event, we extend the analysis period from 2000–2022 to 1997–2022. Due to data scarcity between 1997 and 2000, approximately 1,000 transects along the NAWC are discarded.

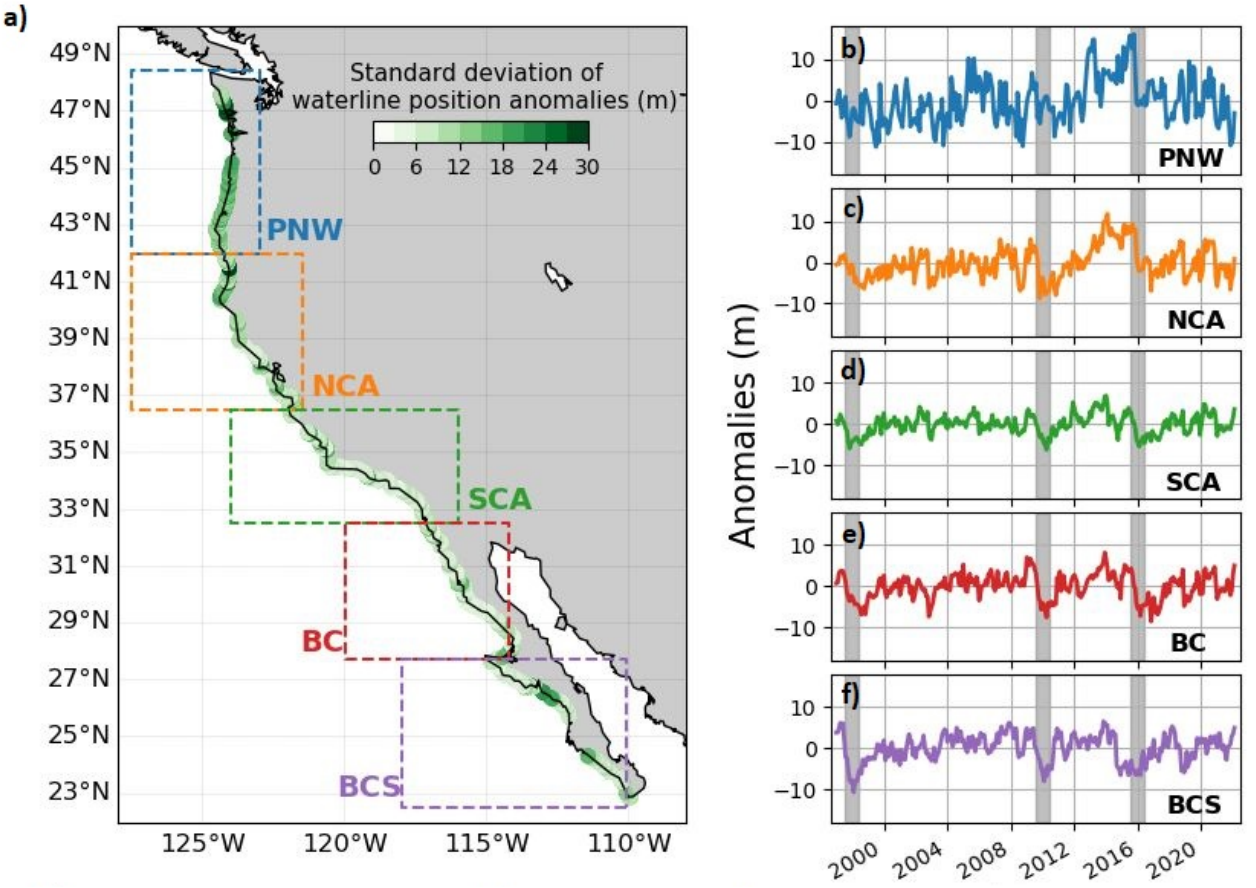

FIGURE III.10 **(a)** Distribution of interannual waterline variability calculated as the the standard deviation of the anomalies between 1997-2022. **(b-f)** Regionally averaged waterline position anomalies along the **(b)** PNW, **(c)** NCA, **(d)** SCA, **(e)** BC and **(f)** BCS regions. Shaded areas on panels b-f highlight the occurence of El Niño events (also refer to Figure III.11), here coinciding with drops in the anomalies in most regions. The background map was generated using Python's mpl_toolkits.basemap library.

Figure III.10 illustrates the behavior of waterline position anomalies along the NAWC from 1997 to 2022. Panel a highlights a latitude-dependent pattern of interannual variability, quantified as the standard deviation of the anomalies over this period. A moderate positive correlation with latitude is observed ($R = 0.37$), indicating that northern regions tend to be more dynamic. Consistent with the seasonal patterns described previously, the PNW and northern NCA exhibit the largest interannual variability, while the southern regions show comparatively subdued fluctuations. Panels b–f present regional averages of the waterline position anomalies, emphasizing the pronounced variability in the PNW and NCA. In contrast, the SCA, BC, and BCS regions exhibit relatively stable anomalies, punctuated only by occasional erosive events followed by recovery.

Across the three southern regions, three major events are clearly evident in the waterline

anomaly time series: the winters of 1997/1998, 2009/2010, and 2015/2016. Figure III.11 shows the evolution of the CP, EP, and MEI indices between 1997 and 2022, revealing that these waterline change events coincide with the main El Niño episodes of the study period: the strong EP peak of 1997/1998, the CP peak of 2009/2010, and the combined EP/CP peaks of 2015/2016, all reflected in peaks of the MEI time series. Smaller events, such as the minor 2002/2003 El Niño, also correspond to modest drops in waterline anomalies along the NAWC.

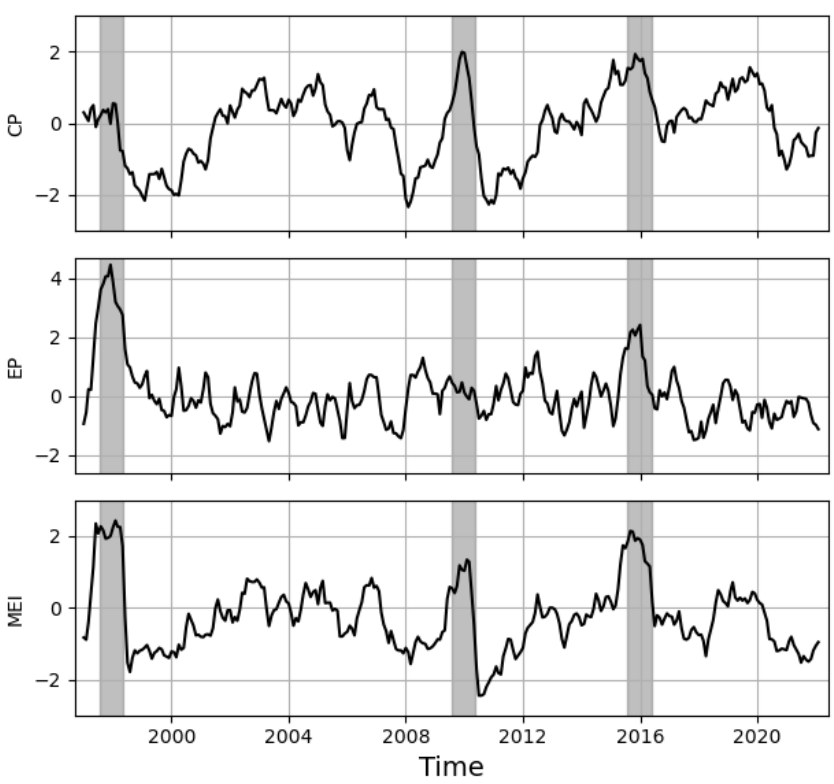

FIGURE III.11 Time series of CP, EP and MEI indices between 1997-2022. The 3 major El Niño events that occured between 1997-2022 are highlighted in grey (same shaded areas as in Figure III.10).

While El Niño events produce pronounced erosion anomalies in the PNW and NCA, their effect on driving regionally averaged anomalies to strongly negative values is less marked than in the southern regions. This suggests that in northern regions, ENSO-related variability is modulated by longer-term coastal dynamics. This pattern is particularly clear during 2011–2016, when regionally averaged waterline anomalies in both the PNW and NCA gradually increased before a sharp decline coinciding with the 2015/2016 El Niño.

Linear regressions between climate modes and regionally averaged anomalies of waterline position reveal intriguing yet modest correlations that merit attention. Notably, waterline anomalies

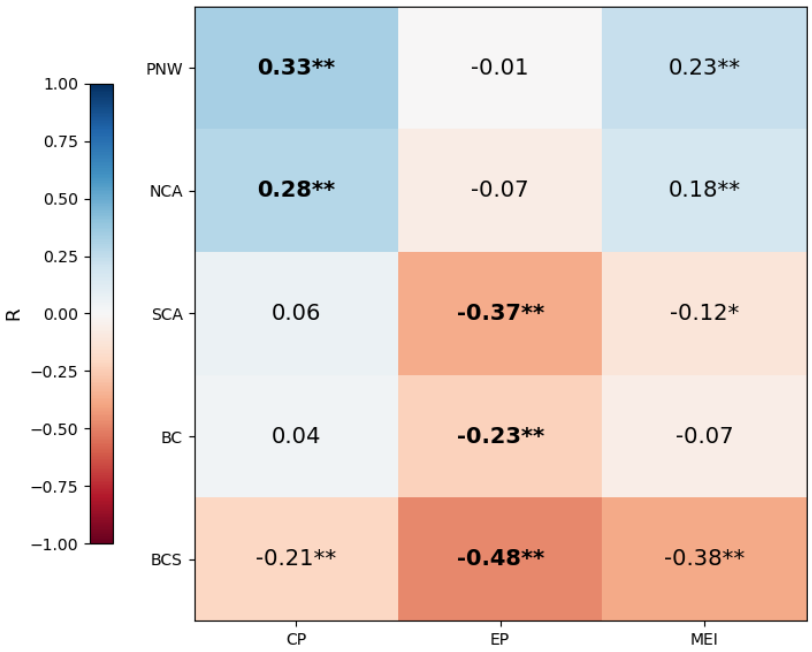

FIGURE III.12 Heatmap of Pearson correlations between regionally averaged waterline anomalies and CP, EP and MEI indices.

in the SCA, BC, and BCS regions exhibit an negative correlation with the EP index, with correlation coefficients of -0.37, -0.23, and -0.48, respectively ($p-value$<0.01). In contrast, the NCA and PNW regions show no significant correlation with the EP index. Conversely, weak-to-moderate correlations emerge between waterline anomalies in the PNW, NCA and BCS and the CP index, yielding coefficients of 0.33 and 0.28, respectively ($p-value$<0.01), while SCA and BC remain largely uncorrelated or exhibit weak and non-significant correlations with this index. The MEI index, integrating both EP and CP flavors show weaker (stronger) correlations than EP (CP) along SCA, BC and BCS ($R = -0.37, -0.23, -0.48$) and reversely along the PNW and NCA ($R = 0.23$, 0.18).

Although the correlations presented are weak and do not imply causality, they suggest potential relationships between waterline anomalies and climate modes. Notably, positive extremes in ENSO indices correspond to pronounced drops in waterline anomalies, indicating that strong El Niño events influence shoreline variability. To assess the robustness of this observation, waterline anomalies are categorized into three ENSO phases: El Niño (MEI > 1), La Niña (MEI < -1), and neutral conditions (remaining values). Using the neutral phase as a reference, we apply a Signal-to-Noise Ratio (SNR) analysis to quantify the influence of ENSO on waterline positions.

To reduce the influence of longer-term variability, particularly in the PNW and NCA, and to homogenize transect-specific differences, waterline anomaly time series are seasonally sampled, scaled by their standard deviation, and analyzed as changes relative to the previous season rather than as absolute anomalies. Values of SNR close to zero indicate minimal influence of the considered ENSO phase on anomaly changes.

Figure III.13 shows the distributions of these classified anomalies and their SNR scores, considering all seasons and winter (DJF) anomalies specifically. Figure B.1 provides corresponding results for spring, summer, and fall. A notable first observation is that SNR scores are generally higher for winter-only anomalies compared to all-season anomalies, except for La Niña in the PNW, where SNR remains weak but slightly higher for all-season values.

Focusing on winter anomalies, clear regional differences emerge: SCA, BC, and BCS exhibit higher SNR_{nino} values (0.65, 0.84, and 0.82) than the PNW and NCA (0.37 and 0.39), and higher SNR_{nina} values (0.35, 0.35, 0.43) compared to 0.05 and 0.07 for the PNW and NCA, respectively. These contrasts highlight the stronger and more coherent responses of southern subregions to El Niño and La Niña relative to the northern subregions.

This disparity in waterline response can be partially explained by the wave climate response along the NAWC to ENSO activity. Figure III.14 illustrates the region-dependent response of coastal wave climate to ENSO. The four panels represent the winter-averaged wave power between 1997 and 2022 (computed from monthly sampled ERA5 wave product) compared to the winter-averaged MEI index -quantifying the intensity of ENSO in the equatorial Pacific- at four distinct locations : Long Beach, WA, USA; Monterey, CA, USA; Torrey Pines, CA, USA; Playa el Suspiro, BCS, Mexico. Pearson's correlations between wave power and MEI are indicated, along with the associated p-values. The three southernmost sites (panels b-d) exhibit moderate and significant (95% level a significance) correlations between winter-averaged wave power and MEI, while the northernmost one (panel a) exhibits a weak and insignificant correlation. At each sites, the 2 winters associated with high MEI values (MEI>1.5 : 1997/1998 and 2015/2016) yield high wave power. At Long Beach, a La Niña event (not the largest, MEI $\sim$ -1) is associated with the

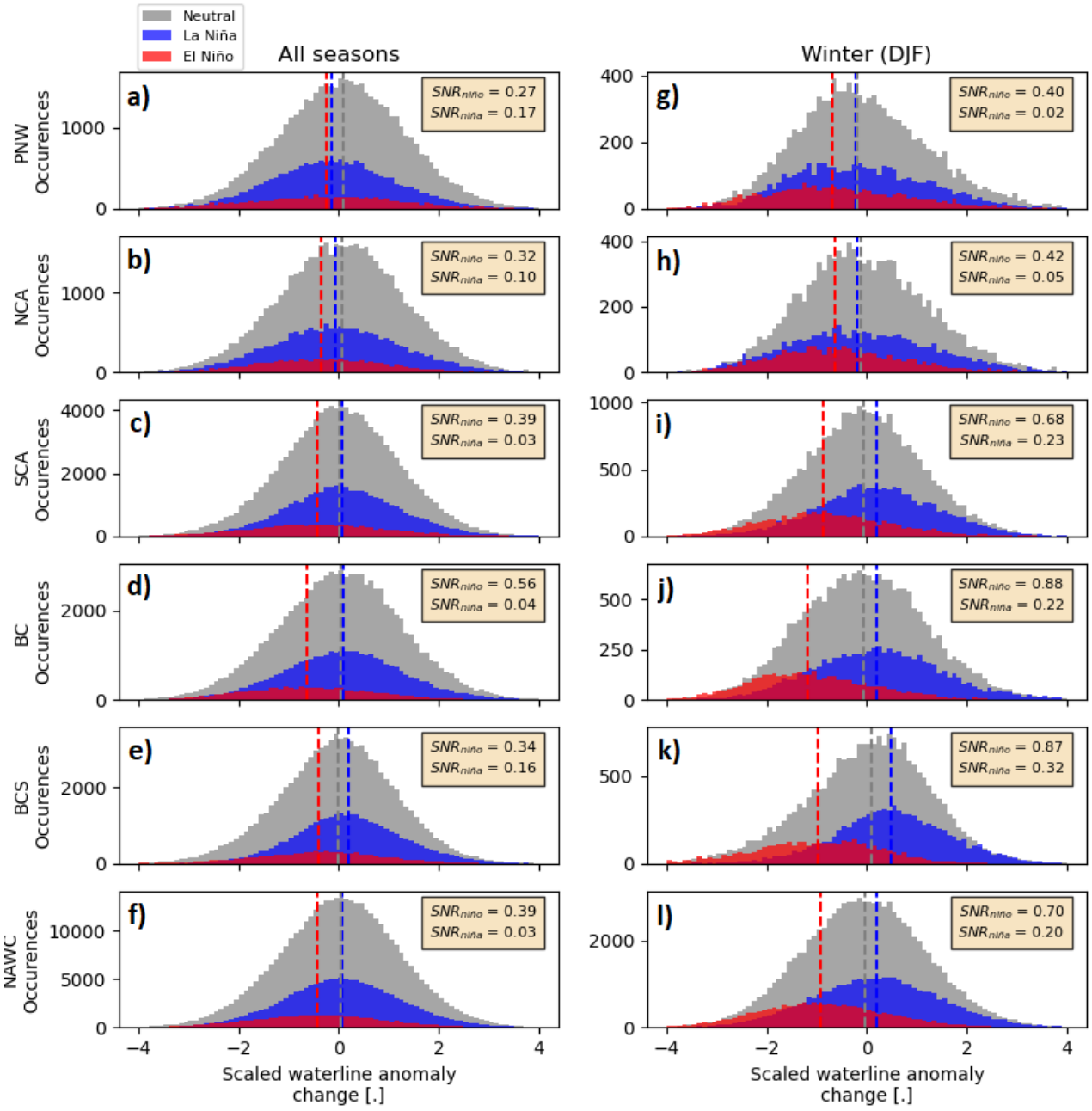

FIGURE III.13 Distributions of waterline anomaly change during ENSO neutral (grey), El Niño (red) and La Niña (blue) phases for **(a-f)** all seasons and **(g-l)** winters along each subregion and the whole NAWC. Waterline anomaly changes are computed at each transect by measuring the difference between the seasonally averaged waterline position anomaly of a given season and that of two seasons earlier. The SNR for El Niño and La Niña phases relatively to neutral ENSO-phases, and calculated as the differences of the median of the distribution of waterline anomaly change between El Niño (or La Niña) and neutral ENSO-phases, scaled by the standard deviation of neutral ENSO-phases.

highest seasonal wave power of 1997-2022. For most of the winters, MEI values are concentrated between -1 and 1, and exhibit not obvious pattern of influence of MEI on wave power.

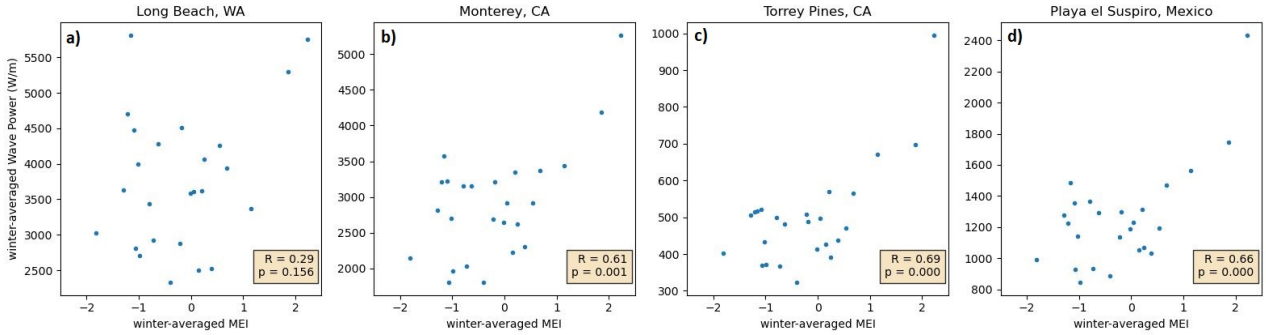

FIGURE III.14 Relationship between ENSO activity, represented by the winter-averaged MEI, and winter-averaged wave energy (at the 4 sites described in Figure 1 in the main manuscript). Winter-averaged wave power is calculated as $P_{\text{wave}} = \rho g^2 H_s^2 T_p/(64\pi)$, where H_s is the significant wave height and T_p is the peak period (data from ERA5, see Figure 1 in the main manuscript for the ERA5 nodes locations). Pearson correlations and associated significance levels are also displayed.

These results further emphasize the non-linear and spatially variable influence of ENSO on wave power along the NAWC. Only extreme El Niño events appear to generate substantially increased wave power capable of driving significant waterline retreat, whereas most intermediate MEI values have little to no impact, or only marginal effects. Moreover, the response of the coast to ENSO forcing shows a clear latitudinal dependency. To provide a comprehensive picture of these contrasted influences, cascading from deep-ocean forcing to coastal response, we introduce Figure III.15, which presents composites of waterline anomalies during winters from 1997 to 2022 under El Niño, La Niña, and neutral conditions. Table III.2 further summarizes these responses by reporting quartile statistics of anomaly changes for each NAWC subregion.

Figure III.15a–c illustrates the average winter (DJF) responses to El Niño, neutral, and La Niña conditions over the period 1997–2022. These responses are presented as composites of winter-averaged wave power anomalies (scaled by their mean winter values between 1997–2022) and winter-averaged waterline position anomaly changes (scaled at each transect by the local mean seasonal waterline excursion, as shown in Figure III.6). El Niño (La Niña) winters are defined as seasons with a mean $MEI > 1$ ($MEI < -1$), identifying 1997/1998, 2009/2010, and 2015/2016 as El Niño winters, and 1998/1999, 1999/2000, 2007/2008, 2010/2011, 2011/2012, 2020/2021, and 2021/2022 as La Niña winters.

During El Niño winters, positive wave power anomalies are pronounced along the entire NAWC, increasing by 30–50% relative to mean winter conditions. This increase coincides with markedly

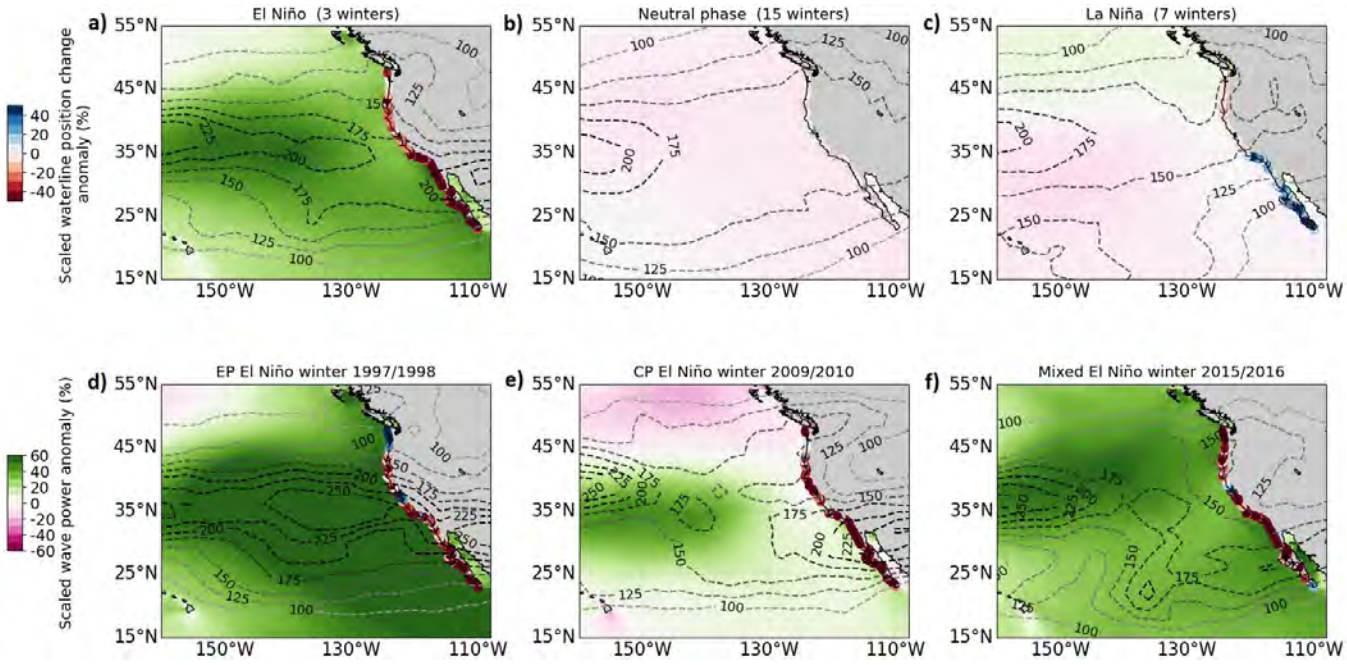

FIGURE III.15 Composites of hydrodynamic and morphological responses to (a-c) ENSO phases and (d-f) the strongest El Niño events during winter (DJF) over 1997-2022. The figure shows spatial distributions of winter waterline position anomalies changes relatively to the summer (JJA) and wave power anomalies (scaled by their standard deviation), along with 200 hPa EKE contours, proxy for storminess and storm tracks position. Waterline position anomalies are scaled by their seasonal cycle amplitude to highlight the magnitude of the anomalies relative to the seasonal cycle. The background map was generated using Python's mpl_toolkits.basemap library.

negative waterline position anomalies, with scaled values ranging from -83% to -18% (first and third quartiles), particularly evident in SCA, BC, and BCS. In neutral winters, wave power anomalies are slightly negative (-8% to -10%), accompanied by minimal waterline position changes (-11% to +7%). La Niña winters display slightly negative wave power anomalies (-1% to -5%) along SCA, BC, and BCS, corresponding to positive waterline position changes (SCA: +1% to +40%; BC: 0% to +30%; BCS: +14% to +51%). Meanwhile, the PNW and NCA exhibit mild positive wave power anomalies (+0% to +8%), with slightly negative waterline position anomalies (PNW: -22% to +6%; NCA: -21% to +14%).

Panels d–f further analyze the distinct responses of the three El Niño winters ($MEI > 1$) between 1997 and 2022, representing different El Niño types: 1997/1998 (Eastern Pacific, EP), 2009/2010 (Central Pacific, CP or Modoki), and 2015/2016 (mixed EP/CP). The EP El Niño exhibits strong positive wave power anomalies (+48% to +93%) along the NAWC, with negative waterline position anomalies across nearly all transects (-98% to +8%), except in the PNW where northern sections experience predominantly positive anomalies (-58% to +31%). The CP El Niño

shows weaker wave power anomalies (+0% to +30% along NCA to BCS; -1% to -11% in PNW) with almost uniformly negative waterline anomalies (-101% to -10%), slightly weaker and more variable in the PNW (-65% to +24%). The mixed EP/CP El Niño generates widespread positive wave power anomalies, especially offshore of the PNW and NCA (+40% to +50%), and a spatially uniform negative waterline response (-101% to 0%), except in NCA (-69% to +11%) where a small region exhibits positive anomalies.

Storm track intensity and position, that can be estimated using upper-level (200 hPa) Eddy Kinetic Energy (EKE, Chang et al. (2002); Hoskins and Valdes (1990)) derived from 14-day high-pass filtered winds, strongly influence wave power anomalies and coastal responses. Higher EKE values indicate stronger transient eddies and increased storm activity. During neutral winters, storm tracks weaken approaching the NAWC, with EKE decreasing from 200 m^2/s^2 over the central North Pacific (35°N, 160°W) to below 175 m^2/s^2 near the coast. La Niña winters exhibit a slight northward shift in storm tracks with reduced southern EKE (125–150 m^2/s^2 in SCA to <100 m^2/s^2 in BCS), aligning with positive waterline anomalies in southern regions. El Niño winters feature intensified and southward-shifted storm tracks, with coastal EKE peaking along BC (>200 m^2/s^2) and the 150 m^2/s^2 contour extending from BCS to NCA. The 1997/1998 EP event shows very intense storm tracks (200–250 m^2/s^2), while the 2009/2010 CP and 2015/2016 mixed events display a southward meander reaching BC and BCS with EKE >200 m^2/s^2.

TABLE III.2 Range of first to third quartiles of scaled winter-averaged waterline position anomaly changes (%) for each ENSO phase, sorted by NAWC subregion (including the entire NAWC). Negative (positive) values indicate landward (seaward) deviations relative to the 1997–2022 average.

	El Niño ($MEI > 1$)	**Neutral ($\|MEI\| < 1$)**	**La Niña ($MEI < -1$)**
PNW	-53 to -4 %	-12 to +6 %	-22 to +6 %
NCA	-49 to -4 %	-10 to +7 %	-21 to +14 %
SCA	-91 to -21 %	-14 to +6 %	+1 to +40 %
BC	-90 to -25 %	-9 to +7 %	0 to +30 %
BCS	-94 to -32 %	-8 to +8 %	+14 to +51 %
NAWC	-82 to -18 %	-11 to +7 %	-3 to +34 %

Figure B.2 in the Appendix B presents the spatial distribution of sea-level anomalies, instead of of the scaled wave power anomalies shown in Figure III.15. FiguresB.3 and B.4 in Appendix B illustrate coastal responses to ENSO phases, analogous to Figures III.15 and B.B.2, but using a reduced threshold ($MEI = \pm 0.5$) to classify ENSO phases.

III.4 Discussion

The SDW data analyzed along the North American West Coast (NAWC) reveal clear spatiotemporal patterns in shoreline variability. At the seasonal scale, waterline retreat in winter and advance in summer generally aligns with fluctuations in wave power, with moderate-to-strong correlations ($0.62 < |R| < 0.78$) across the PNW, NCA, and BC. These results corroborate prior studies documenting strong seasonal shoreline response to wave climate, including Ruggiero et al. (2005) along the PNW coast, Vitousek et al. (2023b) for NCA, and Ruiz de Alegría-Arzaburu et al. (2022a,b) for Baja California. Mechanistically, this is consistent with the classical understanding of cross-shore sediment transport driving seasonal profile adjustments (Wright and Short (1984)) and recent regional analyses in California demonstrating wave-driven seasonal shoreline cycles (Warrick et al. (2025b)).

In contrast, SCA and BCS exhibit weaker or spatially heterogeneous seasonal signals, consistent with prior observations of complex coastal responses in pocketed or rotated beach systems (Warrick et al. (2025b,a)). Seasonal variability in BCS appears influenced by episodic storm activity and seasonal sea-level variations ($\sim$ 25 cm), in line with Franco-Ochoa et al. (2020) who documented hurricane-season storm impacts on Mexican Pacific beaches. The influence of riverine sediment supply, while recognized as important for coastal morphodynamics (Barnard and Warrick (2010); Warrick et al. (2023)), remains difficult to quantify at the seasonal scale due to its sporadic nature and localized magnitude.

At the interannual scale, El Niño events consistently produce extreme shoreline retreat, echoing the findings of Barnard et al. (2017) for the U.S. West Coast, Ruiz de Alegría-Arzaburu and Vidal-Ruiz (2018); Ruiz de Alegría-Arzaburu et al. (2025) for Baja California, and Vos et al. (2023a) for broader Pacific Ocean-scale assessments. Conversely, La Niña winters produce more moderate effects, confirming the asymmetry in ENSO-related coastal responses documented in prior studies (Vos et al. (2023a)). Linear correlations between ENSO indices and regional waterline anomalies are generally weak to moderate ($0.23 < |R| < 0.48$), reflecting heterogeneous geomorphic and exposure conditions (Anderson et al. (2018); Stevens et al. (2024)). Signal-to-noise analyses reinforce a latitude-dependent ENSO response, with stronger impacts in southern regions, in

agreement with observations of episodic El Niño-driven erosion events (Barnard et al. (2017); Ruggiero et al. (2005)).

ENSO influences on wave climate are mediated via storm-track shifts, affecting the frequency, intensity, and trajectory of extratropical cyclones. The differential impacts of EP vs. CP El Niño events on regional wave energy and sea-level anomalies are consistent with prior studies linking El Niño diversity to coastal erosion patterns (Barnard et al. (2011, 2017)). Other climate modes, including PDO, interact with ENSO to modulate interannual variability, echoing conclusions from Allan and Komar (2002a, 2006). This interplay highlights the necessity of considering multiple climate drivers when interpreting interannual shoreline variability (Almar et al. (2023); Odériz et al. (2024)).

As illustrated in the previous chapter, SDW data carry inherent uncertainties, particularly at gently sloped or meso-to-macrotidal sites (Castelle et al. (2021); Konstantinou et al. (2023); Graffin et al. (2023); Vos et al. (2023b)). Validation against in-situ datasets at Torrey Pines (Ludka et al. (2019)) and Ensenada (Ruiz de Alegría-Arzaburu et al. (2022a)) confirms strong agreement ($\sim$ 10 m standard error). Aggregating measurements at monthly or seasonal scales reduces noise, as suggested in earlier regional studies (Warrick et al. (2025b)), allowing the characterization of seasonal and interannual range of variability. while While wave, wind, and sea-level datasets provide valuable information on regional-scale forcing, their coarse spatial and temporal resolution limits their ability to capture nearshore, short-lived events such as individual storms, wave setup, or localized surge, which can drive rapid, event-scale shoreline changes. These limitations might explain the apparent mismatch in BCS, where seasonal waterline retreat overlaps with the Eastern Pacific Hurricane season (Gunther and Cross (1984)) exposing the Pacific Mexican coast to storms (Franco-Ochoa et al. (2020)), yet no clear signal is observed in the monthly wave power data. In other words, episodic storm-driven forcing could be contributing to shoreline retreat, but remains unresolved in the coarse datasets, highlighting the need for higher-resolution observations or models to fully assess the role of short-lived, localized events on seasonal waterline variability in this region. Future studies incorporating high-resolution observations or models could help link these fine-scale processes to observed waterline variability.

III.5 Chapter Conclusion

This study provides new insights into the seasonal and interannual variability of shoreline dynamics along the NAWC, leveraging 25 years of SDW observations. Seasonal shoreline fluctuations exhibit a clear latitudinal structure: the PNW, NCA, and BC respond strongly to seasonal wave power variability, while SCA and BCS display heterogeneous or weaker correlations, suggesting that local morphology, seasonal sea-level changes, and episodic storm activity exert greater influence.

At interannual scales, shoreline variability is dominated by ENSO-related climate forcing. El Niño events induce widespread erosion, particularly in California and Baja California, whereas La Niña phases produce more muted and regionally variable signals. However, these responses are not uniform: in the PNW and NCA, shoreline response to ENSO is more complex and less linear, reflecting a balance between two competing mechanisms: the intensification of storm tracks, which tends to enhance shoreline retreat, and their southward displacement, which can reduce storm exposure in the northern regions. In contrast, SCA, BC, and BCS demonstrate more symmetrical El Niño–La Niña responses, though with reduced amplitudes during La Niña. Statistical analysis (correlations and SNR) and validation against in-situ datasets confirms that SDW approaches are sufficiently robust to detect these climate-driven signals in shoreline variability.

These findings establish a framework for applying automated, large-scale SDW analysis to characterize coastal dynamics over seasonal to interannual timescales. Yet, shoreline position remains a single-metric representation of intertidal variability. To better understand how waterline change reflects broader morphodynamics, future research must integrate shoreline observations within the full topography–bathymetry continuum.

The next chapter addresses this challenge by contextualizing shoreline variability within the larger beach system, using decadal intertidal profile datasets to evaluate the representativeness and limitations of shoreline-derived indicators for capturing morphological evolution.

Chapter IV

The shoreline behaviour among the complex beach system

This chapter examines the inherent ambiguities of shoreline proxies and their ability to represent beach-scale morphodynamics. The analysis is based exclusively on high-resolution ground-truth datasets from intensively monitored sites, thereby minimizing measurement uncertainties and facilitating clearer interpretation of results and conclusions.

Contents

IV.1 Introduction . . . 115

IV.2 Methods . . . 117
IV.2.1 Beach profiles and derived proxies . . . 117
IV.2.2 Temporal decomposition of coastal indicators . . . 121
IV.2.3 Modeling of Beach Profile Changes . . . 122
IV.2.4 Statistical Analysis . . . 123
IV.2.5 Additional Data . . . 124

IV.3 Results . . . 124
IV.3.1 Waterline and shoreline variability . . . 124
IV.3.2 Representativeness of shoreline proxies in describing intertidal beach morphodynamics . . . 127
IV.3.3 The 3D intertidal profile variability . . . 130

IV.4 Discussion . . . 135

IV.5 Chapter Conclusion . . . 138

IV.1 Introduction

Large-scale applications of Satellite-Derived Waterlines (SDW) and Shorelines (SDS) have recently opened new avenues for assessing shoreline change at continental to global scales. These datasets, produced through standardized algorithms applied to multispectral satellite imagery,

have made it possible to observe seasonal to multi-decadal patterns of coastal change, at spatial scales that were previously unattainable (Luijendijk et al. (2018); Vos et al. (2023a); Almar et al. (2023); refer also to the previous chapter). They provide critical insights into how beaches respond to climate variability, sea-level rise, and extreme events, especially in data-scarce regions where in-situ monitoring is sparse or absent. By reducing the complexity of beach morphology to a single two-dimensional contour, SDS approaches deliver intuitive, scalable, and globally consistent shoreline indicators, enabling large-scale comparative analyses that are central for understanding climate-driven coastal change.

However, this simplification comes at a cost. The shoreline, whether derived from a datum (e.g., MSL) or used as a proxy (e.g., the waterline), is only one expression of a highly dynamic and three-dimensional beach system. Waterline displacements observed in SDW time series may arise not only from sediment redistribution and morphological adjustment, but also from hydrodynamic processes and sea-level variability at a range of scales (from tidal to interannual). Moreover, the intertidal beach does not evolve uniformly (e.g., Stive et al. (2002); Konstantinou et al. (2023)): its profile may shift seaward or landward through translation, rotate through slope adjustment, or be modulated by transient changes in coastal sea level. These mechansisms are illustrated on Figure IV.1. Such non-homogeneous adjustments mean that shoreline proxies cannot always be directly extrapolated to infer volumetric or morphological changes across the beach-dune system. This ambiguity highlights both the opportunities and the challenges of using SDS as a standalone coastal monitoring tool.

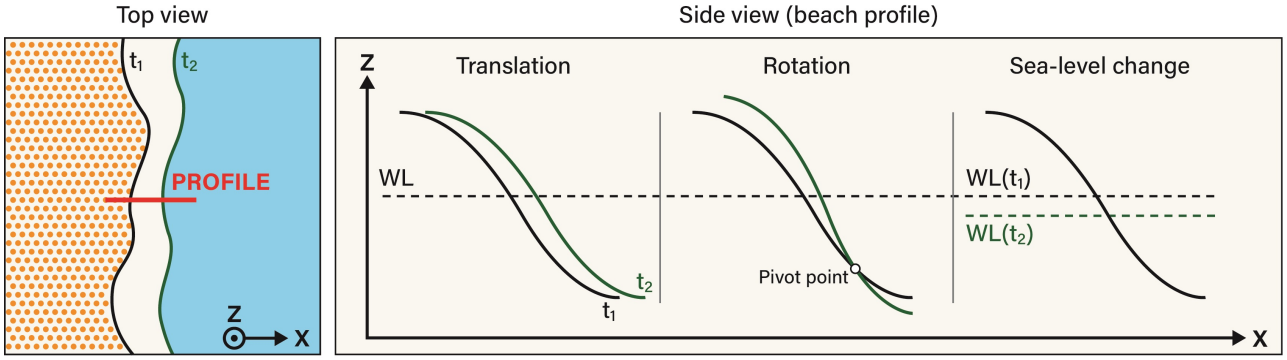

FIGURE IV.1 Schematic representation of the mechanisms behind a visible displacement of the waterline position : 1. profile translation; 2. profile rotation; 3. change of the coastal sea-level.

To better interpret shoreline signals in SDS datasets, it is necessary to investigate the underlying morphodynamic processes at more local scales, where higher-resolution in-situ data are available. In this study, we therefore complement the continental-scale SDW analysis with an in-depth examination of intertidal beach morphodynamics at four well-monitored meso- to macro-tidal sites (Perranporth, Porsmilin, Torrey Pines, and Truc Vert). These sites, which benefit from frequent topographic surveys over more than a decade (McCarroll et al. (2023); Bertin et al. (2022); Ludka et al. (2019); Castelle et al. (2020)), provide a unique opportunity to disentangle the different contributions to shoreline change. Specifically, we compare proxy-based waterlines (defined as the intersection between the beach profile and the monthly mean sea-level elevation) with datum-based 0 m shorelines and with volumetric changes in the intertidal beach. By doing so, we are able to assess (1) how seasonal and interannual sea-level fluctuations affect the interpretation of proxy-based shoreline signals, (2) to what extent shoreline displacements represent the volumetric variability of the intertidal beach, and (3) whether the observed profile changes can be decomposed into simple mechanisms of translation and slope adjustment.

Through this dual-scale approach, we aim to highlight the complementarity between SDS-based large-scale monitoring and local process-based studies. While SDS enables consistent observation of coastal change across entire continents, local analyses reveal the morphodynamic mechanisms that underpin shoreline variability and clarify the limits of shoreline proxies. Together, these perspectives advance a more nuanced understanding of coastal evolution: one that acknowledges the power of SDS for global climate assessments, while recognizing the importance of local morphodynamics in ensuring that shoreline indicators are interpreted in a physically meaningful way.

IV.2 Methods

IV.2.1 Beach profiles and derived proxies

Beach profiles considered in this study are from four sites -Perranporth, Porsmilin, Torrey Pines, and Truc Vert- already described in Chapter II. Beach elevation profiles are publicly available (Ludka et al. (2019); Castelle et al. (2020); Bertin et al. (2022); McCarroll et al. (2023)), and

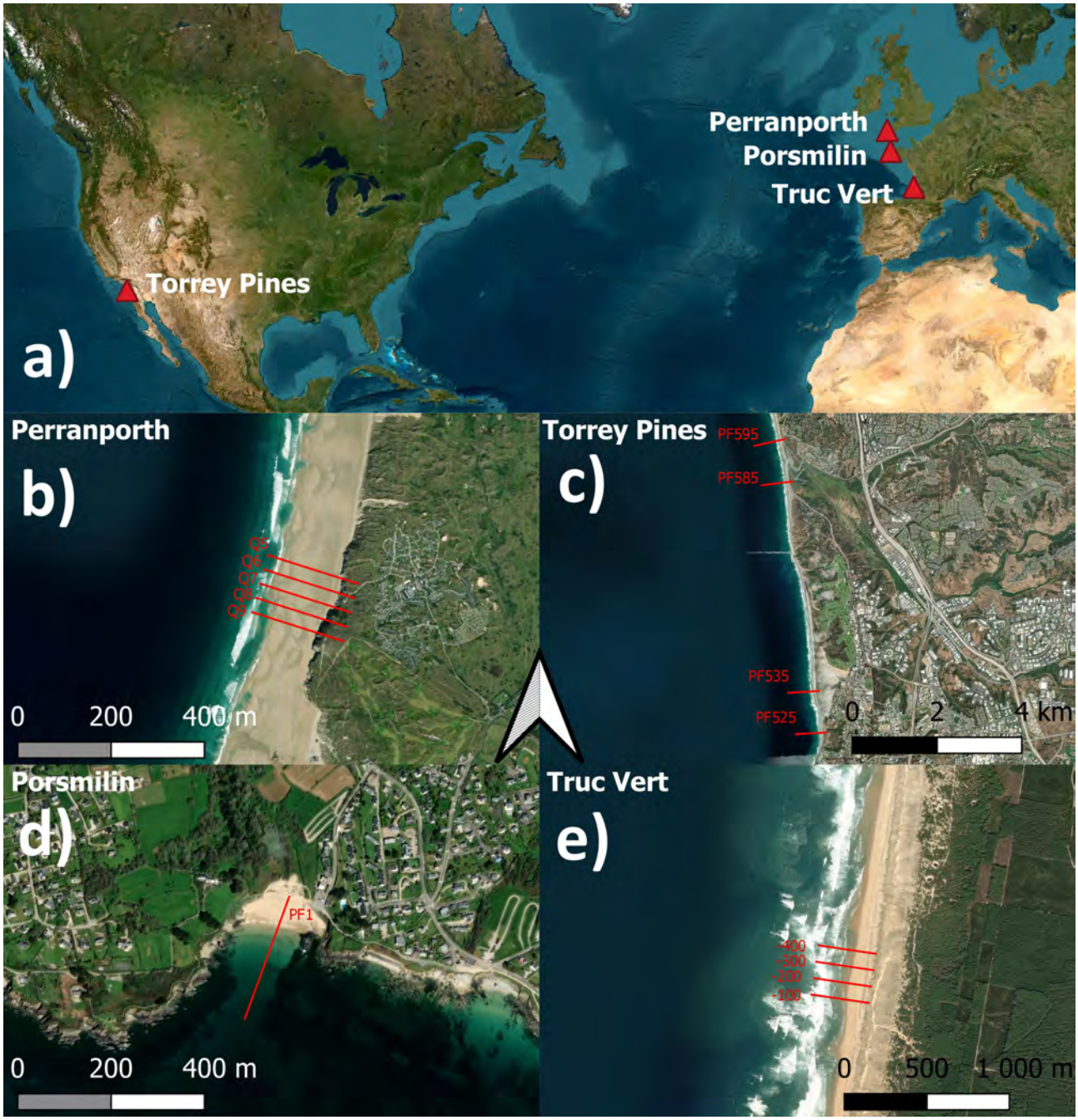

FIGURE IV.2 **a)** Location of the four study sites and **b–e)** corresponding local aerial views: **b)** Perranporth (England), **c)** Porsmilin (France), **d)** Torrey Pines (California, USA), and **e)** Truc Vert (France). Red lines indicate the transects analyzed in this study (panels b–e). Background maps are provided by the ESRI World Imagery basemap.

have been processed the same way to ensure the objectiveness of the study.

- **Definition of the studied system**: In this study, we focus on the intertidal portion of the beach profiles. Although the upper intertidal zone is consistently surveyed, some records lack consistent coverage of the lower intertidal part. We define the usable profile section as

extending from the elevation $z_{\text{up}} = z_{\text{MHW}}$ (mean high water) to $z_{\text{down}} = z_{\text{MSL}} - 0.4 \times (z_{\text{MSL}} - z_{\text{MLW}})$, where MSL and MLW refer to mean sea level and mean low water, respectively. All elevations are expressed relative to local MSL to standardize comparisons across profiles. Beach elevation profiles referenced to other vertical datums (e.g., NAVD88) were adjusted by applying site-specific offsets to align with MSL. The following corrections were used: 0.3 m at Perranporth (Konstantinou et al. (2023)), 0.5 m at Porsmilin (Bertin et al. (2022)), and 0.774 m at Torrey Pines (Vos et al. (2023b)), corresponding to the local differences between the respective datum systems and MSL. Beach elevation profiles at Truc Vert are already provided using the MSL datum (Castelle et al. (2020)).

- **Rationale for lower boundary** z_{down}: This threshold was chosen to achieve a compromise between (i) capturing a sufficiently large portion of the intertidal zone, and (ii) retaining a large number of surveys that cover this range. Additionally, we required this elevation band to present a bijective relationship between elevation and cross-shore position (i.e., each elevation is associated to a single cross-shore position), which ensures robust interpolation in later processing steps.

- **Selection of usable profiles**: Three of the four study sites include multiple monitored cross-shore profiles with varying lengths of record. For consistency across time, we retained only a subset of profiles per site, selected based on their temporal coverage. The goal was to maximize the duration of the common time series across profiles. Selected profiles are shown on Figure IV.2.

- **Gridding the data**: Profiles that met the elevation coverage criteria were interpolated onto a regular grid defined in the elevation-time domain. The vertical resolution of the grid was set to 5 cm, and the temporal resolution to one month.

- **Interpolation procedure**: Elevation data were linearly interpolated along the cross-shore (spatial) dimension, and temporally interpolated using cubic interpolation. Temporal interpolation was only applied to months with missing data if at least 25% of the months in the previous 24-month window were sampled. This constraint aimed to avoid unrealistic extrapolations while allowing interpolation over moderate data gaps.

- **Site-level aggregation**: When several profiles were retained for a given site, we averaged

their gridded representations to produce a single representative elevation-time matrix per site. This averaging helps reduce local noise and emphasize site-scale morphological trends.

The outputs of these pre-processing steps are arrays of cross-shore positions of the beach by elevation and time $X(z,t)$, from which we can subtract the time-averaged position per elevation $\overline{X_t}(z)$ to keep only the temporal variability across elevations. Figure IV.3 shows for the 4 sites the array $X(z,t)$ and $X'(z,t) = X(z,t) - \overline{X_t}(z)$.

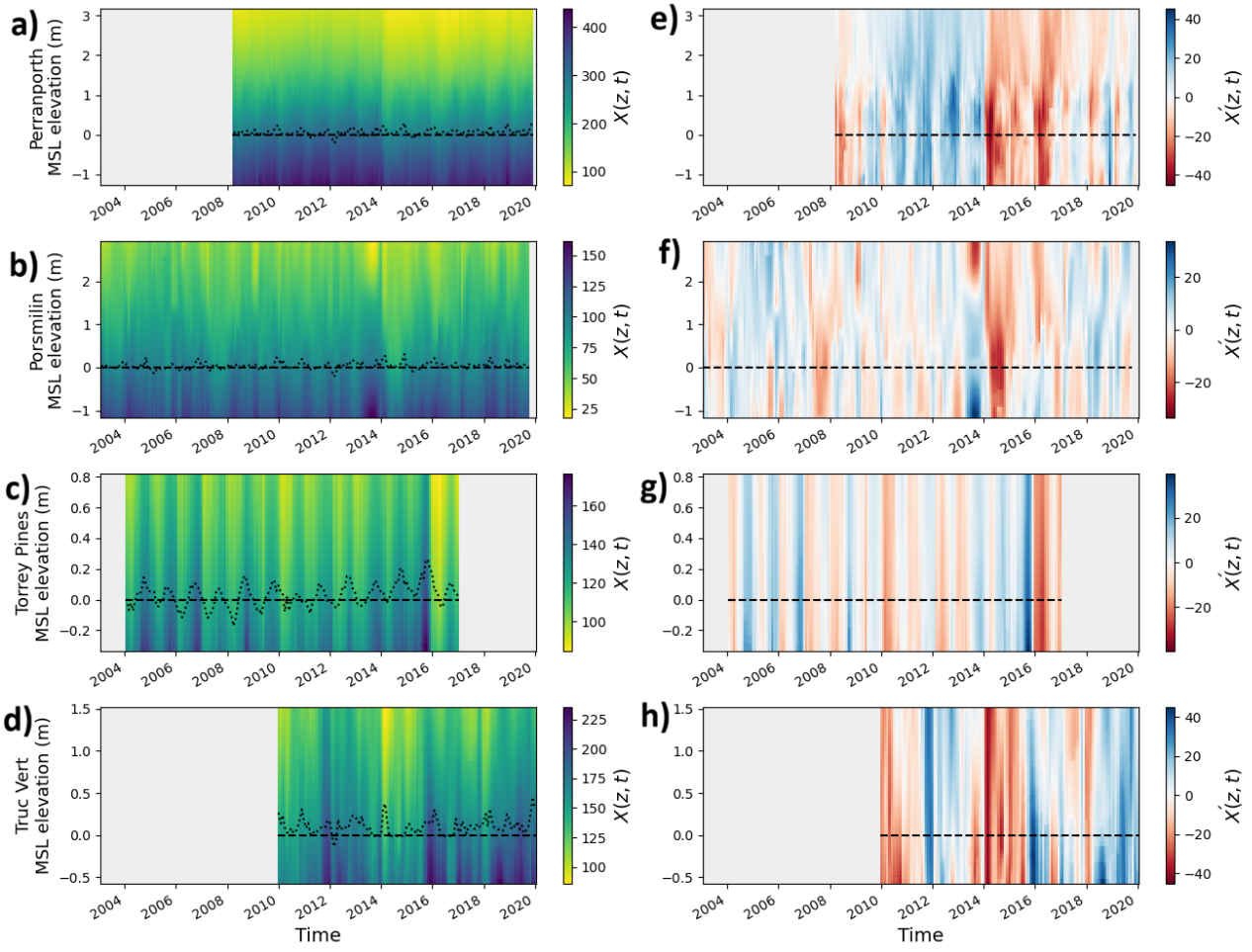

FIGURE IV.3 **a-d)** Timestacks of intertidal beach profiles $X(z,t)$ and **e-h)** their demeaned representations $X'(z,t)$ at the 4 study sites. Profile elevations are reported in MSL datum, the dashed black line highlight the MSL, and the dotted line shows the monthly mean sea-level fluctuations measured by local tide gauges.

IV.2.2 Temporal decomposition of coastal indicators

Temporal variations of any time-dependent variable $Y(t)$ analyzed in this study are considered both in their original form, i.e. monthly-sampled time series, and as decomposed into distinct temporal components: a seasonal cycle and an interannual signal, denoted respectively by $\langle Y(t)\rangle_S$ and $\langle Y(t)\rangle_I$. This decomposition facilitates the analysis of variability operating at different timescales and is consistently applied across all relevant variables in the study (e.g., shoreline position, beach volume, waterline).

The seasonal component is defined as the climatological monthly cycle of $Y(t)$, computed by averaging over all available years for each calendar month m. Let N_m be the number of observations in month m; then the monthly climatology is:

$$Y_{\text{clim}}(m) = \frac{1}{N_m}\Sigma_{t_i \in m} Y(t_i) \tag{IV.1}$$

This yields a 12-month sequence $Y_{\text{clim}}(m)$, which is then repeated to reconstruct the seasonal signal $\langle Y(t)\rangle_S$ over time, indexed to the initial calendar month m_0 (1 for January, 2 for February, etc.):

$$\langle Y(t)\rangle_S = Y_{\text{clim}}(m = 1 + (t + m_0 - 1) \bmod 12) \tag{IV.2}$$

The interannual component $\langle Y(t)\rangle_I$ is extracted by applying a centered 12-month running mean to $Y(t)$, effectively filtering out the seasonal and higher-frequency variability:

$$\langle Y(t)\rangle_I = \frac{1}{12}\Sigma_{k=-5}^{6} Y(t+k) \tag{IV.3}$$

This approach provides a consistent framework for analyzing the temporal structure of variability across different variables and sites. When applied to a specific variable such as cross-shore shoreline position $X'(z,t)$, the resulting components $\langle X'(z,t)\rangle_S$ and $\langle X'(z,t)\rangle_I$ are used to quantify the contribution of seasonal and interannual dynamics to the overall variability (see Figure IV.4).

2D indicators can be derived from the 3D profiles, such as the shoreline and waterline proxies.

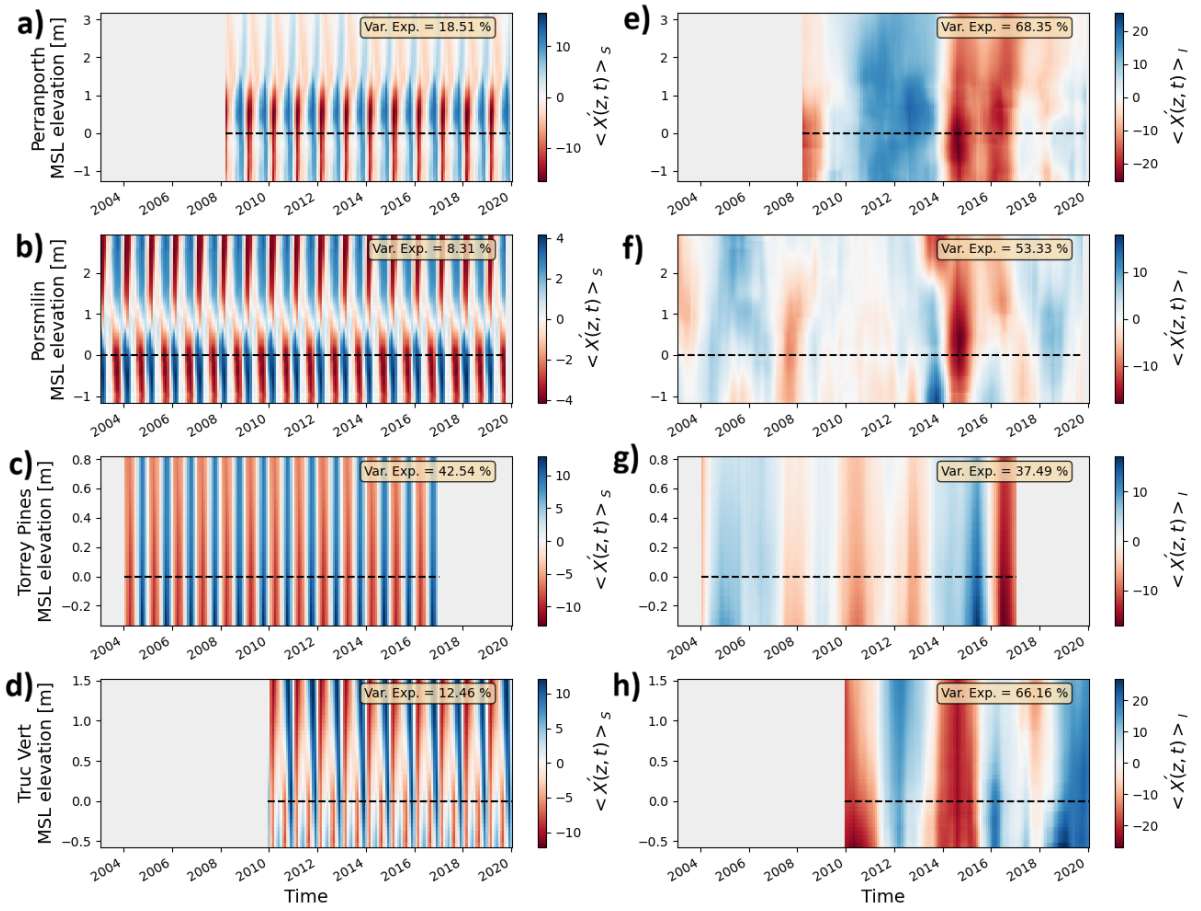

FIGURE IV.4 Timestacks of **a-d)** seasonal and **e-h)** interannual beach profile change noted $< X'(z,t) >_S$ and $< X'(z,t) >_I$, respectively. Profile elevations are reported in MSL datum, the dashed black line highlight the MSL. Share of variance of the total intertidal beach variability explained by these components are shown.

In this paper, we refer to shorelines as intersections between the profile and a fixed given elevation z_{ref} set to 0 m in this study (i.e., MSL, refer to the black dashed line in Figure IV.3 and IV.4); while the waterline is the intersection between the profile and a dynamic elevation following the dynamic sea-level. Here we rely on measured monthly mean sea-level (MMSL) data to get the the reference elevations (Holgate et al. (2013)).

IV.2.3 Modeling of Beach Profile Changes

To characterize the spatial structure of beach profile variability, we model the cross-shore position anomalies $X'(z,t)$ as a combination of two components: a uniform shift and a slope-adjustment term. This formulation captures both translation-like and steepening/flattening behavior of profiles over time, expressed as:

$$X'(z,t) \approx A(t) + B(t) \cdot (z - z_{\text{rot}}) \tag{IV.4}$$

Here, $A(t)$ represents the time-dependent translation of the profile, $B(t)$ describes slope variability, and z_{rot} is the elevation pivot point around which slope changes occur. This compact parametric form provides a tractable yet interpretable representation of complex profile evolution.

The model parameters $A(t)$, $B(t)$, and z_{rot} are estimated independently using a non-linear least squares approach. For each time step t, the anomaly profile $X'(z,t)$ is regressed against elevation z according to:

$$X'(z,t) = A(t) + B(t)(z - z_{\text{rot}}) + \varepsilon(z,t), \tag{IV.5}$$

where $\varepsilon(z,t)$ denotes the residuals between observed and modeled profiles. Parameter estimation is performed using the Levenberg–Marquardt algorithm (Moré (1978)), as implemented in `scipy.optimize.curve_fit`.

IV.2.4 Statistical Analysis

We evaluated the performance of shoreline proxies and profile models using the following statistical indicators:

- **Pearson's Correlation Coefficient.** The linear correlation between two time series $x(t)$ and $y(t)$ was computed as:

$$r = \frac{\Sigma_{t=1}^{N}(x(t)-\overline{x})(y(t)-\overline{y})}{\sqrt{\Sigma_{t=1}^{N}(x(t)-\overline{x})^2}\sqrt{\Sigma_{t=1}^{N}(y(t)-\overline{y})^2}}, \tag{IV.6}$$

  where $\overline{x}$ and $\overline{y}$ are the temporal means of $x(t)$ and $y(t)$, respectively.

- **Explained Variance.** The fraction of variance in a signal $x(t)$ captured by a model or reconstruction $\hat{x}(t)$ was defined as:

$$EV(x,\hat{x}) = 100 \times \left(1 - \frac{\text{Var}(x-\hat{x})}{\text{Var}(x)}\right), \tag{IV.7}$$

with variance calculated as:

$$\mathrm{Var}(x) = \frac{1}{N}\Sigma_{t=1}^{N}(x(t)-\overline{x})^2, \tag{IV.8}$$

where $\overline{x}$ is the mean of x.

- **Relative Contribution of Components.** To quantify the percentage contribution of individual model components $c_i(t)$ to a target signal $x(t)$, we extended the explained variance metric. Because components may not be orthogonal, summed contributions can exceed 100%. To enable comparison across sites and components, we define:

$$rEV_i = \frac{EV(x, c_i)}{\Sigma_j EV(x, c_j)} \times \frac{EV(x, \Sigma_i c_i)}{100}, \tag{IV.9}$$

where EV is the explained variance of either the whole model or a specific component. The relative contribution rEV_i thus provides a normalized measure of how much variability in $x(t)$ can be attributed to each process (e.g., translation, slope change, seasonal or interannual variability).

IV.2.5 Additional Data

Offshore wave characteristics (significant wave height, peak wave period, and mean wave direction) were obtained from the CMEMS Global Ocean Waves Reanalysis, available at 3-hourly resolution and 0.2° spatial resolution. Data were extracted at the grid nodes closest to each study site. MMSL data were retrieved from nearby tide gauges in the PSMSL catalogue (Holgate et al. (2013)). For the four study sites, gauges are located within 50 km (SHOM, CCO, NOAA).

IV.3 Results

IV.3.1 Waterline and shoreline variability

We begin by comparing the evolution of waterline (intersection of the MMSL with the monthly beach profile) and shoreline (0 m, MSL) indicators to assess the influence of sea-level variability on the waterline position. Figure IV.5 shows the evolution of the two coastal indicator at the

four sites. At all sites, waterline and shoreline position time series have a very similar variability, kept almost identical at all scale, from intra-seasonal to inter-annual. At Perranporth and Torrey Pines, slight gaps between the waterline and the shoreline position are visible and seem seasonally consistent. These differences are necessarily dependent of the sea-level.

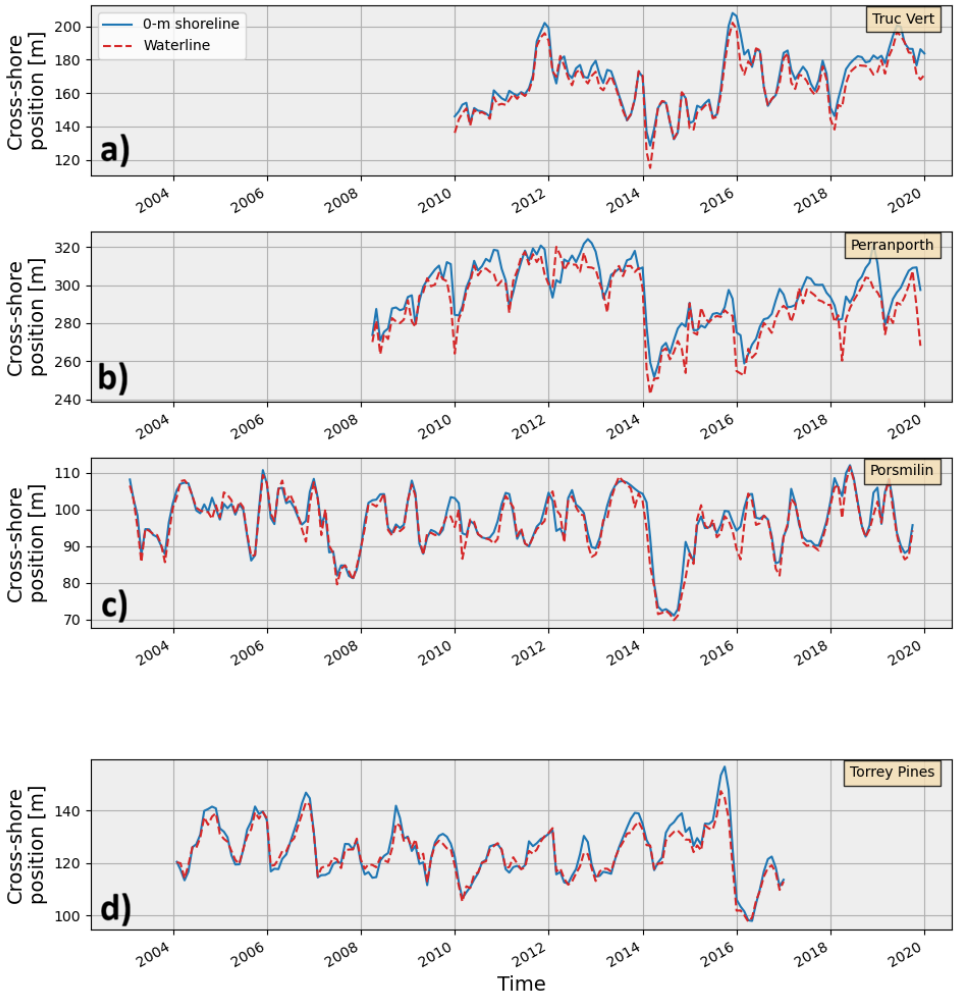

FIGURE IV.5 Temporal evolution of the shoreline and waterline position at **a)** Truc Vert, **b)** Perranporth, **c)** Porsmilin, and **d)** Torrey Pines. The shoreline position is given by the intersection of the 0 m (MSL) elevation with the profile and the waterline position is the intersection of the monthly-mean sea-level with the profile.

A way to quantify the extent of influence of sea-level variability on the waterline position is to separate the contributions driven by sea-level variability to those driven by morphological changes (i.e., sediment transport). To do so, we describe the waterline position X_w as the shoreline position X_s displaced by an hydrodynamic component ΔX_{hydro} :

$$X_w = X_s + \Delta X_{hydro} \tag{IV.10}$$

and to investigate rather the variability of the waterline position, we consider

$$\Delta X_w = \Delta X_s + \Delta X_{hydro} \tag{IV.11}$$

and, as variations of the datum-based shoreline positions ΔX_s are morphological changes, we can rewrite this equation as

$$\Delta X_w = \Delta X_{morpho} + \Delta X_{hydro} \tag{IV.12}$$

where ΔX_{morpho} is the morphological component of the waterline displacement.

Figure IV.6 illustrates the relative contributions of waterline displacement over time at the 4 sites. Again, at the 4 sites, we can see that the morphological component largely dominates the variability of the waterline position. Investigating the seasonal cycle of the two contributions at the 4 sites, we find that the extent of waterline variability driven by dynamic monthly mean sea-level ranges between $\sigma_{hydro} = 0.9$ m (Porsmilin) and $\sigma_{hydro} = 3.8$ m (Perranporth) against $\sigma_{morpho} = 2.6$ m (Porsmilin) to $\sigma_{morpho} = 7.4$ m (Perranporth) for changes driven by morphological changes. In terms of relative variability ($\sigma_{hydro}/(\sigma_{hydro}+\sigma_{morpho})$), sea-level driven waterline change accounts for 34.1 % of the seasonal variability at Perranporth, 22.9 % at Torrey Pines, 25.1 % at Porsmilin and 27.0 % at Turc Vert. At the seasonal scale, dynamic sea-level and morphological components of waterline change are correlated negatively at the 4 sites, from poorly correlated at Porsmilin and Truc Vert ($R = -0.16$ and $R = -0.29$, respectively) to strongly correlated at Perranporth and Torrey Pines ($R = -0.71$ and $R = -0.98$, respectively). Negative correlations implies that the dynamic sea-level and morphological components compensate each rather than exacerbating waterline displacement -especially at Torrey Pines and Truc Vert where correlations are strong.

The same analysis at the interannual scale reveals that waterline change driven by sea-level variability is weaker than these driven by morphological changes, representing 16.7 %, 15.5 %, 19.5 %, and 10.6 % of the morphological variability at Perranporth, Porsmilin, Torrey Pines and Truc Vert, respectively. At this scale, sea-level driven variability show weak correlations with morphological changes at 3 sites ($R = 0.22$ at Perranporth, $R = 0.29$ at Porsmilin, $R = -0.36$ at Torrey Pines), except at Truc vert where the correlation reaches $R = -0.68$, again suggesting that the observed interannual waterline variability is in fact dampened by interannual sea-level

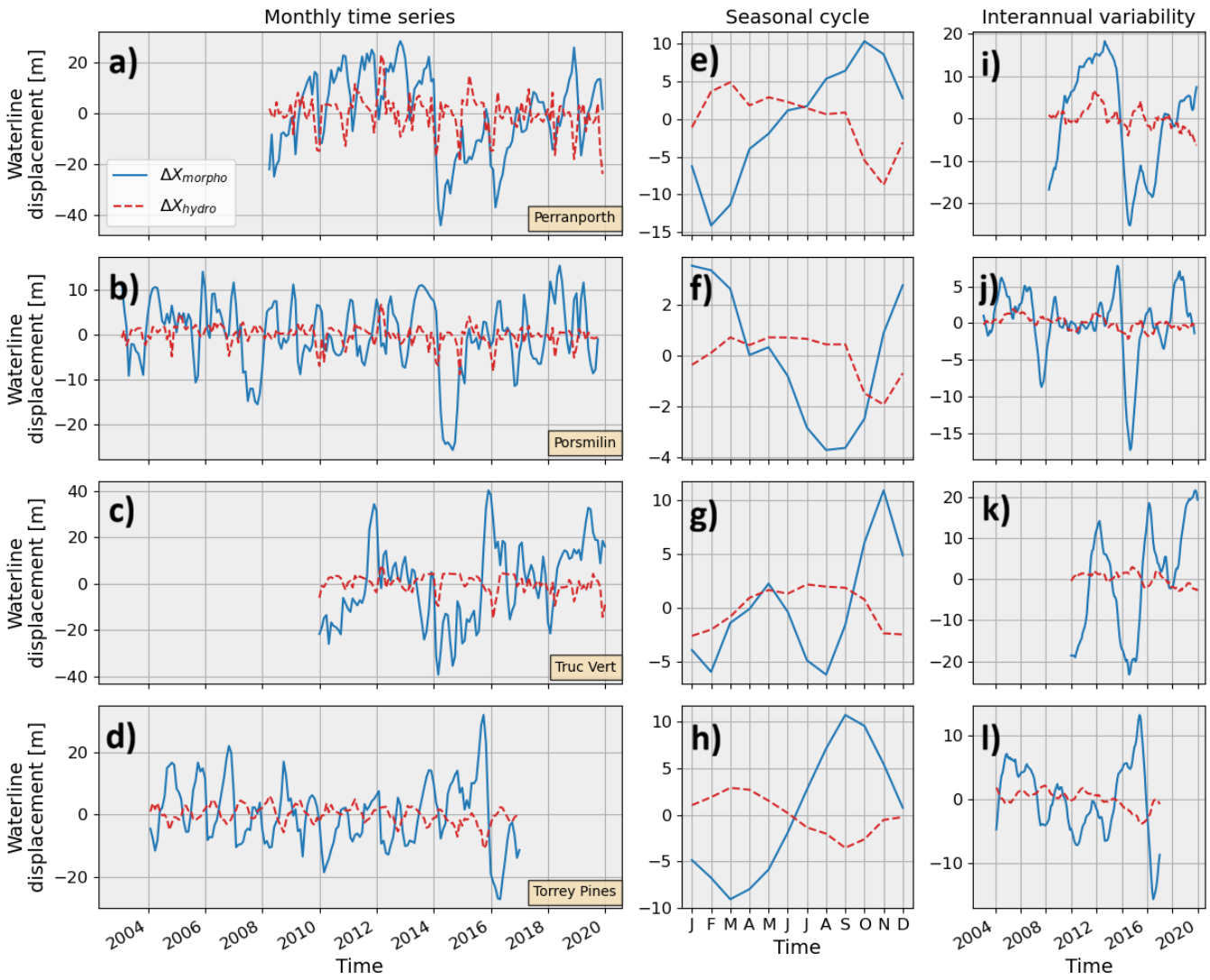

FIGURE IV.6 Evolution of the morphodynamic and sea-level driven components of waterline change at the 4 study sites, displayed as **a-d)** monthly-sampled time series, **e-h)** seasonal cycles, and **i-l)** smoothed interannual fluctuations (12-months runing mean).

variability.

IV.3.2 Representativeness of shoreline proxies in describing intertidal beach morphodynamics

Beyond these differences between waterline and shoreline, there is also the question of the representativeness of these 2D coastal indicators to comprehend the whole 3D dynamics. A first assessment consists in checking how correlated are the MSL-shoreline and waterline positions with all the iso-topography elevation shoreline positions. Figure IV.7 presents the correlation be-

tween shoreline and waterline positions with iso-elevation shoreline proxies across the four study sites and at three temporal scales: the full monthly-sampled time series, the seasonal climatology, and the interannual variability (12-month running mean).

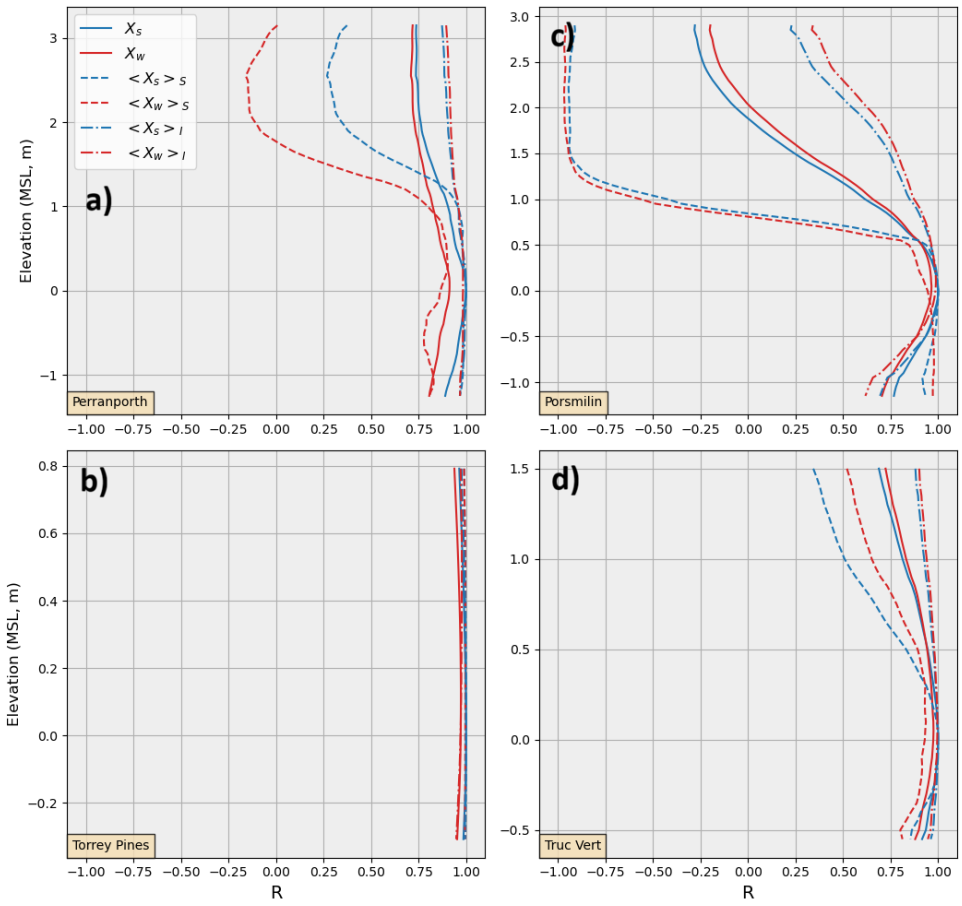

FIGURE IV.7 Pearson's correlations between MSL-shoreline/waterline and the other datum-based shoreline proxies of the intertidal profile at **a)** Perranporth, **b)** Porsmilin, **c)** Torrey Pines, and **d)** Truc Vert. Solid lines show correlations for the full monthly-sampled time series, dashed lines for the seasonal cycles and dash-dotted lines for the interannual variability. Blue lines highlight the correlation scores using the MSL-shoreline and red lines for the waterline.

At Perranporth (Panel a), both shoreline and waterline indicators exhibit strong correlations ($R > 0.75$) with iso-elevation positions in the lower intertidal zone (from −1 m to +1 m MSL), across all temporal scales. Correlations progressively decrease at higher elevations. This decline is most pronounced for the seasonal component, with R values dropping below zero above +2 m MSL. The interannual component maintains relatively high correlations, while the full time series shows moderate reduction. At Porsmilin (Panel b), moderate-to-strong correlations are found in the lower elevations (−1 to +0.5 m MSL), with $R < 0.6$ across all components. However, correlations deteriorate rapidly with elevation: the interannual component drops below R = 0.5, the full series falls below zero, and the seasonal component reaches near R = −1 in the upper intertidal zone, highlighting an contrasted behavior of profile across elevations. Torrey Pines (Panel

c) exhibits uniformly high correlations across all elevations and timescales. Shoreline and waterline positions are highly consistent with iso-elevation proxies, with $R > 0.9$ for all components. This indicates a vertically coherent beach response across spatial and temporal scales. Truc Vert (Panel d) displays a pattern similar to Perranporth, but with slightly stronger correlations. Again, interannual correlations are the highest, followed by the full time series and then the seasonal component. The seasonal correlations decline to $R \approx 0.4$ at the upper elevations. Across all sites, correlations are generally higher for the shoreline than for the waterline. This difference is especially visible when comparing these proxies with higher elevation shorelines. Correlations also decrease when calculated in relation to iso-altimeter reference data located progressively further from sea level, particularly for the seasonal signal.

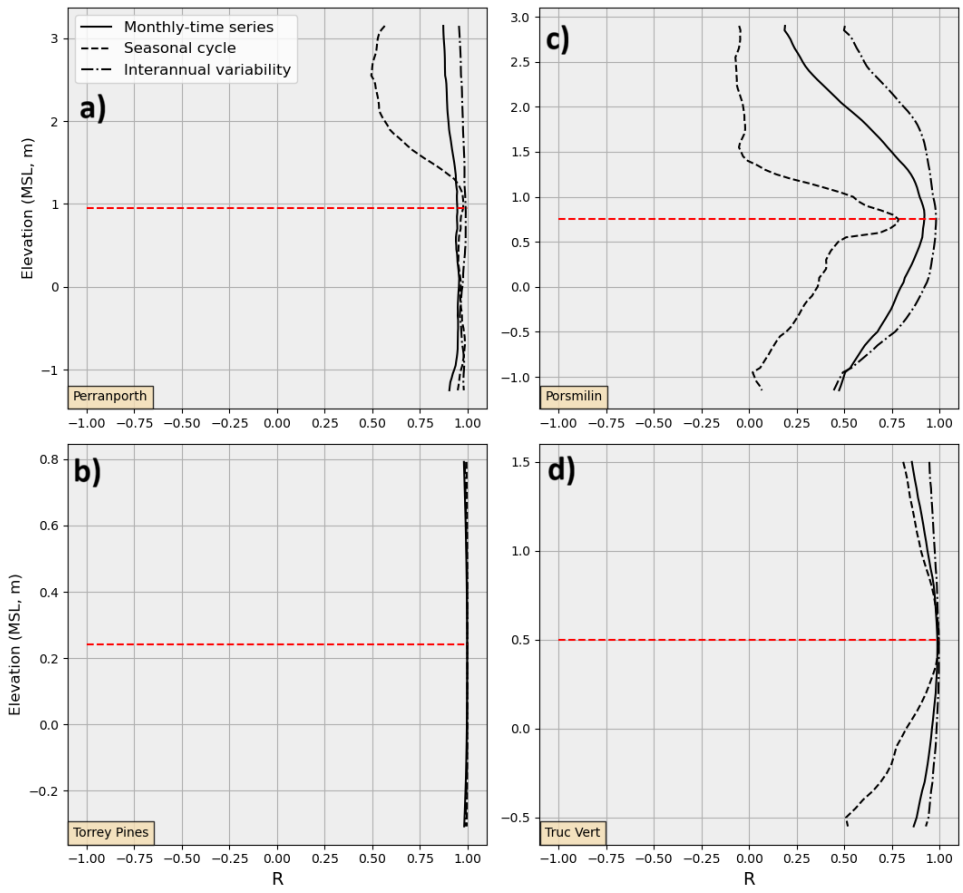

FIGURE IV.8 Pearson's correlations between the MSL-shoreline the volume of the intertidal profile at **a)** Perranporth, **b)** Porsmilin, **c)** Torrey Pines, and **d)** Truc Vert. Solid lines show correlations for the full monthly-sampled time series, dashed lines for the seasonal cycles and dash-dotted lines for the interannual variability.

Figure IV.8 displays the correlation between shoreline proxies at various elevations and the total intertidal beach volume across the four study sites. Correlations are computed separately for three components of the volume time series: the full monthly-sampled signal, the seasonal

cycle (climatology), and the interannual variability (12-month running mean). At Perranporth (Panel a), shoreline time series derived from nearly all elevations capture the variability of the intertidal volume extremely well for both the full and interannual components ($R > 0.8$), with only a slight decline in correlation at the highest elevations. In contrast, at the seasonal timescale, upper-profile shorelines ($z > 2$ m MSL) perform poorly, with correlations dropping below $R = 0.4$, indicating a mismatch between upper beach shoreline fluctuations and the seasonal dynamics of the overall profile volume. Porsmilin (Panel b) shows more spatially variable performance. Correlations with volume peak around $z = 0.8$ m MSL for all components. The interannual component is consistently well represented by shoreline time series across most elevations ($R > 0.5$), while the full time series exhibits a similar but slightly reduced pattern. The seasonal component is again the least well captured, with correlations peaking near $R = 0.75$ around $z = 0.8$ m but falling to near-zero both below $z = 0$ m and above $z = 1.5$ m MSL. At Torrey Pines (Panel c), correlations remain uniformly high ($R > 0.9$) across all elevations and all components, confirming that beach volume variability at this site is consistently and strongly linked to shoreline variability across the intertidal zone, regardless of temporal scale. Truc Vert (Panel d) exhibits a pattern similar to Perranporth. The full and interannual components of volume variability are well captured across all shoreline elevations ($R > 0.8$), while the seasonal cycle is less well represented by shoreline time series derived from lower parts of the beach ($z < 0$ m MSL). Correlations at the seasonal scale peak around $z = 0.5$ m, suggesting this elevation best reflects the seasonal evolution of the intertidal volume.

These results indicate that the interannual variability of beach volume is robustly captured by shoreline proxies across most of the intertidal profile. In contrast, the seasonal volume dynamics are more sensitive to the choice of elevation used for shoreline derivation, with mid-elevation proxies generally offering the best correspondence.

IV.3.3 The 3D intertidal profile variability

To move beyond descriptive temporal patterns and towards a mechanistic understanding of beach profile change, we adopt a geometric decomposition of profile variability. Specifically, we seek to represent the observed anomalies in cross-shore position $X'(z,t)$ at each elevation z and time

t using Equation IV.5. In this framework, $A(t)$ captures the horizontal translation of the profile (e.g., advance or retreat), while $B(t)$ represents a rotation, or tilting, of the profile about a fixed reference elevation z_{rot}, chosen at the node of least variability. $A(t)$, $B(t)$ and z_{rot} have been fitted on the monthly-sampled beach profiles using a least squares algorithm based on the Levenberg-Marquardt method (More, 1977). The fitted terms A and B are shown for the four sites on Figure IV.9. Full $A(t)$ and $B(t)$ time series are shown, along with their seasonal cycles and interannual variability signals. The translation signal $A(t)$ quantifies uniform beach profile change (positive values for seaward positions) and can be directly read in meters, while the rotation signal $B(t)$ is a slope varying signal that should be interpreted regarding elevation relative to the rotation elevation z_{rot}. The greater the elevation difference relatively to z_{rot}, the larger the influence of the rotation term $B(t)$, scaling as $X_{rot} = B(t) \times (z - zrot)$. Positive (negative) values of $B(t)$ imply a steepening (flattening) of the intertidal beach profile. Surprisingly, the application of the least square method led to fixed rotation points (Perranporth: $z_{rot} = 0.950$ m; Porsmilin: $z_{rot} = 0.875$ m; Torrey Pines: $z_{rot} = 0.242$ m; Truc Vert: $z_{rot} = 0.475$ m; all relative to MSL datum) for each site, even if the variable was let free to vary in time in the model (only one time step led to a different z_{rot} output: at Torrey Pines, for the month of November 2004, $z_{rot} = -0.227$ m, this point is further discussed in the Discussion).

Both the translation and rotation components show seasonal variability. At Perranporth and Torrey Pines, the two mechanisms and correlated but in opposite phases, meaning that when the beach erode (A decreasing) the beach steepens (B increasing), and vice versa. At Truc Vert, the components are out of phase, with the beach steepening from May to August and flattening from September to March, while the whole profile slowly recovers February to October, and dramatically erodes during November, December and January. At Porsmilin, there is no obvious seasonal translation of the profile, and a slight rotation, which the beach being the steepest at the end of the summer in September and the flattest at the end of winter in February.

At the interannual scale, we generally observe that both the translation and rotation terms have higher amplitudes than at the seasonal scale. Especially, the translation term fluctuates drastically over the years, highlighting some large patterns of change, like at Torrey Pines where the uniform displacement of the intertidal profile is almost mirrored by beach slope adjustments, steepening

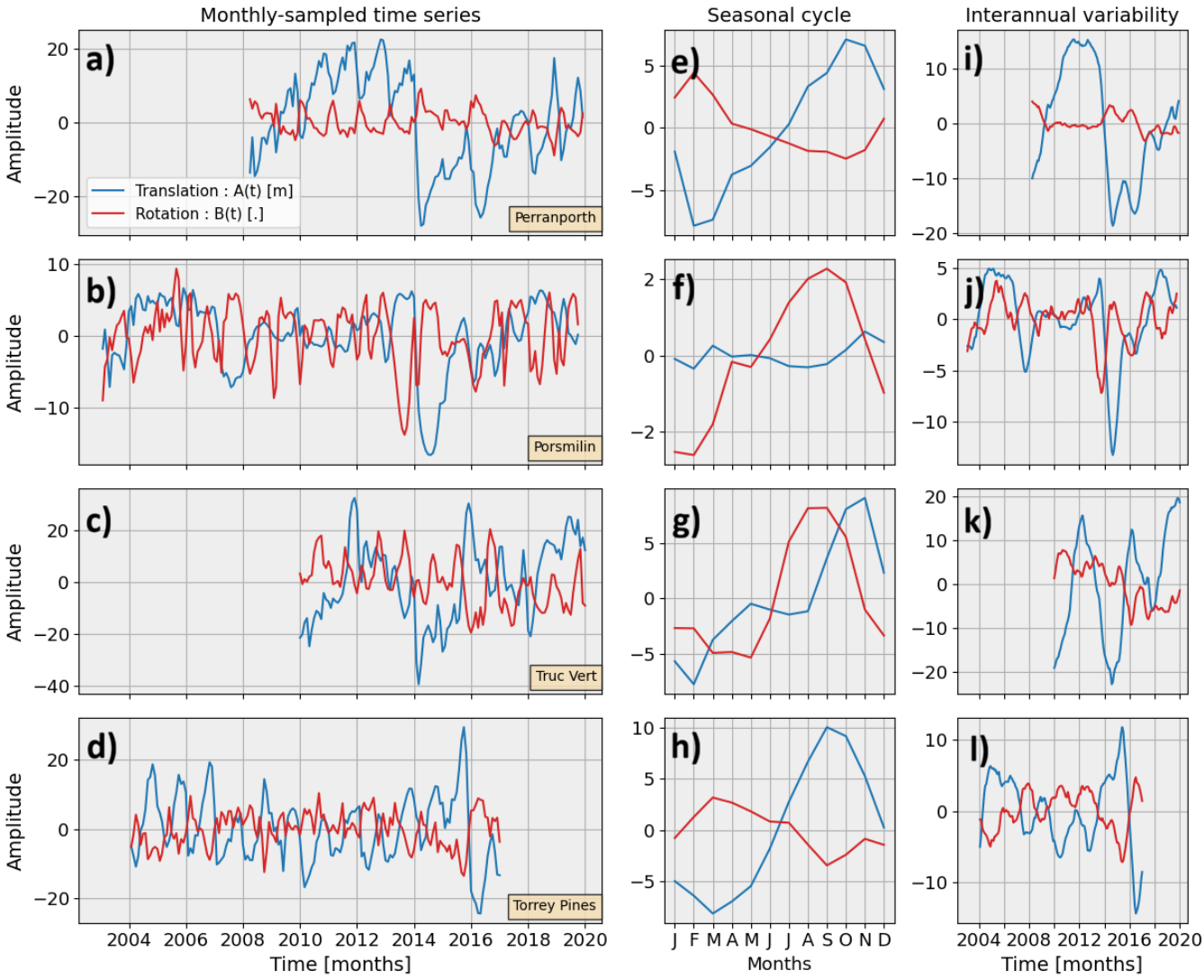

FIGURE IV.9 Evolution of the components $A(t)$ and $B(t)$ of beach profile variability at the 4 study sites, displayed as **a-d)** monthly-sampled time series, **e-h)** seasonal cycles, and **i-l)** smoothed interannual fluctuations (12-months runing mean).

as the profile erodes, and vice versa, similarly to its seasonal pattern. At Truc Vert we observe a trend of beach slope flattening, which is not correlated to the translation of the profile showing large interannual onshore/offshore migrations. Similarly, the rotation and translation terms are mostly uncorrelated at Perranporth, the beach profile also following large interannual patterns of translation relatively to the rather weak rotation term interannual variability. Finally, at Porsmilin, the two terms exhibit similarly large interannual fluctuations, also showing correlated behaviors, with the beach steepening at the same time it erodes.

Figure IV.10 illustrates how the translation and rotation terms shape the intertidal beach profile

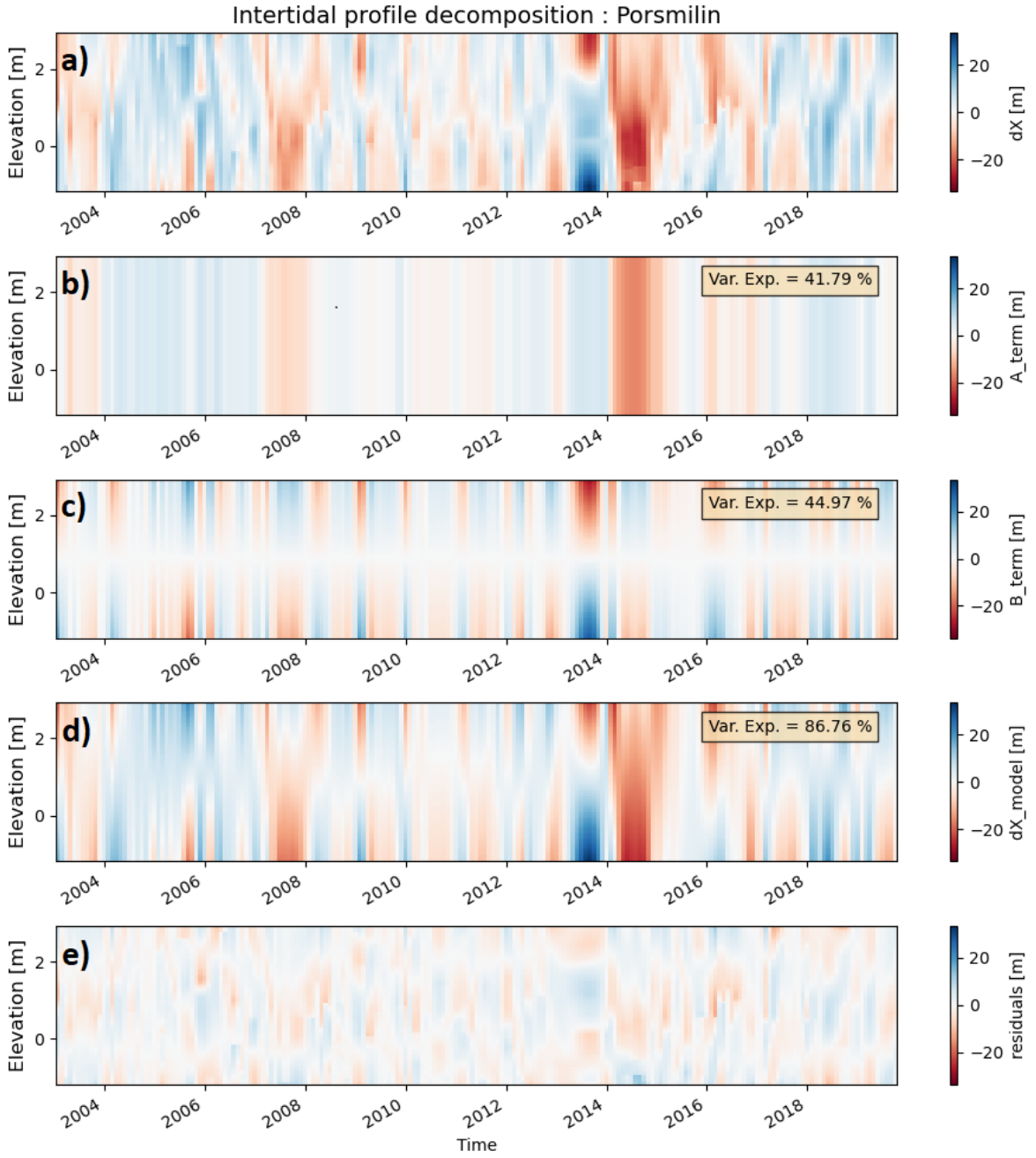

FIGURE IV.10 **a)** Timestack of monthly-sampled intertidal beach profile at Porsmilin, decomposed into **b)** a only-translational component, **c)** a only-rotational component, **d)** the full translation/rotation model and **e)** the associated residuals (intertidal profile variability unexplained by the model). On panels **b-d)** are indicated the shares of explained variance of these models, also displayed on Table IV.1.

with an example at Porsmilin. There, the translation/rotation model of Equation IV.5 reconstruct 86.8 % of the variance of the demeaned profiles $X'(z,t)$, with about half of it attributed to profile translation and the other half to profile rotation. The large erosional event of winter 2013/2014 seems to be mostly attributed to a uniform beach profile retreat, not necessarily associated with

an abnormal intertidal beach slope. Similarly, at Perranporth and Truc Vert, the 2013/2014 winter storms led to a dramatic intertidal profile retreat, but not to dramatic changes of the beach slope.

Overall, beach profile translation alone explains a large portion of total intertidal beach variability, from 41.8 % at Porsmilin to 96.9 % at Torrey Pines. Beach profile rotation is found to be non-negligeable, explaining intertidal beach variability at a rate of 2.1 % at Torrey Pines, 9.1 % at Perranporth, 11.4 % at Truc vert and 45.0 % at Porsmilin. In all, adding the two components together, we find that this profile translation/rotation model explains between 86.8 % and 99.7 % of the intertidal beach variability, leaving only a small part of the observed variability unexplained.

TABLE IV.1 Shares of variance of the demeaned profile $X'(z,t)$ explained by the translation term $A(t)$, the rotation term $B(t)(z-z_{rot})$, and the sum of the two.

Site	$X'(z,t)=A(t)$	$X'(z,t)=B(t)(z-z_{rot})$	Full model
Perranporth	83.2 %	9.1 %	92.3 %
Porsmilin	41.8 %	45.0 %	86.8 %
Torrey Pines	96.9 %	2.1 %	99.7 %
Truc Vert	86.8 %	11.4 %	98.2 %

Now the profile variability has been reconstructed using this simple model, we can quantify the share of variability of each component responsible for MSL-shoreline change, and adding the consideration of sea-level variability we can do this analysis for waterline variability instead. We first quantified the share of variability explained by the sea-level component ΔX_{hydro} in the waterline position signal, than we calculated the share variability explained by the translation and rotation component in the MSL-shoreline position signal. We represented these relative contributions of waterline variability for each of the 4 sites in Figure IV.11. Overall, between 91.1 % (Porsmilin) and 99.7 % (Torrey Pines) of the variability has been reconstructed using these 3 components. The translation component captures between 59.4 % and 90.1 % of the variability, against 14.8 % to 40.0 % for the rotation component. As observed on Figure IV.5, sea-level fluctuations at Torrey Pines and Truc Vert tend to dampen waterline variability relatively to shoreline variability, explaining why we obtain negative rates of explained variance for the passive hydrodynamic component. This passive contribution of dynamic sea-level explain a tiny share of the monthly-sampled waterline position time series variability, with 0.6 % at Porsmilin and 2.3 % at

Perranporth.

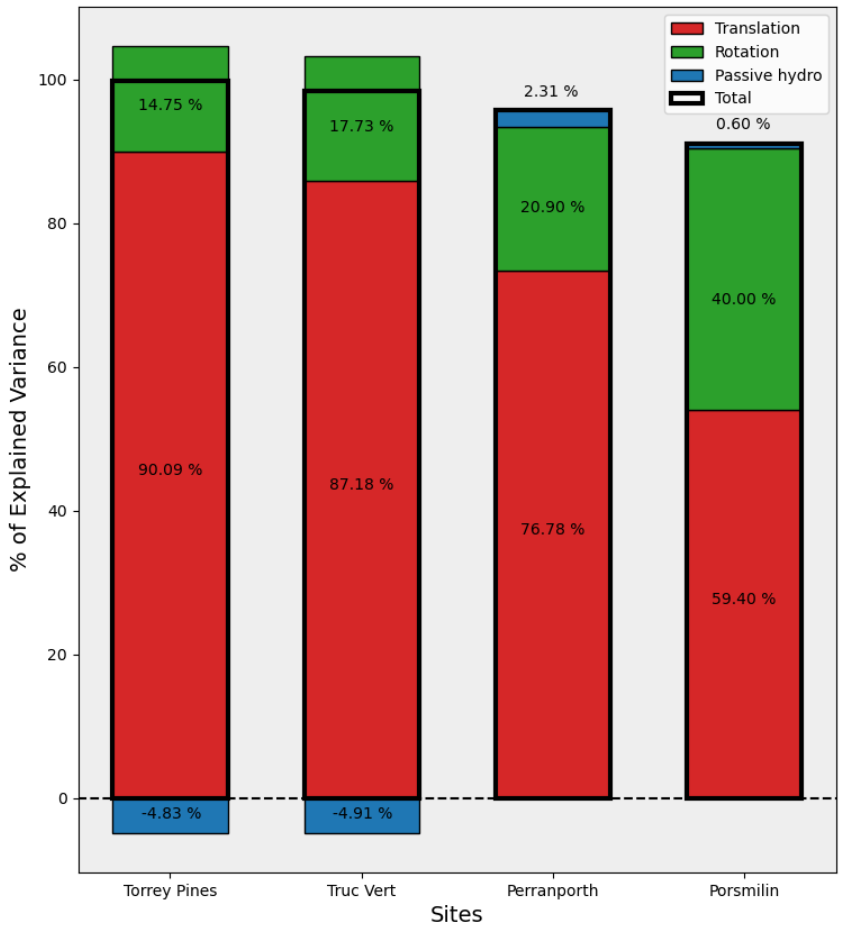

FIGURE IV.11 Share of variance of the waterline position explained by a passive hydrodynamic, a rotation and a translation term. The total variance explained by the sum of the 3 components if displayed in black. Displayed shares of explained variance on the individual components represent relative contributions relative to the total share of explained variance (i.e., sum of the 3 shares of explained variance is equal to 100 %).

IV.4 Discussion

This study examined intertidal beach profile variability through a layered approach. First, we quantified differences between datum-based and synthetic proxy-based shoreline indicators ("shorelines" and "waterlines," respectively). Second, we assessed the extent to which 2D shoreline metrics capture variability in the full 3D beach profile. Finally, we analyzed dominant spatiotemporal modes of intertidal morphodynamics to understand when and why a 2D metric may or may not

reflect broader morphodynamic behavior. The results are discussed in the context of existing knowledge, their implications for interpretation and modeling, and methodological limitations.

Synthetic waterlines reconstructed from monthly mean sea-level data closely match fixed-datum shorelines ($R > 0.9$ at all four sites; Figure IV.5). However, dynamic sea-level fluctuations contribute a non-negligible share of waterline variability, particularly at seasonal scales, explaining roughly 25–33% of the total variance (Figure IV.6.e–h). This has direct implications for remote monitoring, as satellite-derived datasets are increasingly use for climate-driven coastal erosion assessments (e.g., Warrick et al. (2025b); Vos et al. (2023a)) with the share of observed variability driven by a dynamic sea-level often neglected.

Proxy-based shorelines inherently conflate morphodynamic change with dynamic sea-level variability. When these components are correlated, as often occurs seasonally, one may under- or overestimate true morphological change. For example, at Perranporth and Torrey Pines, negative correlations between sea-level variability and morphological change result in underrepresented waterline variability, whereas in the Pacific Northwest, storm-driven erosion coinciding with elevated water levels amplifies apparent beach change (Ruggiero et al. (2005)). At interannual timescales, large morphodynamic changes driven by high-energy wave events dominate over dynamic sea-level fluctuations (Figure IV.6.i–l). Nonetheless, climate modes such as ENSO can induce persistent sea-level anomalies across ocean basins (Woodworth et al. (2019); Vos et al. (2023a), also refer to Chapter III), frequently coinciding with significant erosion or flooding, emphasizing the need to disentangle sea-level-driven displacements from true sediment transport.

Our methodology omits modeled wave runup contributions, relying solely on monthly-sampled observed mean sea-level data (Holgate et al. (2013)). While this ensures consistency across sites, it excludes short-term, site-specific fluctuations driven by waves, tides, or river runoff, which can amplify waterline variability (Woodworth et al. (2019)).

Additionally, sea-level rise projections of 0.43–0.84 m by 2100 (Cazenave and Cozannet (2014); IPCC (2022)) further complicate the interpretation of fixed-elevation shorelines, as rising mean sea levels will gradually shift both the location and definition of beach features. This under-

scores the importance of clearly defining the reference frame—geological or climatic—when using shoreline metrics. Global tide-gauge coverage remains sparse outside Europe, North America, and East Asia (Holgate et al. (2013)), highlighting the critical role of satellite altimetry in under-instrumented regions. Recent advances in coastal altimetry (Cipollini et al. (2017); Cazenave et al. (2022)) promise improved nearshore accuracy, essential for separating sea-level and morphological contributions to shoreline variability.

Beyond sea-level ambiguity, fixed-elevation shoreline proxies capture only a subset of the full intertidal morphodynamics. Correlation analyses across intertidal elevations reveal site-specific differences (Figure IV.7). Narrow intertidal beaches (e.g., Torrey Pines) exhibit strong correlations across elevations, indicating coherent, translation-like profile behavior. In contrast, wider profiles (e.g., Porsmilin) show sharp decorrelation with vertical separation from MSL, with upper and lower profile segments sometimes evolving out of phase. Similar-width profiles, such as Perranporth, exhibit intermediate behaviors.

Correlation analyses with intertidal beach volume show consistent patterns: MSL to roughly mid-MHW elevations capture the most of the variance in volumetric profile change (Figure IV.8). Seasonal components display weaker correlations, likely due to nonuniform cross-shore responses: lower elevations respond to moderate wave forcing, whereas upper elevations react primarily to high-energy events, producing temporally offset cut-and-fill cycles. These findings demonstrate that shoreline proxies cannot fully capture localized rotation, profile steepening/flattening, or nonuniform sediment transport.

Applying a parametric model representing intertidal morphodynamics as a combination of translation and rotation around a pivot point captures 86–99% of monthly variability across four meso- to macro-tidal sites. At Truc Vert, Torrey Pines, and Perranporth, translation dominates (>80%), consistent with prior equilibrium-based modeling (Wright and Short (1984); Castelle et al. (2014); Ludka et al. (2015)). By contrast, Porsmilin exhibits substantial rotational contribution, corroborating previous observations of counter-intuitive responses in lower vs. upper profiles (Lemos et al. (2018)).

Equilibrium-based approaches have successfully modeled translation-dominated dynamics across a range of coastal indicators (shorelines, sandbars, slope, grain size; e.g., Castelle et al. (2014); Plant et al. (1999); Prodger et al. (2016); Labarthe et al. (2023)). However, their ability to capture elevation-dependent, rotation-driven dynamics remains limited, particularly in the presence of non-wave drivers such as dynamic sea level. Methodological simplifications—including alongshore averaging, single pivot rotation, and monthly temporal resolution—further constrain the model's applicability to sub-monthly or storm-driven processes.

These findings highlight a general principle: narrow, translation-dominated beaches allow 2D shoreline proxies to reliably represent 3D intertidal variability, whereas wide, rotation-prone profiles require multi-elevation or volumetric monitoring to capture full morphodynamics. Linking beach state to the dominant mode (translation vs. rotation) offers a promising pathway for predictive modeling, potentially informing equilibrium-based forecasts at ungauged sites.

IV.5 Chapter Conclusion

This study assessed the reliability of shoreline indicators for capturing intertidal beach morphodynamics by reconstructing monthly-sampled datum-based shorelines and synthetic waterlines from high-resolution topographic datasets across four contrasting meso- to macro-tidal sites (Perranporth, Porsmilin, Torrey Pines, and Truc Vert). Results show that dynamic sea level, particularly at seasonal timescales, can account for up to one-third of proxy-based shoreline variability. When sea-level and morphodynamic fluctuations co-vary, this overlap can obscure or exaggerate actual profile changes, posing challenges for interpreting SDS-based remote monitoring in the context of climate-driven variability and rising seas.

Beyond this, we demonstrate that the representativeness of shoreline proxies is constrained by beach profile geometry. At Torrey Pines, proxies at different elevations evolve coherently, reflecting a largely translational response that makes shoreline positions reliable indicators of intertidal profile dynamics. In contrast, Porsmilin exhibits strong decorrelation across elevation contours, especially at seasonal scales, revealing more complex morphodynamics—including sed-

iment partitioning between upper and lower beach zones. Across sites, up to 40% of shoreline proxy variability can be attributed to non-translational behaviors.

A simple parametric model combining translation and rotation around a site-specific pivot point explains 85–99% of observed intertidal profile variability. This physically interpretable model captures both equilibrium-type responses and slope adjustments, highlighting the central role internal sediment redistribution in driving profile change.

As sea-level rise accelerates and satellite-derived shorelines are increasingly used for global monitoring, these results underscore the need for a nuanced treatment of shoreline indicators. Time-varying sea-level corrections, geometry-aware profile representations, and site-specific considerations are essential for improving the interpretability of shoreline variability. Shoreline indicators remain highly valuable as easily scalable proxies for detecting seasonal and interannual patterns of coastal change at large spatial scales, but they cannot substitute for high-resolution 3D profile measurements in terms of volumetric changes of the beach.

Building on these insights, the next chapter synthesizes the thesis findings into a broader conceptual framework for beach morphodynamics, outlines methodological refinements, and discusses how improved predictive understanding can inform coastal risk assessment and climate adaptation.

Chapter V

Discussion and Perspectives

In Chapter I we presented the scientific context of the thesis with a description of current knowledge and existing gaps from which raised several scientific questions situating the thesis work. In Chapter II we addressed the potential and limits associated to satellite-derived methods to accurately track shoreline variability across scales; in Chapter III we built on these results to analyze climate-driven patterns of shoreline change at the continental and decadal scale, informing on how global scale climate variability downscaled to regional shoreline change; in Chapter IV we investigated the limits inherently associated to shoreline indicators in representing the whole beach system morphodynamics, identifying some site specific behaviors of shoreline/beach system variability. In this chapter, we aim to discuss the broader scientific and practical implications of the thesis results, assess their relevance for advancing coastal monitoring and understanding of coastal hydro-morphodynamics, and identify promising avenues for future research.

Contents

V.1 Contrasted shoreline definitions as indicators of coastal change 142
V.1.1 Conceptual distinctions between waterline and datum-based shoreline definitions . . 142
V.1.2 Potential limits of using shoreline indicators as a proxy for beach morphodynamics . 145
V.1.3 A broader conception of the beach and its dynamics 148

V.2 Towards more robust methods for satellite-derived nearshore monitoring 150
V.2.1 Future of satellite-derived shoreline monitoring 150
V.2.2 Integration of alternative satellite-derived beach features for a richer representation of the coastal system 156
V.2.3 The potential of remotely-sensed topography-bathymetry continuum 158

V.3 What role for satellite-based monitoring in predicting coastal risks ? 161

V.1 Contrasted shoreline definitions as indicators of coastal change

V.1.1 Conceptual distinctions between waterline and datum-based shoreline definitions

Shoreline indicators are widely used to infer beach morphodynamic because they provide an accessible, one-dimensional snapshot of a complex three-dimensional system. Yet, the term "shoreline" is inherently ambiguous. It can refer to a fixed-elevation contour (e.g., Barnard et al. (2017)), a land/sea interface as observed at a specific moment (Salameh et al. (2020)), or a dynamically adjusted indicator that accounts specific sea-level variability contributors (e.g., Ruggiero et al. (2003); Moore et al. (2006)). This ambiguity is not trivial: different definitions capture different aspects of the beach hydro-morphodynamics, allowing for different interpretations.

In this thesis, the shoreline has been explicitly deconstructed into multiple conceptualizations to clarify what each indicator measures and how it relates to underlying hydro-morphodynamics:

- Satellite-derived waterlines (SDW): The first proxy we treat is the waterline, understood as the land/sea interface observed in satellite imagery, influenced morphological changes of the beach as well as by tides, wave runup, and all other sorts of sea-level variations. As this proxy captures high-frequency variability, it conflates the full hydro-morphodynamics with transient water-level fluctuations. As such, SDW can only be used to infer topography with accurate total sea-level information, allowing to link at a given time a cross-shore position to a coastal sea-level.

- Satellite-derived shorelines (SDS): This category is itself ambiguous, at least in the way SDS have typically been derived, most often correcting the almost-deterministic astronomical tide elevation (e.g., Vos et al. (2019b)), sometimes additionally accounting for wave runup estimations (Castelle et al. (2021); Graffin et al. (2023)). To partially isolate morphodynamic signals, we applied tide corrections using tide model outputs and beach slope estimations, producing a proxy-based shoreline. This step reduces predictable tidal effects but remains sensitive to other sources of sea-level variability, meaning the resulting shoreline indicator can still be considered as a waterline, integrating a mix of morphological and hydrodynamic forcing as well as errors inherent to satellite-derived methods and tide/wave

runup corrections.

- Synthetic waterlines derived from beach elevation profiles: To further disentangle the influence of sea-level, we derived, in Chapter IV, a synthetic waterline from intertidal topography combined with monthly mean coastal sea-level measurements. This approach produces a "dynamic mean sea-level shoreline," which moves consistently with regional sea-level anomalies but is fundamentally tied to profile evolution. By doing so, it conceptually separates vertical displacements driven by water-level variability from actual beach morphodynamics, allowing for the assessment of heterogeneous nature of waterline displacement.

- Datum-based shoreline : This definition anchors the shoreline to a fixed vertical elevation, most commonly long-term mean sea level (MSL = 0 m), but sometimes to other tidal datums such as MHW. Datum-based shorelines are valued because they provide a stable, repeatable reference for long-term monitoring and allow comparisons across datasets and regions (e.g., Barnard et al. (2017); Konstantinou et al. (2023)). However, datum-based shorelines correspond to a contour of the beach profile that may not align with a clearly identifiable feature in the field. As the reference elevation used to define shoreline positions is usually tied to a tidal datum (e.g., MHW: Graffin et al. (2023); or MSL: Vos et al. (2023b)), and therefore linked to local tidal conditions, these tidal datums will gradually shift, rendering the currently adopted reference levels increasingly obsolete with ongoing sea-level rise.

This layered framework further emphasizes that the "shoreline" is not a single, universally defined feature (Boak and Turner (2005)). Depending on the chosen metric, the same beach can appear more or less morphologically dynamic and even show contrasting trends (regardless of the observation accuracy, which itself adds a layer of uncertainties). If interpreted as purely morphological indicators, raw SDW observations overestimate short-term morphodynamics, mainly because of tides, whereas fixed elevation datum-based shoreline reliably mirror beach morphodynamics but may not represent faithfully the level of coastal vulnerability associated to large variations of the sea-level, or even long-term sea-level rise. Understanding these nuances is critical for interpreting shoreline variability in the context of sediment budgets, hazard and vulnerability assessment, or even coastal evolution modeling.

Criticisms raised against the global and SDW approach of Almar et al. (2023) have initiated debates between geomorphology and climate-oceanography communities (Warrick et al. (2024); Almar et al. (2024b)) which help to conceptualize the purpose of coastal monitoring. The choice of shoreline indicator and the eventual post-processes applied to it must be dictated by the purpose of the study. In the case of coastal responses to ENSO, for example, several studies have aimed to quantify ENSO-driven beach erosion (e.g., Barnard et al. (2017); Ruiz de Alegría-Arzaburu et al. (2025)). To do so, these studies have mostly relied on datum-based shoreline positions or even beach volume changes, enabling a robust quantification of the beach morphological response to ENSO. Other studies have related to the influence of ENSO on SDW position advance or retreat (e.g.; Almar et al. (2023); Vos et al. (2023a)), relying on SDW data from coarse resolution monthly composite of NDWI images in the work of Almar et al. (2023) and fine scale monthly-sampled (time-corrected) SDS data in the work of Vos et al. (2023a)]. While the work of Vos et al. (2023a) presents a higher resolution and shoreline detection closer to the methodological standards expected for accurate local assessments of shoreline change (Warrick et al. (2024)), the metrics used in both studies still incorporate variability driven by sea-level fluctuations, which are amplified during El Niño events. This integration, which is also present in our data and analyses in Chapter III, makes it more challenging to distinguish between morphological evolution under erosion and shoreline shift due to water level variability associated with ENSO. However, these studies do provide valuable insights into multi-facet regional patterns of waterline variability, which, not only morphological, give highly relevant insights for assessing coastal vulnerability associated to ENSO. In particular, such indicators capture sea-level fluctuations informing on extreme water levels which directly influence flooding risks and the exposure of coastal populations and infrastructure (Almar et al. (2021b)). In this sense, while they may not isolate morphodynamic patterns, satellite-derived waterline methods still serve as critical mean of observation for understanding coastal hazards under present climate variability, and provide valuable data materials for anticipating future coastal hazards in under changing climate.

Acknowledging and explicitly defining the chosen shoreline indicator is essential for robust interpretation. Without such clarity, comparisons across studies or monitoring programs risk conflating hydrodynamic variability with true morphological change. By unpacking the multiple con-

ceptions of the shoreline, this thesis aimed to emphasize both the potential and the limitations of each approach, and stresses that progress in coastal monitoring and modeling will depend equally conceptual and methodological advances.

V.1.2 Potential limits of using shoreline indicators as a proxy for beach morphodynamics

Beyond the ambiguity in defining shoreline, beach profiles exhibit spatially nonuniform dynamics, which limit the representativeness of any single 2D indicator. For narrow intertidal profiles, such as Torrey Pines, morphodynamics is found to be largely uniform across the intertidal beach, allowing to reliably extrapolate a fixed-elevation datum-based shoreline position time series to overall intertidal beach morphodynamics, and thus to infer volumetric changes. By contrast, wider profiles, as observed at Porsmilin or Perranporth, display contrasting behaviors between different elevations, especially at the seasonal scale. This vertical-dependent pattern highlights a fundamental limitation: shoreline indicators, even when corrected for tides or sea-level anomalies, cannot fully represent the complex internal sediment distribution, resulting for example in local profile translation, slope adjustments (both highlighted across intertidal beaches in Chapter IV), and sandbar migration.

The parametric model of intertidal morphodynamics used in Chapter IV further highlights these processes. By decomposing intertidal beach profile variability into translation and rotation components, we observed that some sites are dominated by translational behavior (e.g., Torrey Pines, Truc Vert), while rotation contributes more significantly at others (e.g., Porsmilin). Translation of the intertidal profile can be interpreted in two ways: it may reflect a broader erosion or accretion trend of the entire beach profile, or it may represent a local adjustment, where the intertidal zone exchanges sediment with the upper and lower parts of the profile. In this latter case, translation is more ambiguous with respect to whether the beach as a whole is eroding or accreting. In contrast, in the first scenario—where the entire beach section uniformly shifts seaward or landward—translation necessarily reflects an imbalance in the sediment budget, i.e., between sediment input to and output from the beach section.

This interconnection between beach features is well illustrated by the control exerted by the sandbar on shoreline position (e.g., Janušaitė et al. (2023); Medellín et al. (2025)). At sites exposed to seasonal variations in wave climate, sandbar displacement is highly seasonal: higher wave energy generally drives the sandbar seaward while simultaneously shifting the shoreline landward, whereas calmer conditions favor the landward return of the sandbar and a seaward advance of the shoreline, with eventually a merge of the two feature resulting in a further accreted shoreline. Preliminary investigations of these links, presented in Appendix C, illustrate these strong and significant negative correlations between satellite-derived shoreline and sandbar positions at the seasonal scale at Torrey Pines and Ensenada, consistent with results from Medellín et al. (2025) for beaches in northwestern Yucatán, Mexico. Most importantly, these preliminary results suggest that equilibrium shoreline model outputs—in this case, the ShoreFor model (Davidson et al. (2013); Splinter et al. (2014))—can be improved with the incorporation of an additional term coupling the shoreline and sandbar through a mechanical spring link, conceptually representing the distance of wave energy dissipation. When the sandbar is located further offshore, incoming wave energy is partially dissipated before reaching the shoreline, reducing direct erosion of the intertidal beach. In contrast, when the sandbar migrates shoreward, the zone over which waves dissipate energy becomes narrower, and a greater proportion of wave energy reaches the shoreline, mobilizing sand and causing erosion under energetic storm conditions. So far, the spring link between the sandbar and the shoreline has been associated with a constant stiffness coefficient, but in fact it should vary with wave conditions to capture more complex mechanisms: the progressive attachment of the sandbar to the intertidal beach, which can result in shoreline accretion of the shoreline under calm wave conditions (Bergsma et al. (2019b)); or the net offshore migration of the sandbar, not necessarily forced by a trend in the wave conditions but gradually depriving the upper shoreface from a crucial buffer and causing the creation of a sandbar directly from the intertidal beach, resulting in shoreline erosion (e.g., Ruessink et al. (2003); Anderson et al. (2023)).

Similar internal sand redistribution can be observed within the berm-dune system, with the dune known to evolve on interannual and longer timescales (e.g., Stive et al. (2002); Burvingt and Castelle (2023)). Dune erosion can supply sediment to the intertidal beach, resulting in

shoreline accretion, as illustrated in Figure V.1, which shows beach elevation profiles from a section of Grayland Beach (WA, USA). In such cases, where different components of the beach system display contrasting behaviors, it becomes challenging to define the overall state of the beach or to anticipate its future profile.

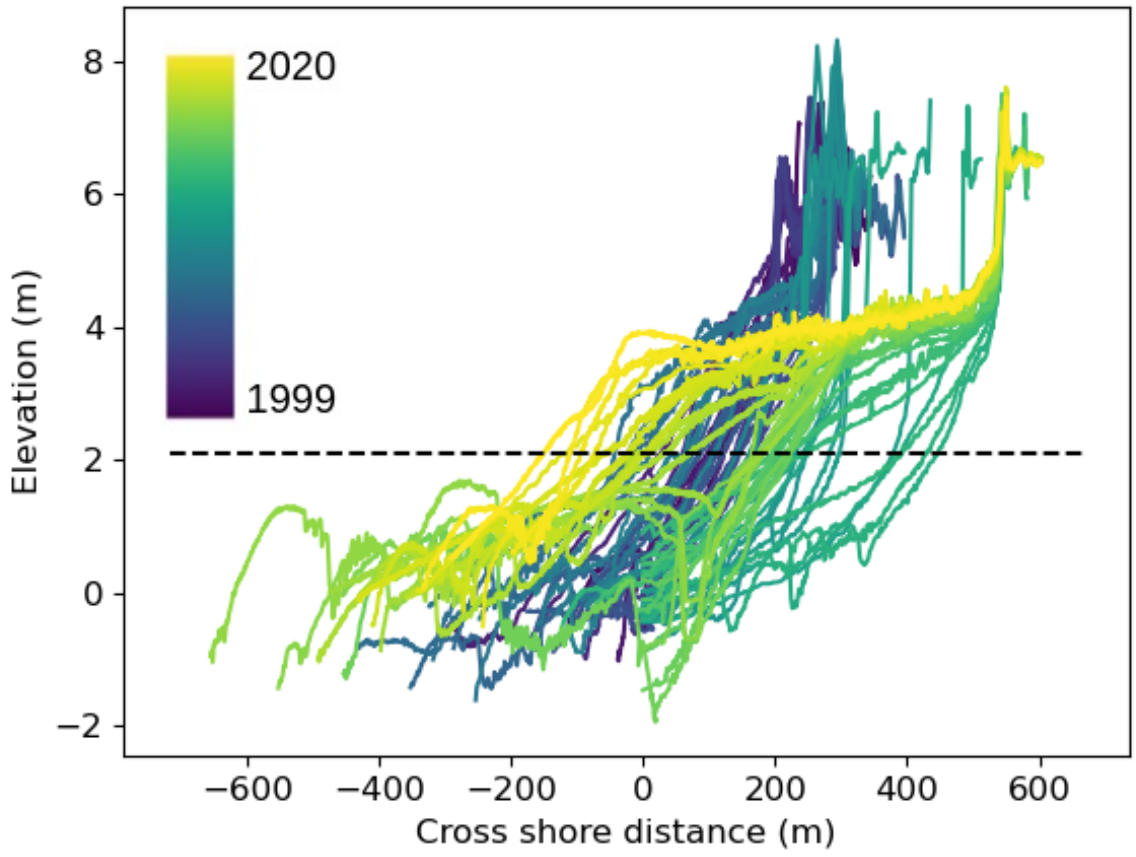

FIGURE V.1 Quarterly beach elevation profiles surveyed between 1999 and 2020 (*Ruggiero et al., 2005*), with elevations referenced to the NAVD88 datum. The black dashed line represent the MHW elevation.

In this integrated and multi-scale conception of the beach system, apparent accretion of the shoreline part may mask erosion elsewhere, and vice versa. Robust assessments of coastal change therefore require not only shoreline indicators, but also a characterization of sediment exchanges among dunes, intertidal zones, and offshore bars.

V.1.3 A broader conception of the beach and its dynamics

Current reliance of coastal managers and decision makers on shoreline indicators inevitably raises the question of how well they capture profile-wide morphodynamics and risk exposure to flooding, and points toward the need for an integrated framework to bridge this gap. Fully resolved explicitly resolved beach hydro-morphodynamic modeling is likely to become increasingly feasible in coming years (e.g.,Wilson (2023)), yet for now it remains computationally costly and demands fine-tuned calibration, restricting applications to a few hindcast cases [e.g., reproduction of the DUCK94 experiment, (Stauble and Cialone (1996))]. Anticipating beach evolution therefore still relies heavily on simplified physics and data-driven approaches.

Among these, equilibrium and hybrid shoreline models have gained wide popularity, with coordinated community benchmarking efforts such as ShoreShop (Montaño et al. (2020); Mao et al. (2025)). Models that were once limited to wave-driven cross-shore mechanisms now increasingly account for additional processes, including alongshore sediment transport and sea-level rise (e.g., Vitousek et al. (2017); Robinet et al. (2018)). Data pre-processing techniques have also been identified as key to improving model performance (Mao et al. (2025)), contributing to recent advances in reproducing shoreline variability at test sites. However, these methods are associated to their own limitations: (i) they depend on extensive calibration data and retain strong predictive capacity only over short windows after calibration (e.g., Azorakos et al. (2024)), and (ii) their focus on shoreline position inherits the ambiguity of this multi-definition proxy, leaving them unequipped to capture full-profile morphodynamics. In an opinion piece, Seenath (2025) state that shoreline models should incorporate probabilistic approaches coupled with more detailed information on the depth of closure and the human-induced alteration of sediment transport.

The very notion of 'equilibrium' must itself be treated with caution as beaches are open systems where sediment inputs and outputs are rarely balanced, meaning that truly stable states are statistically improbable over meaningful timescales (Pranzini and Williams (2021)). Instead, many morphodynamic changes are driven by non-equilibrium processes such as migrating sand waves (e.g., Zhou et al. (2020); Warrick et al. (2023)) or abrupt storm-driven rearrangements (e.g., Harley et al. (2022)). This limitation is becoming particularly critical in a context where anthropogenic drivers of coastal change — from damming and dredging to hard coastal defenses

— increasingly rival or even exceed natural process-driven morphodynamics at many sites [e.g., the massive sediment input to the coast after the removal of a dam on the Elwha River (Warrick et al. (2019))]. Infrastructure proliferation, river damming and sand mining/nourishment reshape coastal sediment fluxes (Syvitski et al. (2022)). Although case studies show how these anthropogenic influences can be observed, like the beach evolution in response to sand nourishment (e.g., Cabezas-Rabadán et al. (2025)), no comprehensive modeling framework currently exists to systematically incorporate them. The data requirements for doing so remain prohibitive beyond local, finely tuned applications (e.g., Dibajnia et al. (2004)). This widening gap between the scale of anthropogenic impacts and the capacity of existing models underscores the urgency of developing integrated approaches that go beyond shoreline indicators toward profile-wide, behaviorally informed morphodynamic frameworks incorporating sediment budget data.

The long-standing concept of beach state (Wright and Short (1984)) provides a powerful basis for comparing sites according to their environmental conditions, and offers a natural foundation for extending shoreline-based models beyond their current limitations. The beach state classification, framed through the dimensionless fall velocity number $\Omega = H_b/(T_p\omega)$ (H_b being the breaking wave height, that can be estimated from H_s and T_p), distinguish reflective, dissipative, and intermediate states, the latter spanning a rich diversity of sandbar morphologies. Extensions of this framework that incorporate tidal range normalized by significant wave height [$RTR = TR/H_b$ (Masselink and Short (1993); Castelle and Masselink (2023)] have further broadened its relevance across coastal settings. Beach state classifications theoretically allow the comparison of sites sharing similar Ω and RTR values, thus enabling, by similarity, to characterize a whole class of sites by the description of one site of the class.

These classifications are valuable for cross-site comparisons and for guiding interpretations of beach morphology. They also open opportunities for dynamic considerations. First, beaches are not fixed in one category, but rather shift between states on seasonal scales (e.g., Dubarbier et al. (2017)), and potentially on interannual and longer scales under evolving forcing conditions. Beach state change mirror the redistribution of sediment across the beach–dune–bar continuum, highlighting the importance of connectivity between beach features.

Building on this perspective, one promising avenue is to complement traditional morphological classifications of beach states with classifications of their dynamic behaviors across timescales. For example, the rotational profile patterns observed at Porsmilin (Lemos et al. (2018) and Chapter IV) highlight how some beaches exhibit characteristic modes of adjustment that differ from simple profile translation. Identifying such modes of dynamics—whether seasonal rotation, interannual bar migration, or dune–berm exchanges—could help define a richer typology of beach responses. This framework can not only capture the static shape of the beach profile but also its characteristic pathways of adjustment during upstate and downstate sequences.

Such a framework could also enhance the use of shoreline indicators in predictive models. Knowing the dominant dynamic behavior of a given beach type, a measured shoreline displacement at a specific timescale can be more meaningfully translated into system-wide morphodynamic implications. For instance, a shoreline retreat may reflect berm erosion only, a profile-wide erosion, or a redistribution of sediment between the berm and sandbars/dunes. Embedding these behavioral typologies into shoreline modeling would make it possible to extrapolate shoreline variability into broader morphodynamic contexts, thereby strengthening both scientific interpretations and the predictive power of coastal models.

V.2 Towards more robust methods for satellite-derived nearshore monitoring

V.2.1 Future of satellite-derived shoreline monitoring

In a recent review paper called "The future of coastal monitoring through satellite remote sensing", Vitousek et al. (2023a) highlighted several challenges associated with satellite monitoring methods. They identified as key issues the pixel resolution of satellite imagery, the co-registration/georeferencing of the imagery, corrections of wave induced variations of the sea level in shoreline position signals and the sensitivity of shoreline detections to the algorithms used. Several of these issues are seemingly on the path to being solved. Recent satellite missions, such as PlanetScope, offer multi-spectral imagery with finer pixel resolution than Landsat or Sentinel-2,

yielding improved shoreline detection accuracy (e.g., Doherty et al. (2022)) with high revisit frequency (Turner et al. (2021)). While these missions currently cover a relatively short period (less than 10 years), they hold promise for shoreline monitoring over the coming decades, and future missions may provide even finer-resolution images for more precise and frequent detections.

Errors associated to co-registration and georeferencing, also highlighted as a key limitation for reliable SDW/SDW acquisition by Vos et al. (2023b), were not explicitly corrected nor quantified in our validation study in Chapter II. Images are quality-controlled by data publishers (ESA, USGS) to ensure that georeferencing errors remain below 0.5 pixel with 95% confidence, corresponding roughly to 5 m for Sentinel-2 and 15 m for Landsat (Enache (2022)). Recent methods have demonstrated the ability to reduce georeferencing errors by up to 1 pixel (e.g., the publicly-available Simarro et al. (2025)). Given that SDW extracted at microtidal sites in Chapter II already exhibit sub-pixel variability with the best-performing methods, we expect errors due to georeferencing issues to have minimal impact on our results. Even under ideal conditions, SDW position errors remain fundamentally constrained by the spatial resolution of Landsat and Sentinel-2 sensors, never dropping below a few meters (Bishop-Taylor et al. (2019a); Sánchez-García et al. (2020)).

However, accurate corrections for sea-level variations remain challenging, and a critical point in areas subject to large fluctuations of the coastal sea-level (e.g., meso- and macrotidal environments, upwelling areas). Regarding wave-driven sea level variability, Vitousek et al. (2023a) outlined that empirical wave runup models, such as that of Stockdon et al. (2006), allow estimation of the setup contribution to coastal sea level and the statistical extent of wave swash. These wave setup/runup corrections have been applied in several studies (e.g., Castelle et al. (2021); Konstantinou et al. (2023); Graffin et al. (2023)), successfully improving the accuracy of shoreline detections when compared to validation with datum-based shorelines. However, as noted by Toomey et al. (2024), the systematic use of empirical wave setup formulations over large spatio-temporal scales can lead to erroneous SDS corrections, partly because they rely on coastal wave and beach slope data that are sparsely available and often need to be derived from coarse-resolution products. Wave setup can be modeled in a more robust way by explicitly simulating wave propagation toward the shore, using numerical models such as SCHISM, which can

account for wave transformation as it interacts with the bathymetry to provide spatially resolved estimates of the nearshore wave-driven sea-level contribution (Martins et al. (2022)). In addition to the uncertainty in estimating wave setup, the contribution of wave swash, the high frequency oscillation of waves washing up and down the beach, remains unresolved at large scales, introducing an unknown sea-level component that affects waterline positions without allowing for accurate quantification or correction. Additionnally, sea level variability is not only driven by tides and waves. Upwelling/downwelling, steric and inverse barometer effects are known to drive coastal sea level changes at various spatio-temporal scales (Woodworth et al. (2019)) but remain largely overlooked when it comes estimate sea-level contributions in shoreline position signals. To this end, altimetry products, such as DUACS-SSALTO, can provide first order estimations of sea-level anomalies induced by these mechanisms. More generally, behind the assessment of vertical coastal sea level variability lies the goal for estimations of horizontal sea level-driven waterline displacement. This step currently relies on the assumption of a constant, linear beach profile derived from the waterline position time series (Vos et al. (2020)), which is particularly unrealistic at mesotidal and macrotidal sites.

In Chapter II, we addressed the challenge of designing reliable algorithms for SDW extraction. Building on the work of Bishop-Taylor et al. (2019a) and Vos et al. (2023b), we compared 20 algorithms constructed from five water-differentiating indices and four thresholding methods, validating their performance in retrieving waterline positions across eight reference sites. While we observed substantial differences in the accuracy of these algorithms, no single method consistently outperformed the others. The first-order factors of uncertainty we identified were beach slope and tidal excursion, both of which were linearly correlated with detection errors across sites (with a slightly better correlation for tide excursion), enabling the formulation of empirical laws to estimate errors. As discussed in this chapter, the site-dependent nature of SDW/SDS detection error can be attributed to three main sources:

- **Waterline detection at low tide.** At sites with a large tidal range and/or a gentle slope, the intertidal zone is wide. At low tide, parts of this zone may remain wet, with darker sand surfaces creating ambiguity in the spectral signature. This can result in erroneous detections, where the algorithm misclassifies the wet/dry sand line as the instantaneous waterline (Castelle et al. (2021); Graffin et al. (2023)).

- **Projection of vertical sea-level variability into horizontal waterline variability.** A key assumption when projecting waterline positions to a reference shoreline (at a fixed elevation enabling comparison across images acquired under different sea levels) is that the beach profile is linear. This assumption holds reasonably well when the elevation difference between the acquisition-time sea level and the reference elevation is small (< 1 m). However, at larger elevation differences, deviations from the linear profile—particularly at low tide—lead to systematic errors when projecting to reference datums such as MSL or MHW.

- **Coastal sea-level uncertainties.** Small errors in sea-level estimation translate into larger uncertainties in horizontal waterline position at gently sloping beaches. Tide model outputs (e.g., FES2022) have typical accuracies on the order of 10 cm (see Figure III.2), an other sources of coastal sea-level variability are generally neglected. As a result, shoreline position estimates derived from waterlines are especially uncertain at low-gradient sites.

These limitations are particularly constraining for monitoring deltaic environments, which exhibit extensive, low-gradient morphological surfaces. In such settings, the nearshore topography is extremely flat, typically in the order of $\tan\beta = 10^{-4}$ (Zavala et al. (2021)), with the river influencing the water level at a large range of timescales, exacerbating the aforementioned limitations for flat environments subject to large sea level fluctuations. For these reasons, mapping such environments on large scale based on the automated approaches presented in this thesis seems, to date, out of reach.

Recommendations from this validation regarding algorithm of waterline detection are simple : over microtidal and/or steep sites, which are recognized as less challenging for waterline detections, differences between algorithms are small and most yield sub-pixelic performances with Sentinel-2 and Landsat imagery even if SCoWI, AWEIns and AWEIsh indices coupled with any thresholding yielded good performances; over macrotidal and/or gently slopped sites, the choice of thresholding method become crucial as the pixel distribution in the image after band combination is likely to deviate greatly from a bimodal distribution, potentially biasing the threshold values from Otsu or WP methods.

Another important point, largely neglected in the literature but found highly relevant during

the research for this thesis, is the need to develop robust algorithms for detecting and removing erroneous observations from SDW/SDS time series. Two main factors can compromise the quality of waterline detection: (i) insufficient image contrast, for instance due to sensor issues or atmospheric conditions such as fog, and (ii) partial cloud cover obscuring parts of the coastline. In both cases, simple automated band-combination and thresholding methods will still return an output, even though the resulting detection is erroneous. To prevent the presence of misdetected waterlines in the SDW/SDS time series, we developed two tools : i) an image filter, complementing the cloud filters based on full-image Landsat or Sentinel-2 cloud coverage metadata, that specifically analyze the cropped image used for the waterline detection to assess if the image is contaminated or not with cloud cover, and ii) an outlier removal function, applied to the time series of cross-shore waterline position, that remove data points deviating too much from the gaussian-like distribution of cross-shore waterline values of the time series. Although effective, these methods have their limitations. For example, at sites with significant tidal ranges, the range of possible values of cross-shore waterline position is wide, making it difficult to identify specific outliers.

The use of SAR imagery is expected to expand the monitoring capacity, especially in tropical and high-latitude areas where persistent cloud cover severely limits the number of exploitable optical images. However, recent applications of satellite-derived waterline methods to SAR imagery reveal significant challenges in automatically retrieving waterline positions from radar time series, primarily due to speckle noise, orbit-dependent image quality, and the sensitivity of radar signals to surface roughness and moisture conditions rather than purely to the land–water boundary (Paz-Delgado et al. (2022); Zollini et al. (2023); Savastano et al. (2024)). SAR-Optical fusion methods, which leverage deep learning to reconstruct cloud-contaminated optical images using SAR inputs, have recently shown promising results for recovering shorelines otherwise obscured by persistent cloud cover (Mao and Splinter (2025)). By combining the cloud-penetrating capacity of SAR with the spectral sensitivity of optical imagery, and taking advantage of increasingly high spatio-temporal resolution, these methods can extend satellite-derived shoreline datasets from monthly to near-daily resolution, enabling the detection of fine-scale and event-driven coastal change.

Together, these advances open promising avenues for tackling shoreline monitoring from regional to global scales. At CNES, the Shoreliner method (Bergsma et al. (2024), with additions from Chapter II), is already being applied at continental scales, including Western Europe, Africa, and the American West Coast, with further acquisitions planned. The framework developed in Chapter III will in turn be extended to other regions, enabling the characterization of long-term trends, seasonal cycles, and interannual variability of the shoreline along coastal areas that remain largely undocumented. Nevertheless, the reliance on cloud platforms for accessing historical multispectral satellite imagery has so far limited the speed of these large-scale assessments. By fully exploiting the computational efficiency of cloud platforms (e.g., Calkoen et al. (2025)) or complementing them with institutional high-performance computing clusters (e.g., TREX at CNES), the implementation of SDW/SDS pipelines to obtain multidecadal time series of shoreline position at the global scale now appears within reach.

Looking ahead, future work will focus on assessing accuracy of large scale satellite-derived products, informing on how many noisy measurements must be aggregated to generate a robust shoreline product (e.g., within a given accuracy threshold), and, by extension, what mechanisms can be reliably captured at such coarse resolutions. As emphasized by Castelle et al. (2022), the same question arises in space: how many noisy measurements must be averaged spatially to obtain a reliable signal, and what does this imply for our ability to observe fine-scale morphodynamics? These considerations also raise a broader issue: how frequently must shorelines be measured to provide reliable knowledge of their state at a given time? The answer depends on the dominant scale of variability at each site and over the study period. Bergsma et al. (2022) analyzed coastal wave variability over 24 years (1993–2017) and highlighted that dominant time scales of wave energy variability vary across regions, with mid- and high-latitude coasts generally controlled by higher-frequency variability (weekly to bi-weekly), while tropical coasts are more strongly influenced by lower-frequency variability (monthly to seasonal). These observations are partially reflected in coastal morphodynamics, particularly at wave-dominated sites, and sub-sampling the variability of shoreline position relative to its dominant timescales can result in misrepresenting coastal evolution. On the other hand, variability at one site is generally mirrored by distant sites, with spatial coherence typically increasing as the characteristic timescale lengthens—short-term fluctuations tend to remain local, while interannual or decadal modes can synchronize responses

across entire ocean basins (e.g., Barnard et al. (2015)). Taken together, these considerations point toward the development of global shoreline datasets enriched with reliability flags, explicitly indicating for given product (e.g., a monthly-sampled global shoreline product derived from Sentinel-2 and Landsat imagery) the mode of variability that can or cannot be captured at each site. Such a framework would not only standardize the interpretation of satellite-derived shoreline products but also highlight the regions where additional finer monitoring efforts are most urgently required.

V.2.2 Integration of alternative satellite-derived beach features for a richer representation of the coastal system

In parallel with SDW developments, additional methods have emerged to monitor the coast, focusing on alternative coastal indicators. For instance, the Coastal Toolkit—commonly used to derive SDW/SDS from satellite imagery—has been adapted to create VedgeSat (Muir et al. (2024)), which enables the monitoring of the vegetation front, considered by (Boak and Turner (2005) as an alternative definition of the shoreline. The vegetation front is an interesting proxy: while it has certain limitations for global monitoring (as not all beaches are bordered by natural vegetation), it also presents several valuable advantages. (i) The vegetation edge is both a morphological and biological proxy (whereas the waterline is primarily morphological and hydrodynamic), and as such it is not impacted by short-term sea-level variations, making it detectable independently of tidal stage and wave activity. (ii) Because beach vegetation is rarely submerged under normal conditions (outside of storms), the vegetation edge is generally visible, and its greenish color contrasts strongly with the darker tones of the beach, making it easily extractable using vegetation indices such as NDVI (Normalized Difference Vegetation Index, based on near-infrared and red reflectance). (iii) The vegetation edge is the only shoreline indicator directly visible in near-nadir remote sensing observations that informs on the state of the beach-dune system. Mechanistically, its evolution drives dune development, as vegetation acts as a catalyst for dune growth (Moore et al. (2025)). This potential for coastal monitoring is particularly valuable in areas with a large tidal range and/or energetic wave climate, such as Northwestern Europe (see Figure I.5). In a recent study, Kümmerer et al. (2025) applied a custom methodology similar to VedgeSat to derive cross-shore vegetation edge positions in the Outer Hebrides, Western Scotland, where the

tidal range reaches up to 4 meters. Using PlanetScope imagery, the satellite-derived vegetation lines achieved an accuracy of 3 m, a significant improvement compared to the expected 15–30 m errors typically observed for SDW retrieval at such sites with Sentinel-2 or Landsat imagery (corresponding to intertidal beach widths of 112–220 m, refer to Eq. II.13 and II.14).

Optical satellite imagery has also been recently applied to retrieve sandbar positions (Tătui and Constantin (2020); Taveneau et al. (2024); Frugier et al. (2025)). These methods generally operate by detecting white water (foam generated by wave breaking) through band combinations that enhance its contrast with surrounding water. White water patches located offshore from the shoreline are typically associated with wave breaking over shallow features, most often corresponding to submerged sandbars. The recent implementation by Frugier et al. (2025) has enabled the automation of sandbar detection on Landsat (5, 7, 8, and 9), Sentinel-2, and VENuS imagery, with successful applications at Duck, NC, USA. The method achieved an accuracy of around 20 m, which is relatively coarse compared to SDW time series at the same site. However, because sandbar position variability at Duck is much larger than shoreline variability, the resulting signal-to-noise ratio remains favorable for accurate sandbar migration tracking. This method is associated to its own limitations, sea level fluctuations do not alter significantly the detection (in the limit of still allowing wave breaking) as vertical sea level variability does not project into horizontal sandbar displacement, contrary to waterline position, but exact position of the top and the sandbar is ambiguous when inferred from white water patches. Additionally, this method relies on wave breaking, which restricts the range of applicable sites and limits the number of exploitable images where suitable wave-breaking conditions are present.

In addition to these methods based on distinct coastal indicators, 'data cube' approaches have emerged. These consist of deriving intertidal beach topography by acquiring numerous SDW measurements close in time. By associating the waterline (e.g., Bishop-Taylor et al. (2019b)) or water-differentiating index maps (e.g., Chen and Wang (2025)) time series with corresponding coastal sea-level records, it becomes possible to reconstruct the intertidal beach profile, under the assumption that the beach morphology does not undergo drastic changes between successive waterline extractions (Bishop-Taylor et al. (2019b); Salameh et al. (2020)). A key consideration for this approach is the trade-off between the number of observations used and the ability to cap-

ture the full range of dynamic intertidal profiles, particularly in highly energetic environments. SAR imagery could complement these methods, expanding the temporal and spatial coverage in regions frequently obscured by clouds. Data-cube approaches have already been applied at the continental scale to map intertidal beach areas in Australia (Bishop-Taylor et al. (2019b)), and publicly-available algorithms facilitating the application of the approach have recently emerged (*eo-tides* : Bishop-Taylor et al. (2025)). This methodology is especially valuable for meso- and macro-tidal beaches where tidal variability dominates the waterline signal. Importantly, the reconstructed profiles derived from such datasets could also be used to apply sea-level corrections and thus refine SDS estimations from SDW. Yet, the same limitations and perspectives raised above for SDW and SDS also apply to intertidal topography mapping: because these methods rely on aggregating large numbers of waterline measurements at different sea levels, they necessarily reduce the temporal resolution at which intertidal morphodynamics can be resolved. This raises a key question for future applications—what are the typical timescales of intertidal morphodynamics, and how well can they be captured within the constraints of data-cube methodologies? Future work could leverage higher-frequency revisit missions such as VENμS (daily acquisitions, with several tiles in Northwestern France, where the tidal range is high) to map intertidal topography in macrotidal environments (available VENμS tiles: Morbihan Bay, Brest, or Guérande). In such settings, SDW extractions could be rigorously validated against SHOM tide-gauge records (e.g., Le Crouesty, Brest, Saint-Nazaire), while sub-sampling the observations would allow testing the sensitivity of data-cube methods and the accuracy of the derived intertidal topography to monitoring frequency.

V.2.3 The potential of remotely-sensed topography-bathymetry continuum

The comprehensive 3D mapping of coastal zones, capturing the full topography–bathymetry continuum $z(x, y)$, is currently under active research development (e.g., Almar et al. (2021a); Bergsma et al. (2021); Palaseanu-Lovejoy et al. (2023); Klotz et al. (2025); Frugier et al. (2026)). This research (to which could be added the aforementionned intertidal topographhy mapping methods) can be divided into the remote measure of i) subaerial beach topography, ii) surfzone bathymetry, and iii) nearshore bathymetry.

Subaerial beach topography can be remotely derived from satellite data using stereo-imagery

methods, which rely on observing the same object from at least two different viewing angles to reconstruct its external 3D structure. Using satellites, this can be achieved from a single satellite taking images of a same object at different time, or using a constellation (two satellites or more) taking images of the same object at the same time with different angles. The optical satellite VENuS enabled the generation of stereo-imagery using a single-pass multispectral image as a same spectral band (600-640 nm) is captured twice at (B5/B6 bands) with 2.7 s of lag, allowing to capture images of a site with 1.5° observation angle difference (Dick et al. (2022)). Bergsma et al. (2021) derived topography (and bathymetry, see below) using this methodology applied to VENuS satellite imagery and obtained at Duck a reconstruction of the subaerial topography with a vertical accuracy of 1 meter. The constellation of agile satellites Pleiades, can also be used (here as synchronous acquisitions) to derive subaerial beach topography, yielding submetric accuracy (Almeida et al. (2019); Burvingt et al. (2025)). The recent launch of the CNES CO3D satellite mission, comprising four optical satellites with a 50 cm ground resolution and specifically designed to derive topography through synchronous image acquisition, is expected to provide a crucial source of data for deriving sub-aerial beach topography at the global scale. A global static product of topography is anticipated to be published by 2027, and the revisit capability could allow the generation of a dynamic product, with all data made available on the GEODES platform (Lebègue et al. (2020); Michel et al. (2020)).

Surfzone bathymetry, which approximately encompasses the first five meters of depth in the coastal area, can be estimated from satellite imagery. The most widely used method to derive bathymetry from optical satellite imagery is the ratio-transform approach developed by Stumpf et al. (2003), which estimates depth from the log ratio of reflectances in different spectral bands. This method requires only two tunable parameters and can retrieve depths down to 25 m in clear waters, with reported RMSE typically on the order of 0.5–1.5 m in shallow water. In practice, outside of low-energy and clear-water environments, the method performs reliably only within the first meters of depth. Under adverse environmental conditions (e.g., turbidity, sunglint, strong sky reflectance), it cannot be applied robustly. Despite these limitations, the methodology provides a widely adopted framework to estimate water depth from multispectral satellite imagery. Recently, Frugier et al. (2026) proposed an automated calibration procedure that exploits the position of the shoreline (detected using standard SDW algorithms) and the offshore breaking line (as an in-

dicator of sandbar position) to constrain the two free parameters of the Stumpf model. Applied at Duck, NC, USA, the method yielded sub-metric accuracy compared to in-situ bathymetric surveys down to 4 m depth, demonstrating its potential as a valuable tool for shallow-water bathymetry monitoring worldwide.

Nearshore bathymetry, extending beyond the surfzone into deeper waters (typically 5–25 m depth), can also be inferred from satellite imagery by exploiting wave inversion techniques. These methods rely on the principle that wave propagation is affected by the underlying bathymetry, as wave celerity decreases with decreasing water depth. Recent advances have enabled the detection of wave propagation patterns directly from optical imagery, particularly using Sentinel-2, by exploiting the temporal lag between different spectral band acquisitions to observe wave displacement. The S2Shores pipeline (Bergsma et al. (2019a); Almar et al. (2019); Bergsma et al. (2021); Almar et al. (2024a)) proposes three methods to derive wave celerity fields from which the local water depth can then be obtained using the linear wave dispersion relation:

$$c^2 = \frac{g}{k} tanh(kh) \Leftrightarrow h = \frac{tanh^{-1}(c^2 k/g)}{k} \tag{V.1}$$

with k the wave number (inverse of the wavelength L) and c the celerity.

A large-scale application of this satellite-derived bathymetry method (Radon-discrete Fourier transform) along the West African coast (Marchesiello et al. (2024)) successfully produced regional bathymetry maps, highlighting the potential of such approaches to monitor bathymetry in data-scarce regions. Bergsma et al. (2021) applied the same method at Duck, combining wave detection from VENμS with inversion schemes, to retrieve bathymetry in complex nearshore environments (in addition of the aforementioned subarial topography). While promising, these methods face important limitations: (i) their success depends on the ability to accurately track coherent wave propagation over space and time, which is sensitive to image quality, and (ii) they require sufficient wave energy and organized wave fields, excluding calm or strongly energetic conditions. These conditions have so far only enabled the generation of static bathymetries (aggregate of different noisy estimations to get a reliable composite), under the form of a global atlas (Almar et al. (2021a)). Despite these challenges, wave-inversion approaches complement optical-reflectance methods by extending bathymetry inversion to greater depths (up to 25 m)

and over larger areas, providing valuable insights into coastal morphology and sediment dynamics at regional scales.

Altogether, these methods pave the way for deriving the full topography–bathymetry continuum entirely from satellite-based observations. In this context, waterline, shoreline, and intertidal beach detections remain crucial, as they provide a reference interface for merging subaerial topography with subaqueous bathymetry. Achieving the ultimate objective of mapping, at large spatial scales, a dynamic topography–bathymetry continuum would enable more comprehensive analyses of coastal morphodynamics, including the quantification of sediment budgets within the nearshore zone. Such an integrated perspective would extend our understanding of contemporary coastal dynamics beyond the shoreline position alone which, while valuable, captures only part of the total sediment transport processes shaping the nearshore.

V.3 What role for satellite-based monitoring in predicting coastal risks ?

A central motivation for studying coastal morphodynamics lies in its societal relevance. Communities, infrastructure, and ecosystems along the coast are exposed both to chronic erosion and to episodic vulnerability during extreme events. Anticipating these episodes—whether arising from long-term shoreline retreat under sea-level rise or from storm-driven erosion—is critical for risk assessment, climate adaptation, and sustainable coastal management. In this perspective, the applied purpose of coastal research extends beyond describing past and present shoreline variability: it is to translate observations into predictive tools, capable of anticipating future coastal states across timescales relevant for emergency response (hours to weeks) and long-term planning (years to decades). Figure V.2 presents a conceptual framework summarizing the tools available to describe future coastal hazard assessment, informed by the expanding availability of globally consistent remote-sensing datasets.

At short timescales (daily to weekly forecast), coastal change is mostly driven by meteorological extremes that reshape beaches within hours or days (Pugh and Woodworth (2014); Benveniste

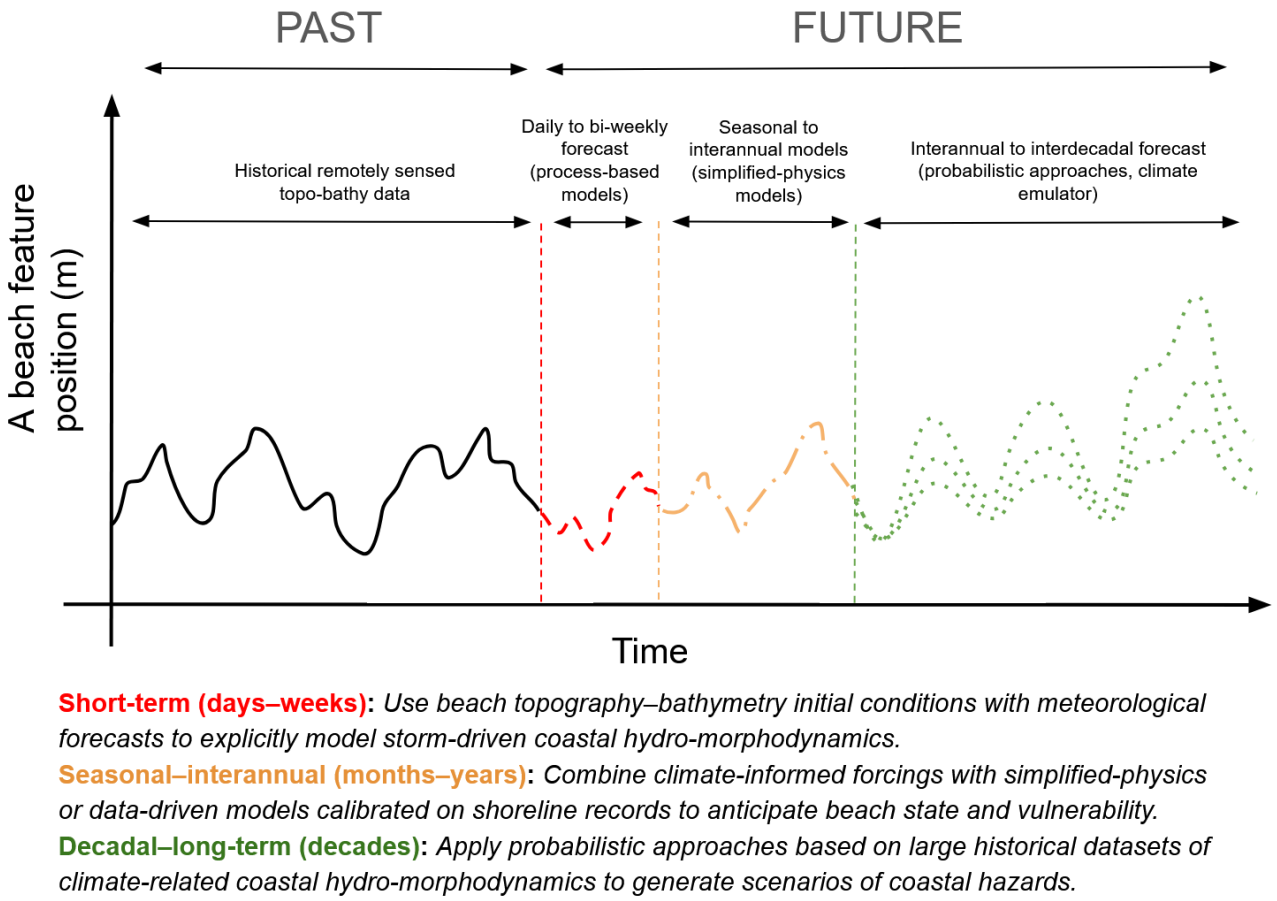

FIGURE V.2 Conceptual pathways for coastal hazard assessment at different timescales, coupling remotely-sensed morphodynamics with forecast of sea-level and wave characteristic data and modeling approaches.

et al. (2019)). Predicting these impacts remains highly challenging. Short-term fluctuations of atmospheric and oceanic conditions are chaotic and associated with large uncertainties when forecasted beyond two weeks (Gettelman et al. (2022)), limiting our ability to anticipate long in advance the forcing conditions that drive extreme coastal change. Moreover, the morphodynamic response to such events is strongly site-specific, reflecting local topography, sediment availability, and antecedent beach states (Garzon et al. (2023)). As a result, operational predictability of storm-induced morphodynamics at large scales remains limited, even though new tools are emerging to support emergency planning and early warning systems for storm events (Turner et al. (2024); Doyle et al. (2025)).. However, expected advances in remotely sensed topo-bathymetric products could provide the initialization data necessary to explicit model coastal hydro-morphodynamics, bridging operational forecasting with morphological realism.

At seasonal to interannual scales, prediction windows widen. Reduced-complexity models,

such as equilibrium approaches, can capture beach morphodynamics when forced with climate-informed estimates of sea-level and wave variability. Seasonal cycles are relatively repeatable, and interannual climate modes (e.g., ENSO, NAO, IOD) are increasingly well forecast. For example, ENSO event type and timing can now be anticipated up to 12 months in advance, creating new opportunities for climate-informed coastal forecasting (Boucharel et al. (2024)). Linking these forecasts to hydro-morphodynamic models—and embedding site-specific beach state behaviors—and remotely-sensed shoreline or topography-bathymetry measurements creates a pathway toward routine forecasts of shoreline variability driven by known seasonal and interannual climate variability.

At longer timescales, tackling decadal and climate-change related coastal vulnerability, we face a ceil of anticipation. For decadal climate modes such as the PDO and the Atlantic Multidecadal Oscillation (AMO), the multiplicity of interacting drivers and the short length of observational records hinder our ability to characterize their variability, making reliable forecasting challenging (Cassou et al. (2018); Mann et al. (2020)). Similarly, climate-change related mechanisms are still associated with large uncertainties and heavily depend on socio-economical scenarios that are impossible to anticipate, leaving the long-term evolution of oceanic and atmospheric variables associated to large uncertainties. However, a promising pathway lies in statistical–dynamical approaches such as the TESLA (Time-varying Emulator for Short- and Long-Term Analysis of coastal flooding and erosion; Anderson et al. (2019)) model, which builds on weather-type classification (Camus et al. (2014b,a)) to connect atmospheric circulation patterns with wave and sea-level conditions. This framework is used to reconstruct realistic coastal sea-level and wave-climate time series at multiple timescales (e.g., Cagigal et al. (2020)), and, when combined with beach morphological data, it enables projections of climate-induced beach response to long-term climate variability (Cohn and Anderson (2025)) and associated flooding risks (Leung et al. (2024)). Such frameworks offer a pathway to move from scenario-based vulnerability assessments to probabilistic predictions of coastal risk evolution under decadal climate variability and climate change (e.g., Ranasinghe (2016); Hanslow et al. (2018); Li et al. (2018); Ranasinghe et al. (2023)). Remote sensing will play a critical role in these predictions, providing consistent data for model training and/or calibration and/or assimilation, and informing non-forced, stochastic processes that are otherwise poorly represented in models, such as sand-wave propagation (Warrick et al. (2023)).

Taken together, these advances in coastal monitoring and predictive modeling could enable systematic assessments of coastal vulnerability across timescales . By combining remotely sensed shoreline and topography-bathymetry datasets, climate-informed forcing predictions, and behaviorally constrained morphodynamic models, it becomes possible to derive Coastal Vulnerability Indexes (CVI) that are not static descriptors but dynamic tools. At short timescales, CVIs or similar indices for coastal threat can inform emergency response by characterizing storm-induced exposure (Turner et al. (2024); Doyle et al. (2025)); at seasonal to interannual scales, they could guide adaptation strategies linked to climate modes such as ENSO; and at longer timescales, they can frame planning decisions under scenarios of sea-level rise and shifting wave climates (Rocha et al. (2023); Dada et al. (2024)). Within this multi-timescale framework, CVIs provide a way to condense remotely-sensed data and model outputs into usable metrics for decision-making.

Conclusion générale (FR)

Cette thèse présente un cadre méthodologique pour le suivi de la dynamique du trait de côte sur les plages sableuses, intégrant des observations satellitaires de la ligne d'eau (indicateur du trait de côte) validées par des mesures de terrain, la génération et l'analyse d'un jeu de données mensuelles de positions du trait de côte à l'échelle continentale, ainsi que l'étude de la variabilité du trait de côte en lien avec la morphodynamique intertidale. Autour des trois axes principaux de recherche — évaluation méthodologique de l'extraction du trait de côte par télédétection, analyse de la variabilité du trait de côte aux échelles saisonnière à décennale, et représentativité des indicateurs du trait de côte vis à vis de la morphodynamique intertidale — émergent des résultats clés sur les mécanismes, les approches de mesure et les limites des techniques actuelles de suivi.

Sur le plan méthodologique, cette thèse propose un cadre transparent et modulaire pour l'évaluation des méthodes d'extraction du trait de côte dérivé des images satellitaires (SDW et SDS). Les comparaisons menéesdes sites divers du point de vue morphologique et hydrodynamique montrent que la performance des algorithmes dépend fortement du site d'application, mais que des combinaisons robustes d'indices et de méthodes de segmentation permettent de produire des séries temporelles fiables. Les métriques intégrées — telles que les cycles saisonniers, les tendances à long terme et la variabilité interannuelle — demeurent robustes même lorsque certaines observations individuelles sont bruitées, permettant de ressortir des informations utiles pour le suivi de l'évolution des littoraux aux grandes échelles. Certaines limites persistent, notamment celels liées aux contraintes inhérentes à l'imagerie optique (e.g., couverture nuageuse), aux incertitudes des modèles de marée et à l'ambiguité visuelle de la nature des pixels (humide/sec), mais des pistes d'amélioration sont identifiées, incluant l'utilisation de jeux de données satellitaires complémentaires (p. ex. SAR, capteurs à plus haute résolution), le filtrage automatisé des données erronnées, et le traitement géospatial des images satellitaires sur des plateformes cloud.

Cette validation permet d'appliquer ces méthodes aux larges échelles avec une connaissance des incertitudes liées à l'observation. La variabilité de la position du trait de côte le long de la façade pacifique nord-américaine révèle des cycles saisonniers et interannuels marqués. Les cycles saisonniers sont largement liés aux fluctuations de la puissance des vagues, avec de forts

contrastes latitudinaux : le PNW, la NCA et la BC présentent des corrélations élevées avec l'énergie des vagues, tandis que les réponses de la SCA et de la BCS sont plus hétérogènes et influencées par la morphologie locale, la variabilité du niveau de la mer et les événements de tempête ponctuels. La variabilité interannuelle est dominée par les événements liés à l'ENSO : El Niño induit une érosion marquée le long de la Californie et de la Basse-Californie, tandis que La Niña produit des effets plus modérés et modulés régionalement. Ces résultats soulignent l'interaction entre les forçages climatiques et la géomorphologie locale dans l'évolution du trait de côte, et démontrent que les observations satellitaires offrent un cadre robuste pour détecter et quantifier de tels signaux.

La capacité des indicateurs du trait de côte à représenter la morphodynamique de la plage intertidale est ensuite étudiée. Les analyses menées sur quatre sites montrent que la variabilité du niveau d'eau peut expliquer jusqu'à un tiers de la variabilité de la position du trait de côte à l'échelle saisonnière, et que la géométrie du profil contraint la représentativité des positions de trait de côte vis à vis du reste de la plage intertidal. Certaines plages, comme Torrey Pines, présentent un comportement de translation cohérent le long du profil de plage, rendant les proxys de trait de côte fiables comme indicateurs morphodynamique de la plage, tandis que d'autres, comme Porsmilin, affichent une variabilité non translationnelle significative. Un modèle paramétrique simple combinant des déplacements de translation et rotation explique 85 à 99 % des changements observés de profil, mettant en évidence le rôle de l'ajustement de pente (rotation) dans la morphodynamique intertidale. Ces résultats soulignent que si les mesures de trait de côte sont précieuses pour détecter les tendances à grande échelle, leur interprétation doit toujours être replacée dans le contexte des morphodynamiques locales et des effets liés au niveau d'eau dynamique.

Dans l'ensemble, cette thèse démontre qu'une combinaison de techniques de télédétection adaptées et validées par des données de terrain permet une évaluation pertinente des changements côtiers aux différentes échelles temporelles (du mensuel à l'interannuel) et spatiales (du sub-kilometrique à l'échelle globale). Ce travail propose un cadre scientifique et pratique pour le suivi et l'interprétation de la variabilité du trait de côte au sein de la plage dans son ensemble, contribuant à améliorer la compréhension des processus côtiers liés au climat. À l'avenir, l'intégration

des interactions locales vagues–niveau de la mer, l'amélioration des méthodes d'extraction automatisées, l'apport de données de télédétection complémentaires et l'ancrage des observations de trait de côte dans un cadre plus large intégrant topographie, bathymétrie et bilans sédimentaires renforceront les capacités de prédiction des aléas côtiers. De tels développements seront déterminants pour améliorer la capacité d'anticipation et soutenir la gestion côtière, l'évaluation des risques et les stratégies d'adaptation dans un contexte de changement climatique et d'élévation du niveau de la mer.

General conclusion (EN)

This thesis presents a framework for monitoring shoreline dynamics along sandy beaches, integrating satellite-derived waterline observations validated against ground-truth measurements, the generation and analysis of a monthly-sampled cross-shore waterline position dataset at the continental scale, and the analysis of shoreline variability in relation with intertidal beach morphodynamics. Across the three main research axes—methodological evaluation of satellite-derived waterline extraction, shoreline variability from seasonal to decadal scale, and the representativeness of shoreline proxies for beach morphodynamics—key insights emerge regarding the mechanisms, measurement approaches, and limitations of current monitoring techniques.

Methodologically, this thesis establishes a transparent and modular framework for evaluating satellite-derived waterline (SDW) and shoreline (SDS) extraction methods. Benchmarking across multiple morphologically and hydrodynamically diverse sites shows that algorithm performance is site-dependent, with robust combinations of indices and segmentation approaches producing reliable, stable time series. Integrated metrics—such as seasonal cycles, long-term trends, and interannual variability—remain robust even when individual observations are noisy, supporting large-scale coastal monitoring. Limitations persist due to optical imagery constraints, tide model uncertainty, and ambiguous wet/dry pixels, but the study demonstrates pathways for improvement, including complementary datasets (e.g., SAR, higher-resolution sensors), automated filtering, and cloud-based geospatial processing.

Shoreline variability along the North American West Coast exhibits clear seasonal and interannual patterns. Seasonal cycles are largely driven by wave power fluctuations, with strong latitudinal contrasts: the PNW, NCA, and BC show high correlations with wave energy, while SCA and BCS responses are more heterogeneous and influenced by local morphology, sea-level variability, and episodic storm events. Interannual variability is dominated by ENSO-related events: El Niño induces pronounced erosion along California and Baja California, whereas La Niña produces more moderate, regionally modulated effects. These findings highlight how climate-driven forcing interacts with local geomorphology to shape shoreline evolution, and demonstrate that satellite-derived waterline observations provide a robust framework to detect and quantify such

signals.

Shoreline proxies are further evaluated in their ability to represent intertidal beach morphodynamics. Analyses across four sites show that dynamic sea level can account for up to one-third of proxy variability, and that profile geometry constrains the representativeness of shoreline positions. While some beaches, like Torrey Pines, exhibit coherent translational behavior making proxies reliable indicators of morphodynamics, others, such as Porsmilin, display significant non-translational variability. A simple parametric model combining translation and rotation explains 85–99% of observed profile changes, highlighting the role of slope adjustment in shaping intertidal dynamics. These results emphasize that while shoreline proxies are valuable for detecting broad-scale trends, they must be interpreted within the context of site-specific morphodynamics and dynamic sea-level effects.

Overall, this thesis demonstrates that a combination of qualified remote sensing techniques, careful methodological evaluation, and ground-truth validation enables meaningful assessment of coastal change across temporal (from monthly to interannual) and spatial (sub-kilometric to global) scales. The work provides both a scientific and practical framework for monitoring and interpreting shoreline variability within the broader beach system, contributing to improved understanding of climate-driven coastal processes. Looking forward, integrating local wave–sea level interactions, refining automated extraction methods, incorporating complementary remote sensing datasets, and embedding shoreline observations within broader topography–bathymetry and sediment budget contexts will enhance predictive capacity. Such developments will be critical to enhance predictive capacity and better support coastal management, risk assessment, and adaptation strategies in the face of ongoing climate change and sea-level rise.

Appendix A

Analyses of the SDW/SDS validation : Supplementary Figures

This appendix contains figures that provide additional showcases of the validation of SDW methods. It is divided in 3 sections, in the first one, distributions of SDW errors are shown for each segmentation method used, at the eight sites and coupled with the 5 indices. In the second section, the validation of beach slopes, long-term trends, seasonal cycles and interannual variability of shoreline positions are displayed for each methods (except LM-based methods, already shown in the Chapter II, Figures II.9,II.16,II.17,II.18). The last section provides some additional tests on the influence of the satellite mission and the ROI size on the SDW errors.

A.1 Distribution of SDW errors

Figures A.1, A.2, A.3, and A.4 show the SDW error distributions across all sites, thresholding methods and indices. Each panel is associated with a median erros which corresponds to the bias, and a standard deviaiton of the error, also refered to as cRMSE. Gaussian distributions are represented built on these median and standard deviation, to highlight the correspondence or deviations of the actual SDW error distributions to gaussian distributions. In most cases (especially with the LM-based methods), distributions are found to be close to gaussian, reinforcing the relevance of the Eq. II.12 linking the minimum detectable change at a 95 % significance level to the number of aggregated observations and the inherent observation error.

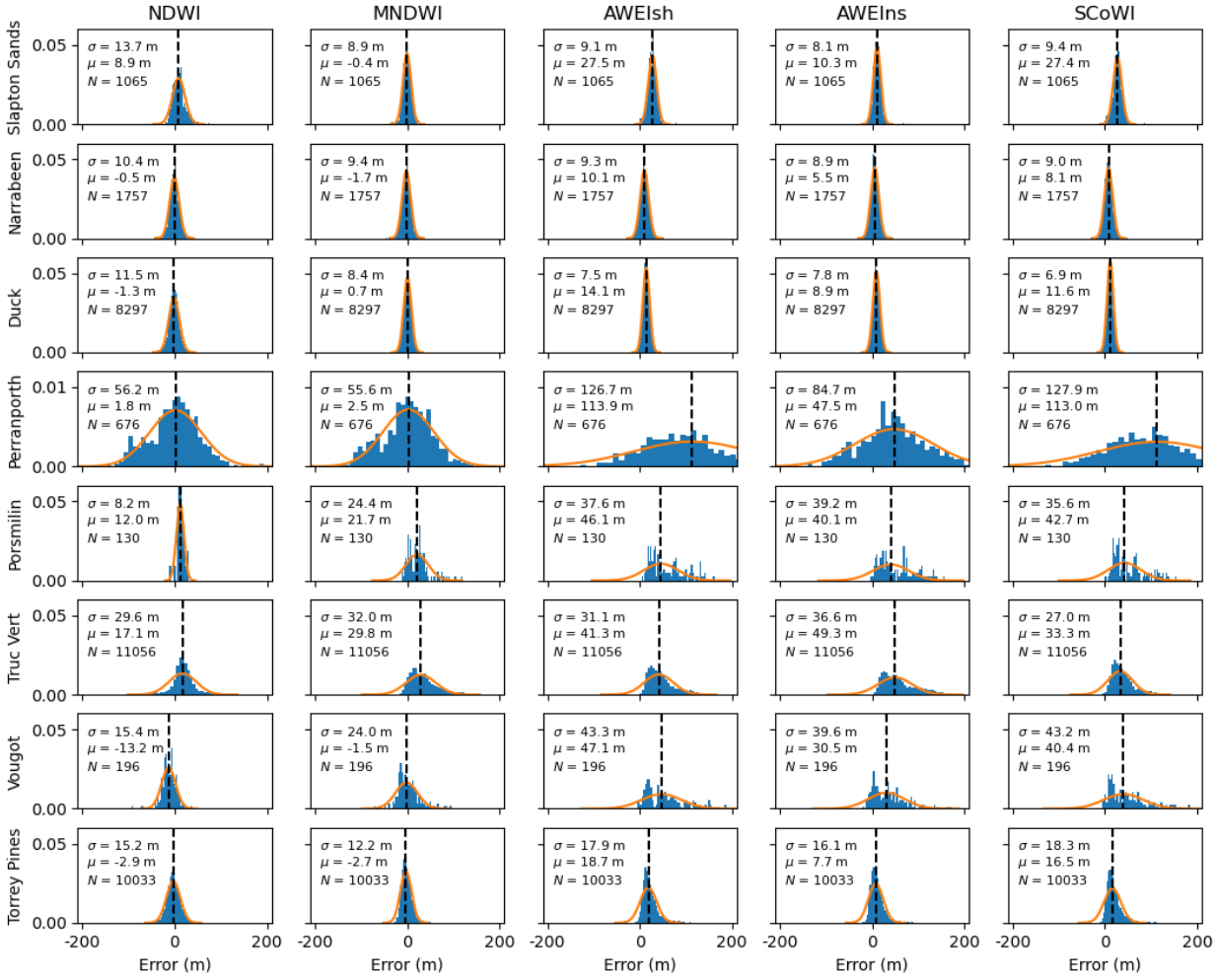

Figure A.1: Distributions at SDW errors obtained using Otsu-based SDW methods applied at the 8 validation sites, results are declined in columns, each showing the validation results using a different index.

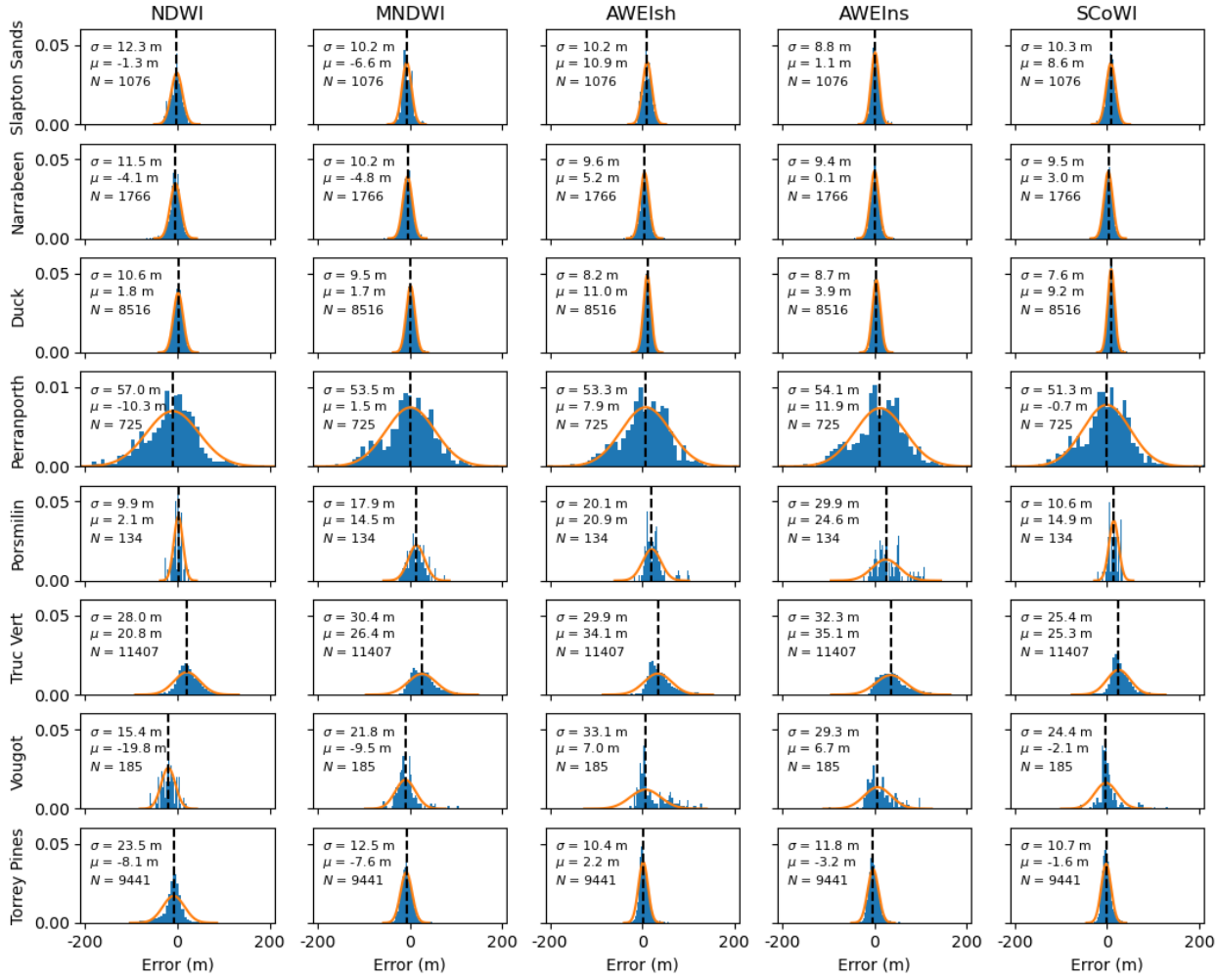

Figure A.2: Distributions at SDW errors obtained using LM-based SDW methods applied at the 8 validation sites, results are declined in columns, each showing the validation results using a different index.

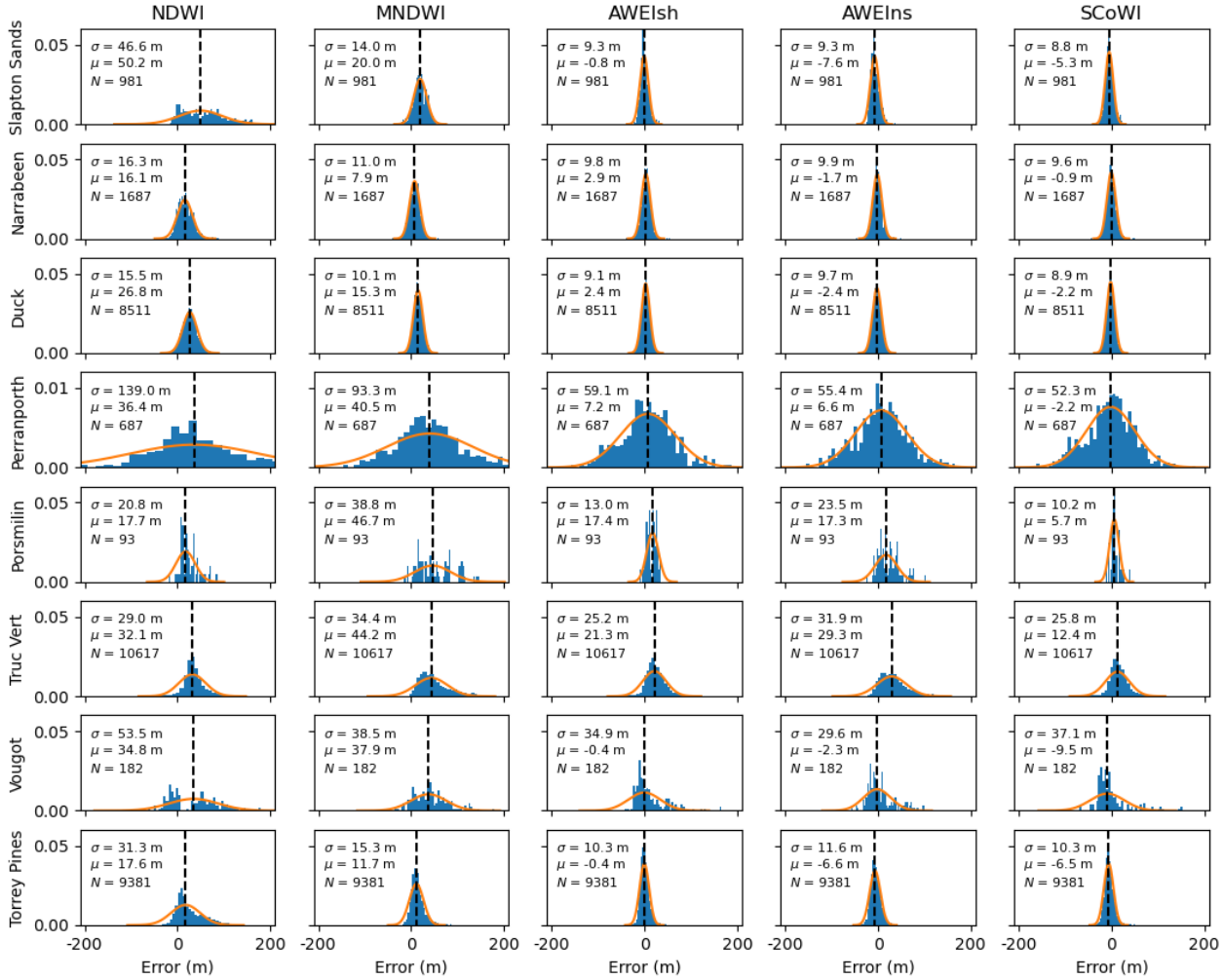

Figure A.3: Distributions at SDW errors obtained using MSV-based SDW methods applied at the 8 validation sites, results are declined in columns, each showing the validation results using a different index.

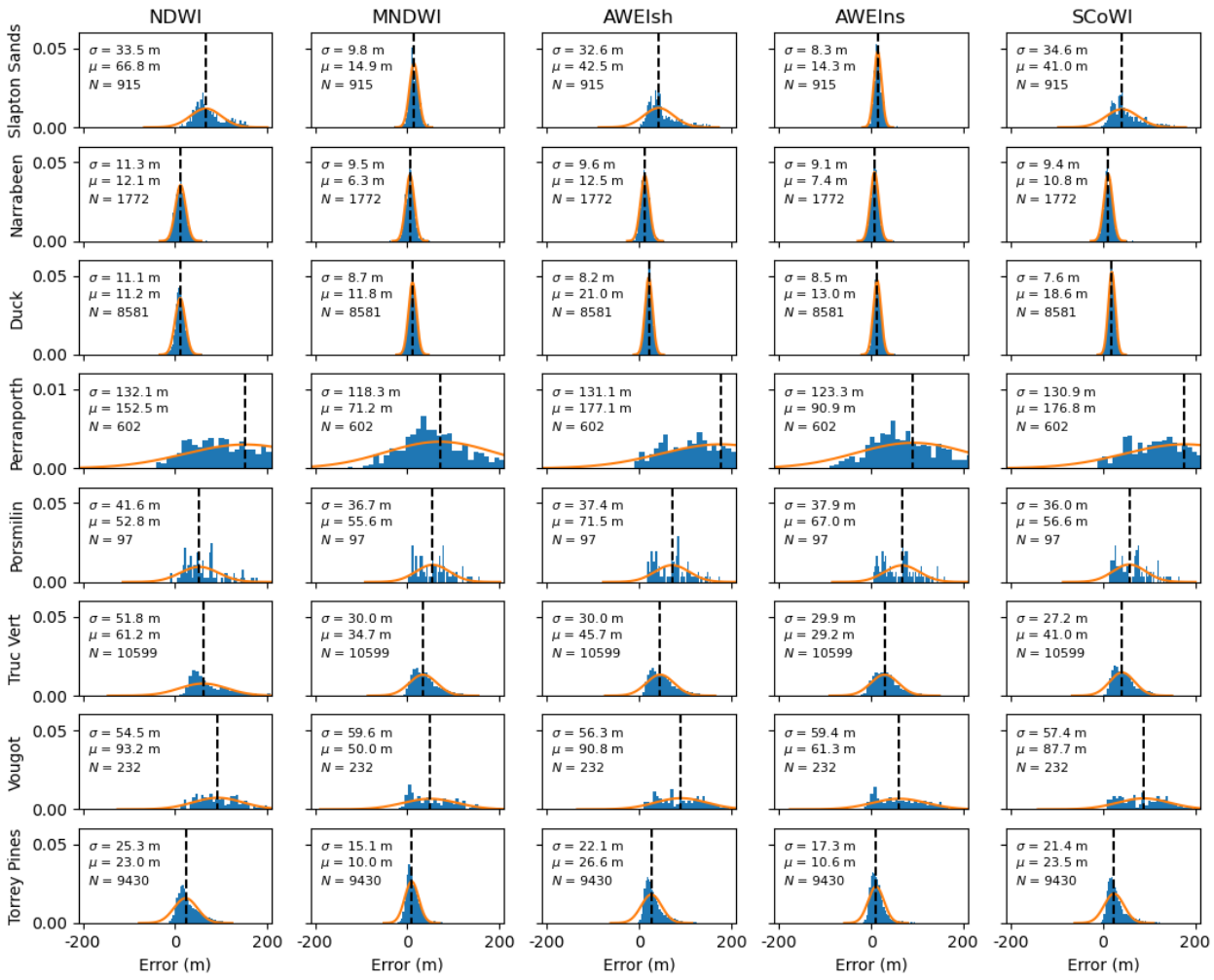

Figure A.4: Distributions at SDW errors obtained using WP-based SDW methods applied at the 8 validation sites, results are declined in columns, each showing the validation results using a different index.

A.2 Validation : Beach slopes, trends, seasonal cycles and inter-annual varaibility

The following figures are similar to Figures II.9, II.16, II.17, and II.18, but represent validation of beach slopes, as well as long-term trends, seasonal cycles and interannual variability of shoreline position obtained using Otsu-based, MSV-based and LM-based methods.

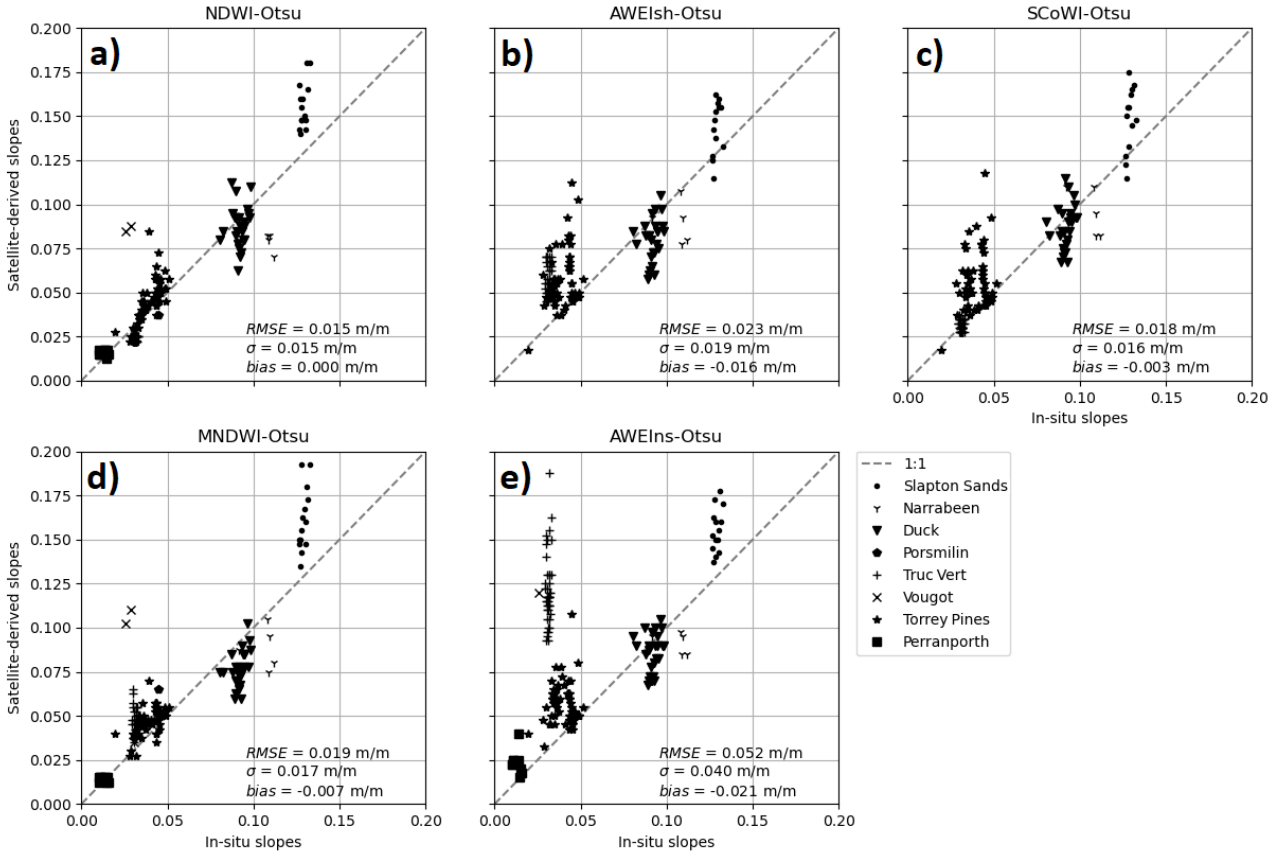

Figure A.5: Comparison between satellite-derived and in-situ intertidal beach slopes over 8 validation sites. Satellite-derived beach slopes are obtained from satellite-derived waterline position time series computed using algorithms based on **a)** NDWI, **b)** AWEIsh, **c)** SCoWI, **d)** MNDWI, and **e)** AWEIns indices, combined with the Otsu thresholding method.

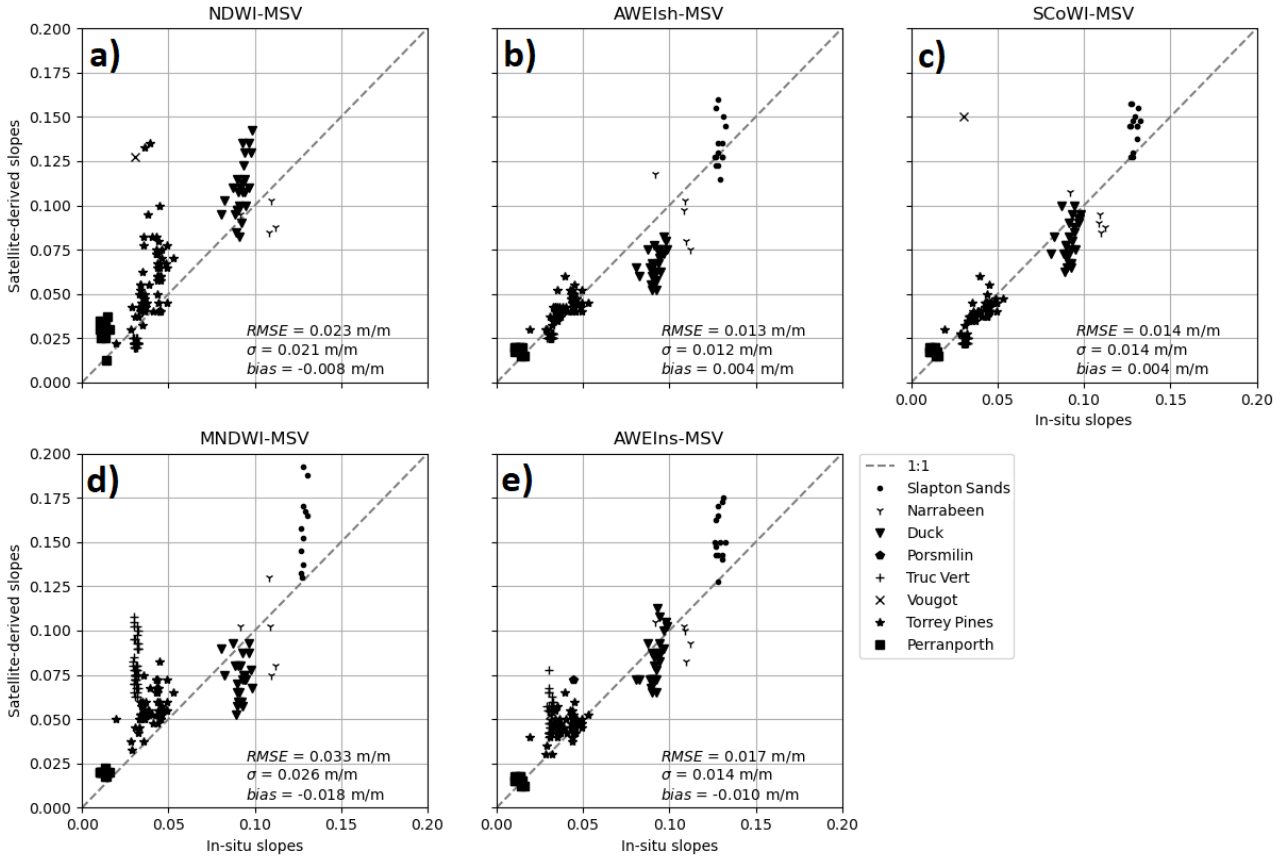

Figure A.6: Comparison between satellite-derived and in-situ intertidal beach slopes over 8 validation sites. Satellite-derived beach slopes are obtained from satellite-derived waterline position time series computed using algorithms based on **a)** NDWI, **b)** AWEIsh, **c)** SCoWI, **d)** MNDWI, and **e)** AWEIns indices, combined with the MSV thresholding method.

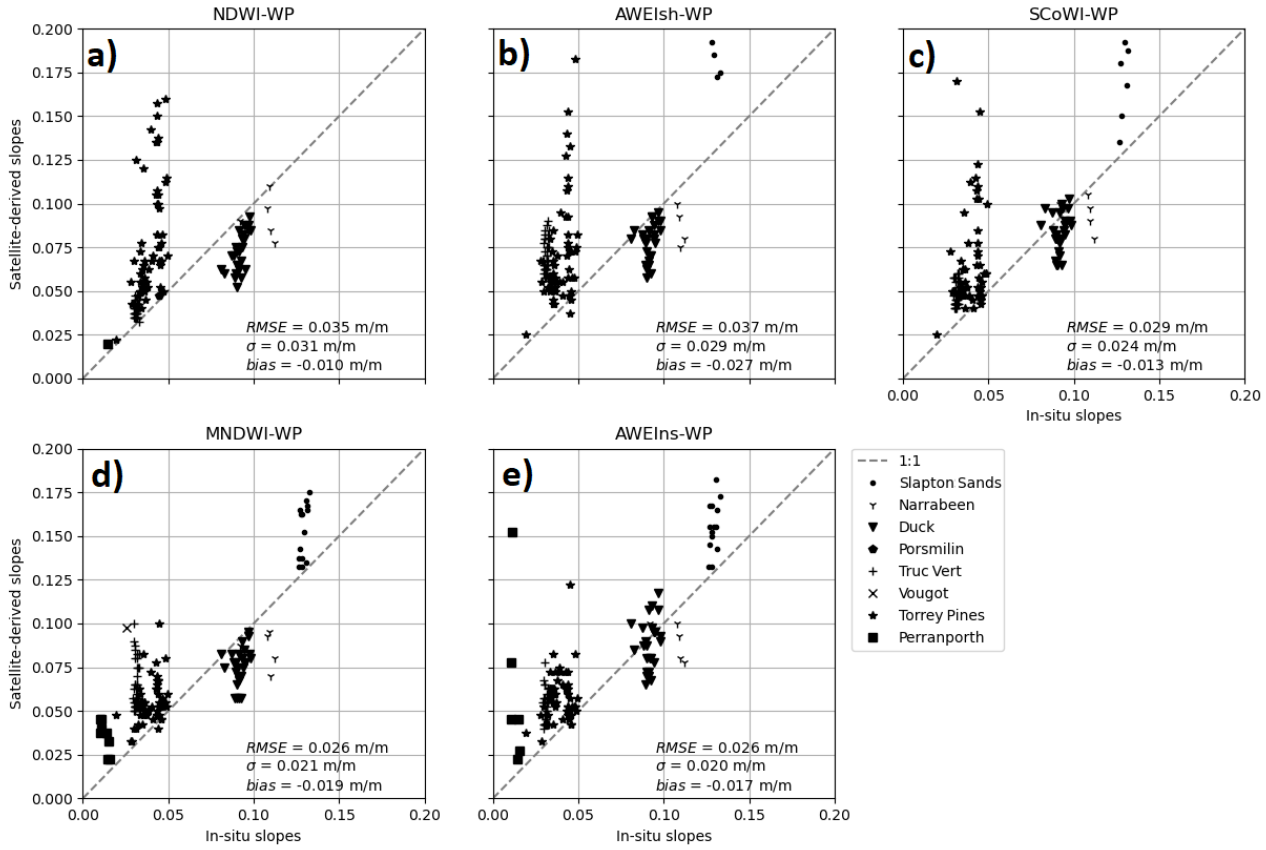

Figure A.7: Comparison between satellite-derived and in-situ intertidal beach slopes over 8 validation sites. Satellite-derived beach slopes are obtained from satellite-derived waterline position time series computed using algorithms based on **a)** NDWI, **b)** AWEIsh, **c)** SCoWI, **d)** MNDWI, and **e)** AWEIns indices, combined with the WP thresholding method.

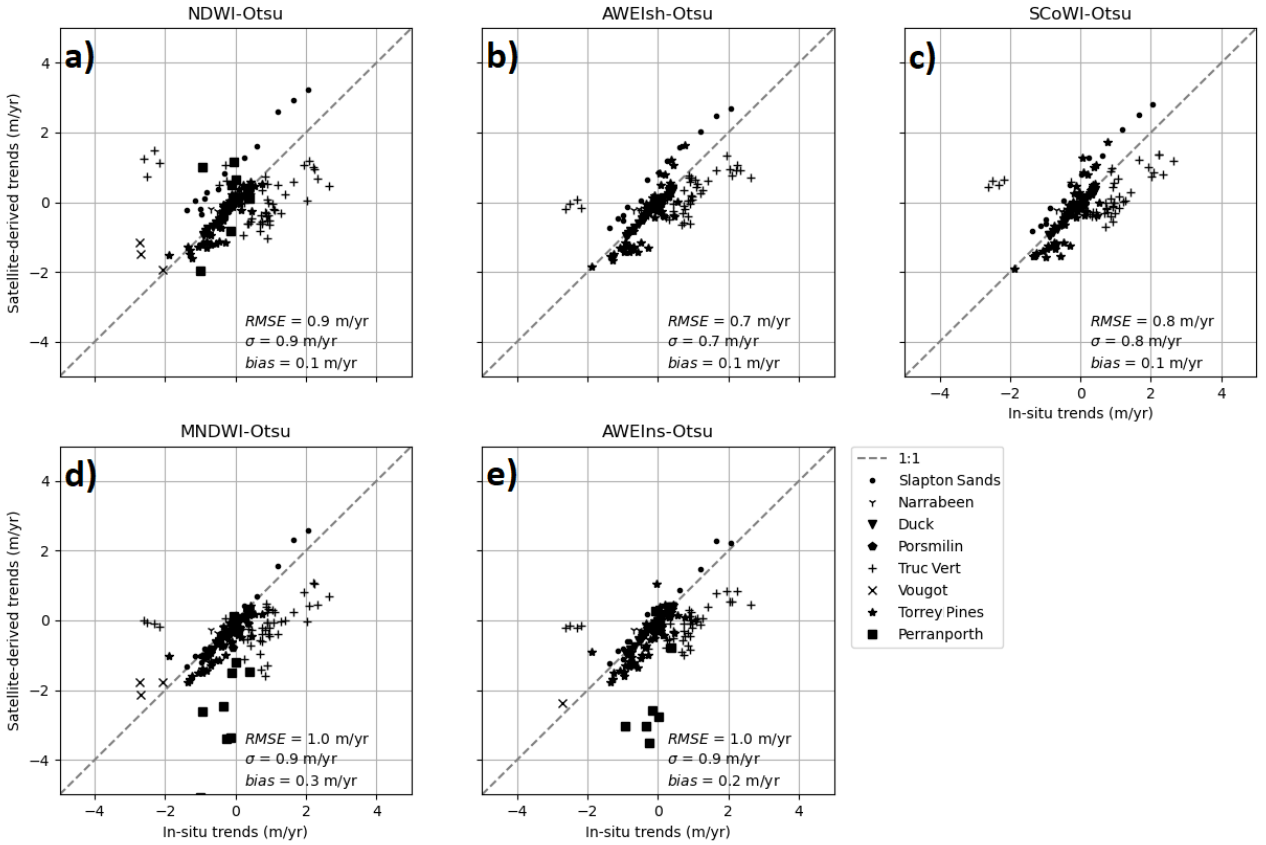

Figure A.8: Comparison between satellite-derived and in-situ seasonal variability of shoreline change over 8 validation sites. Trends are obtained from satellite-derived waterline position time series computed using algorithms based on **a)** NDWI, **b)** AWEIsh, **c)** SCoWI, **d)** MNDWI, and **e)** AWEIns indices, combined with the Otsu thresholding method.

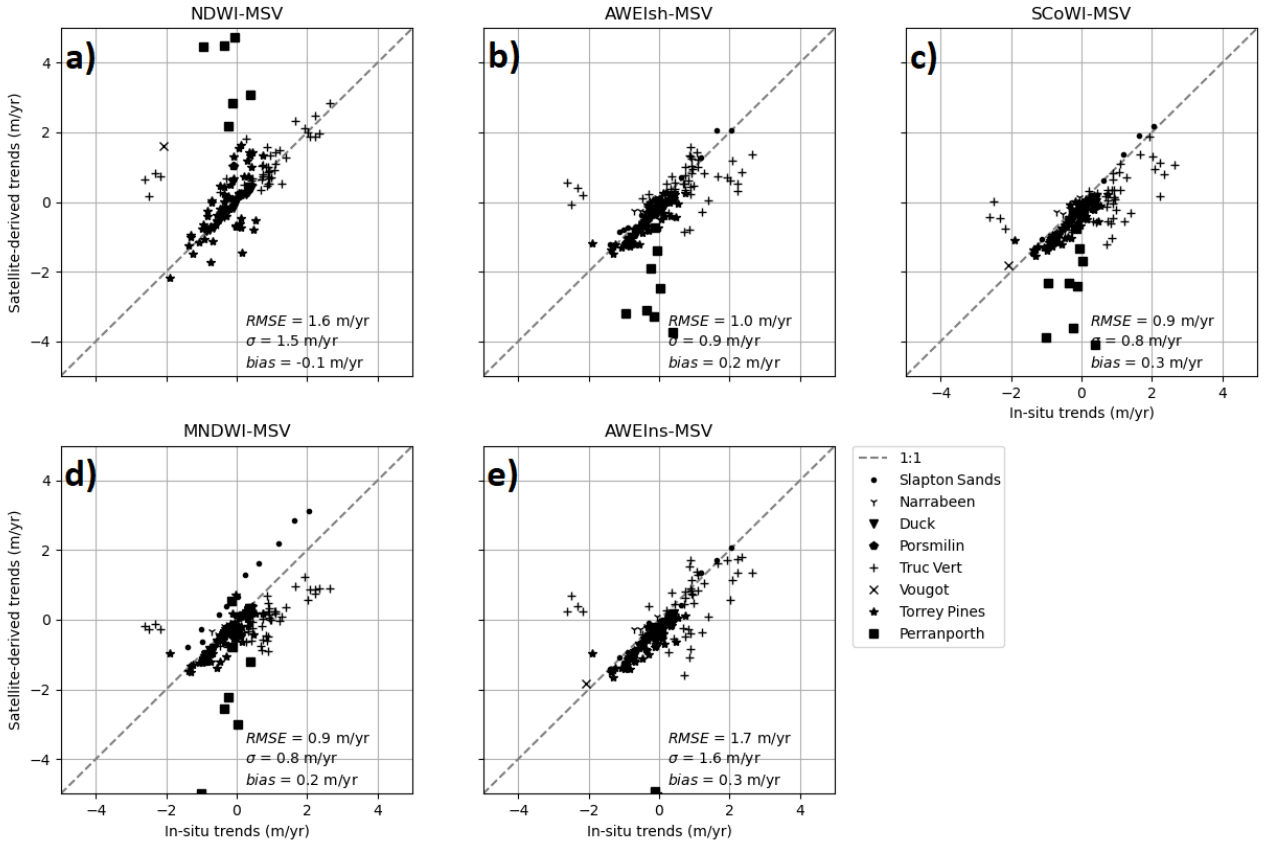

Figure A.9: Comparison between satellite-derived and in-situ seasonal variability of shoreline change over 8 validation sites. Trends are obtained from satellite-derived waterline position time series computed using algorithms based on **a)** NDWI, **b)** AWEIsh, **c)** SCoWI, **d)** MNDWI, and **e)** AWEIns indices, combined with the MSV thresholding method.

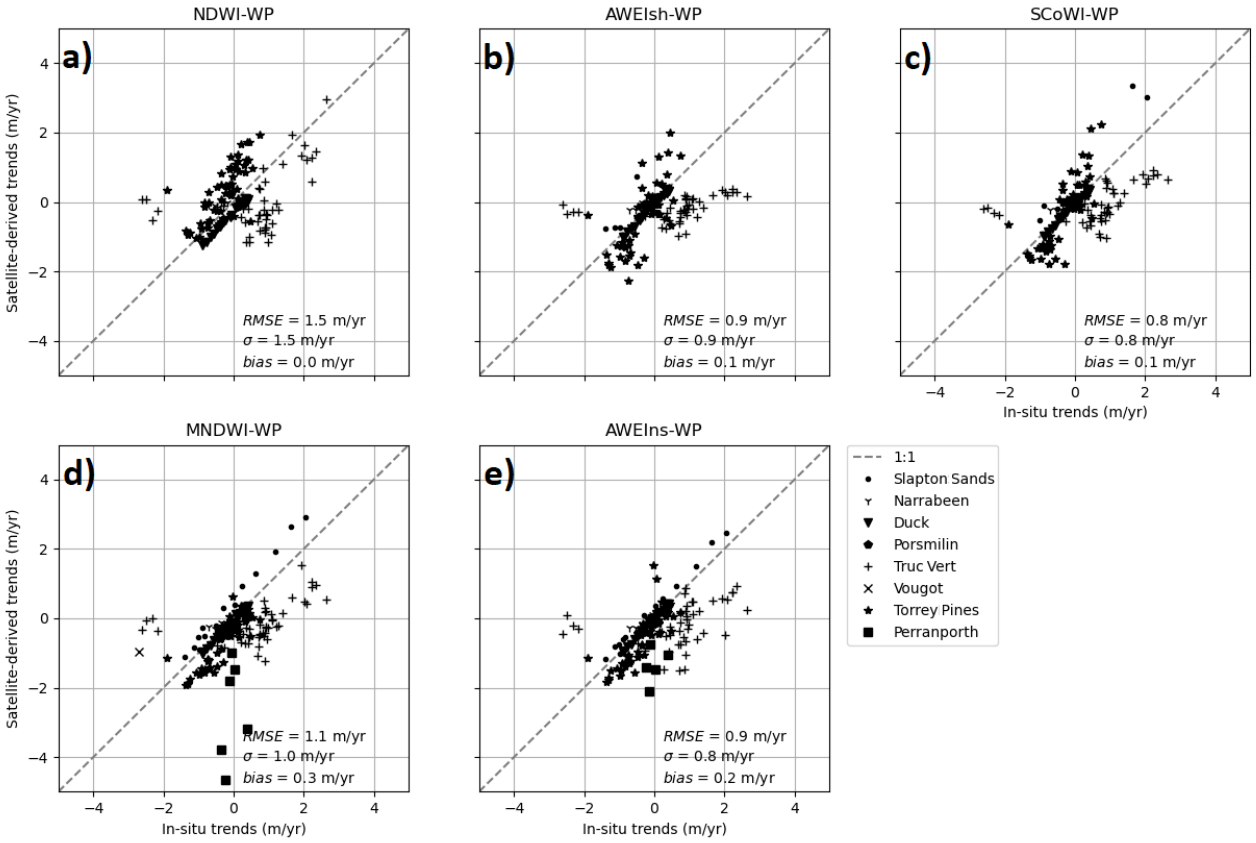

Figure A.10: Comparison between satellite-derived and in-situ seasonal variability of shoreline change over 8 validation sites. Trends are obtained from satellite-derived waterline position time series computed using algorithms based on **a)** NDWI, **b)** AWEIsh, **c)** SCoWI, **d)** MNDWI, and **e)** AWEIns indices, combined with the WP thresholding method.

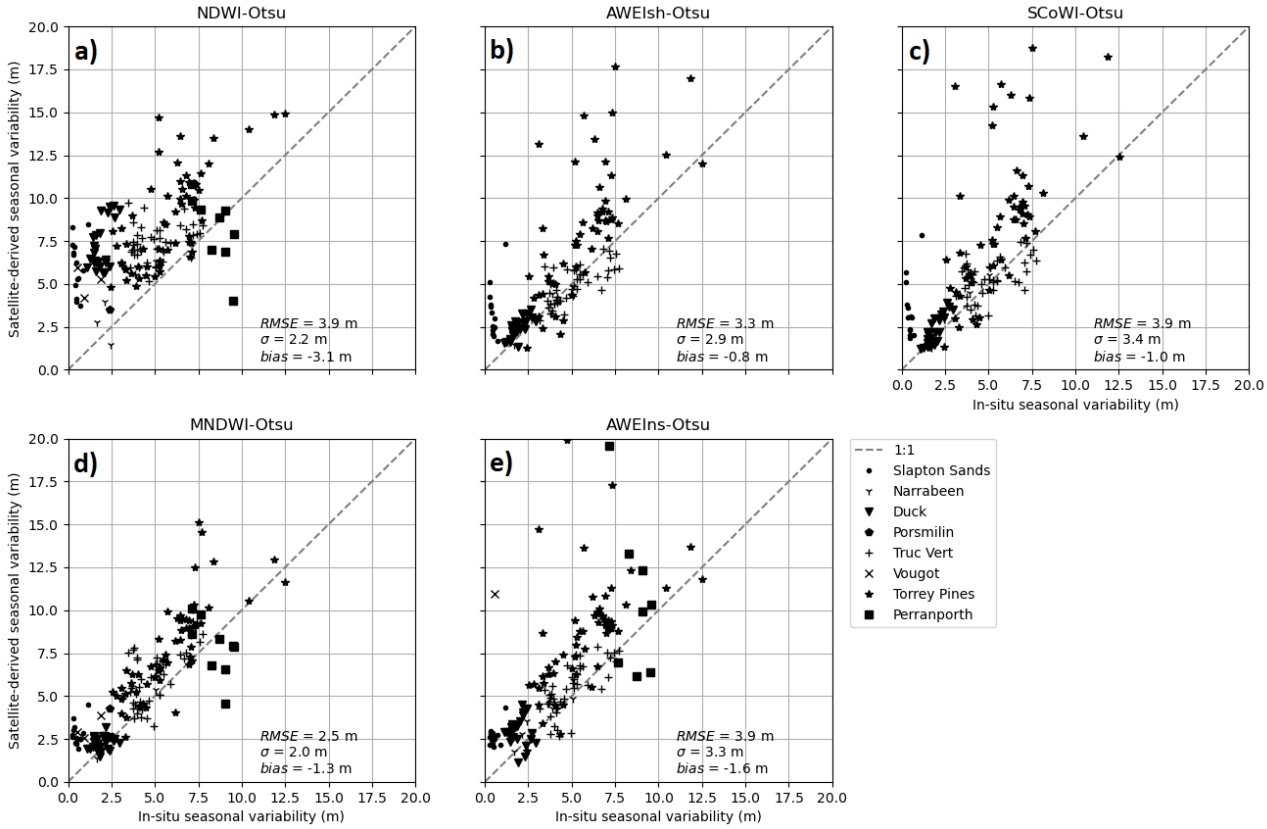

Figure A.11: Comparison between satellite-derived and in-situ seasonal variability of shoreline change over 8 validation sites. The seasonal variability of shoreline change is obtained from satellite-derived waterline position time series computed using algorithms based on **a)** NDWI, **b)** AWEIsh, **c)** SCoWI, **d)** MNDWI, and **e)** AWEIns indices, combined with the Otsu thresholding method.

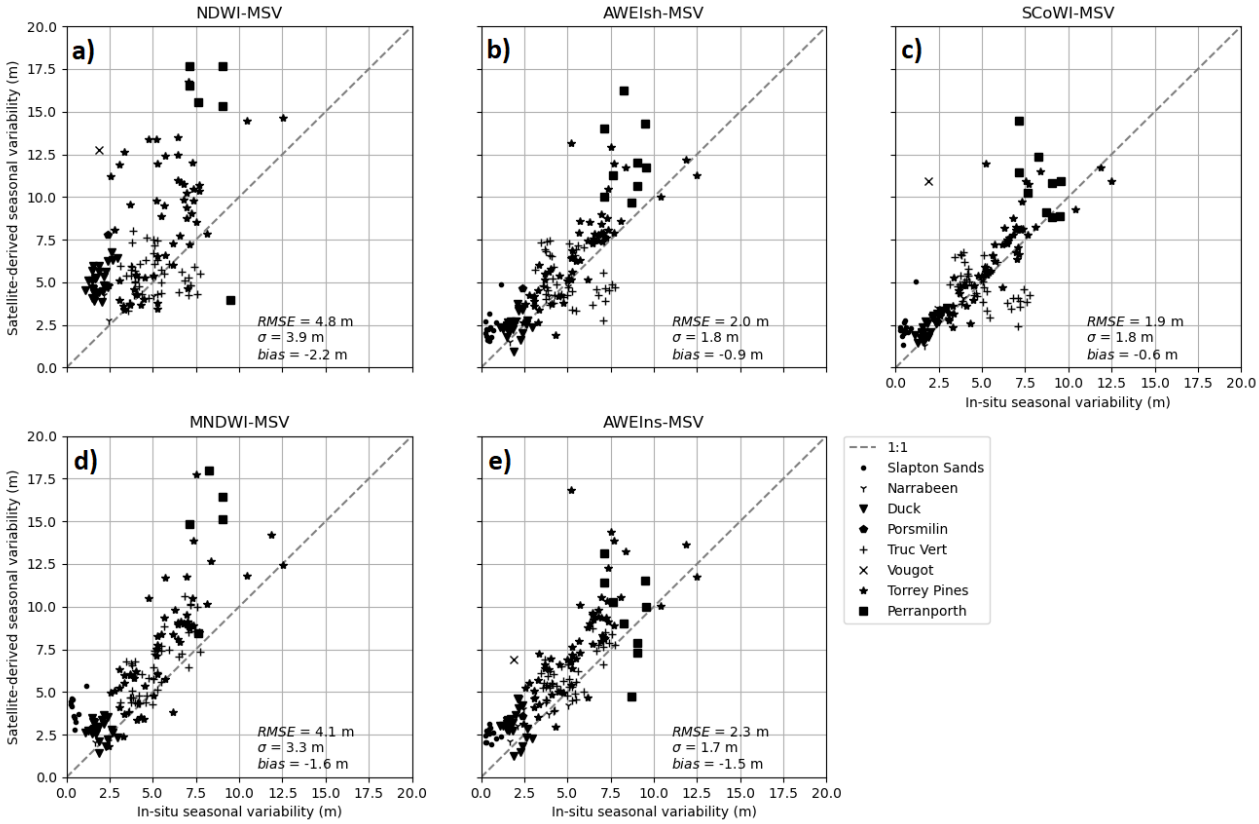

Figure A.12: Comparison between satellite-derived and in-situ seasonal variability of shoreline change over 8 validation sites. The seasonal variability of shoreline change is obtained from satellite-derived waterline position time series computed using algorithms based on **a)** NDWI, **b)** AWEIsh, **c)** SCoWI, **d)** MNDWI, and **e)** AWEIns indices, combined with the MSV thresholding method.

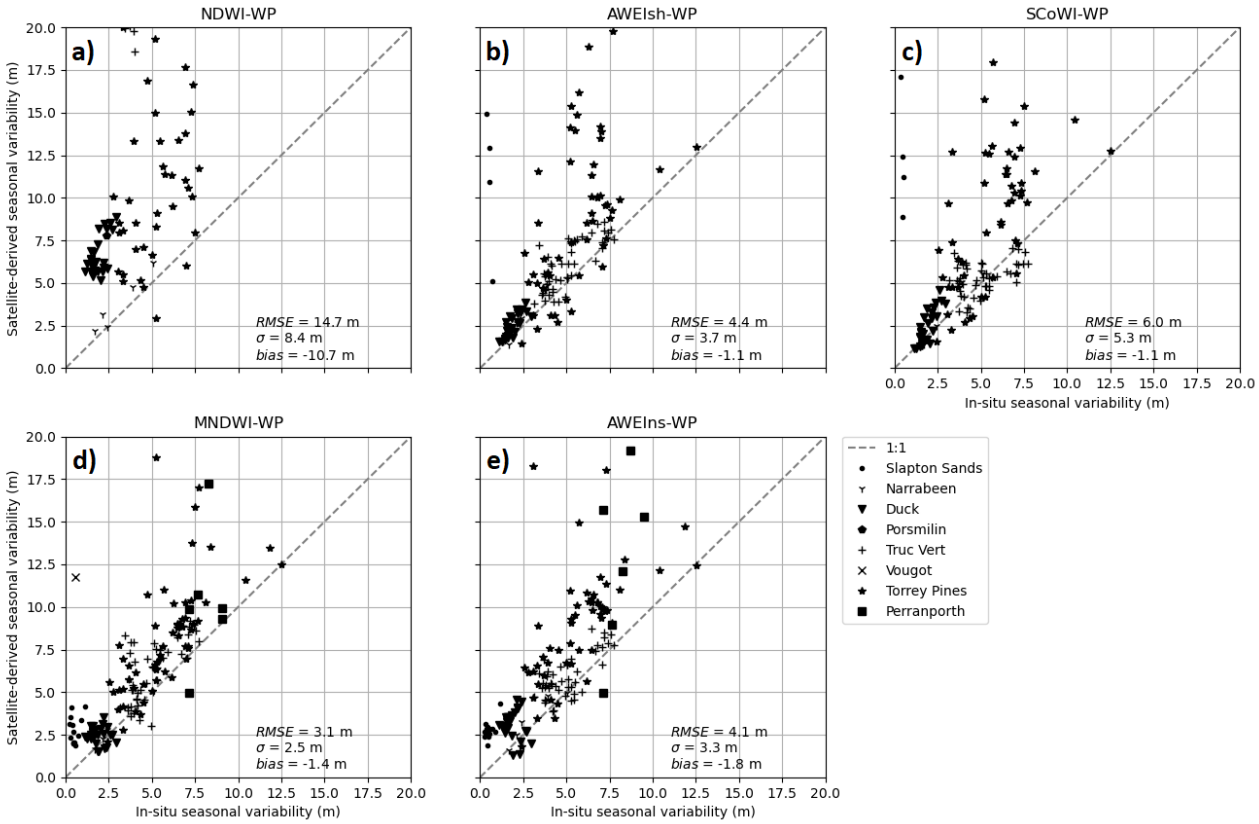

Figure A.13: Comparison between satellite-derived and in-situ seasonal variability of shoreline change over 8 validation sites. The seasonal variability of shoreline change is obtained from satellite-derived waterline position time series computed using algorithms based on **a)** NDWI, **b)** AWEIsh, **c)** SCoWI, **d)** MNDWI, and **e)** AWEIns indices, combined with the WP thresholding method.

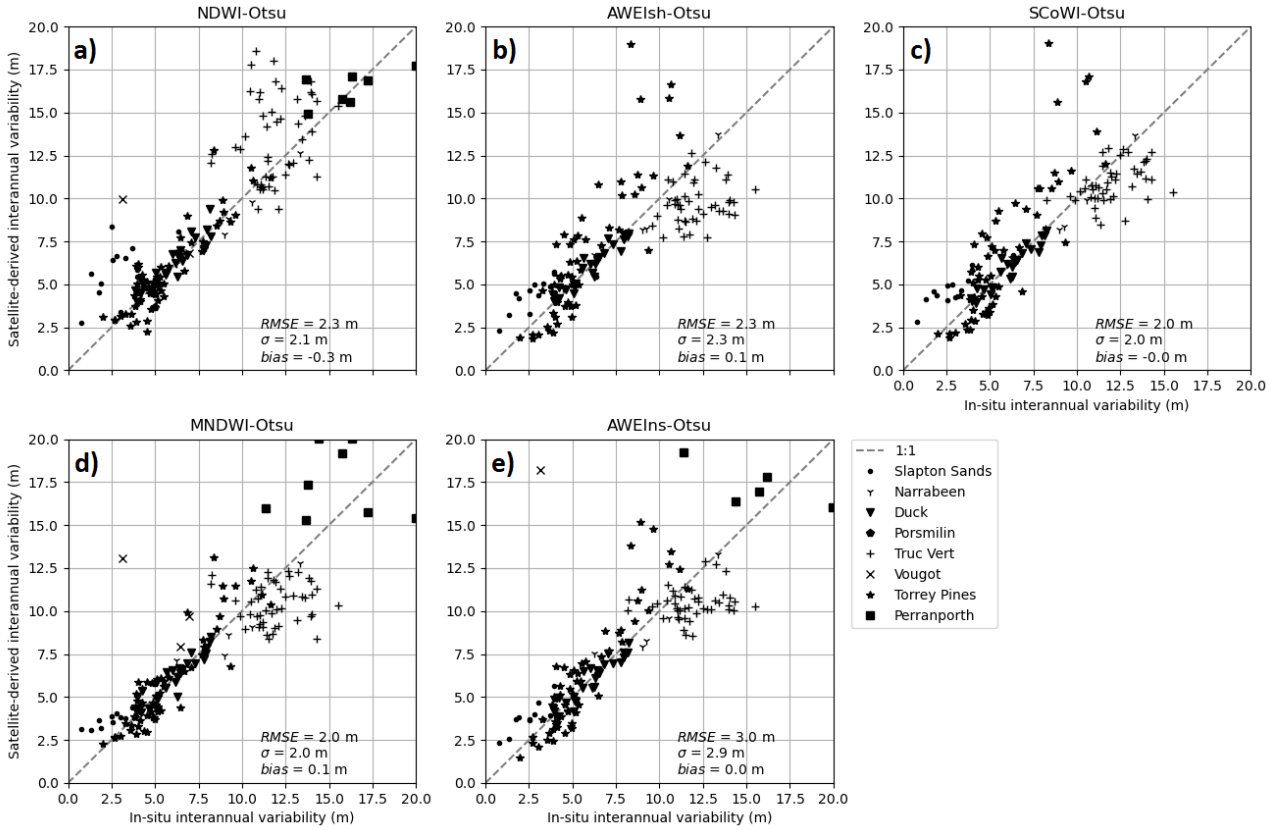

Figure A.14: Satellite-derived standard deviations of the yearly-averaged shoreline change are obtained from satellite-derived waterline position time series computed using algorithms based on **a)** NDWI, **b)** AWEIsh, **c)** SCoWI, **d)** MNDWI, and **d)** AWEIns indices, combined with the Otsu thresholding method.

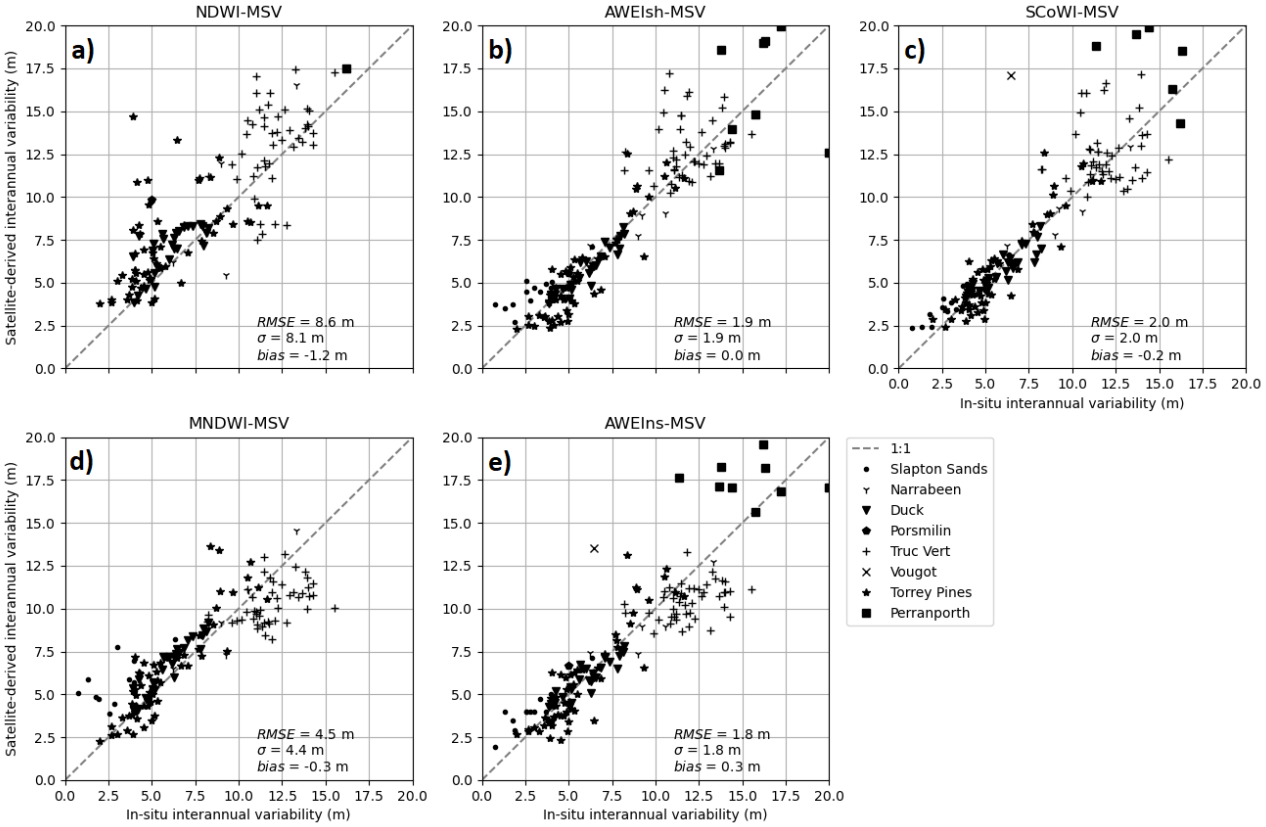

Figure A.15: Satellite-derived standard deviations of the yearly-averaged shoreline change are obtained from satellite-derived waterline position time series computed using algorithms based on **a)** NDWI, **b)** AWEIsh, **c)** SCoWI, **d)** MNDWI, and **d)** AWEIns indices, combined with the MSV thresholding method.

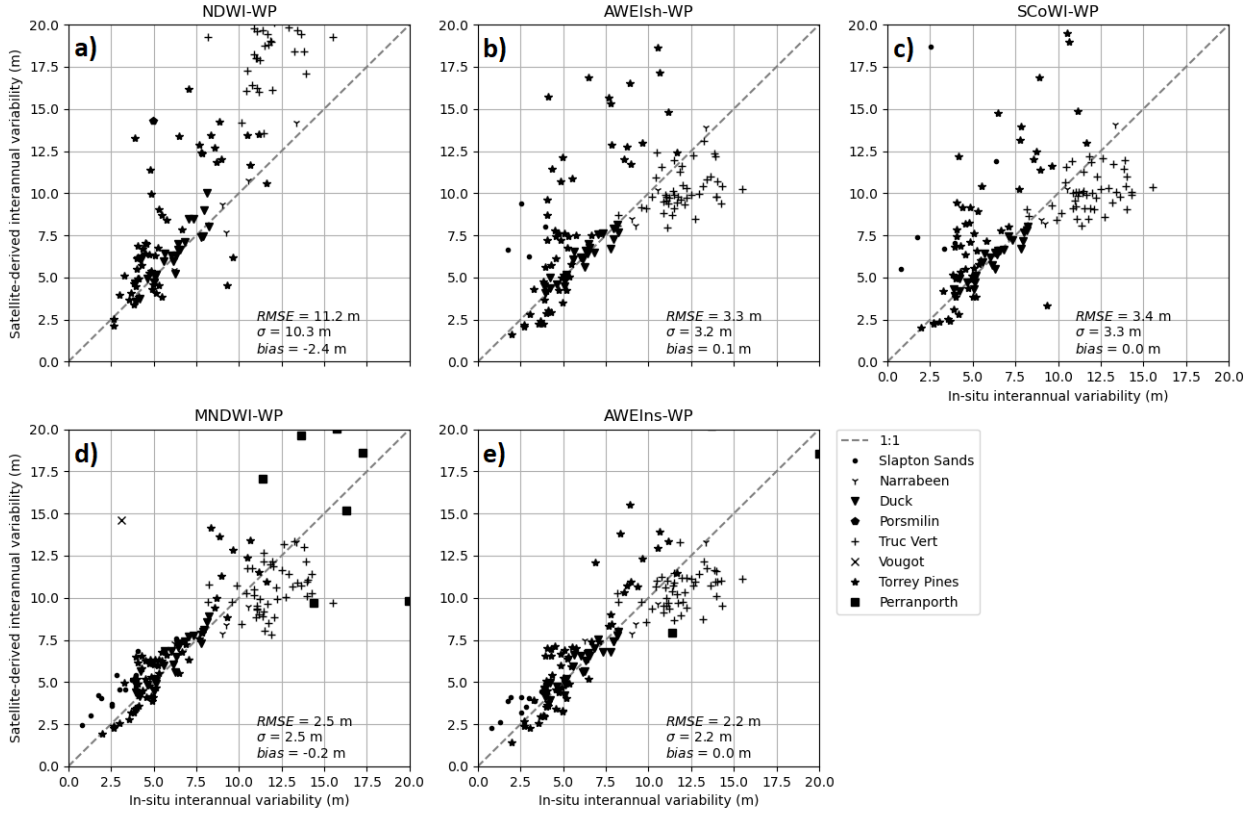

Figure A.16: Satellite-derived standard deviations of the yearly-averaged shoreline change are obtained from satellite-derived waterline position time series computed using algorithms based on **a)** NDWI, **b)** AWEIsh, **c)** SCoWI, **d)** MNDWI, and **d)** AWEIns indices, combined with the WP thresholding method.

A.3 Influence of the ROI size and satellite mission used

The two following figures provide additional validation of the SDW, investigating here the sensitivity of the detections to i) the size of the Region of Interest (ROI) used to derived the warterlines and ii) the satellite mission considered (between Sentinel-2 and Landsat missions).

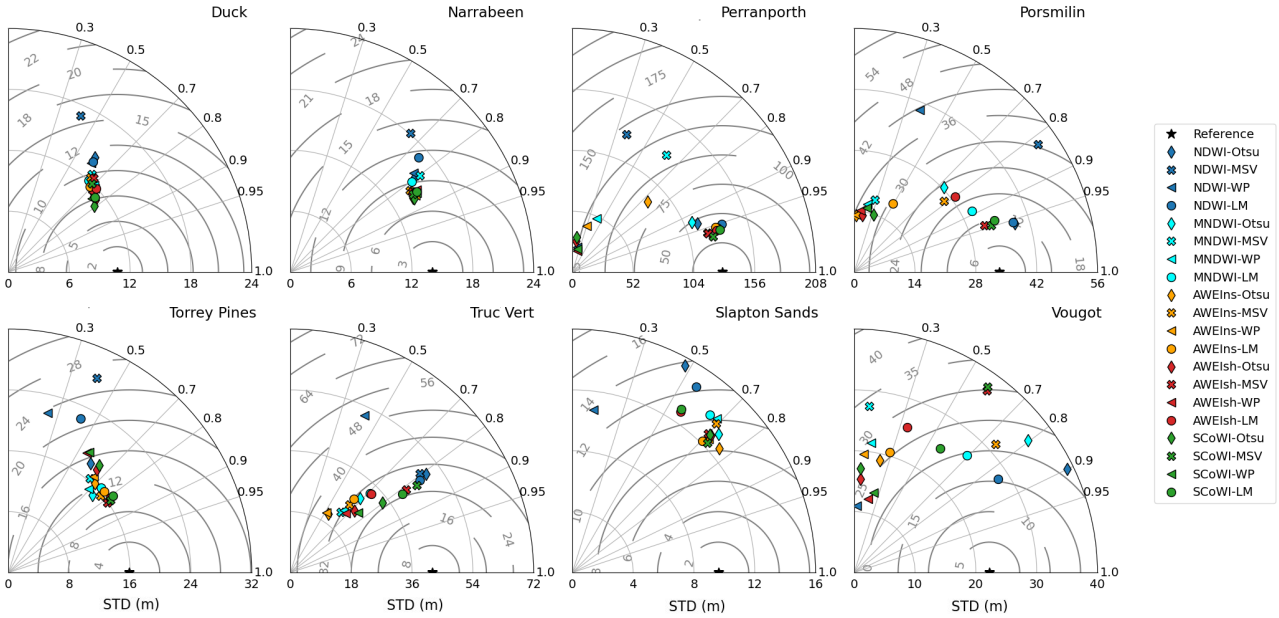

Figure A.17: Taylor's diagrams for the SDW uncertainties obtained at the 8 sites with 20 different SDW methods, using small ROIs.

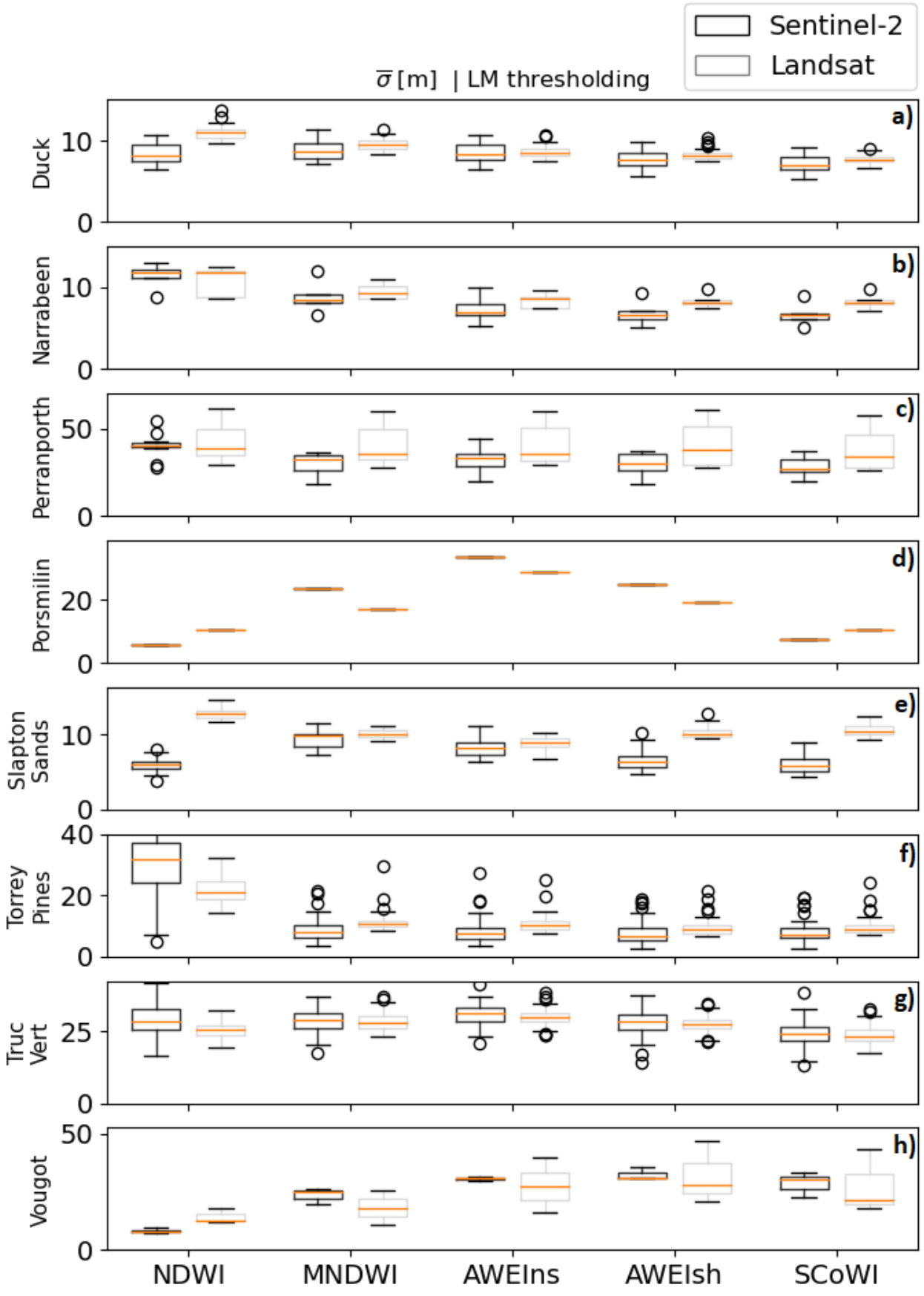

Figure A.18: Box plots of SDW errors obtained with LM-based methods across the 8 sites using the 5 indices, separated by Sentinel-2 and Landsat imagery.

Appendix B

Influence of ENSO on coastal hydro-morphodynamics : Supplementary Figures

This appendix contains several figures echoing with Chapter III, further empahsizing the contrasted influence of ENSO on the hydro-morphodynammics of the North American.

B.1 Statistical links between ENSO and coastal hydrodynamics along the NAWC

Figure B.1 is an extension of Figure III.13, showing the El Niño/neutral/La Niña anomalies of waterline position per season and region. As already stated in Chapter III, the influence of ENSO is mostly marked in winter, where the SNR scores are higher for El Niño across all regions, and across the southernmost regions for La Niña. In the PNW, the SNR scores for La Niña are higher in spring and summer, with medians of the anomaly distributions shifted negatively relatively to the neutral years anomalies, meaning that this pair of ENSO variability and season cycle is generally associated with waterline retreat.

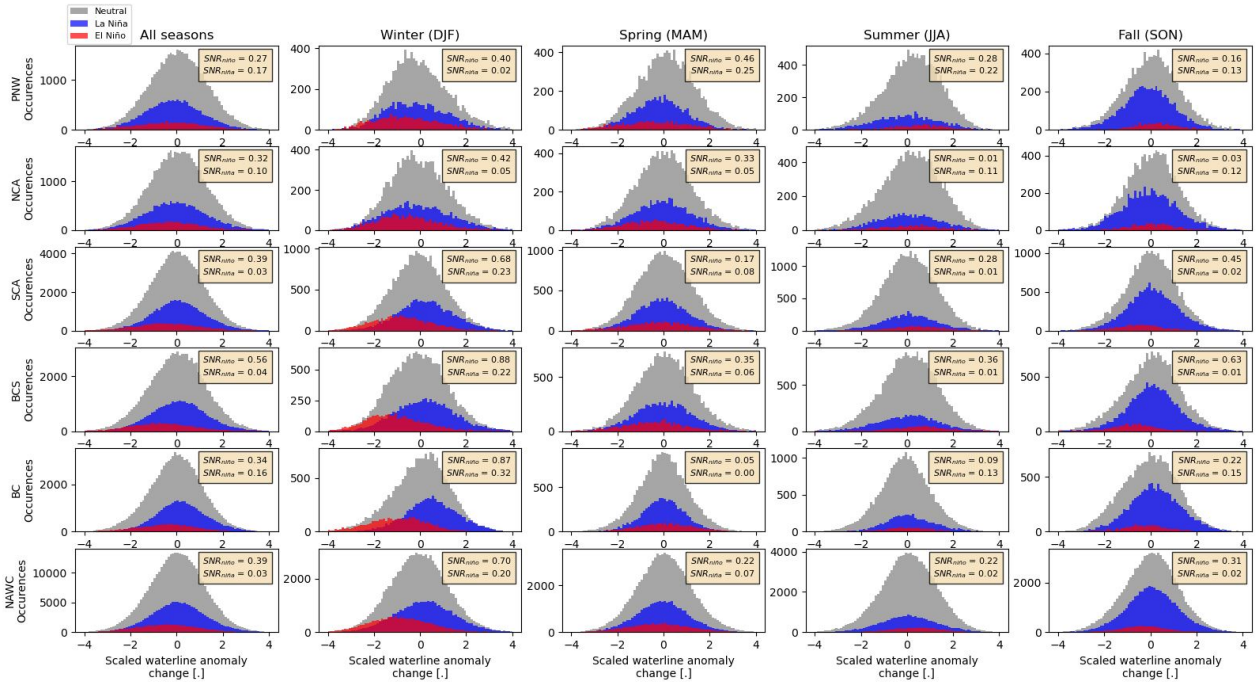

Figure B.1: SNR ratio analysis of waterline anomaly change during El Niño (red) and La Niña (blue) relatively to neutral years (grey). These distributions show seasonal anomaly changes, meaning changes in the seasonally-averaged waterline position anomaly between a given season and two seasons prior. The first column show these changes all seasons confounded and the other columns show these changes per season. SNR scores are calculated as $SNR = (\mu_{event} - \mu_{ref})/\sigma_{ref}$, with the event being El Niño or La Niña, and the reference being the neutral years.

B.2 Northeastern Pacific response to ENSO

The three following figures follow the same design that Figure III.15. The only differences are the oceanic forcings displayed (wave power or SLA) and the thresholds (m=1 or m=0.5) for categorizing El Niño/neutral/La Niña winters.

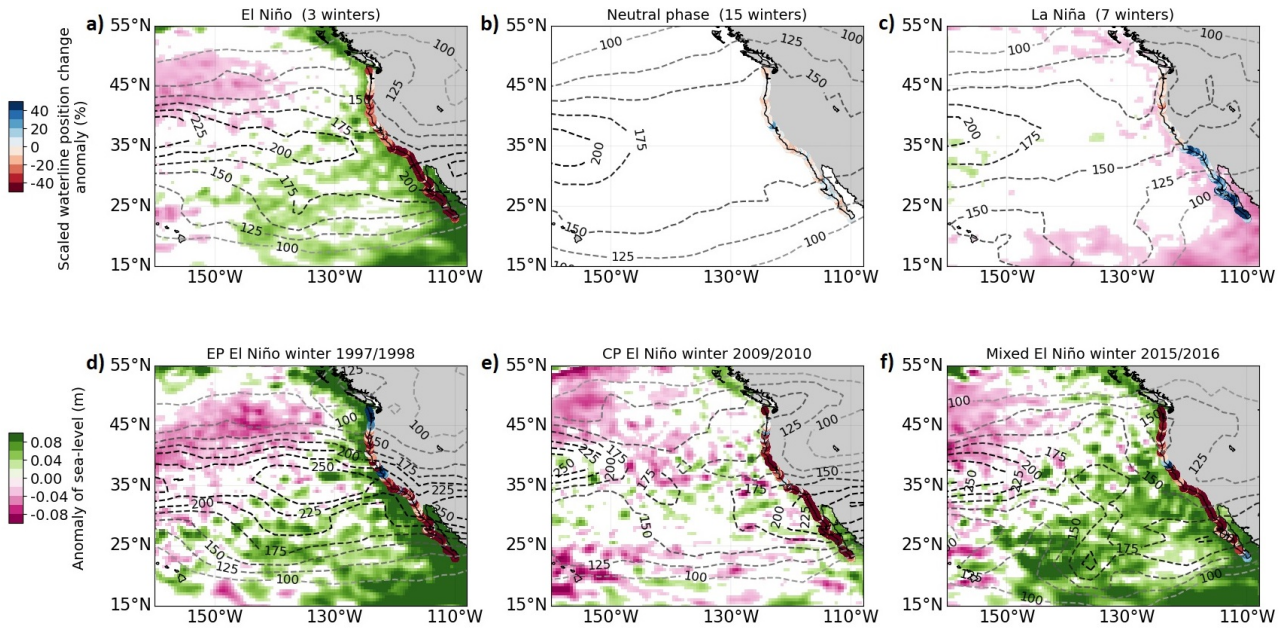

Figure B.2: Same figure as Figure III.15, except that it displays the sea-level anomalies instead of the scaled wave power anomalies. The background map was generated using Python's mpl_toolkits.basemap library.

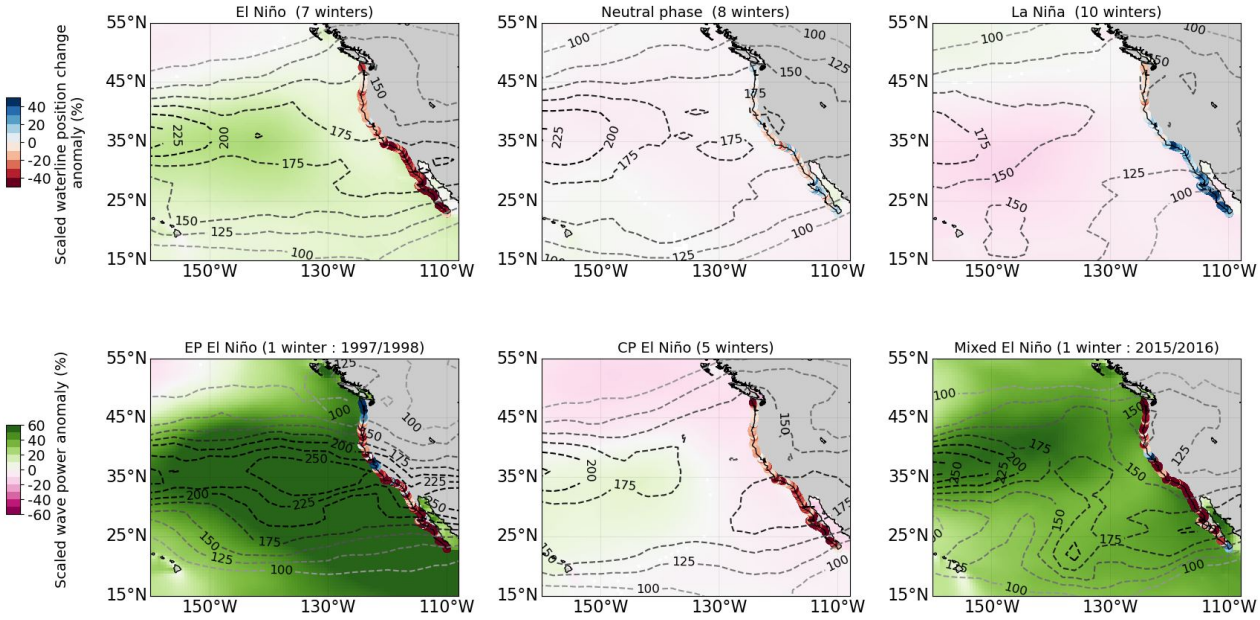

Figure B.3: Same figure as Figure III.15, except that it displays the responses to ENSO events considering a smaller threshold m=0.5 to identify these events. The background map was generated using Python's mpl_toolkits.basemap library.

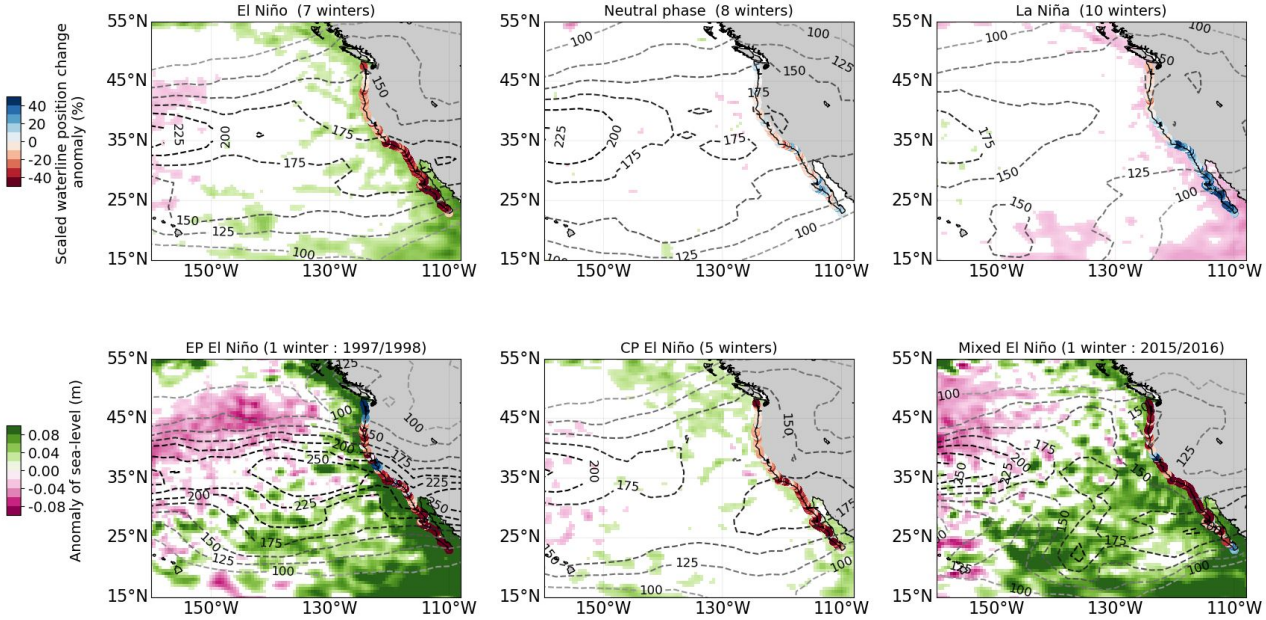

Figure B.4: Same figure as Figure III.15, except that it displays the responses to ENSO events considering a smaller threshold m=0.5 to identify these events and that it shows the sea-level anomalies instead of the scaled wave power anomalies. The background map was generated using Python's mpl_toolkits.basemap library.

Appendix C

Coupled dynamics of the waterline and the sandbar

This appendix presents an outline of research on the coupled dynamics of the shoreline and the sandbar at two sites (Torrey Pines, CA, USA and Ensenada, BC, Mexico). This work has been conducted in collaboration with two PhD students : Salomé Frugier (conceptualization and extraction of sandbar data) and Marius Aparicio (conceptualization).

C.1 Short context of the research

Understanding the coupled dynamics of shorelines and sandbars is central to coastal morphodynamics, as exchanges between these features drive much of the variability in beach response to waves and storms (Wright and Short (1984); van de Lageweg et al. (2013)). Sandbar and shoreline changes are strongly interlinked as bars act as buffers that modulate wave energy reaching the shore. Recently developed sandbar detection methods based on optical satellite imagery (Frugier et al. (2025)) enable to investigate these interactions. We want to study how coupled are sandbar and shoreline evolutions at the seasonal and interannual scale, following modulation of incident wave energy. This study is applied at two sites, Torrey Pines (a high-energy, open coast) and Ensenada (a more sheltered embayment), both exposed to an highly seasonal wave climate and episodic El Niño events.

C.2 Methods

C.2.1 Satellite-derived waterline data

SDW data have been derived from Sentinel-2 imagery using the same SCoWI-LM method introduced in Chapter II and applied at the continental scale in Chapter III (including the use of tide

correction using FES2022 and beach slope estimation). The resulting dataset has been resampled at a monthly resolution.

C.2.2 Satellite-derived sandbar data

To retrieve sandbar position timeseries we followed the approach developed by Frugier et al. (2025). This approach consists in identifying white water due to wave breaking on multispectral satellite imagery. Sentinel-2 images have been used to derive the SandBar Index (SBI) expressed as

$$SBI = 2 \times (B - R) + G - 0.25 \times NIR \tag{C.1}$$

with R, G, B and NIR representing the reflectance values of the respective spectral bands red, green, blue, and near-infrared, respectively. SBI maps are then normalized as

$$NSBI = \frac{SBI - SBI_{min}}{SBI_{90} - SBI_{min}} \tag{C.2}$$

with SBI_{90} and SBI_{min} being the 90th percentile of SBI values and the minimum SBI value, respectively.

From NSBI maps, white water patches are identified along user-defined transects, perpendicular to the coast. From the sections of NSBI values, peaks with a prominence greater than 0.2 are identified as white water patches. The method is coupled with the SCoWI-LM SDW algorithm to extract waterline position, and if a white water patch is found to be close enough to the waterline position (threshold of 40 meters), the corresponding wave breaking is considered to be wave breaking on the shoreline and not on a sandbar and is thus not considered in the rest of the process.

C.2.3 Equilibrium model

To model the evolution of the shoreline, we use the ShoreFor model (Davidson et al. (2013); Splinter et al. (2014)) which models the evolution of the shoreline position as

$$\frac{dx}{dt} = c(F^+ + rF^-) + b \tag{C.3}$$

where x is the shoreline position, F^+ and F^- are the positive and negative forcing terms, r a ratio set to make the forcing terms balanced ($\Sigma(F^+ + rF^-) = 0$), and c and b are two free parameters.

In the ShoreFor model, the forcing term is expressed as

$$F = P^{0.5}\frac{\Delta\Omega}{\sigma_{\Delta\Omega}} \tag{C.4}$$

with P the breaking wave energy flux, itself expressed as $P = (1/16)\rho g H_{s,b}^2\sqrt{gh_b}$ with the depth at breaking $h_b = H_{s,b}/0.78$ and the breaking significant wave height $H_{s,b} = 0.39g^{1/5}(T_p H_{o,s})^{2/5}$, with T_p and $H_{o,s}$ the offshore peak wave period and significant wave height, as these modeled in CMEMS (see below). σ is the standard deviation operator, here applied to $\Delta\Omega$, the difference between the instantaneous (Ω) and time-varying equilibrium (Ω_{eq}) dimensionless fall velocity $\Delta\Omega = \Omega_{eq} - \Omega$.

The time-varying equilibrium dimensionless fall velocity is a weighted integration of the previous states of instantaneous dimensionless fall-velocity, they are expressed as

$$\Omega = \frac{H_s}{T_p\omega} \tag{C.5}$$

and

$$\Omega_{eq} = (\Sigma_{i=1}^{2\phi} 10^{-i/\phi})^{-1}\Sigma_{i=1}^{2\phi}\Omega_i 10^{-i/\phi}. \tag{C.6}$$

The formulation of Ω_{eq} bring a third free parameter ϕ called the response factor, or beach memory parameter.

To this framework we added a conceptual term, linking the shoreline position to the sandbar position as if they were connected by a mechanical spring. As such, we developed an alternative equilibrium model expressed as

$$\frac{dX}{dt} = c(F^+ + rF^-) + k(\Delta X_{s,sb} - \Delta X_{s,sb,eq}) + b \tag{C.7}$$

with $\Delta X_{s,sb}$ the difference in position of the sandbar and the shoreline, $\Delta X_{s,sb,eq}$ an equilibrium

distance between the shoreline and the sandbar, set as a free parameter, and k a spring stiffness free parameter of the shoreline/sandbar system.

We used a differential evolution global optimization algorithm (Storn and Price (1997); implemented as *scipy.optimize.differential_evolution* function in Python) to derive the optimal free parameters (b, c and ϕ) of the ShoreFor model, plus k and $\Delta X_{s,sb,eq}$ in the modified model. The cost function is defined as the root-mean-square error (RMSE) between the simulated shoreline position and the observed SDS, ensuring the model fit captures the shoreline dynamics accurately. Model outputs are sampled at a monthly resolution to match the monthly sampled observations, and averaged across transects to have a more robust sandbar position estimation.

C.2.4 Additional data

The wave forcing data are from the Global Ocean Waves Reanalysis product from CMEMS. This dataset provide 3-hourly sampled significant wave height and peak wave period, with a spatial resolution of 0.2°.

C.3 Preliminary results

C.3.1 Shoreline and sandbar positions patterns

This section presents six figures illustrating the correlations between wave power flux time series, shoreline positions, and sandbar positions. The data are processed in three different ways: (i) seasonal cycle time series, (ii) 12-month running mean time series, and (iii) event residuals, defined as the original monthly time series minus the 12-month running mean. These figures highlight well-documented behaviors: the sandbar is positively correlated with wave forcing, such that increasing wave power tends to shift the sandbar seaward. In contrast, the shoreline generally responds in the opposite direction, though in a noisier manner. Consequently, negative correlations between sandbar and shoreline positions are expected. However, this relationship depends on the temporal scale: at the seasonal scale, a strong negative correlation is observed, whereas at interannual and event scales the linear link becomes much weaker or even absent.

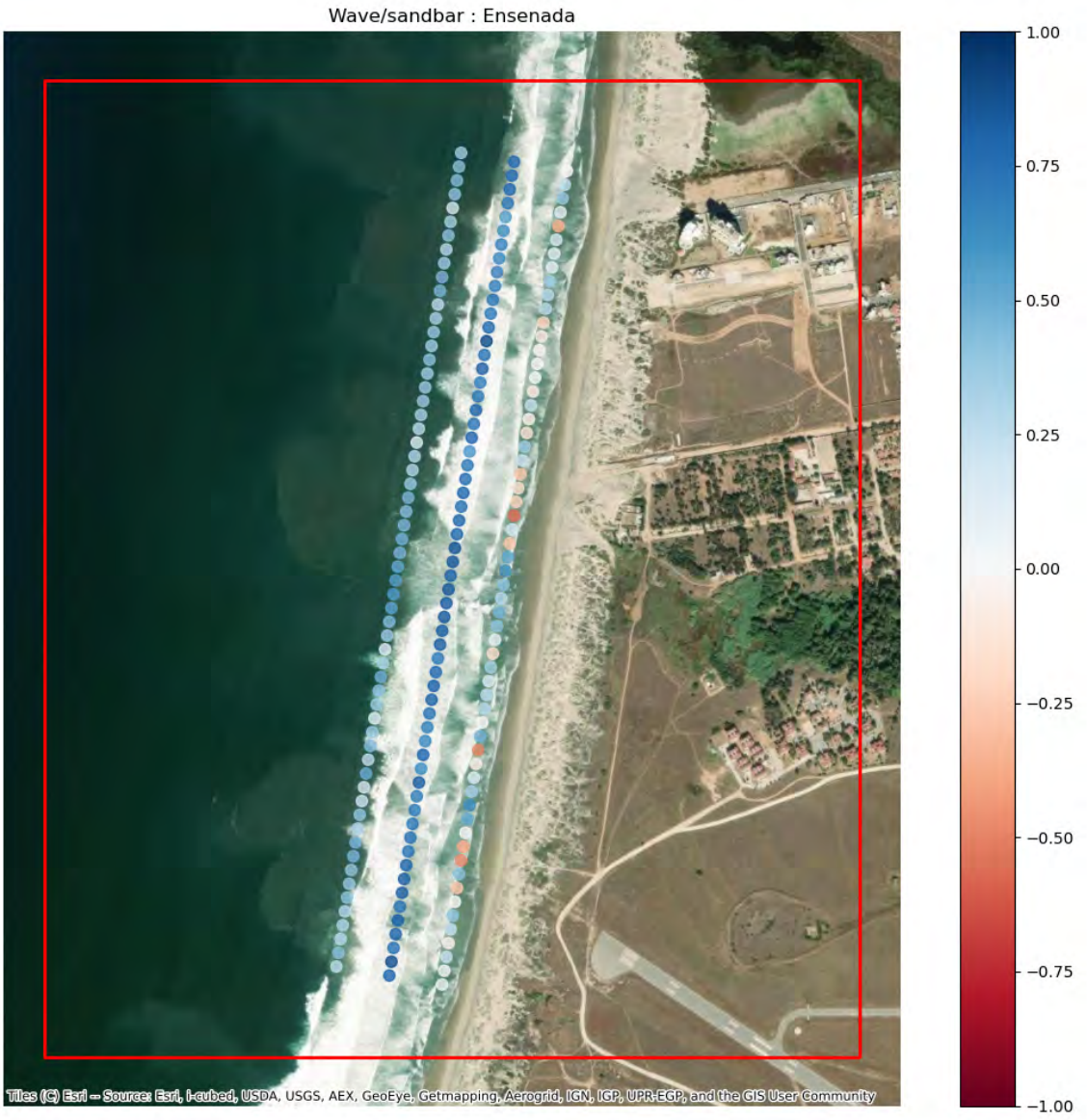

Figure C.1: Pearson's correlations between monthly sampled wave power flux and satellite-derived sandbar positions at multiple transects at Ensenada. The correlations are represented as three parallel lines of data points, with the first (landward) row showing interannual correlation, the middle row seasonal correlation, and the last row the high-frequency correlation.

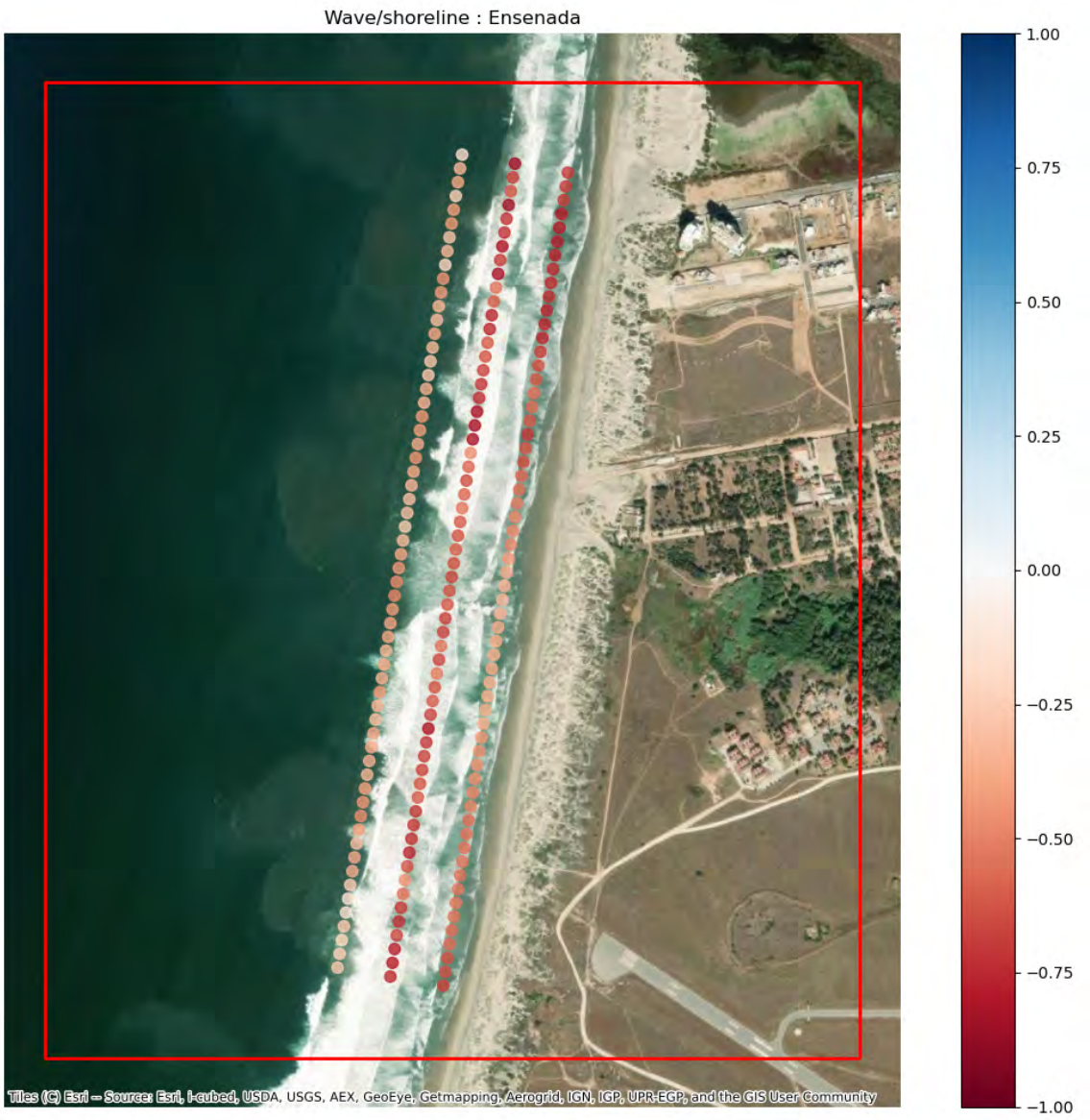

Figure C.2: Pearson's correlations between monthly sampled wave power flux and SDS at multiple transects at Ensenada. The correlations are represented as three parallel lines of data points, with the first (landward) row showing interannual correlation, the middle row seasonal correlation, and the last row the high-frequency correlation.

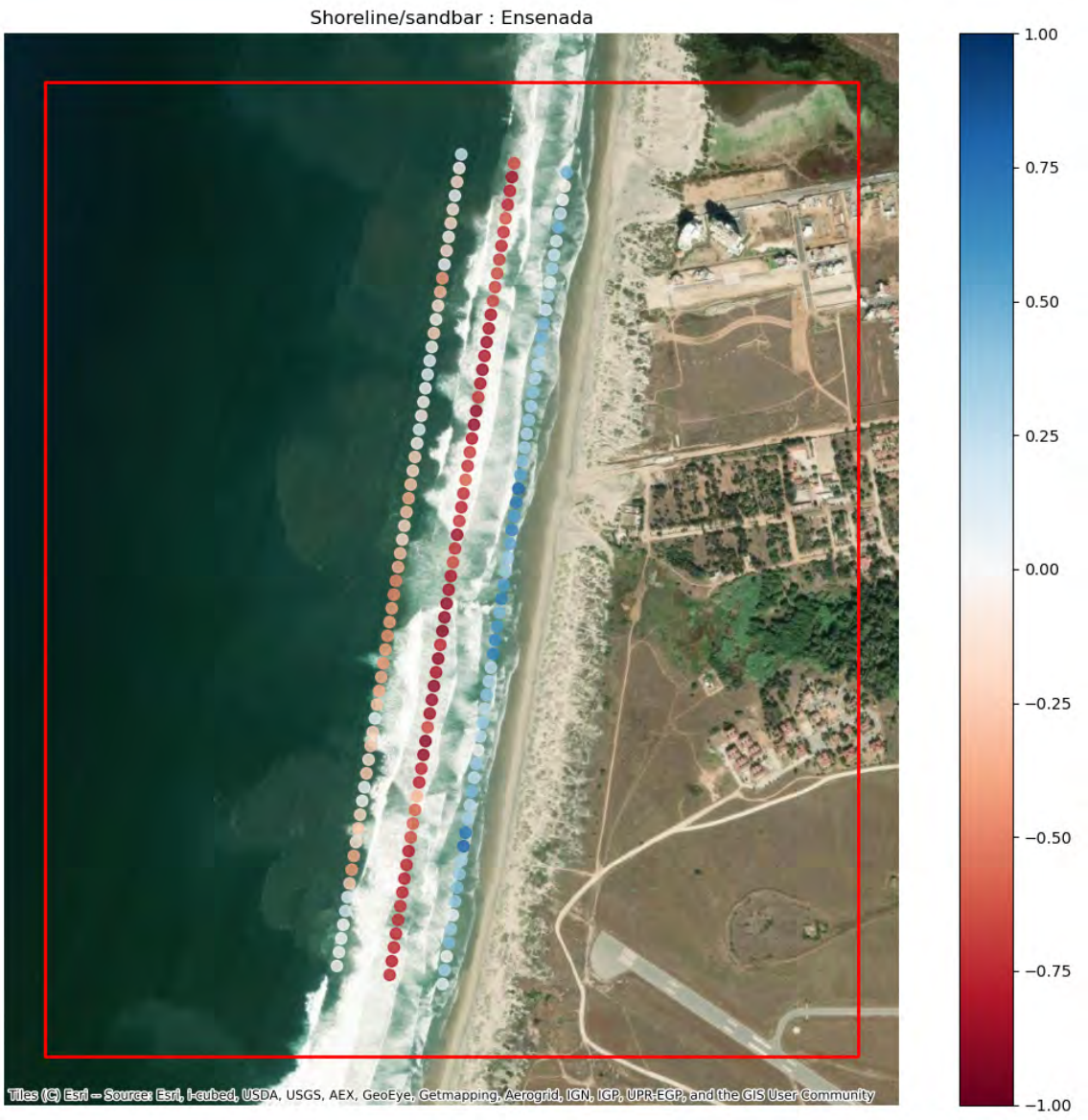

Figure C.3: Pearson's correlations between monthly sampled SDS and satellite-derived sandbar positions at multiple transects at Ensenada. The correlations are represented as three parallel lines of data points, with the first (landward) row showing interannual correlation, the middle row seasonal correlation, and the last row the high-frequency correlation.

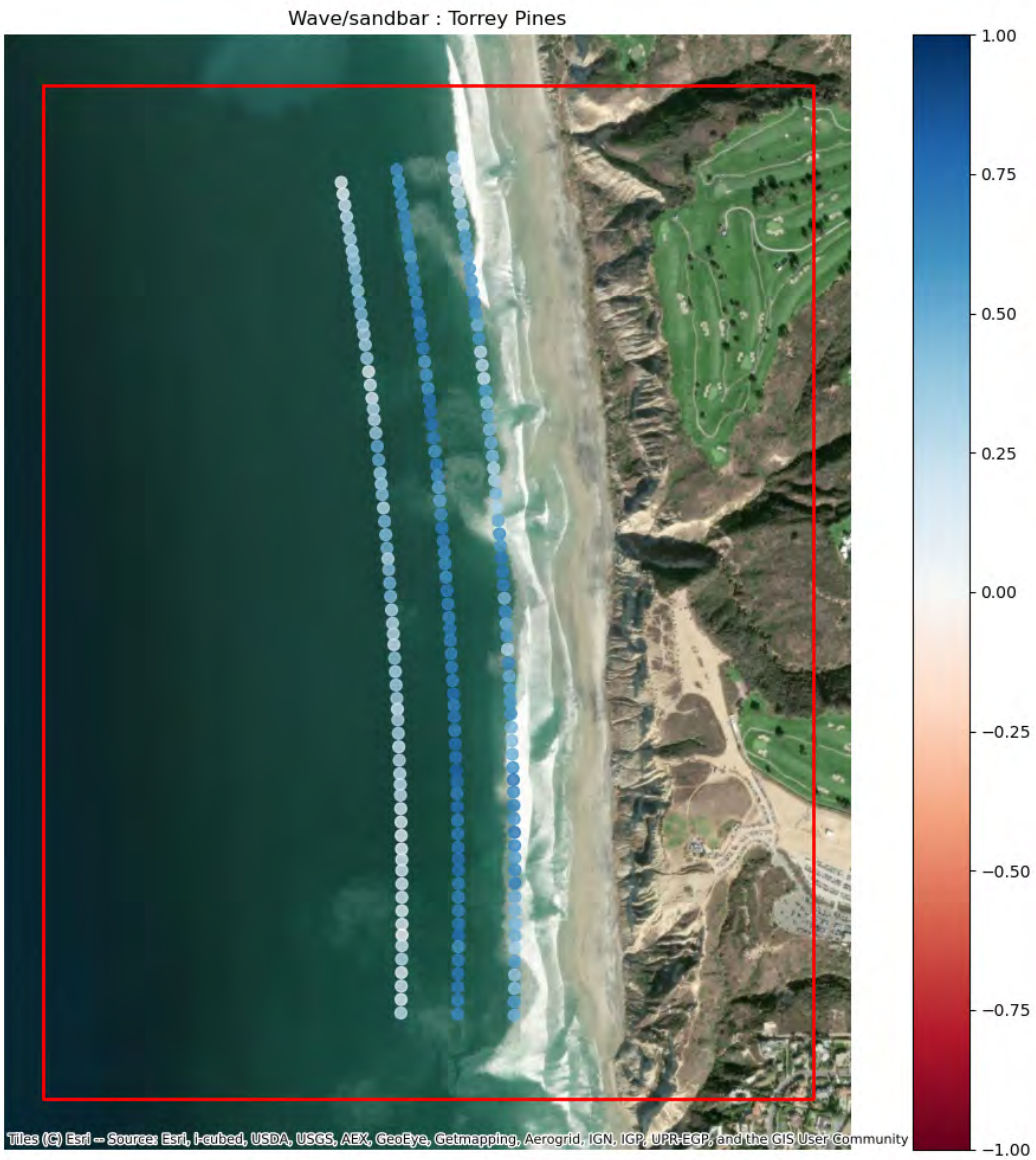

Figure C.4: Pearson's correlations between monthly sampled wave power flux and satellite-derived sandbar positions at multiple transects at Torrey Pines. The correlations are represented as three parallel lines of data points, with the first (landward) row showing interannual correlation, the middle row seasonal correlation, and the last row the high-frequency correlation.

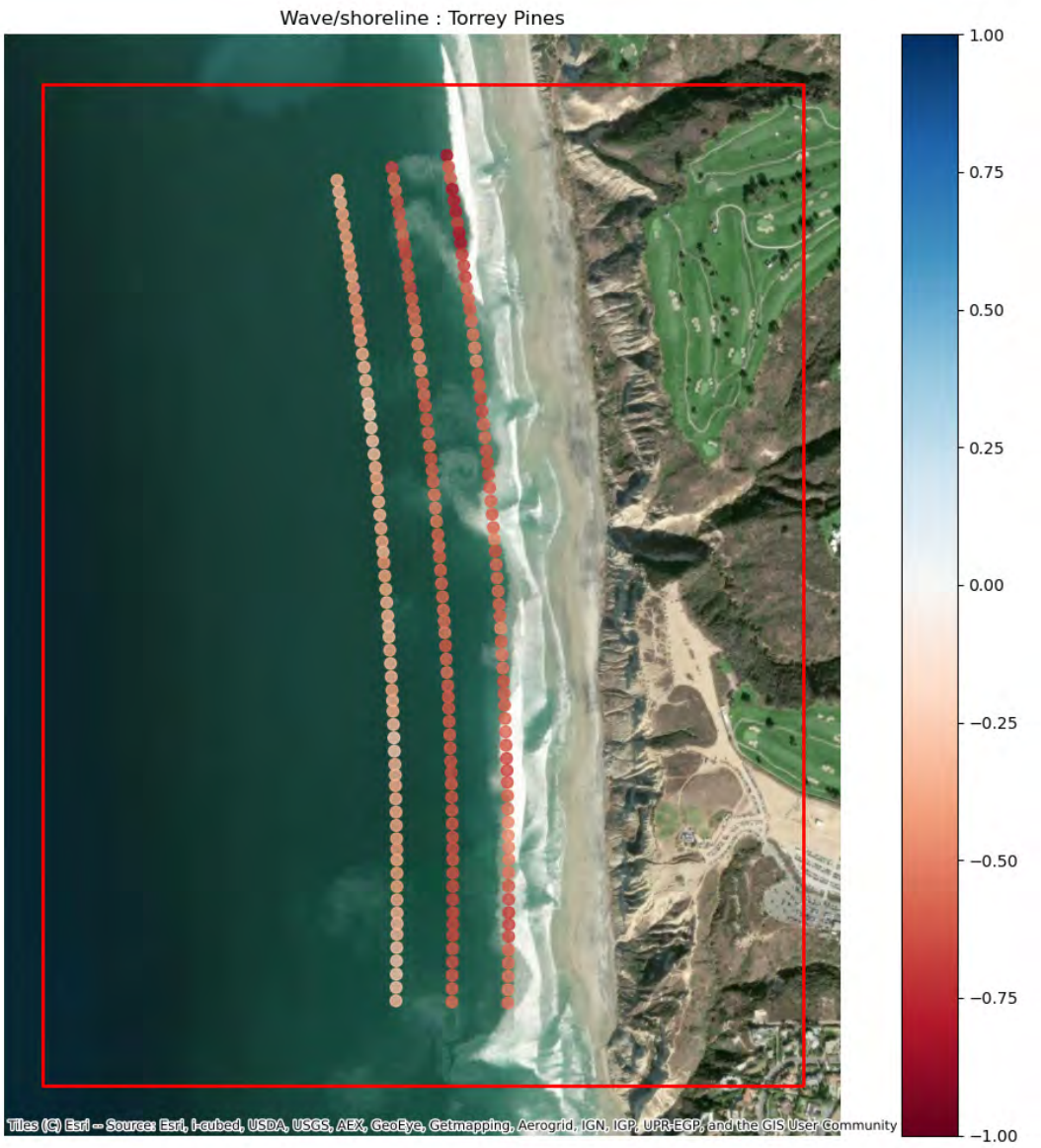

Figure C.5: Pearson's correlations between monthly sampled wave power flux and SDS at multiple transects at Torrey Pines. The correlations are represented as three parallel lines of data points, with the first (landward) row showing interannual correlation, the middle row seasonal correlation, and the last row the high-frequency correlation.

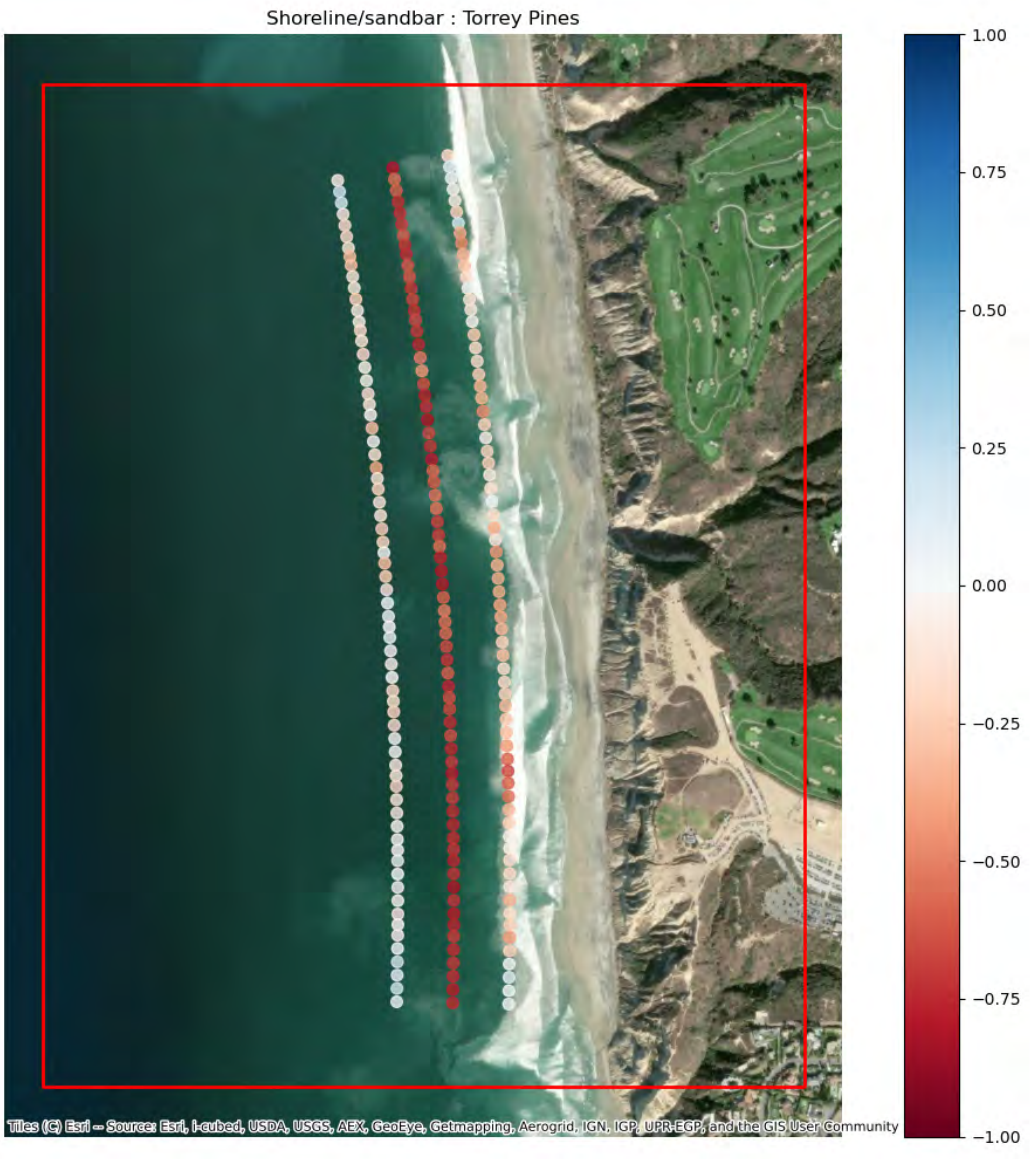

Figure C.6: Pearson's correlations between monthly sampled SDS and satellite-derived sandbar positions at multiple transects at Torrey Pines. The correlations are represented as three parallel lines of data points, with the first (landward) row showing interannual correlation, the middle row seasonal correlation, and the last row the high-frequency correlation.

C.3.2 Accounting for the sandbar positions to model shoreline positions based on equilibrium models

In this section are presented the results of the optimization of ShoreFor, and its modified version with a mechanical spring term. The two first figures display the ShoreFor result as described by Eq. C.3, and the two following figures display the results with the modified version described by Eq. C.7.

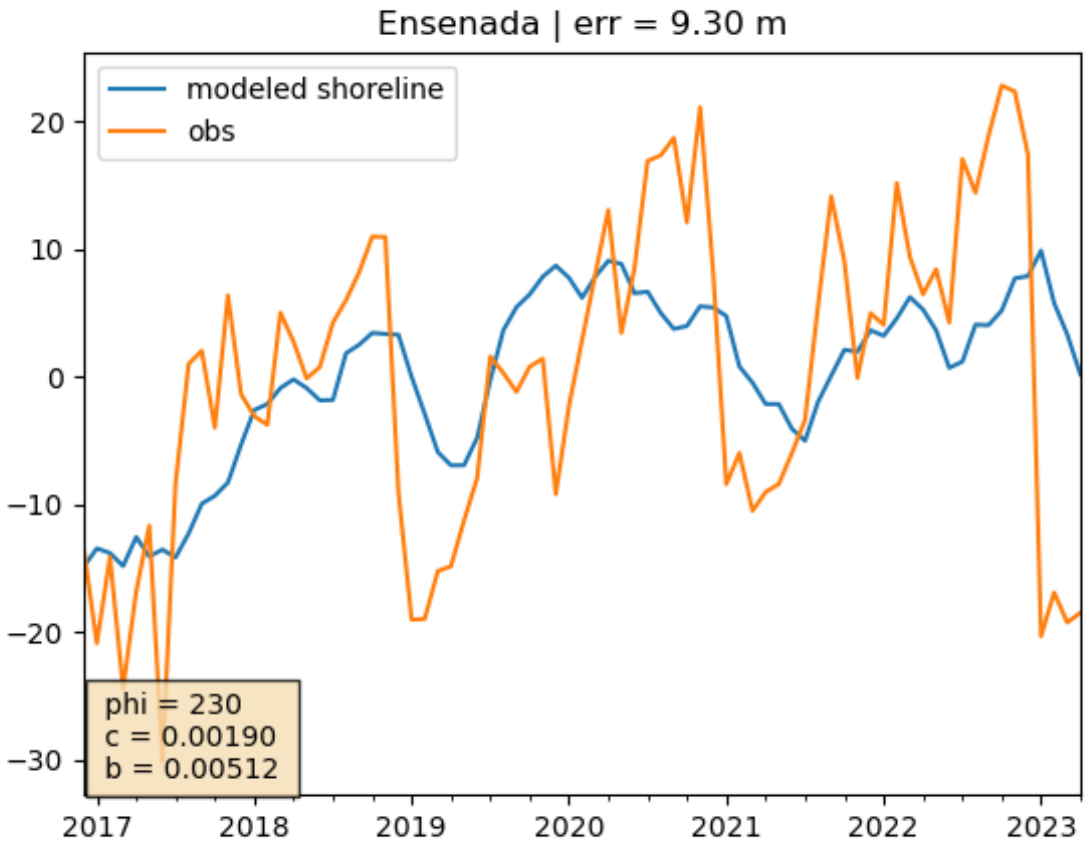

Figure C.7: Output of the ShoreFor model at Ensenada. SDS are represented in orange and modeled shoreline position are represented in blue. Optimized free parameter values are indicated. The indicated error is the centered RMSE, standard deviation of the errors.

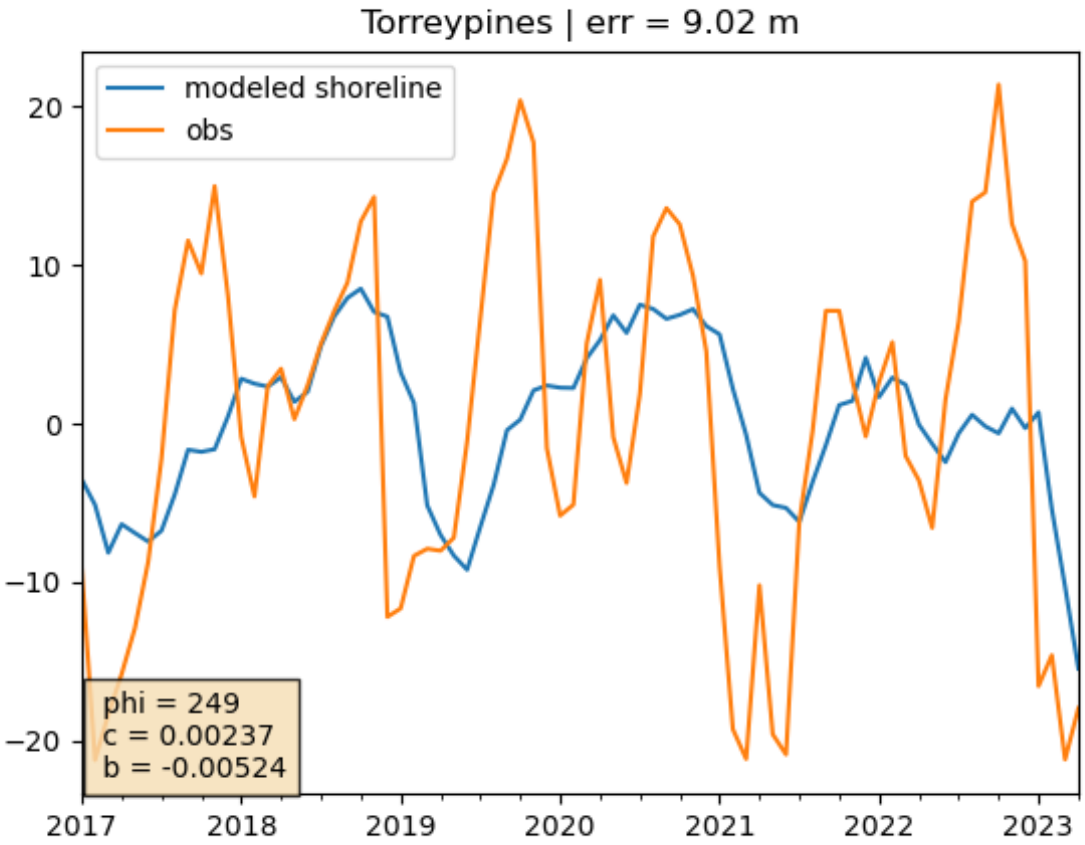

Figure C.8: Output of the ShoreFor model at Torrey Pines. SDS are represented in orange and modeled shoreline position are represented in blue. Optimized free parameter values are indicated. The indicated error is the centered RMSE, standard deviation of the errors.

Accounting for the sandbar position in the ShoreFor model improved the modeled shoreline position accuracy by 0.56 m in Ensenada and 2.9 m at Torrey Pines. The improvements in the capacity of the model to capture the seasonal variability of the shoreline position suggest that explicitly incorporating sandbar dynamics holds potential for improving shoreline modeling. While these results are site-specific and further testing is needed, they indicate that coupling sandbar and shoreline processes may provide a promising pathway for improved coastal morphodynamics predictions.

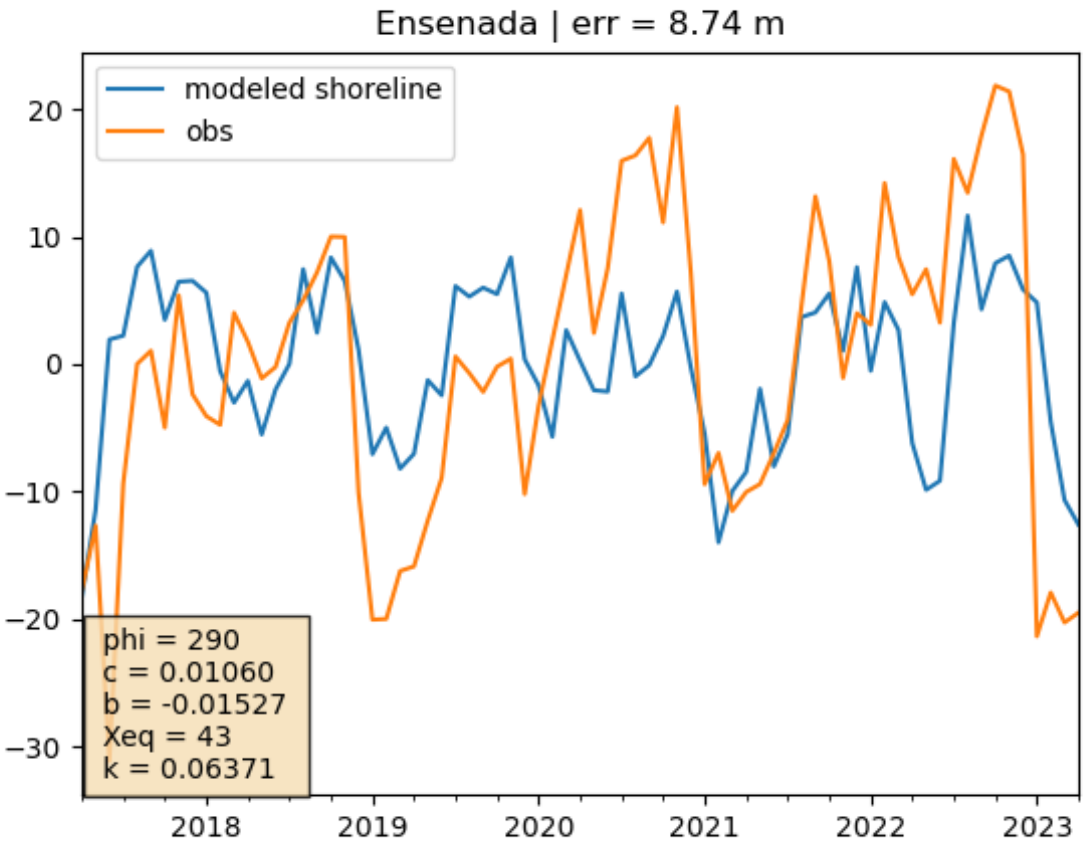

Figure C.9: Output of the modified ShoreFor model at Ensenada. SDS are represented in orange and modeled shoreline position are represented in blue. Optimized free parameter values are indicated. The indicated error is the centered RMSE, standard deviation of the errors.

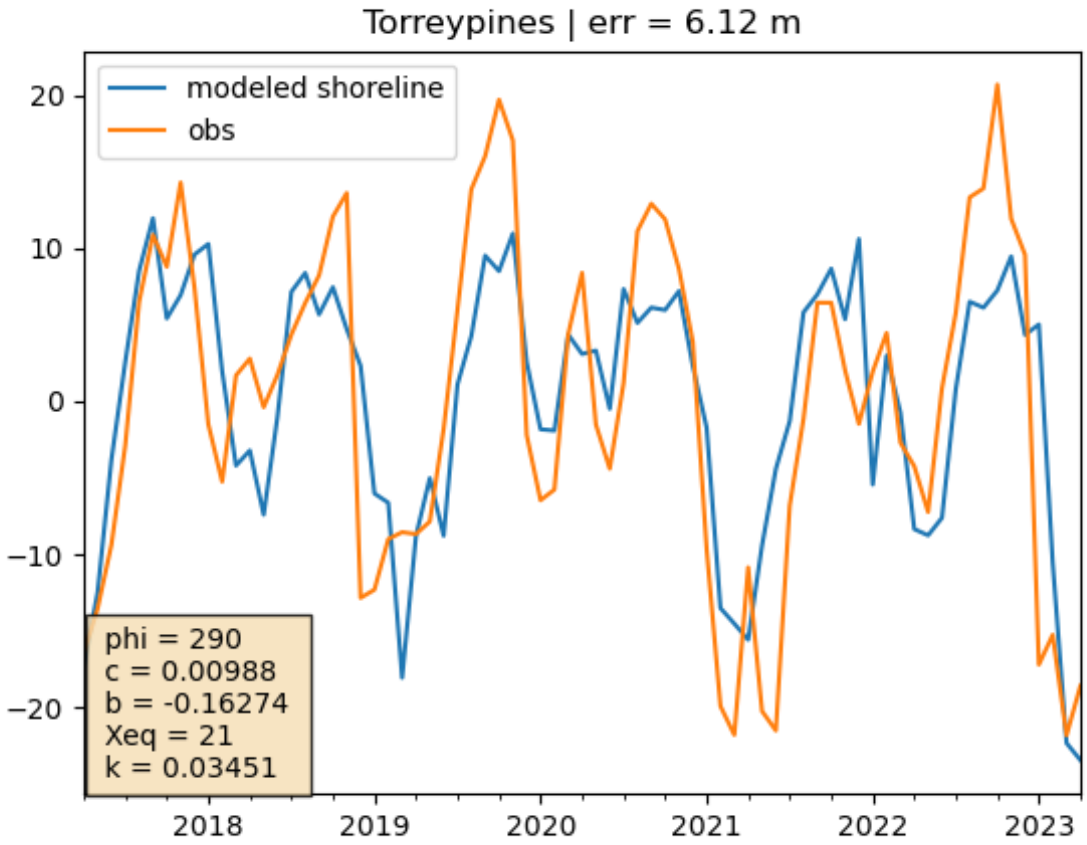

Figure C.10: Output of the modified ShoreFor model at Torrey Pines. SDS are represented in orange and modeled shoreline position are represented in blue. Optimized free parameter values are indicated. The indicated error is the centered RMSE, standard deviation of the errors.

Acronyms

ADCP : Acoustic Doppler Current Profiler

AMO : Atlantic Multidecadal Oscillation

AWEI : Automated Water Extraction Index

AWEIns : Automated Water Extraction Index non-shadowed

AWEIsh : Automated Water Extraction Index shadowed

BC : Baja California

BCS : Baja California Sur

CP : Central Pacific

cRMSE : centered Root-Mean-Square Error

CVI : Coastal Vulnerability Index

DoC : Depth of Closure

EKE : Eddy Kinetic Energy

ENSO : El Niño - Southern Oscillation

EP : Easter Pacific

EPH : Eastern Pacific Hurricane

GNSS : Global Navigation Satellite System

IOD : Indien Ocean Dipole

IQR : Interquartile Range

LM : Local Minimum

MEI : Multivariate ENSO Index

MHW : Mean High Water

MLW : Mean Low Water

MMSL : Monthly Mean Sea Level

MNDWI : Modified Normalized Difference Water Index

MSL : Mean Sea Level

MSV : Minimul Shoreline Variability

NAWC : North American West Coast

NCA : Northern California

NDWI : Normalized Difference Water Index

NIR : Near Infrared

NAO : Northern Atlantic Oscillation

ONI : Oceanic Niño Index

PDO : Pacific Decadal Oscillation

PNW : Pacific Northwest

ROI : Region Of Interest

SAR : Synthetic-Aperture Radar

SCA : Southern California

SCoWI : Substractive Coastal Water Index

SDS : Satellite-Derived Shoreline

SDW : Satellite-Derived Waterline

SLP : Sea Level Pressure

SLR : Sea Level Rise

SNR : Signal-to-Noise Ratio

SST : Sea Surface Temperature

SWIR : Short-wave Infrared

WP : Weighted Peaks

Bibliography

A. H. Sallenger, J., Krabill, W. B., Swift, R. N., Brock, J., List, J., Hansen, M., Holman, R. A., Manizade, S., Sontag, J., Meredith, A., Morgan, K., Yunkel, J. K., Frederick, E. B., & Stockdon, H. (2003). Evaluation of Airborne Topographic Lidar for Quantifying Beach Changes [Publisher: Coastal Education & Research Foundation, Inc.]. *Journal of Coastal Research 19*(1), 125–133. https://www.jstor.org/stable/4299152

Aagaard, T. (2014). Sediment supply to beaches: Cross-shore sand transport on the lower shoreface [_eprint: https://agupubs.onlinelibrary.wiley.com/doi/pdf/10.1002/2013JF003041]. *Journal of Geophysical Research: Earth Surface 119*(4), 913–926. https://doi.org/10.1002/2013JF003041

Adams, P. N., Inman, D. L., & Graham, N. E. (2008). Southern California Deep-Water Wave Climate: Characterization and Application to Coastal Processes [Publisher: Coastal Education and Research Foundation]. *Journal of Coastal Research 2008*(244), 1022–1035. https://doi.org/10.2112/07-0831.1

Ruiz de Alegría-Arzaburu, A., Costas, S., & Delgado-Fernández, I. (2025). Impacts of El Niño on the sediment balance of a transgressive dune-beach system. *Science of The Total Environment 999*, 180348. https://doi.org/10.1016/j.scitotenv.2025.180348

Ruiz de Alegría-Arzaburu, A., Gasalla-LOpez, B., & Benavente, J. (2022a). Morphological response of an embayed beach to swell-driven storminess cycles over an 8-year period. *Geomorphology 403*, 108164. https://doi.org/10.1016/j.geomorph.2022.108164

Ruiz de Alegría-Arzaburu, A., Gracia-Barrera, A. D., Kono-Martínez, T., & Coco, G. (2022b). Subaerial and upper-shoreface morphodynamics of a highly-dynamic enclosed beach in NW Baja California. *Geomorphology 413*, 108336. https://doi.org/10.1016/j.geomorph.2022.108336

Ruiz de Alegría-Arzaburu, A., & Vidal-Ruiz, J. A. (2018). Beach recovery capabilities after El Niño 2015–2016 at Ensenada Beach, Northern Baja California. *Ocean Dynamics 68*(6), 749–759. https://doi.org/10.1007/s10236-018-1164-6

Allan, J., & Komar, P. (2006). Climate Controls on US West Coast Erosion Processes. *Journal of Coastal Research - J COASTAL RES 22*, 511–529. https://doi.org/10.2112/03-0108.1

Allan, J. C., & Komar, P. D. (2002a). Extreme Storms on the Pacific Northwest Coast during the 1997-98 El Niño and 1998-99 La Niña [Publisher: Coastal Education & Research Foundation, Inc.]. *Journal of Coastal Research 18*(1), 175–193. https://www.jstor.org/stable/4299063

Allan, J. C., & Komar, P. D. (2002b). Wave Climate Change and Coastal Erosion in the US Pacific Northwest [Publisher: American Society of Civil Engineers], 680–689. https://doi.org/10.1061/40604(273)70

Almar, R., Bergsma, E., Thoumyre, G., Baba, M. W., Cesbron, G., Daly, C., Garlan, T., & Lifermann, A. (2021a). Global Satellite-Based Coastal Bathymetry from Waves. *Remote Sensing 13*, 4628. https://doi.org/10.3390/rs13224628

Almar, R., Bergsma, E. W. J., Maisongrande, P., & de Almeida, L. P. M. (2019). Wave-derived coastal bathymetry from satellite video imagery: A showcase with Pleiades persistent mode. *Remote Sensing of Environment 231*, 111263. https://doi.org/10.1016/j.rse.2019.111263

Almar, R., Bergsma, E. W. J., Thoumyre, G., Solange, L. C., Loyer, S., Artigues, S., Salles, G., Garlan, T., & Lifermann, A. (2024a). Satellite-derived bathymetry from correlation of Sentinel-2 spectral bands to derive wave kinematics: Qualification of Sentinel-2 S2Shores estimates with hydrographic standards. *Coastal Engineering 189*, 104458. https://doi.org/10.1016/j.coastaleng.2024.104458

Almar, R., Boucharel, J., Abessolo, G. O., Papa, F., & Bergsma, E. W. J. (2024b). Reply to: Coastal shoreline change assessments at global scales [Publisher: Nature Publishing Group]. *Nature Communications 15*(1), 2317. https://doi.org/10.1038/s41467-024-46609-w

Almar, R., Boucharel, J., Graffin, M., Abessolo, G. O., Thoumyre, G., Papa, F., Ranasinghe, R., Montano, J., Bergsma, E. W. J., Baba, M. W., & Jin, F. F. (2023). Influence of El Niño on the variability of global shoreline position [Number: 1 Publisher: Nature Publishing Group]. *Nature Communications 14*(1), 3133. https://doi.org/10.1038/s41467-023-38742-9

Almar, R., Ranasinghe, R., Bergsma, E. W. J., Diaz, H., Melet, A., Papa, F., Vousdoukas, M., Athanasiou, P., Dada, O., Almeida, L. P., & Kestenare, E. (2021b). A global analysis of extreme coastal water levels with implications for potential coastal overtopping [Publisher: Nature Publishing Group]. *Nature Communications 12*(1), 3775. https://doi.org/10.1038/s41467-021-24008-9

Almar, R., Ranasinghe, R., Sénéchal, N., Bonneton, P., Roelvink, D., Bryan, K. R., Marieu, V., & Parisot, J. P. (2012). Video-Based Detection of Shorelines at Complex Meso–Macro Tidal Beaches [Publisher: Coastal Education and Research Foundation]. *Journal of Coastal Research 28*(5), 1040–1048. https://doi.org/10.2112/JCOASTRES-D-10-00149.1

Almeida, L., Almar, R., Bergsma, E., Berthier, E., Baptista, P., Garel, E., Dada, O., & Alves, B. (2019). Deriving High Spatial-Resolution Coastal Topography From Sub-meter Satellite Stereo Imagery. *Remote Sensing 11*(5), 590. https://doi.org/10.3390/rs11050590

Almeida, L. P., Efraim de Oliveira, I., Lyra, R., Scaranto Dazzi, R. L., Martins, V. G., & Henrique da Fontoura Klein, A. (2021). Coastal Analyst System from Space Imagery Engine (CASSIE): Shoreline management module. *Environmental Modelling & Software 140*, 105033. https://doi.org/10.1016/j.envsoft.2021.105033

Amrouni, O., Heggy, E., & Hzami, A. (2024). Shoreline retreat and beach nourishment are projected to increase in Southern California [Publisher: Nature Publishing Group]. *Communications Earth & Environment 5*(1), 1–17. https://doi.org/10.1038/s43247-024-01388-6

Anderson, D., Bak, A. S., Cohn, N., Brodie, K. L., Johnson, B., & Dickhudt, P. (2023). The Impact of Inherited Morphology on Sandbar Migration During Mild Wave Seasons [_eprint: https://agupubs.onlinelibrary.wiley.com/doi/pdf/10.1029/2022GL101219]. *Geophysical Research Letters 50*(3), e2022GL101219. https://doi.org/10.1029/2022GL101219

Anderson, D., Rueda, A., Cagigal, L., Antolinez, J. a. A., Mendez, F. J., & Ruggiero, P. (2019). Time-Varying Emulator for Short and Long-Term Analysis of Coastal Flood Hazard Potential [Publisher: John Wiley & Sons, Ltd]. *Journal of Geophysical Research: Oceans 124*(12), 9209–9234. https://doi.org/10.1029/2019JC015312

Anderson, D., Ruggiero, P., Antolínez, J. A. A., Méndez, F. J., & Allan, J. (2018). A Climate Index Optimized for Longshore Sediment Transport Reveals Interannual and Multidecadal Littoral Cell Rotations. *Journal of Geophysical Research: Earth Surface 123*(8), 1958–1981. https://doi.org/10.1029/2018JF004689

Angelini, R., Angelats, E., Luzi, G., Masiero, A., Simarro, G., & Ribas, F. (2024). Development of Methods for Satellite Shoreline Detection and Monitoring of Megacusp Undulations [Number: 23 Publisher: Multidisciplinary Digital Publishing Institute]. *Remote Sensing 16*(23), 4553. https://doi.org/10.3390/rs16234553

Anthony, E. J., & Aagaard, T. (2020). The lower shoreface: Morphodynamics and sediment connectivity with the upper shoreface and beach. *Earth-Science Reviews 210*, 103334. https://doi.org/10.1016/j.earscirev.2020.103334

Anthony, E. J., Vanhee, S., & Ruz, M. H. (2006). Short-term beach–dune sand budgets on the north sea coast of France: Sand supply from shoreface to dunes, and the role of wind and fetch. *Geomorphology 81*(3), 316–329. https://doi.org/10.1016/j.geomorph.2006.04.022

Arias, A., Almar, R., Regard, V., Bergsma, E. W. J., Castelle, B., & Garlan, T. (2025). Assessment of Beach Slope and Sediment Grain Size Anywhere in the World: Review of Existing Formulae, Integration of Tidal Influence, and Perspectives from Satellite Observations [Number: 1 Publisher: Multidisciplinary Digital Publishing Institute]. *Journal of Marine Science and Engineering 13*(1), 58. https://doi.org/10.3390/jmse13010058

Azorakos, G., Castelle, B., Marieu, V., & Idier, D. (2024). Satellite-derived equilibrium shoreline modelling at a high-energy meso-macrotidal beach. *Coastal Engineering 191*, 104536. https://doi.org/10.1016/j.coastaleng.2024.104536

Banno, M., Nakamura, S., Kosako, T., Nakagawa, Y., Yanagishima, S. i., & Kuriyama, Y. (2020). Long-Term Observations of Beach Variability at Hasaki, Japan [Number: 11 Publisher: Multidisciplinary Digital Publishing Institute]. *Journal of Marine Science and Engineering 8*(11), 871. https://doi.org/10.3390/jmse8110871

Barnard, P. L., Allan, J., Hansen, J. E., Kaminsky, G. M., Ruggiero, P., & Doria, A. (2011). The impact of the 2009–10 El Niño Modoki on U.S. West Coast beaches [_eprint: https://onlinelibrary.wiley.com/doi/pdf/10.1029/2011GL047707]. *Geophysical Research Letters 38*(13). https://doi.org/10.1029/2011GL047707

Barnard, P. L., Dugan, J. E., Page, H. M., Wood, N. J., Hart, J. A. F., Cayan, D. R., Erikson, L. H., Hubbard, D. M., Myers, M. R., Melack, J. M., & Iacobellis, S. F. (2021). Multiple climate change-driven tipping points for coastal systems [Publisher: Nature Publishing Group]. *Scientific Reports 11*(1), 15560. https://doi.org/10.1038/s41598-021-94942-7

Barnard, P. L., Hoover, D., Hubbard, D. M., Snyder, A., Ludka, B. C., Allan, J., Kaminsky, G. M., Ruggiero, P., Gallien, T. W., Gabel, L., McCandless, D., Weiner, H. M., Cohn, N., Anderson, D. L., & Serafin, K. A. (2017). Extreme oceanographic forcing and coastal response due to the 2015–2016 El Niño [Number: 1 Publisher: Nature Publishing Group]. *Nature Communications 8*(1), 14365. https://doi.org/10.1038/ncomms14365

Barnard, P. L., Short, A. D., Harley, M. D., Splinter, K. D., Vitousek, S., Turner, I. L., Allan, J., Banno, M., Bryan, K. R., Doria, A., Hansen, J. E., Kato, S., Kuriyama, Y., Randall-Goodwin, E., Ruggiero, P., Walker, I. J., & Heathfield, D. K. (2015). Coastal vulnerability across the Pacific dominated by El Niño/Southern Oscillation. *Nature Geoscience 8*(10), 801–807. https://doi.org/10.1038/ngeo2539

Barnard, P. L., & Warrick, J. A. (2010). Dramatic beach and nearshore morphological changes due to extreme flooding at a wave-dominated river mouth. *Marine Geology 271*(1-2), 131–148. https://doi.org/10.1016/j.margeo.2010.01.018

Barroso, A., Wahl, T., Li, S., Enriquez, A., Morim, J., Dangendorf, S., Piecuch, C., & Thompson, P. (2024). Observed Spatiotemporal Variability in the Annual Sea Level Cycle Along the Global Coast [_eprint: https://agupubs.onlinelibrary.wiley.com/doi/pdf/10.1029/2023JC020300]. *Journal of Geophysical Research: Oceans 129*(4), e2023JC020300. https://doi.org/10.1029/2023JC020300

Benveniste, J., Cazenave, A., Vignudelli, S., Fenoglio-Marc, L., Shah, R., Almar, R., Andersen, O., Birol, F., Bonnefond, P., Bouffard, J., Calafat, F., Cardellach, E., Cipollini, P., Le Cozannet, G., Dufau, C., Fernandes, M. J., Frappart, F., Garrison, J., Gommenginger, C., Han, G., Høyer, J. L., Kourafalou, V., Leuliette, E., Li, Z., Loisel, H., Madsen, K. S., Marcos, M., Melet, A., Meyssignac, B., Pascual, A., Passaro, M., RibO, S., Scharroo, R., Song, Y. T., Speich, S., Wilkin, J., Woodworth, P., & Wöppelmann, G. (2019). Requirements for a Coastal Hazards Observing System [Publisher: Frontiers]. *Frontiers in Marine Science 6*. https://doi.org/10.3389/fmars.2019.00348

Bergsma, E., Klotz, A., Artigues, S., Graffin, M., Prenowitz, A., Delvit, J. M., & Almar, R. (2024). Shoreliner: A Sub-Pixel Coastal Waterline Extraction Pipeline for Multi-Spectral Satellite Optical Imagery. *Remote Sensing 16*, 2795. https://doi.org/10.3390/rs16152795

Bergsma, E. W., Almar, R., Rolland, A., Binet, R., Brodie, K. L., & Bak, A. S. (2021). Coastal morphology from space: A showcase of monitoring the topography-bathymetry continuum. *Remote Sensing of Environment 261*, 112469. https://doi.org/10.1016/j.rse.2021.112469

Bergsma, E. W. J., & Almar, R. (2020). Coastal coverage of ESA' Sentinel 2 mission. *Advances in Space Research 65*(11), 2636–2644. https://doi.org/10.1016/j.asr.2020.03.001

Bergsma, E. W. J., Almar, R., Anthony, E. J., Garlan, T., & Kestenare, E. (2022). Wave variability along the world's continental shelves and coasts: Monitoring opportunities from satellite

Earth observation. *Advances in Space Research 69*(9), 3236–3244. https://doi.org/10.1016/j.asr.2022.02.047

Bergsma, E. W. J., Almar, R., & Maisongrande, P. (2019a). Radon-Augmented Sentinel-2 Satellite Imagery to Derive Wave-Patterns and Regional Bathymetry. *Remote Sensing 11*(16), 1918. https://doi.org/10.3390/rs11161918

Bergsma, E. W. J., Conley, D. C., Davidson, M. A., O'Hare, T. J., & Almar, R. (2019b). Storm Event to Seasonal Evolution of Nearshore Bathymetry Derived from Shore-Based Video Imagery [Publisher: Multidisciplinary Digital Publishing Institute]. *Remote Sensing 11*(5), 519. https://doi.org/10.3390/rs11050519

Bertin, S., Floc'h, F., Le Dantec, N., Jaud, M., Cancouët, R., Franzetti, M., Cuq, V., Prunier, C., Ammann, J., Augereau, E., Lamarche, S., Belleney, D., Rouan, M., David, L., Deschamps, A., Delacourt, C., & Suanez, S. (2022). A long-term dataset of topography and nearshore bathymetry at the macrotidal pocket beach of Porsmilin, France [Number: 1 Publisher: Nature Publishing Group]. *Scientific Data 9*(1), 79. https://doi.org/10.1038/s41597-022-01170-3

Bertin, X., Oliveira, A., & Fortunato, A. B. (2009). Simulating morphodynamics with unstructured grids: Description and validation of a modeling system for coastal applications. *Ocean Modelling 28*(1), 75–87. https://doi.org/10.1016/j.ocemod.2008.11.001

Bevacqua, E., Maraun, D., Vousdoukas, M. I., Voukouvalas, E., Vrac, M., Mentaschi, L., & Widmann, M. (2019). Higher probability of compound flooding from precipitation and storm surge in Europe under anthropogenic climate change [Publisher: American Association for the Advancement of Science]. *Science Advances 5*(9), eaaw5531. https://doi.org/10.1126/sciadv.aaw5531

Bishop-Taylor, R., Nanson, R., Sagar, S., & Lymburner, L. (2021). Mapping Australia's dynamic coastline at mean sea level using three decades of Landsat imagery. *Remote Sensing of Environment 267*, 112734. https://doi.org/10.1016/j.rse.2021.112734

Bishop-Taylor, R., Phillips, C., Sagar, S., Newey, V., & Sutterley, T. (2025). eo-tides: Tide modelling tools for large-scale satellite Earth observation analysis. *Journal of Open Source Software 10*(109), 7786. https://doi.org/10.21105/joss.07786

Bishop-Taylor, R., Sagar, S., Lymburner, L., Alam, I., & Sixsmith, J. (2019a). Sub-Pixel Waterline Extraction: Characterising Accuracy and Sensitivity to Indices and Spectra [Number: 24 Publisher: Multidisciplinary Digital Publishing Institute]. *Remote Sensing 11*(24), 2984. https://doi.org/10.3390/rs11242984

Bishop-Taylor, R., Sagar, S., Lymburner, L., & Beaman, R. J. (2019b). Between the tides: Modelling the elevation of Australia's exposed intertidal zone at continental scale. *Estuarine, Coastal and Shelf Science 223*, 115–128. https://doi.org/10.1016/j.ecss.2019.03.006

Boak, E. H., & Turner, I. L. (2005). Shoreline Definition and Detection: A Review [Publisher: Coastal Education & Research Foundation, Inc.]. *Journal of Coastal Research 21*(4), 688–703. https://www.jstor.org/stable/4299462

Boucharel, J., Almar, R., & Dewitte, B. (2024). Seasonal forecasts of the world's coastal waterline: what to expect from the coming El Niño? [Publisher: Nature Publishing Group]. *npj Climate and Atmospheric Science 7*(1), 37. https://doi.org/10.1038/s41612-024-00570-z

Boucharel, J., Almar, R., Kestenare, E., & Jin, F. F. (2021a). On the influence of ENSO complexity on Pan-Pacific coastal wave extremes [Publisher: Proceedings of the National Academy of Sciences]. *Proceedings of the National Academy of Sciences 118*(47), e2115599118. https://doi.org/10.1073/pnas.2115599118

Boucharel, J., Santiago, L., Almar, R., & Kestenare, E. (2021b). Coastal Wave Extremes around the Pacific and Their Remote Seasonal Connection to Climate Modes [Number: 12 Publisher: Multidisciplinary Digital Publishing Institute]. *Climate 9*(12), 168. https://doi.org/10.3390/cli9120168

Bromirski, P. D. (2023). Climate-Induced Decadal Ocean Wave Height Variability From Microseisms: 1931–2021 [_eprint: https://onlinelibrary.wiley.com/doi/pdf/10.1029/2023JC019722]. *Journal of Geophysical Research: Oceans 128*(8), e2023JC019722. https://doi.org/10.1029/2023JC019722

Bruun, P. (1954). *Coast Erosion and the Development of Beach Profiles* [Google-Books-ID: I1YOmK4aYI0C]. U.S. Beach Erosion Board.

Bruun Per. (1962). Sea-Level Rise as a Cause of Shore Erosion [Publisher: American Society of Civil Engineers]. *Journal of the Waterways and Harbors Division 88*(1), 117–130. https://doi.org/10.1061/JWHEAU.0000252

Burvingt, O., & Castelle, B. (2023). Storm response and multi-annual recovery of eight coastal dunes spread along the Atlantic coast of Europe. *Geomorphology 435*, 108735. https://doi.org/10.1016/j.geomorph.2023.108735

Burvingt, O., Castelle, B., Marieu, V., Lubac, B., Nicolae Lerma, A., & Robin, N. (2025). Using Pleiades Satellite Imagery to Monitor Multi-Annual Coastal Dune Morphological Changes [Publisher: Multidisciplinary Digital Publishing Institute]. *Remote Sensing 17*(9), 1522. https://doi.org/10.3390/rs17091522

Cabezas-Rabadán, C., Pardo-Pascual, J. E., Palomar-Vázquez, J., & Cooper, A. (2025). A remote monitoring approach for coastal engineering projects [Publisher: Nature Publishing Group]. *Scientific Reports 15*(1), 2955. https://doi.org/10.1038/s41598-025-86485-y

Cagigal, L., Rueda, A., Anderson, D., Ruggiero, P., Merrifield, M. A., Montaño, J., Coco, G., & Méndez, F. J. (2020). A multivariate, stochastic, climate-based wave emulator for shoreline change modelling. *Ocean Modelling 154*, 101695. https://doi.org/10.1016/j.ocemod.2020.101695

Cai, W., Santoso, A., Collins, M., Dewitte, B., Karamperidou, C., Kug, J. S., Lengaigne, M., McPhaden, M. J., Stuecker, M. F., Taschetto, A. S., Timmermann, A., Wu, L., Yeh, S. W., Wang, G., Ng, B., Jia, F., Yang, Y., Ying, J., Zheng, X. T., Bayr, T., Brown, J. R., Capotondi, A., Cobb, K. M., Gan, B., Geng, T., Ham, Y. G., Jin, F. F., Jo, H. S., Li, X., Lin, X., McGregor, S., Park, J. H., Stein, K., Yang, K., Zhang, L., & Zhong, W. (2021). Changing El Niño–Southern Oscillation in

a warming climate [Publisher: Nature Publishing Group]. *Nature Reviews Earth & Environment 2*(9), 628–644. https://doi.org/10.1038/s43017-021-00199-z

Calkoen, F. R., Luijendijk, A. P., Vos, K., Kras, E., & Baart, F. (2025). Enabling coastal analytics at planetary scale. *Environmental Modelling & Software 183*, 106257. https://doi.org/10.1016/j.envsoft.2024.106257

Camus, P., Menéndez, M., Méndez, F. J., Izaguirre, C., Espejo, A., Cánovas, V., Pérez, J., Rueda, A., Losada, I. J., & Medina, R. (2014a). A weather-type statistical downscaling framework for ocean wave climate [_eprint: https://agupubs.onlinelibrary.wiley.com/doi/pdf/10.1002/2014JC010141]. *Journal of Geophysical Research: Oceans 119*(11), 7389–7405. https://doi.org/10.1002/2014JC010141

Camus, P., Méndez, F. J., Losada, I. J., Menéndez, M., Espejo, A., Pérez, J., Rueda, A., & Guanche, Y. (2014b). A method for finding the optimal predictor indices for local wave climate conditions. *Ocean Dynamics 64*(7), 1025–1038. https://doi.org/10.1007/s10236-014-0737-2

Cassou, C., Kushnir, Y., Hawkins, E., Pirani, A., Kucharski, F., Kang, I. S., & Caltabiano, N. (2018). Decadal Climate Variability and Predictability: Challenges and Opportunities [Publisher: American Meteorological Society Section: Bulletin of the American Meteorological Society]. *Bulletin of the American Meteorological Society 99*(3), 479–490. https://doi.org/10.1175/BAMS-D-16-0286.1

Castelle, B., Bujan, S., Marieu, V., & Ferreira, S. (2020). 16 years of topographic surveys of rip-channelled high-energy meso-macrotidal sandy beach [Number: 1 Publisher: Nature Publishing Group]. *Scientific Data 7*(1), 410. https://doi.org/10.1038/s41597-020-00750-5

Castelle, B., Kras, E., Masselink, G., Scott, T., Konstantinou, A., & Luijendijk, A. (2024). Satellite-derived sandy shoreline trends and interannual variability along the Atlantic coast of Europe [Publisher: Nature Publishing Group]. *Scientific Reports 14*(1), 13002. https://doi.org/10.1038/s41598-024-63849-4

Castelle, B., Marieu, V., Bujan, S., Ferreira, S., Parisot, J. P., Capo, S., Sénéchal, N., & Chouzenoux, T. (2014). Equilibrium shoreline modelling of a high-energy meso-macrotidal multiple-barred beach. *Marine Geology 347*, 85–94. https://doi.org/10.1016/j.margeo.2013.11.003

Castelle, B., & Masselink, G. (2023). Morphodynamics of wave-dominated beaches. *Cambridge Prisms: Coastal Futures 1*, e1. https://doi.org/10.1017/cft.2022.2

Castelle, B., Masselink, G., Scott, T., Stokes, C., Konstantinou, A., Marieu, V., & Bujan, S. (2021). Satellite-derived shoreline detection at a high-energy meso-macrotidal beach. *Geomorphology 383*, 107707. https://doi.org/10.1016/j.geomorph.2021.107707

Castelle, B., Ritz, A., Marieu, V., Nicolae Lerma, A., & Vandenhove, M. (2022). Primary drivers of multidecadal spatial and temporal patterns of shoreline change derived from optical satellite imagery. *Geomorphology 413*, 108360. https://doi.org/10.1016/j.geomorph.2022.108360

Cazenave, A., & Cozannet, G. L. (2014). Sea level rise and its coastal impacts [_eprint: https://agupubs.onlinelibrary.wiley.com/doi/pdf/10.1002/2013EF000188]. *Earth's Future 2*(2), 15–34. https://doi.org/10.1002/2013EF000188

Cazenave, A., Gouzenes, Y., Birol, F., Leger, F., Passaro, M., Calafat, F. M., Shaw, A., Nino, F., Legeais, J. F., Oelsmann, J., Restano, M., & Benveniste, J. (2022). Sea level along the world's coastlines can be measured by a network of virtual altimetry stations [Publisher: Nature Publishing Group]. *Communications Earth & Environment 3*(1), 117. https://doi.org/10.1038/s43247-022-00448-z

Chambers, D. P. (2006). Observing seasonal steric sea level variations with GRACE and satellite altimetry [_eprint: https://agupubs.onlinelibrary.wiley.com/doi/pdf/10.1029/2005JC002914]. *Journal of Geophysical Research: Oceans 111*(C3). https://doi.org/10.1029/2005JC002914

Chang, E. K. M., Lee, S., & Swanson, K. L. (2002). Storm Track Dynamics [Publisher: American Meteorological Society Section: Journal of Climate]. *Journal of Climate 15*(16), 2163–2183. https://doi.org/10.1175/1520-0442(2002)015<02163:STD>2.0.CO;2

Chen, Y. C., & Wang, S. F. (2025). LogiTide2DEM: A method for reconstructing intertidal topography in complex tidal flats using logistic regression with multi-temporal Sentinel-2 and Landsat imagery. *International Journal of Applied Earth Observation and Geoinformation 139*, 104561. https://doi.org/10.1016/j.jag.2025.104561

Church, J. A., & White, N. J. (2011). Sea-Level Rise from the Late 19th to the Early 21st Century. *Surveys in Geophysics 32*(4), 585–602. https://doi.org/10.1007/s10712-011-9119-1

Cipolletti, M. P., Delrieux, C. A., Perillo, G. M. E., & Cintia Piccolo, M. (2012). Superresolution border segmentation and measurement in remote sensing images. *Computers & Geosciences 40*, 87–96. https://doi.org/10.1016/j.cageo.2011.07.015

Cipollini, P., Calafat, F. M., Jevrejeva, S., Melet, A., & Prandi, P. (2017). Monitoring Sea Level in the Coastal Zone with Satellite Altimetry and Tide Gauges. *Surveys in Geophysics 38*(1), 33–57. https://doi.org/10.1007/s10712-016-9392-0

Clift, P. D., & Jonell, T. N. (2021). Monsoon controls on sediment generation and transport: Mass budget and provenance constraints from the Indus River catchment, delta and submarine fan over tectonic and multimillennial timescales. *Earth-Science Reviews 220*, 103682. https://doi.org/10.1016/j.earscirev.2021.103682

Cohn, N., & Anderson, D. (2025). Projecting the Longevity of Coastal Foredunes Under Stochastic Meteorological and Oceanographic Forcing [_eprint: https://agupubs.onlinelibrary.wiley.com/doi/pdf/10.1029/2024EF005335]. *Earth's Future 13*(6), e2024EF005335. https://doi.org/10.1029/2024EF005335

Dada, O. A., Almar, R., & Morand, P. (2024). Coastal vulnerability assessment of the West African coast to flooding and erosion [Publisher: Nature Publishing Group]. *Scientific Reports 14*(1), 890. https://doi.org/10.1038/s41598-023-48612-5

Dalinghaus, C., Coco, G., & Higuera, P. (2023). A predictive equation for wave setup using genetic programming [Publisher: Copernicus GmbH]. *Natural Hazards and Earth System Sciences 23*(6), 2157–2169. https://doi.org/10.5194/nhess-23-2157-2023

D'Anna, M., Idier, D., Castelle, B., Rohmer, J., Cagigal, L., & Mendez, F. J. (2022). Effects of stochastic wave forcing on probabilistic equilibrium shoreline response across the 21st century including sea-level rise. *Coastal Engineering 175*, 104149. https://doi.org/10.1016/j.coastaleng.2022.104149

Davidson, M. A., Splinter, K. D., & Turner, I. L. (2013). A simple equilibrium model for predicting shoreline change. *Coastal Engineering 73*, 191–202. https://doi.org/10.1016/j.coastaleng.2012.11.002

Davies, J. L. (1964). A morphogenic approach to world shorelines [Publisher: Schweizerbart'sche Verlagsbuchhandlung]. *Zeitschrift für Geomorphologie*, 127–142. https://doi.org/10.1127/zfg/mortensen/8/1964/127

Dibajnia, M., Nairn, R. B., & Ross, P. (2004). Analysis of long-term sand accumulation at a harbor using 2DH numerical simulation. *Coastal Engineering 51*(8), 863–882. https://doi.org/10.1016/j.coastaleng.2004.07.013

Dick, A., Raynaud, J. L., Rolland, A., Pelou, S., Coustance, S., Dedieu, G., Hagolle, O., Burochin, J. P., Binet, R., & Moreau, A. (2022). VENS: Mission Characteristics, Final Evaluation of the First Phase and Data Production [Publisher: Multidisciplinary Digital Publishing Institute]. *Remote Sensing 14*(14), 3281. https://doi.org/10.3390/rs14143281

Doherty, Y., Harley, M. D., Vos, K., & Splinter, K. D. (2022). A Python toolkit to monitor sandy shoreline change using high-resolution PlanetScope cubesats. *Environmental Modelling & Software 157*, 105512. https://doi.org/10.1016/j.envsoft.2022.105512

Doyle, T. B., Bradford, A., Garber, S., Ibaceta, R., Morris, B. D., Kinsela, M. A., Ingleton, T. C., Jizan, I., Taylor, D., Hanslow, D. J., & Bilham, K. (2025). The New South Wales nearshore wave tool – an interactive platform integrating high-resolution wave data for enhanced coastal science and management. *Environmental Modelling & Software 194*, 106686. https://doi.org/10.1016/j.envsoft.2025.106686

Dubarbier, B., Castelle, B., Ruessink, G., & Marieu, V. (2017). Mechanisms controlling the complete accretionary beach state sequence [_eprint: https://agupubs.onlinelibrary.wiley.com/doi/pdf/10.1002/2017GL073094]. *Geophysical Research Letters 44*(11), 5645–5654. https://doi.org/10.1002/2017GL073094

Durand, F., Piecuch, C. G., Becker, M., Papa, F., Raju, S. V., Khan, J. U., & Ponte, R. M. (2019). Impact of Continental Freshwater Runoff on Coastal Sea Level. *Surveys in Geophysics 40*(6), 1437–1466. https://doi.org/10.1007/s10712-019-09536-w

Elghannay, H., & Tafti, D. (2018). LES-DEM simulations of sediment transport. *International Journal of Sediment Research 33*(2), 137–148. https://doi.org/10.1016/j.ijsrc.2017.09.006

Emery, K. O. (1961). A Simple Method of Measuring Beach Profiles [_eprint: https://aslopubs.onlinelibrary.wiley.com/doi/pdf/10.4319/lo.1961.6.1.0090]. *Limnology and Oceanography 6*(1), 90–93. https://doi.org/10.4319/lo.1961.6.1.0090

Enache, S. (2022). Annual Performance Report.

Enfield, D. B., & Allen, J. S. (1980). On the Structure and Dynamics of Monthly Mean Sea Level Anomalies along the Pacific Coast of North and South America [Publisher: American Meteorological Society Section: Journal of Physical Oceanography]. *Journal of Physical Oceanography 10*(4), 557–578. https://doi.org/10.1175/1520-0485(1980)010<0557:OTSADO>2.0.CO;2

Feyisa, G. L., Meilby, H., Fensholt, R., & Proud, S. R. (2014). Automated Water Extraction Index: A new technique for surface water mapping using Landsat imagery. *Remote Sensing of Environment 140*, 23–35. https://doi.org/10.1016/j.rse.2013.08.029

Floc'h, F., Dantec, N. L., Lemos, C., Cancouët, R., Sous, D., Petitjean, L., Bouchette, F., Ardhuin, F., Suanez, S., & Delacourt, C. (2016). Morphological Response of a Macrotidal Embayed Beach, Porsmilin, France [Publisher: Coastal Education and Research Foundation]. *Journal of Coastal Research 75*(sp1), 373–377. https://doi.org/10.2112/SI75-075.1

Fortunato, A. B., Bertin, X., & Oliveira, A. (2009). Space and time variability of uncertainty in morphodynamic simulations. *Coastal Engineering 56*(8), 886–894. https://doi.org/10.1016/j.coastaleng.2009.04.006

Franco-Ochoa, C., Zambrano-Medina, Y., Plata-Rocha, W., Monjardín-Armenta, S., Rodríguez-Cueto, Y., Escudero, M., & Mendoza, E. (2020). Long-Term Analysis of Wave Climate and Shoreline Change along the Gulf of California [Number: 23 Publisher: Multidisciplinary Digital Publishing Institute]. *Applied Sciences 10*(23), 8719. https://doi.org/10.3390/app10238719

Friedlingstein, P. (2015). Carbon cycle feedbacks and future climate change [Publisher: Royal Society]. *Philosophical Transactions of the Royal Society A: Mathematical, Physical and Engineering Sciences 373*(2054), 20140421. https://doi.org/10.1098/rsta.2014.0421

Frugier, S., Almar, R., Bergsma, E., & Granjou, A. (2025). SBI: A sandbar extraction spectral index for multi-spectral satellite optical imagery. *Coastal Engineering 200*, 104752. https://doi.org/10.1016/j.coastaleng.2025.104752

Frugier, S., Almar, R., Bergsma, E. W. J., & Bak, S. A. (2026). Standalone color-based bathymetry over 10 years at Duck (NC, USA) from optical satellite imagery and wave breaking analysis. *Coastal Engineering 203*, 104855. https://doi.org/10.1016/j.coastaleng.2025.104855

Garzon, J. L., Plomaritis, T. A., & Ferreira, O. (2023). Uncertainty Analysis Related to Beach Morphology and Storm Duration for More Reliable Early Warning Systems for Coastal Hazards [_eprint: https://agupubs.onlinelibrary.wiley.com/doi/pdf/10.1029/2022JC019339]. *Journal of Geophysical Research: Oceans 128*(6), e2022JC019339. https://doi.org/10.1029/2022JC019339

Gettelman, A., Geer, A. J., Forbes, R. M., Carmichael, G. R., Feingold, G., Posselt, D. J., Stephens, G. L., van den Heever, S. C., Varble, A. C., & Zuidema, P. (2022). The future of Earth system prediction: Advances in model-data fusion [Publisher: American Association for the Advancement of Science]. *Science Advances 8*(14), eabn3488. https://doi.org/10.1126/sciadv.abn3488

Gill, A. E., & Niller, P. P. (1973). The theory of the seasonal variability in the ocean. *Deep Sea Research and Oceanographic Abstracts 20*(2), 141–177. https://doi.org/10.1016/0011-7471(73)90049-1

Gorelick, N., Hancher, M., Dixon, M., Ilyushchenko, S., Thau, D., & Moore, R. (2017). Google Earth Engine: Planetary-scale geospatial analysis for everyone. *Remote Sensing of Environment 202*, 18–27. https://doi.org/10.1016/j.rse.2017.06.031

Graffin, M., Almar, R., Bergsma, E. W. J., Boucharel, J., Vitousek, S., Taherkhani, M., & Ruggiero, P. (2025). Waterline responses to climate forcing along the North American West Coast [Publisher: Nature Publishing Group]. *Communications Earth & Environment 6*(1), 1–15. https://doi.org/10.1038/s43247-025-02414-x

Graffin, M., Taherkhani, M., Leung, M., Vitousek, S., Kaminsky, G., & Ruggiero, P. (2023). Monitoring interdecadal coastal change along dissipative beaches via satellite imagery at regional scale [Publisher: Cambridge University Press]. *Cambridge Prisms: Coastal Futures 1*, e42. https://doi.org/10.1017/cft.2023.30

Graham, N. E., & Diaz, H. F. (2001). Evidence for Intensification of North Pacific Winter Cyclones since 1948 [Publisher: American Meteorological Society Section: Bulletin of the American Meteorological Society]. *Bulletin of the American Meteorological Society 82*(9), 1869–1894. https://doi.org/10.1175/1520-0477(2001)082<1869:EFIONP>2.3.CO;2

Gunther, E. B., & Cross, R. L. (1984). Eastern North Pacific Tropical Cyclones of 1983 [Publisher: American Meteorological Society Section: Monthly Weather Review]. *Monthly Weather Review 112*(7), 1419–1440. https://doi.org/10.1175/1520-0493(1984)112<1419:ENPTCO>2.0.CO;2

Ha, K. J., Heo, K. Y., Lee, S. S., Yun, K. S., & Jhun, J. G. (2012). Variability in the East Asian Monsoon: a review [_eprint: https://rmets.onlinelibrary.wiley.com/doi/pdf/10.1002/met.1320]. *Meteorological Applications 19*(2), 200–215. https://doi.org/10.1002/met.1320

Hallermeier, R. J. (1980). A profile zonation for seasonal sand beaches from wave climate. *Coastal Engineering 4*, 253–277. https://doi.org/10.1016/0378-3839(80)90022-8

Hanslow, D. J., Morris, B. D., Foulsham, E., & Kinsela, M. A. (2018). A Regional Scale Approach to Assessing Current and Potential Future Exposure to Tidal Inundation in Different Types of Estuaries [Publisher: Nature Publishing Group]. *Scientific Reports 8*(1), 7065. https://doi.org/10.1038/s41598-018-25410-y

Harley, M. D., Kinsela, M. A., Sánchez-García, E., & Vos, K. (2019). Shoreline change mapping using crowd-sourced smartphone images. *Coastal Engineering 150*, 175–189. https://doi.org/10.1016/j.coastaleng.2019.04.003

Harley, M. D., Masselink, G., Ruiz de Alegría-Arzaburu, A., Valiente, N. G., & Scott, T. (2022). Single extreme storm sequence can offset decades of shoreline retreat projected to result from sea-level rise [Publisher: Nature Publishing Group]. *Communications Earth & Environment 3*(1), 1–11. https://doi.org/10.1038/s43247-022-00437-2

Hegermiller, C. A., Rueda, A., Erikson, L. H., Barnard, P. L., Antolinez, J. a. A., & Mendez, F. J. (2017). Controls of Multimodal Wave Conditions in a Complex Coastal Setting [_eprint: https://onlinelibrary.wiley.com/doi/pdf/10.1002/2017GL075272]. *Geophysical Research Letters 44*(24), 12,315–12,323. https://doi.org/10.1002/2017GL075272

Holgate, S. J., Matthews, A., Woodworth, P. L., Rickards, L. J., Tamisiea, M. E., Bradshaw, E., Foden, P. R., Gordon, K. M., Jevrejeva, S., & Pugh, J. (2013). New Data Systems and Products at the Permanent Service for Mean Sea Level [Publisher: Coastal Education and Research Foundation]. *Journal of Coastal Research 29*(3), 493–504. https://doi.org/10.2112/JCOASTRES-D-12-00175.1

Holman, R. (2007). The history and technical capabilities of Argus. *Coastal Engineering*. https://www.academia.edu/24476512/The_history_and_technical_capabilities_of_Argus

Hoskins, B. J., & Valdes, P. J. (1990). On the Existence of Storm-Tracks [Publisher: American Meteorological Society Section: Journal of the Atmospheric Sciences]. *Journal of the Atmospheric Sciences 47*(15), 1854–1864. https://doi.org/10.1175/1520-0469(1990)047<1854:OTEOST>2.0.CO;2

Hulskamp, R., Luijendijk, A., van Maren, B., Moreno-Rodenas, A., Calkoen, F., Kras, E., Lhermitte, S., & Aarninkhof, S. (2023). Global distribution and dynamics of muddy coasts [Number: 1 Publisher: Nature Publishing Group]. *Nature Communications 14*(1), 8259. https://doi.org/10.1038/s41467-023-43819-6

Hurrell, J. W. (1995). Decadal Trends in the North Atlantic Oscillation: Regional Temperatures and Precipitation [Publisher: American Association for the Advancement of Science]. *Science 269*(5224), 676–679. https://doi.org/10.1126/science.269.5224.676

Huyer, A. (1983). Coastal upwelling in the California current system. *Progress in Oceanography 12*(3), 259–284. https://doi.org/10.1016/0079-6611(83)90010-1

Ibaceta, R., & Harley, M. D. (2024). Data-driven modelling of coastal storm erosion for real-time forecasting at a wave-dominated embayed beach. *Coastal Engineering 193*, 104596. https://doi.org/10.1016/j.coastaleng.2024.104596

IPCC. (2022). Sea Level Rise and Implications for Low-Lying Islands, Coasts and Communities. In *The Ocean and Cryosphere in a Changing Climate: Special Report of the Intergovernmental Panel on Climate Change* (pp. 321–446). Cambridge University Press. https://doi.org/10.1017/9781009157964.006

Janušaitė, R., Jarmalavičius, D., Pupienis, D., Žilinskas, G., & Jukna, L. (2023). Nearshore sandbar switching episodes and their relationship with coastal erosion at the Curonian Spit, Baltic Sea. *Oceanologia 65*(1), 71–85. https://doi.org/10.1016/j.oceano.2021.11.004

Jaramillo, C., González, M., Medina, R., & Turki, I. (2021). An equilibrium-based shoreline rotation model. *Coastal Engineering 163*, 103789. https://doi.org/10.1016/j.coastaleng.2020.103789

Jessin, J., Heinzlef, C., Long, N., & Serre, D. (2023). A Systematic Review of UAVs for Island Coastal Environment and Risk Monitoring: Towards a Resilience Assessment [Number: 3

Publisher: Multidisciplinary Digital Publishing Institute]. *Drones 7*(3), 206. https://doi.org/10.3390/drones7030206

Ji, L., Zhang, L., & Wylie, B. (2009). Analysis of Dynamic Thresholds for the Normalized Difference Water Index. *Photogrammetric Engineering & Remote Sensing 75*(11), 1307–1317. https://doi.org/10.14358/PERS.75.11.1307

Jung, J., & Cho, Y. K. (2020). Persistence of coastal upwelling after a plunge in upwelling-favourable wind. *Scientific Reports 10*, 11938. https://doi.org/10.1038/s41598-020-67785-x

Kamphuis, J. W. (1991). Alongshore Sediment Transport Rate [Publisher: American Society of Civil Engineers]. *Journal of Waterway, Port, Coastal, and Ocean Engineering 117*(6), 624–640. https://doi.org/10.1061/(ASCE)0733-950X(1991)117:6(624)

Klotz, A. N., Gurruchaga, P., Almar, R., Lange, A. M. Z., & Bergsma, E. W. J. (2025). Deriving nearshore bathymetry and waves characteristics from a single UAV video. *Coastal Engineering 202*, 104820. https://doi.org/10.1016/j.coastaleng.2025.104820

Konstantinou, A., Scott, T., Masselink, G., Stokes, K., Conley, D., & Castelle, B. (2023). Satellite-based shoreline detection along high-energy macrotidal coasts and influence of beach state. *Marine Geology 462*, 107082. https://doi.org/10.1016/j.margeo.2023.107082

Kuriyama, Y., Banno, M., & Suzuki, T. (2012). Linkages among interannual variations of shoreline, wave and climate at Hasaki, Japan [_eprint: https://agupubs.onlinelibrary.wiley.com/doi/pdf/10.1029/2011GL050704]. *Geophysical Research Letters 39*(6). https://doi.org/10.1029/2011GL050704

Kümmerer, V., Ferreira, O., & Loureiro, C. (2025). Distinct shoreline behaviour along storm-dominated and geologically controlled coastal barriers [_eprint: https://onlinelibrary.wiley.com/doi/pdf/10.1002/esp.70042]. *Earth Surface Processes and Landforms 50*(4), e70042. https://doi.org/10.1002/esp.70042

Labarthe, C., Castelle, B., Marieu, V., Garlan, T., & Bujan, S. (2023). Observation and Modeling of the Equilibrium Slope Response of a High-Energy Meso-Macrotidal Sandy Beach [Number: 3 Publisher: Multidisciplinary Digital Publishing Institute]. *Journal of Marine Science and Engineering 11*(3), 584. https://doi.org/10.3390/jmse11030584

van de Lageweg, W. I., Bryan, K. R., Coco, G., & Ruessink, B. G. (2013). Observations of shoreline–sandbar coupling on an embayed beach. *Marine Geology 344*, 101–114. https://doi.org/10.1016/j.margeo.2013.07.018

Larson, M., Larson, M., Byrnes, M. R., Kraus, N. C., Center (U.S.), C. E. R., Station (U.S.), W. E., & States, U. (1989). *SBEACH : numerical model for simulating storm-induced beach change*. U.S. Army Engineer Waterways Experiment Station. https://doi.org/10.5962/bhl.title.47893

Le Xuan, T., Ba, H. T., Thanh, V. Q., Wright, D. P., Hasan Tanim, A., & Tran Anh, D. (2022). Evaluation of coastal protection strategies and proposing multiple lines of defense under climate change in the Mekong Delta for sustainable shoreline protection. *Ocean & Coastal Management 228*, 106301. https://doi.org/10.1016/j.ocecoaman.2022.106301

Lebègue, L., Cazala-Hourcade, E., Languille, F., Artigues, S., & Melet, O. (2020). CO3D, A WORLDWIDE ONE ONE-METER ACCURACY DEM FOR 2025 [Conference Name: XXIV ISPRS Congress, Commission I (Volume XLIII-B1-2020) - 2020 edition Publisher: Copernicus GmbH]. *The International Archives of the Photogrammetry, Remote Sensing and Spatial Information Sciences XLIII-B1-2020*, 299–304. https://doi.org/10.5194/isprs-archives-XLIII-B1-2020-299-2020

Lemos, C., Floc'h, F., Yates, M., Le Dantec, N., Marieu, V., Hamon, K., Cuq, V., Suanez, S., & Delacourt, C. (2018). Equilibrium modeling of the beach profile on a macrotidal embayed low tide terrace beach. *Ocean Dynamics 68*(9), 1207–1220. https://doi.org/10.1007/s10236-018-1185-1

Leung, M., Cagigal, L., Mendez, F., & Ruggiero, P. (2024). Projecting Future Chronic Coastal Hazard Impacts, Hotspots, and Uncertainty at Regional Scale [_eprint: https://onlinelibrary.wiley.com/doi/pdf/10.1029/2024EF005523]. *Earth's Future 12*(12), e2024EF005523. https://doi.org/10.1029/2024EF005523

Li, N., Yamazaki, Y., Roeber, V., Cheung, K. F., & Chock, G. (2018). Probabilistic mapping of storm-induced coastal inundation for climate change adaptation. *Coastal Engineering 133*, 126–141. https://doi.org/10.1016/j.coastaleng.2017.12.013

Lionel, T. M., Florent, L., Loren, C., Mathilde, C., Damien, A., Ergane, F., Mei-ling, D., Ramiro, F., Yannice, F., Gerald, D., & Nicolas, P. (2023). *The new FES2022 tidal atlas. EGU23-9008* [Conference Name: EGU23]. Copernicus Meetings. https://doi.org/10.5194/egusphere-egu23-9008

Lippmann, T. C., & Holman, R. A. (1990). The spatial and temporal variability of sand bar morphology [_eprint: https://agupubs.onlinelibrary.wiley.com/doi/pdf/10.1029/JC095iC07p11575]. *Journal of Geophysical Research: Oceans 95*(C7), 11575–11590. https://doi.org/10.1029/JC095iC07p11575

Long, C. E., & Oltman-Shay, J. M. (1991). Directional Characteristics of Waves in Shallow Water.

Lorensen, W. E., & Cline, H. E. (1987). Marching cubes: A high resolution 3D surface construction algorithm. *SIGGRAPH Comput. Graph. 21*(4), 163–169. https://doi.org/10.1145/37402.37422

Ludka, B. C., Guza, R. T., O'Reilly, W. C., & Yates, M. L. (2015). Field evidence of beach profile evolution toward equilibrium [_eprint: https://agupubs.onlinelibrary.wiley.com/doi/pdf/10.1002/2015JC010893]. *Journal of Geophysical Research: Oceans 120*(11), 7574–7597. https://doi.org/10.1002/2015JC010893

Ludka, B. C., Guza, R. T., O'Reilly, W. C., Merrifield, M. A., Flick, R. E., Bak, A. S., Hesser, T., Bucciarelli, R., Olfe, C., Woodward, B., Boyd, W., Smith, K., Okihiro, M., Grenzeback, R., Parry, L., & Boyd, G. (2019). Sixteen years of bathymetry and waves at San Diego beaches [Number: 1 Publisher: Nature Publishing Group]. *Scientific Data 6*(1), 161. https://doi.org/10.1038/s41597-019-0167-6

Luijendijk, A., Hagenaars, G., Ranasinghe, R., Baart, F., Donchyts, G., & Aarninkhof, S. (2018). The State of the World's Beaches [Number: 1 Publisher: Nature Publishing Group]. *Scientific Reports 8*(1), 6641. https://doi.org/10.1038/s41598-018-24630-6

Mann, H. B. (1945). Nonparametric Tests Against Trend [Publisher: [Wiley, Econometric Society]]. *Econometrica 13*(3), 245–259. https://doi.org/10.2307/1907187

Mann, M. E., Steinman, B. A., & Miller, S. K. (2020). Absence of internal multidecadal and interdecadal oscillations in climate model simulations [Publisher: Nature Publishing Group]. *Nature Communications 11*(1), 49. https://doi.org/10.1038/s41467-019-13823-w

Mantua, N. J., & Hare, S. R. (2002). The Pacific Decadal Oscillation. *Journal of Oceanography 58*(1), 35–44. https://doi.org/10.1023/A:1015820616384

Mao, Y., Coco, G., Vitousek, S., Antolinez, J. A. A., Azorakos, G., Banno, M., Bouvier, C., Bryan, K. R., Cagigal, L., Calcraft, K., Castelle, B., Chen, X., D'Anna, M., de Freitas Pereira, L., de Santiago, I., Deshmukh, A. N., Dong, B., Elghandour, A., Gohari, A., Gomez-de la Peña, E., Harley, M. D., Ibrahim, M., Idier, D., Cardona, C. J., Lim, C., Mingo, I., O'Grady, J., Pais, D., Repina, O., Robinet, A., Roelvink, D., Simmons, J., Sogut, E., Wilson, K., & Splinter, K. D. (2025). Benchmarking shoreline prediction models over multi-decadal timescales [Publisher: Nature Publishing Group]. *Communications Earth & Environment 6*(1), 581. https://doi.org/10.1038/s43247-025-02550-4

Mao, Y., & Splinter, K. D. (2025). Application of SAR-Optical fusion to extract shoreline position from Cloud-Contaminated satellite images. *ISPRS Journal of Photogrammetry and Remote Sensing 220*, 563–579. https://doi.org/10.1016/j.isprsjprs.2025.01.013

Marchesiello, P., Thoumyre, G., Dieye, A., Almar, R., Bergsma, E., Sow, B. A., & Duong, H. T. (2024). Exploring Fine-Scale Satellite-Derived Coastal Bathymetry for Ocean Modeling: A Case Study from West Africa. *Estuaries and Coasts 47*(8), 2696–2712. https://doi.org/10.1007/s12237-024-01398-9

Martins, K., Bertin, X., Mengual, B., Pezerat, M., Lavaud, L., Guérin, T., & Zhang, Y. J. (2022). Wave-induced mean currents and setup over barred and steep sandy beaches. *Ocean Modelling 179*, 102110. https://doi.org/10.1016/j.ocemod.2022.102110

Masselink, G., Castelle, B., Scott, T., Dodet, G., Suanez, S., Jackson, D., & Floc'h, F. (2016). Extreme wave activity during 2013/2014 winter and morphological impacts along the Atlantic coast of Europe [_eprint: https://onlinelibrary.wiley.com/doi/pdf/10.1002/2015GL067492]. *Geophysical Research Letters 43*(5), 2135–2143. https://doi.org/10.1002/2015GL067492

Masselink, G., & Short, A. (1993). The effect of tide range on beach morphodynamics and morphology: a conceptual beach model. *Journal of Coastal Research 9*, 785–800.

Maurin, R., Chauchat, J., & Frey, P. (2018). Revisiting slope influence in turbulent bedload transport: consequences for vertical flow structure and transport rate scaling. *Journal of Fluid Mechanics 839*, 135–156. https://doi.org/10.1017/jfm.2017.903

McAllister, E., Payo, A., Novellino, A., Dolphin, T., & Medina-Lopez, E. (2022). Multispectral satellite imagery and machine learning for the extraction of shoreline indicators. *Coastal Engineering 174*, 104102. https://doi.org/10.1016/j.coastaleng.2022.104102

McCarroll, R. J., Valiente, N. G., Wiggins, M., Scott, T., & Masselink, G. (2023). Coastal survey data for Perranporth Beach and Start Bay in southwest England (2006–2021) [Publisher: Nature Publishing Group]. *Scientific Data 10*(1), 258. https://doi.org/10.1038/s41597-023-02131-0

McFEETERS, S. K. (1996). The use of the Normalized Difference Water Index (NDWI) in the delineation of open water features [Publisher: Taylor & Francis _eprint: https://doi.org/10.1080/01431169608948714]. *International Journal of Remote Sensing 17*(7), 1425–1432. https://doi.org/10.1080/01431169608948714

McPhaden, M. J., Zebiak, S. E., & Glantz, M. H. (2006). ENSO as an Integrating Concept in Earth Science [Publisher: American Association for the Advancement of Science]. *Science 314*(5806), 1740–1745. https://doi.org/10.1126/science.1132588

Meade, R. H., & Emery, K. O. (1971). Sea Level as Affected by River Runoff, Eastern United States [Publisher: American Association for the Advancement of Science]. *Science 173*(3995), 425–428. https://doi.org/10.1126/science.173.3995.425

Medellín, G., Torres-Freyermuth, A., & Cohn, N. (2025). Distinct sandbar behavior on a gently sloping shoreface sea-breeze dominated beach. *Marine Geology 484*, 107543. https://doi.org/10.1016/j.margeo.2025.107543

Melet, A., Teatini, P., Le Cozannet, G., Jamet, C., Conversi, A., Benveniste, J., & Almar, R. (2020). Earth Observations for Monitoring Marine Coastal Hazards and Their Drivers. *Surveys in Geophysics 41*(6), 1489–1534. https://doi.org/10.1007/s10712-020-09594-5

Mentaschi, L., Vousdoukas, M. I., Pekel, J. F., Voukouvalas, E., & Feyen, L. (2018). Global long-term observations of coastal erosion and accretion [Number: 1 Publisher: Nature Publishing Group]. *Scientific Reports 8*(1), 12876. https://doi.org/10.1038/s41598-018-30904-w

Michel, J., Sarrazin, E., Youssefi, D., Cournet, M., Buffe, F., Delvit, J. M., Emilien, A., Bosman, J., Melet, O., & L'Helguen, C. (2020). A NEW SATELLITE IMAGERY STEREO PIPELINE DESIGNED FOR SCALABILITY, ROBUSTNESS AND PERFORMANCE [Conference Name: XXIV ISPRS Congress, Commission II (Volume V-2-2020) - 2020 edition Publisher: Copernicus GmbH]. *ISPRS Annals of the Photogrammetry, Remote Sensing and Spatial Information Sciences V-2-2020*, 171–178. https://doi.org/10.5194/isprs-annals-V-2-2020-171-2020

Middleton, J. F., & Cirano, M. (1999). Wind-Forced Downwelling Slope Currents: A Numerical Study [Publisher: American Meteorological Society Section: Journal of Physical Oceanography]. *Journal of Physical Oceanography 29*(8), 1723–1743. https://doi.org/10.1175/1520-0485(1999)029<1723:WFDSCA>2.0.CO;2

Miller, J. K., & Dean, R. G. (2004). A simple new shoreline change model. *Coastal Engineering 51*(7), 531–556. https://doi.org/10.1016/j.coastaleng.2004.05.006

Montaño, J., Coco, G., Antolínez, J. A. A., Beuzen, T., Bryan, K. R., Cagigal, L., Castelle, B., Davidson, M. A., Goldstein, E. B., Ibaceta, R., Idier, D., Ludka, B. C., Masoud-Ansari, S., Méndez, F. J., Murray, A. B., Plant, N. G., Ratliff, K. M., Robinet, A., Rueda, A., Sénéchal, N., Simmons, J. A., Splinter, K. D., Stephens, S., Townend, I., Vitousek, S., & Vos, K. (2020). Blind

testing of shoreline evolution models [Publisher: Nature Publishing Group]. *Scientific Reports 10*(1), 2137. https://doi.org/10.1038/s41598-020-59018-y

Moore, L. J., Hacker, S. D., Breithaupt, J., de Vries, S., Miller, T., Ruggiero, P., & Zinnert, J. C. (2025). Ecomorphodynamics of coastal foredune evolution [Number: 6 Publisher: Nature Publishing Group]. *Nature Reviews Earth & Environment 6*(6), 417–432. https://doi.org/10.1038/s43017-025-00672-z

Moore, L. J., Ruggiero, P., & List, J. H. (2006). Comparing Mean High Water and High Water Line Shorelines: Should Proxy-Datum Offsets be Incorporated into Shoreline Change Analysis? *Journal of Coastal Research 224*, 894–905. https://doi.org/10.2112/04-0401.1

Moré, J. J. (1978). The Levenberg-Marquardt algorithm: Implementation and theory. In G. A. Watson (Ed.), *Numerical Analysis* (pp. 105–116). Springer, Berlin, Heidelberg. https://doi.org/10.1007/BFb0067700

Muir, F. M. E., Hurst, M. D., Richardson-Foulger, L., Rennie, A. F., & Naylor, L. A. (2024). VedgeSat: An automated, open-source toolkit for coastal change monitoring using satellite-derived vegetation edges [_eprint: https://onlinelibrary.wiley.com/doi/pdf/10.1002/esp.5835]. *Earth Surface Processes and Landforms 49*(8), 2405–2423. https://doi.org/10.1002/esp.5835

Najar, M. A., Benshila, R., Bennioui, Y. E., Thoumyre, G., Almar, R., Bergsma, E. W. J., Delvit, J. M., & Wilson, D. G. (2022). Coastal Bathymetry Estimation from Sentinel-2 Satellite Imagery: Comparing Deep Learning and Physics-Based Approaches [Publisher: Multidisciplinary Digital Publishing Institute]. *Remote Sensing 14*(5), 1196. https://doi.org/10.3390/rs14051196

Nienhuis, J. H., Ashton, A. D., Edmonds, D. A., Hoitink, A. J. F., Kettner, A. J., Rowland, J. C., & Törnqvist, T. E. (2020). Global-scale human impact on delta morphology has led to net land area gain [Publisher: Nature Publishing Group]. *Nature 577*(7791), 514–518. https://doi.org/10.1038/s41586-019-1905-9

Nienhuis, J. H., Ashton, A. D., Edmonds, D. A., Hoitink, A. J. F., Kettner, A. J., Rowland, J. C., & Törnqvist, T. E. (2023). Reply to: Concerns about data linking delta land gain to human action [Publisher: Nature Publishing Group]. *Nature 614*(7947), E26–E28. https://doi.org/10.1038/s41586-022-05625-w

Odériz, I., Losada, I. J., Silva, R., & Mori, N. (2024). On the need to integrate interannual natural variability into coastal multihazard assessments [Publisher: Nature Publishing Group]. *Scientific Reports 14*(1), 16998. https://doi.org/10.1038/s41598-024-67679-2

Otsu, N. (1979). A Threshold Selection Method from Gray-Level Histograms [Conference Name: IEEE Transactions on Systems, Man, and Cybernetics]. *IEEE Transactions on Systems, Man, and Cybernetics 9*(1), 62–66. https://doi.org/10.1109/TSMC.1979.4310076

Palaseanu-Lovejoy, M., Alexandrov, O., Danielson, J., & Storlazzi, C. (2023). SaTSeaD: Satellite Triangulated Sea Depth Open-Source Bathymetry Module for NASA Ames Stereo Pipeline [Number: 16 Publisher: Multidisciplinary Digital Publishing Institute]. *Remote Sensing 15*(16), 3950. https://doi.org/10.3390/rs15163950

Paz-Delgado, M. V., Payo, A., GOmez-Pazo, A., Beck, A. L., & Savastano, S. (2022). Shoreline Change from Optical and Sar Satellite Imagery at Macro-Tidal Estuarine, Cliffed Open-Coast and Gravel Pocket-Beach Environments [Publisher: Multidisciplinary Digital Publishing Institute]. *Journal of Marine Science and Engineering 10*(5), 561. https://doi.org/10.3390/jmse10050561

Pekel, J. F., Cottam, A., Gorelick, N., & Belward, A. S. (2016). High-resolution mapping of global surface water and its long-term changes [Number: 7633 Publisher: Nature Publishing Group]. *Nature 540*(7633), 418–422. https://doi.org/10.1038/nature20584

Pianca, C., Holman, R., & Siegle, E. (2015). Shoreline variability from days to decades: Results of long-term video imaging [_eprint: https://onlinelibrary.wiley.com/doi/pdf/10.1002/2014JC010329]. *Journal of Geophysical Research: Oceans 120*(3), 2159–2178. https://doi.org/10.1002/2014JC010329

Piecuch, C. G., Huybers, P., Hay, C. C., Kemp, A. C., Little, C. M., Mitrovica, J. X., Ponte, R. M., & Tingley, M. P. (2018). Origin of spatial variation in US East Coast sea-level trends during 1900–2017 [Publisher: Nature Publishing Group]. *Nature 564*(7736), 400–404. https://doi.org/10.1038/s41586-018-0787-6

Pilkey, O. H., & Cooper, J. A. G. (2002). Longshore Transport Volumes: A Critical View [Publisher: Coastal Education & Research Foundation, Inc.]. *Journal of Coastal Research*, 572–580. https://www.jstor.org/stable/26477845

Plant, N. G., Holman, R. A., Freilich, M. H., & Birkemeier, W. A. (1999). A simple model for interannual sandbar behavior [_eprint: https://agupubs.onlinelibrary.wiley.com/doi/pdf/10.1029/1999JC900112]. *Journal of Geophysical Research: Oceans 104*(C7), 15755–15776. https://doi.org/10.1029/1999JC900112

Pranzini, E., & Williams, A. T. (2021). The Equilibrium Concept, or... (Mis)concept in Beaches [Publisher: Multidisciplinary Digital Publishing Institute]. *Geosciences 11*(2), 59. https://doi.org/10.3390/geosciences11020059

Prodger, S., Russell, P., Davidson, M., & Miles, J. (2016). Beach Morphological Predictions: The Impact of a Temporally Varying Sediment Fall Velocity [Publisher: Coastal Education and Research Foundation]. *Journal of Coastal Research 75*(sp1), 447–451. https://doi.org/10.2112/SI75-090.1

Pugh, D., & Woodworth, P. (2014). Tidal analysis and prediction. *Sea-Level Science: Understanding Tides, Surges, Tsunamis and Mean Sea-Level Changes*, 60–96. https://doi.org/10.1017/CBO9781139235778.007

Pähtz, T., Omeradžić, A., Carneiro, M. V., Araújo, N. A. M., & Herrmann, H. J. (2015). Discrete Element Method simulations of the saturation of aeolian sand transport [_eprint: https://agupubs.onlinelibrary.wiley.com/doi/pdf/10.1002/2014GL062945]. *Geophysical Research Letters 42*(6), 2063–2070. https://doi.org/10.1002/2014GL062945

Ranasinghe, R. (2016). Assessing climate change impacts on open sandy coasts: A review. *Earth-Science Reviews 160*, 320–332. https://doi.org/10.1016/j.earscirev.2016.07.011

Ranasinghe, R., Callaghan, D. P., Li, F., Wainwright, D. J., & Duong, T. M. (2023). Assessing coastline recession for adaptation planning: sea level rise versus storm erosion [Number: 1 Publisher: Nature Publishing Group]. *Scientific Reports 13*(1), 8286. https://doi.org/10.1038/s41598-023-35523-8

Ranasinghe, R., McLoughlin, R., Short, A., & Symonds, G. (2004). The Southern Oscillation Index, wave climate, and beach rotation. *Marine Geology 204*(3), 273–287. https://doi.org/10.1016/S0025-3227(04)00002-7

Ranasinghe, R., & Stive, M. J. F. (2009). Rising seas and retreating coastlines. *Climatic Change 97*(3), 465–468. https://doi.org/10.1007/s10584-009-9593-3

Rasmusson, E. M., & Carpenter, T. H. (1982). Variations in Tropical Sea Surface Temperature and Surface Wind Fields Associated with the Southern Oscillation/El Niño [Publisher: American Meteorological Society Section: Monthly Weather Review]. *Monthly Weather Review 110*(5), 354–384. https://doi.org/10.1175/1520-0493(1982)110<0354:VITSST>2.0.CO;2

Robinet, A., Idier, D., Castelle, B., & Marieu, V. (2018). A reduced-complexity shoreline change model combining longshore and cross-shore processes: The LX-Shore model. *Environmental Modelling & Software 109*, 1–16. https://doi.org/10.1016/j.envsoft.2018.08.010

Rocha, C., Antunes, C., & Catita, C. (2023). Coastal indices to assess sea-level rise impacts - A brief review of the last decade. *Ocean & Coastal Management 237*, 106536. https://doi.org/10.1016/j.ocecoaman.2023.106536

Roelvink, J. A., & Brøker, I. (1993). Cross-shore profile models. *Coastal Engineering 21*(1), 163–191. https://doi.org/10.1016/0378-3839(93)90049-E

Ropelewski, C. F., & Jones, P. D. (1987). An Extension of the Tahiti–Darwin Southern Oscillation Index [Publisher: American Meteorological Society Section: Monthly Weather Review]. *Monthly Weather Review 115*(9), 2161–2165. https://doi.org/10.1175/1520-0493(1987)115<2161:AEOTTS>2.0.CO;2

Ruessink, B. G., Wijnberg, K. M., Holman, R. A., Kuriyama, Y., & van Enckevort, I. M. J. (2003). Intersite comparison of interannual nearshore bar behavior [_eprint: https://agupubs.onlinelibrary.wiley.com/doi/pdf/10.1029/2002JC001505]. *Journal of Geophysical Research: Oceans 108*(C8). https://doi.org/10.1029/2002JC001505

Ruggiero, P., Kaminsky, G. M., & Gelfenbaum, G. (2003). Linking Proxy-Based and Datum-Based Shorelines on a High-Energy Coastline: Implications for Shoreline Change Analyses [Publisher: Coastal Education & Research Foundation, Inc.]. *Journal of Coastal Research*, 57–82. https://www.jstor.org/stable/25736600

Ruggiero, P., Kaminsky, G. M., Gelfenbaum, G., & Cohn, N. (2016). Morphodynamics of prograding beaches: A synthesis of seasonal- to century-scale observations of the Columbia River littoral cell. *Marine Geology 376*, 51–68. https://doi.org/10.1016/j.margeo.2016.03.012

Ruggiero, P., Kaminsky, G. M., Gelfenbaum, G., & Voigt, B. (2005). Seasonal to Interannual Morphodynamics along a High-Energy Dissipative Littoral Cell. *Journal of Coastal Research 213*, 553–578. https://doi.org/10.2112/03-0029.1

Ruggiero, P., Komar, P. D., & Allan, J. C. (2010). Increasing wave heights and extreme value projections: The wave climate of the U.S. Pacific Northwest. *Coastal Engineering 57*(5), 539–552. https://doi.org/10.1016/j.coastaleng.2009.12.005

Rykaczewski, R. R., & Checkley, D. M. (2008). Influence of ocean winds on the pelagic ecosystem in upwelling regions [Publisher: Proceedings of the National Academy of Sciences]. *Proceedings of the National Academy of Sciences 105*(6), 1965–1970. https://doi.org/10.1073/pnas.0711777105

Saji, N. H., & Yamagata, T. (2003a). Possible impacts of Indian Ocean Dipole mode events on global climate [Publisher: Inter-Research Science Center]. *Climate Research 25*(2), 151–169. https://www.jstor.org/stable/24868393

Saji, N. H., & Yamagata, T. (2003b). Structure of SST and Surface Wind Variability during Indian Ocean Dipole Mode Events: COADS Observations [Publisher: American Meteorological Society Section: Journal of Climate]. *Journal of Climate 16*(16), 2735–2751. https://doi.org/10.1175/1520-0442(2003)016<2735:SOSASW>2.0.CO;2

Salameh, E., Frappart, F., Turki, I., & Laignel, B. (2020). Intertidal topography mapping using the waterline method from Sentinel-1 & -2 images: The examples of Arcachon and Veys Bays in France. *ISPRS Journal of Photogrammetry and Remote Sensing 163*, 98–120. https://doi.org/10.1016/j.isprsjprs.2020.03.003

Savastano, S., Gomes da Silva, P., Sánchez, J. M., Tort, A. G., Payo, A., Pattle, M. E., Garcia-Mondéjar, A., Castillo, Y., & Monteys, X. (2024). Assessment of Shoreline Change from SAR Satellite Imagery in Three Tidally Controlled Coastal Environments [Number: 1 Publisher: Multidisciplinary Digital Publishing Institute]. *Journal of Marine Science and Engineering 12*(1), 163. https://doi.org/10.3390/jmse12010163

Seenath, A. (2025). Fundamental limitations of shoreline models [Publisher: Nature Publishing Group]. *Nature Water 3*(5), 510–511. https://doi.org/10.1038/s44221-025-00443-6

Sen, P. K. (1968). Estimates of the Regression Coefficient Based on Kendall's Tau [Publisher: ASA Website _eprint: https://www.tandfonline.com/doi/pdf/10.1080/01621459.1968.10480934]. *Journal of the American Statistical Association 63*(324), 1379–1389. https://doi.org/10.1080/01621459.1968.10480934

Senechal, N., Coco, G., Bryan, K. R., & Holman, R. A. (2011). Wave runup during extreme storm conditions [_eprint: https://agupubs.onlinelibrary.wiley.com/doi/pdf/10.1029/2010JC006819]. *Journal of Geophysical Research: Oceans 116*(C7). https://doi.org/10.1029/2010JC006819

Serafin, K. A., Ruggiero, P., & Stockdon, H. F. (2017). The relative contribution of waves, tides, and nontidal residuals to extreme total water levels on U.S. West Coast sandy beaches [_eprint: https://agupubs.onlinelibrary.wiley.com/doi/pdf/10.1002/2016GL071020]. *Geophysical Research Letters 44*(4), 1839–1847. https://doi.org/10.1002/2016GL071020

Shalowitz, A. (1962). Shore and Sea Boundaries - Volume One. In US. Department of Commerce.

Shalowitz, A. (1964). Shore and Sea Boundaries - Volume Two. In US. Department of Commerce.

Simarro, G., Calvete, D., Ribas, F., Castillo, Y., & Puig-Polo, C. (2025). UOrtos: Methodology for Co-Registration and Subpixel Georeferencing of Satellite Imagery for Coastal Monitoring [Publisher: Multidisciplinary Digital Publishing Institute]. *Remote Sensing 17*(7), 1160. https://doi.org/10.3390/rs17071160

Splinter, K. D., Turner, I. L., Davidson, M. A., Barnard, P., Castelle, B., & Oltman-Shay, J. (2014). A generalized equilibrium model for predicting daily to interannual shoreline response [_eprint: https://onlinelibrary.wiley.com/doi/pdf/10.1002/2014JF003106]. *Journal of Geophysical Research: Earth Surface 119*(9), 1936–1958. https://doi.org/10.1002/2014JF003106

Stauble, D. K., & Cialone, M. A. (1996). Sediment Dynamics and Profile Interactions: DUCK94 [Publisher: American Society of Civil Engineers], 3921–3934. https://doi.org/10.1061/9780784402429.303

Stevens, A. W., Ruggiero, P., Parker, K. A., Vitousek, S., Gelfenbaum, G., & Kaminsky, G. M. (2024). Climate controls on longshore sediment transport and coastal morphology adjacent to engineered inlets. *Coastal Engineering 194*, 104617. https://doi.org/10.1016/j.coastaleng.2024.104617

Stive, M. J. F., Aarninkhof, S. G. J., Hamm, L., Hanson, H., Larson, M., Wijnberg, K. M., Nicholls, R. J., & Capobianco, M. (2002). Variability of shore and shoreline evolution. *Coastal Engineering 47*(2), 211–235. https://doi.org/10.1016/S0378-3839(02)00126-6

Stockdon, H. F., Holman, R. A., Howd, P. A., & Sallenger, A. H. (2006). Empirical parameterization of setup, swash, and runup. *Coastal Engineering 53*(7), 573–588. https://doi.org/10.1016/j.coastaleng.2005.12.005

Storn, R., & Price, K. (1997). Differential Evolution – A Simple and Efficient Heuristic for global Optimization over Continuous Spaces. *Journal of Global Optimization 11*(4), 341–359. https://doi.org/10.1023/A:1008202821328

Stumpf, R. P., Holderied, K., & Sinclair, M. (2003). Determination of water depth with high-resolution satellite imagery over variable bottom types [_eprint: https://aslopubs.onlinelibrary.wiley.com/doi/pdf/10.4319/lo.2003.48.1_part_2.0547]. *Limnology and Oceanography 48*(1part2), 547–556. https://doi.org/10.4319/lo.2003.48.1_part_2.0547

Suanez, S., Yates, M. L., Floc'h, F., & Accensi, M. (2023). Using 17 years of beach/dune profile monitoring to characterize morphological dynamics related to significant extreme water level events in North Brittany (France). *Geomorphology 433*, 108709. https://doi.org/10.1016/j.geomorph.2023.108709

Syvitski, J., & Milliman, J. (2007). Geology, Geography, and Humans Battle for Dominance over the Delivery of Fluvial Sediment to the Coastal Ocean [Publisher: The University of Chicago Press]. *The Journal of Geology 115*(1), 1–19. https://doi.org/10.1086/509246

Syvitski, J., Ángel, J. R., Saito, Y., Overeem, I., Vörösmarty, C. J., Wang, H., & Olago, D. (2022). Earth's sediment cycle during the Anthropocene [Publisher: Nature Publishing Group]. *Nature Reviews Earth & Environment 3*(3), 179–196. https://doi.org/10.1038/s43017-021-00253-w

Syvitski, J. P. M., Peckham, S. D., Hilberman, R., & Mulder, T. (2003). Predicting the terrestrial flux of sediment to the global ocean: a planetary perspective. *Sedimentary Geology 162*(1), 5–24. https://doi.org/10.1016/S0037-0738(03)00232-X

Sánchez-García, E., Palomar-Vázquez, J. M., Pardo-Pascual, J. E., Almonacid-Caballer, J., Cabezas-Rabadán, C., & GOmez-Pujol, L. (2020). An efficient protocol for accurate and massive shoreline definition from mid-resolution satellite imagery. *Coastal Engineering 160*, 103732. https://doi.org/10.1016/j.coastaleng.2020.103732

Taherkhani, M., Vitousek, S., Barnard, P. L., Frazer, N., Anderson, T. R., & Fletcher, C. H. (2020). Sea-level rise exponentially increases coastal flood frequency [Number: 1 Publisher: Nature Publishing Group]. *Scientific Reports 10*(1), 6466. https://doi.org/10.1038/s41598-020-62188-4

Takahashi, K., Montecinos, A., Goubanova, K., & Dewitte, B. (2011). ENSO regimes: Reinterpreting the canonical and Modoki El Niño [_eprint: https://onlinelibrary.wiley.com/doi/pdf/10.1029/2011GL047364]. *Geophysical Research Letters 38*(10). https://doi.org/10.1029/2011GL047364

Taveneau, A., Almar, R., Bergsma, E. W. J., Cissé, C. O. T., Sy, B. A., & Ndour, A. (2024). Monitoring Temporal Sandbar and Shoreline Changes at Saint Louis, Senegal: Using Sentinel-2 Imagery (2015–2022) [Publisher: Multidisciplinary Digital Publishing Institute]. *Remote Sensing 16*(19), 3551. https://doi.org/10.3390/rs16193551

Taylor, K. E. (2001). Summarizing multiple aspects of model performance in a single diagram [_eprint: https://onlinelibrary.wiley.com/doi/pdf/10.1029/2000JD900719]. *Journal of Geophysical Research: Atmospheres 106*(D7), 7183–7192. https://doi.org/10.1029/2000JD900719

Tebaldi, C., Debeire, K., Eyring, V., Fischer, E., Fyfe, J., Friedlingstein, P., Knutti, R., Lowe, J., O'Neill, B., Sanderson, B., van Vuuren, D., Riahi, K., Meinshausen, M., Nicholls, Z., Tokarska, K. B., Hurtt, G., Kriegler, E., Lamarque, J. F., Meehl, G., Moss, R., Bauer, S. E., Boucher, O., Brovkin, V., Byun, Y. H., Dix, M., Gualdi, S., Guo, H., John, J. G., Kharin, S., Kim, Y., Koshiro, T., Ma, L., Olivié, D., Panickal, S., Qiao, F., Rong, X., Rosenbloom, N., Schupfner, M., Séférian, R., Sellar, A., Semmler, T., Shi, X., Song, Z., Steger, C., Stouffer, R., Swart, N., Tachiiri, K., Tang, Q., Tatebe, H., Voldoire, A., Volodin, E., Wyser, K., Xin, X., Yang, S., Yu, Y., & Ziehn, T. (2021). Climate model projections from the Scenario Model Intercomparison Project (ScenarioMIP) of CMIP6 [Publisher: Copernicus GmbH]. *Earth System Dynamics 12*(1), 253–293. https://doi.org/10.5194/esd-12-253-2021

Theil, H. (1992). A Rank-Invariant Method of Linear and Polynomial Regression Analysis. In B. Raj & J. Koerts (Eds.), *Henri Theil's Contributions to Economics and Econometrics: Econometric Theory and Methodology* (pp. 345–381). Springer Netherlands. https://doi.org/10.1007/978-94-011-2546-8_20

Thompson, R. O. R. Y., & Hamon, B. V. (1980). Wave setup of harbor water levels [_eprint: https://agupubs.onlinelibrary.wiley.com/doi/pdf/10.1029/JC085iC02p01151]. *Journal of Geophysical Research: Oceans 85*(C2), 1151–1152. https://doi.org/10.1029/JC085iC02p01151

Timmermann, A., An, S. I., Kug, J. S., Jin, F. F., Cai, W., Capotondi, A., Cobb, K. M., Lengaigne, M., McPhaden, M. J., Stuecker, M. F., Stein, K., Wittenberg, A. T., Yun, K. S., Bayr, T., Chen, H. C., Chikamoto, Y., Dewitte, B., Dommenget, D., Grothe, P., Guilyardi, E., Ham, Y. G., Hayashi, M., Ineson, S., Kang, D., Kim, S., Kim, W., Lee, J. Y., Li, T., Luo, J. J., McGregor, S., Planton, Y., Power, S., Rashid, H., Ren, H. L., Santoso, A., Takahashi, K., Todd, A., Wang, G., Wang, G., Xie, R., Yang, W. H., Yeh, S. W., Yoon, J., Zeller, E., & Zhang, X. (2018). El Niño–Southern Oscillation complexity [Publisher: Nature Publishing Group]. *Nature 559*(7715), 535–545. https://doi.org/10.1038/s41586-018-0252-6

Timmermann, A., Lorenz, S. J., An, S. I., Clement, A., & Xie, S. P. (2007). The Effect of Orbital Forcing on the Mean Climate and Variability of the Tropical Pacific [Publisher: American Meteorological Society Section: Journal of Climate]. *Journal of Climate 20*(16), 4147–4159. https://doi.org/10.1175/JCLI4240.1

Toomey, T., Marcos, M., Wahl, T., Agulles, M., Enríquez, A. R., Amores, A., & Orfila, A. (2024). Wave setup estimation at regional scale: Empirical and modeling-based multi-approach analysis in the Mediterranean Sea. *Weather and Climate Extremes 44*, 100685. https://doi.org/10.1016/j.wace.2024.100685

Trenberth, K. E., & Hurrell, J. W. (1994). Decadal atmosphere-ocean variations in the Pacific. *Climate Dynamics 9*(6), 303–319. https://doi.org/10.1007/BF00204745

Tsimplis, M. N., & Woodworth, P. L. (1994). The global distribution of the seasonal sea level cycle calculated from coastal tide gauge data [_eprint: https://agupubs.onlinelibrary.wiley.com/doi/pdf/10.1029/94JC01115]. *Journal of Geophysical Research: Oceans 99*(C8), 16031–16039. https://doi.org/10.1029/94JC01115

Turner, I. L., Harley, M. D., Almar, R., & Bergsma, E. W. J. (2021). Satellite optical imagery in Coastal Engineering. *Coastal Engineering 167*, 103919. https://doi.org/10.1016/j.coastaleng.2021.103919

Turner, I. L., Harley, M. D., Short, A. D., Simmons, J. A., Bracs, M. A., Phillips, M. S., & Splinter, K. D. (2016). A multi-decade dataset of monthly beach profile surveys and inshore wave forcing at Narrabeen, Australia [Number: 1 Publisher: Nature Publishing Group]. *Scientific Data 3*(1), 160024. https://doi.org/10.1038/sdata.2016.24

Turner, I. L., Leaman, C. K., Harley, M. D., Thran, M. C., David, D. R., Splinter, K. D., Matheen, N., Hansen, J. E., Cuttler, M. V. W., Greenslade, D. J. M., Zieger, S., & Lowe, R. J. (2024). A framework for national-scale coastal storm hazards early warning. *Coastal Engineering 192*, 104571. https://doi.org/10.1016/j.coastaleng.2024.104571

Tătui, F., & Constantin, S. (2020). Nearshore sandbars crest position dynamics analysed based on Earth Observation data. *Remote Sensing of Environment 237*, 111555. https://doi.org/10.1016/j.rse.2019.111555

Vitousek, S., Barnard, P. L., Limber, P., Erikson, L., & Cole, B. (2017). A model integrating longshore and cross-shore processes for predicting long-term shoreline response to climate change [_eprint: https://onlinelibrary.wiley.com/doi/pdf/10.1002/2016JF004065]. *Journal of Geophysical Research: Earth Surface 122*(4), 782–806. https://doi.org/10.1002/2016JF004065

Vitousek, S., Buscombe, D., Vos, K., Barnard, P. L., Ritchie, A. C., & Warrick, J. A. (2023a). The future of coastal monitoring through satellite remote sensing. *Cambridge Prisms: Coastal Futures 1*, e10. https://doi.org/10.1017/cft.2022.4

Vitousek, S., Vos, K., Splinter, K. D., Erikson, L., & Barnard, P. L. (2023b). A Model Integrating Satellite-Derived Shoreline Observations for Predicting Fine-Scale Shoreline Response to Waves and Sea-Level Rise Across Large Coastal Regions [_eprint: https://onlinelibrary.wiley.com/doi/pdf/10.1029/2022JF006936]. *Journal of Geophysical Research: Earth Surface 128*(7), e2022JF006936. https://doi.org/10.1029/2022JF006936

Vos, K., Harley, M., Turner, I., & Splinter, K. (2023a). Pacific shoreline erosion and accretion patterns controlled by El Niño/Southern Oscillation. *Nature Geoscience 16*, 140–146. https://doi.org/10.1038/s41561-022-01117-8)

Vos, K., Harley, M. D., Splinter, K. D., Simmons, J. A., & Turner, I. L. (2019a). Sub-annual to multi-decadal shoreline variability from publicly available satellite imagery. *Coastal Engineering 150*, 160–174. https://doi.org/10.1016/j.coastaleng.2019.04.004

Vos, K., Harley, M. D., Splinter, K. D., Walker, A., & Turner, I. L. (2020). Beach Slopes From Satellite-Derived Shorelines [_eprint: https://onlinelibrary.wiley.com/doi/pdf/10.1029/2020GL088365]. *Geophysical Research Letters 47*(14), e2020GL088365. https://doi.org/10.1029/2020GL088365

Vos, K., Splinter, K. D., Harley, M. D., Simmons, J. A., & Turner, I. L. (2019b). CoastSat: A Google Earth Engine-enabled Python toolkit to extract shorelines from publicly available satellite imagery. *Environmental Modelling & Software 122*, 104528. https://doi.org/10.1016/j.envsoft.2019.104528

Vos, K., Splinter, K. D., Palomar-Vázquez, J., Pardo-Pascual, J. E., Almonacid-Caballer, J., Cabezas-Rabadán, C., Kras, E. C., Luijendijk, A. P., Calkoen, F., Almeida, L. P., Pais, D., Klein, A. H. F., Mao, Y., Harris, D., Castelle, B., Buscombe, D., & Vitousek, S. (2023b). Benchmarking satellite-derived shoreline mapping algorithms [Number: 1 Publisher: Nature Publishing Group]. *Communications Earth & Environment 4*(1), 1–17. https://doi.org/10.1038/s43247-023-01001-2

Vousdoukas, M. I., Mentaschi, L., Voukouvalas, E., Verlaan, M., Jevrejeva, S., Jackson, L. P., & Feyen, L. (2018). Global probabilistic projections of extreme sea levels show intensification of coastal flood hazard [Publisher: Nature Publishing Group]. *Nature Communications 9*(1), 2360. https://doi.org/10.1038/s41467-018-04692-w

Wahl, T., Jain, S., Bender, J., Meyers, S. D., & Luther, M. E. (2015). Increasing risk of compound flooding from storm surge and rainfall for major US cities [Publisher: Nature Publishing Group]. *Nature Climate Change 5*(12), 1093–1097. https://doi.org/10.1038/nclimate2736

Wang, C., Deser, C., Yu, J. Y., DiNezio, P., & Clement, A. (2017). El Niño and Southern Oscillation (ENSO): A Review. *Coral Reefs of the Eastern Tropical Pacific: Persistence and Loss in a Dynamic Environment*, 85–106. https://doi.org/10.1007/978-94-017-7499-4_4

Warrick, J. A., Buscombe, D., Vos, K., Bryan, K. R., Castelle, B., Cooper, J. A. G., Harley, M. D., Jackson, D. W. T., Ludka, B. C., Masselink, G., Palmsten, M. L., Ruiz de Alegria-Arzaburu, A., Sénéchal, N., Sherwood, C. R., Short, A. D., Sogut, E., Splinter, K. D., Stephenson, W. J., Syvitski, J., & Young, A. P. (2024). Coastal shoreline change assessments at global scales [Publisher: Nature Publishing Group]. *Nature Communications 15*(1), 2316. https://doi.org/10.1038/s41467-024-46608-x

Warrick, J. A., Buscombe, D., Vos, K., Kenyon, H., Ritchie, A. C., Harley, M. D., Janda, C., L'Heureux, J., & Vitousek, S. (2025a). Shoreline Seasonality of California's Beaches [_eprint: https://onlinelibrary.wiley.com/doi/pdf/10.1029/2024JF007836]. *Journal of Geophysical Research: Earth Surface 130*(2), e2024JF007836. https://doi.org/10.1029/2024JF007836

Warrick, J. A., Buscombe, D., Vos, K., Ritchie, A. C., & Battalio, B. (2025b). Seasonal rotation of California pocket beaches [_eprint: https://onlinelibrary.wiley.com/doi/pdf/10.1002/esp.70115]. *Earth Surface Processes and Landforms 50*(8), e70115. https://doi.org/10.1002/esp.70115

Warrick, J. A., Stevens, A. W., Miller, I. M., Harrison, S. R., Ritchie, A. C., & Gelfenbaum, G. (2019). World's largest dam removal reverses coastal erosion [Publisher: Nature Publishing Group]. *Scientific Reports 9*(1), 13968. https://doi.org/10.1038/s41598-019-50387-7

Warrick, J. A., Vos, K., Buscombe, D., Ritchie, A. C., & Curtis, J. A. (2023). A Large Sediment Accretion Wave Along a Northern California Littoral Cell [_eprint: https://onlinelibrary.wiley.com/doi/pdf/10.1029/2023JF007135]. *Journal of Geophysical Research: Earth Surface 128*(7), e2023JF007135. https://doi.org/10.1029/2023JF007135

Warrick, J. A., Vos, K., East, A. E., & Vitousek, S. (2022). Fire (plus) flood (equals) beach: coastal response to an exceptional river sediment discharge event [Publisher: Nature Publishing Group]. *Scientific Reports 12*(1), 3848. https://doi.org/10.1038/s41598-022-07209-0

Wessel, P., & Smith, W. H. F. (1996). A global, self-consistent, hierarchical, high-resolution shoreline database [_eprint: https://onlinelibrary.wiley.com/doi/pdf/10.1029/96JB00104]. *Journal of Geophysical Research: Solid Earth 101*(B4), 8741–8743. https://doi.org/10.1029/96JB00104

Wilson, G. (2023). Uncertainty in Nearshore Sand Bar Migration [_eprint: https://agupubs.onlinelibrary.wiley.com/doi/pdf/10.1029/2022JF006928]. *Journal of Geophysical Research: Earth Surface 128*(3), e2022JF006928. https://doi.org/10.1029/2022JF006928

Wolter, K., & Timlin, M. S. (1998). Measuring the strength of ENSO events: How does 1997/98 rank? [_eprint: https://onlinelibrary.wiley.com/doi/pdf/10.1002/j.1477-8696.1998.tb06408.x]. *Weather 53*(9), 315–324. https://doi.org/10.1002/j.1477-8696.1998.tb06408.x

Woodworth, P. L., Melet, A., Marcos, M., Ray, R. D., Wöppelmann, G., Sasaki, Y. N., Cirano, M., Hibbert, A., Huthnance, J. M., Monserrat, S., & Merrifield, M. A. (2019). Forcing Factors Affecting Sea Level Changes at the Coast. *Surveys in Geophysics 40*(6), 1351–1397. https://doi.org/10.1007/s10712-019-09531-1

Wright, L. D., & Short, A. D. (1984). Morphodynamic variabilityof surf zones and beaches: A synthesis.

Xu, H. (2006). Modification of normalised difference water index (NDWI) to enhance open water features in remotely sensed imagery [Publisher: Taylor & Francis _eprint: https://doi.org/10.1080/01431160600589179]. *International Journal of Remote Sensing 27*(14), 3025–3033. https://doi.org/10.1080/01431160600589179

Xu, J. P. (1999). Local wave climate and long-term bed shear stress characteristics in Monterey Bay, CA. *Marine Geology 159*(1), 341–353. https://doi.org/10.1016/S0025-3227(98)00192-3

Yates, M. L., Guza, R. T., & O'Reilly, W. C. (2009). Equilibrium shoreline response: Observations and modeling [_eprint: https://onlinelibrary.wiley.com/doi/pdf/10.1029/2009JC005359]. *Journal of Geophysical Research: Oceans 114*(C9). https://doi.org/10.1029/2009JC005359

Young, I. (1999). Seasonal variability of the global ocean wind and wave climate [_eprint: https://rmets.onlinelibrary.wiley.com/doi/pdf/10.1002/%28SICI%291097-0088%28199907%2919%3A9%3C931%3A%3AAID-JOC412%3E3.0.CO%3B2-O]. *International Journal of Climatology 19*(9), 931–950. https://doi.org/10.1002/(SICI)1097-0088(199907)19:9<931::AID-JOC412>3.0.CO;2-O

Zavala, C., Arcuri, M., Di Meglio, M., Zorzano, A., Otharán, G., Irastorza, A., & Torresi, A. (2021). Deltas: a new classification expanding Bates's concepts. *Journal of Palaeogeography 10*(1), 23. https://doi.org/10.1186/s42501-021-00098-w

Zemp, M., Huss, M., Thibert, E., Eckert, N., McNabb, R., Huber, J., Barandun, M., Machguth, H., Nussbaumer, S. U., Gärtner-Roer, I., Thomson, L., Paul, F., Maussion, F., Kutuzov, S., & Cogley, J. G. (2019). Global glacier mass changes and their contributions to sea-level rise from 1961 to 2016 [Publisher: Nature Publishing Group]. *Nature 568*(7752), 382–386. https://doi.org/10.1038/s41586-019-1071-0

Zhou, J., Wu, Z., Zhao, D., Guan, W., Zhu, C., & Flemming, B. (2020). Giant sand waves on the Taiwan Banks, southern Taiwan Strait: Distribution, morphometric relationships, and hydrologic influence factors in a tide-dominated environment. *Marine Geology 427*, 106238. https://doi.org/10.1016/j.margeo.2020.106238

Zollini, S., Dominici, D., Alicandro, M., Cuevas-González, M., Angelats, E., Ribas, F., & Simarro, G. (2023). New Methodology for Shoreline Extraction Using Optical and Radar (SAR) Satellite Imagery [Publisher: Multidisciplinary Digital Publishing Institute]. *Journal of Marine Science and Engineering 11*(3), 627. https://doi.org/10.3390/jmse11030627

Zăinescu, F., Anthony, E., Vespremeanu-Stroe, A., Besset, M., & Tătui, F. (2023). Concerns about data linking delta land gain to human action [Publisher: Nature Publishing Group]. *Nature 614*(7947), E20–E25. https://doi.org/10.1038/s41586-022-05624-x

RÉPUBLIQUE FRANÇAISE
Liberté Égalité Fraternité

Université de Toulouse

Titre : Observation de l'influence de la variabilité climatique sur la morphodynamique côtière à partir de l'imagerie satellitaire optique

Mots clés : Morphologie côtière, Trait de côte, Variabilité climatique, Satellite, Télédétection

Résumé : L'évolution des côtes sableuses, soumises à une large variétés de pressions naturelles et anthropiques, demeure encore mal comprise à l'échelle globale. Parallèlement, l'essor de l'observation de la Terre par satellite offre un accès sans précédent à des données spatio-temporelles étendues, ouvrant de nouvelles perspectives pour l'analyse de la morphodynamique côtière.
Dans ce contexte, cette thèse vise à mieux comprendre la dynamique des côtes sableuses à l'échelle mondiale à travers l'étude de l'évolution du trait de côte, ligne d'interface terre/mer, sur plusieurs décennies, en lien avec les modes de variabilité climatique. À cette fin, une chaîne de traitement automatisée a été développée en Python, pour extraire, traiter et analyser les images des missions Sentinel-2 et Landsat (5, 7, 8, 9). Combinant plusieurs indices spectraux et méthodes de seuillage, elle permet l'application systématique d'approches personnalisables.
1) Une validation sur huit sites ateliers met en évidence une forte dépendance de la précision des mesures aux conditions environnementales locales. Les sites macro-tidaux, en particulier, présentent une sensibilité accrue aux méthodes utilisées, générant des séries temporelles de positions du trait de côte plus bruitées. Cette hétérogénéité a permis d'établir des lois empiriques liant l'erreur de détection à la pente de plage et l'amplitude de marée, offrant un cadre pour évaluer la fiabilité des observations dans des zones dépourvues de données de terrain.
2) L'outil a ensuite été appliqué à la façade pacifique nord-américaine pour produire un jeu de données couvrant 25 ans (1997–2022). L'analyse met en évidence des variations saisonnières marquées selon la latitude, avec des excursions du trait de côte dépassant 25 m dans les états de Washington et Oregon, contre moins de 10 m au sud de la Californie. Ces fluctuations sont fortement corrélées à la puissance des vagues dans le nord de la région, tandis qu'en Basse-Californie, elles sont davantage liées aux variations du niveau de la mer. À l'échelle interannuelle, les réponses morphodynamiques varient selon les régions : au sud, les variations sont modérées et concentrées lors des épisodes ENSO (El Niño Southern Oscillation), alors qu'au nord, les réponses sont plus complexes et moins systématiques. Cette étude souligne l'influence spatiale différenciée d'ENSO, qui module la trajectoire et l'intensité des tempêtes hivernales, affectant les dynamiques d'érosion.
3) Une étude complémentaire approfondit ensuite la compréhension du trait de côte en se basant sur des données de terrain sur quatre sites pour étudier l'évolution des profils de plage intertidaux à l'aide de méthodes statistiques. Cette étude permet d'identifier une dynamique structurées autour de deux mécanismes principaux : la translation du profil intertidal et l'évolution de sa pente. Cette étude intérroge la nature ambivalente du trait de côte, qui peut être appréhendé soit comme un indicateur purement morphologique — défini comme l'intersection entre une élévation donnée et le profil de plage —, soit comme un indicateur hydro-morphologique, dont la position intègre les variations spatio-temporelles du niveau d'eau liées aux forçages climatiques. Ces deux conceptions impliquent des dynamiques distinctes, compliquant davantage l'interprétation de l'évolution du trait de côte, qui elle même n'est qu'un indicateur de l'évolution globale de la plage.
Enfin, cette thèse ouvre des perspectives concrètes pour la surveillance côtière à grande échelle, en proposant une méthodologie reproductible qui s'imbrique dans d'autres axes d'observations et de modélisations de la hydro-morphodynamique côtière, permettant de mieux comprendre et anticiper les évolutions littorales et d'appuyer la prise de décision dans un contexte de changement global.

Title: Climate signals in coastal morphodynamics observed from optical satellite imagery

Key words: Coastal morphology, Shoreline, Climate variabiility, Satellite, Remote Sensing

Abstract: The evolution of sandy coasts, subject to a wide variety of natural and anthropogenic pressures, remains poorly understood at the global scale. At the same time, the rapid expansion of Earth observation from satellites provides unprecedented access to extensive spatio-temporal datasets, opening new perspectives for the analysis of coastal morphodynamics.
In this context, this thesis aims to improve our understanding of sandy coast dynamics worldwide through the study of shoreline evolution — the land–sea interface — over several decades, in connection with large-scale climate variability modes. To this end, an automated processing chain was developed in Python to extract, process, and analyze images from the Sentinel-2 and Landsat (5, 7, 8, 9) missions. Combining multiple spectral indices and thresholding methods, it allows for the systematic application of customizable approaches.
1) Validation across eight pilot sites highlights a strong dependence of measurement accuracy on local environmental conditions. Macrotidal sites, in particular, exhibit increased sensitivity to the methods applied, producing noisier shoreline position time series. This heterogeneity enabled the derivation of empirical relationships linking detection errors to beach slope and tidal range, providing a framework for assessing the reliability of observations in areas lacking in situ data.
2) The tool was then applied to the North American Pacific coast to generate a dataset spanning 25 years (1997–2022). The analysis reveals pronounced seasonal variations according to latitude, with shoreline excursions exceeding 25 m in Washington and Oregon, compared to less than 10 m in southern California. These fluctuations are strongly correlated with wave power in the north of the region, while in Baja California they are more closely linked to sea-level variability. At the interannual scale, morphodynamic responses vary across regions: in the south, changes are moderate and concentrated during ENSO (El Niño–Southern Oscillation) events, whereas in the north responses are more complex and less systematic. This study underscores the differentiated spatial influence of ENSO, which modulates the trajectory and intensity of winter storms, thereby affecting erosion dynamics.
3)A complementary study further explores the shoreline concept by analyzing field data from four sites to investigate the evolution of intertidal beach profiles using statistical methods. This analysis identifies a dynamic structured around two main mechanisms: translation of the intertidal profile and changes in its slope. It also questions the ambivalent nature of the shoreline, which can be understood either as a purely morphological indicator — defined as the intersection between a given elevation and the beach profile — or as a hydro-morphological indicator, whose position reflects spatio-temporal variations in water level driven by climatic forcing. These two conceptualizations imply distinct dynamics, further complicating the interpretation of shoreline change, which is itself not directly representative of the overall beach evolution.
Finally, this thesis opens concrete perspectives for large-scale coastal monitoring by proposing a reproducible methodology that integrates with other observational and modeling approaches in coastal hydro-morphodynamics. This framework contributes to the understanding and anticipation of coastal change and supporting decision-making in the context of global change.